Compact Integrated Active-Passive Approach for Axial Fan Noise Control

Kenji Homma

Dissertation submitted to the Faculty of the Virginia Polytechnic Institute and State University in partial fulfillment of the requirements of the degree of

Doctor of Philosophy
in
Mechanical Engineering

Dr. Chris R. Fuller, Chairman
Dr. William T. Baumann
Dr. Daniel J. Inman
Dr. Marty E. Johnson
Dr. Donald J. Leo

September, 2004
Blacksburg, VA

Keyword: axial fan noise, active-passive control, sound propagation in ducts

Compact Integrated Active-Passive Approach for Axial Fan Noise Control

by

Kenji Homma

Committee Chairman: Chris R. Fuller

Mechanical Engineering

(ABSTRACT)

A new active-passive approach for the control of noise radiated from a small axial fan was investigated. The approach involved the installation of an axial fan into a short duct with both passive and active noise control functions. First, a systematic methodology for the analytical modeling of finite-length ducts with multiple discontinuities was formulated. The procedure involved the modeling of a duct as a collection of simple duct sections, which were interconnected at multiple junctions.

Analytical studies have shown that a short lined duct provides passive noise reduction effects through the mass-loading effect of the duct air volume at low frequencies and the sound absorption by a passive liner at high frequencies. It was also shown that active control can provide further noise attenuations at low-to-mid frequencies, thereby enhancing the overall noise control performance. Two alternate designs of active-passive noise control fan duct were considered. One was a simple non-segmented duct with a 2x2 active control and the other was an internally segmented duct with an 8x8 active control. It was indicated that the latter design possesses a significantly higher global noise control potential than the former with respect to both bandwidth and attenuation level. This was attributed to the reduction of the unwanted pressure contributions from the duct cross modes through the high frequency shifting of the associated cut-on frequencies.

The experimental validation of the noise control approach was also carried out. An active-passive noise control fan duct incorporating the segmented duct design with 8x8 active control was constructed in conjunction with a hybrid feedforward-feedback control system. Experimental results have shown significant reductions in the total fan

noise power associated with the first four BPF tones by the feedforward control and the broadband fan noise power by the feedback control. The overall active-passive noise control characteristics were observed to be in accordance with the analytical results.

Acknowledgements

First of all, I would like to thank my research advisor, Dr. Chris Fuller for giving me the opportunity to work under his guidance. He has provided me with an excellent research environment, which made it possible for me to carry out my Ph.D. study and to gain valuable knowledge and experience in the field of acoustics and vibration. I would also like to thank Dr. Marty Johnson for his guidance and suggestions. His advice has been particularly helpful. I would also express my gratitude to Dr. William Baumann, Dr. Daniel Inman and Dr. Donald Leo for serving as the members of my dissertation committee.

I would also like to thank Dr. Mike Kidner for his advice. Thanks are also due to the staff and colleagues in the Vibration and Acoustics Laboratories for their support. I would also like to express thanks to, Dr. Kaleen Man, Dr. Marco Beltman, Mr. Daryl Nelson of Intel Corp. for sponsoring the research and their assistance.

I also wish to express gratitude to my parents and brothers in Japan and my parents-in-law in Sri Lanka for their support and encouragement throughout my graduate studies. And most importantly, I would like to give thanks to my wife, Sharmila. I would not have come this far if it was not for her support. We have achieved this together.

Contents

List of Figures

List of Tables

Chapter 1

Introduction

Fans continue to be a major source of noise pollution. They are used in a multitude of situations, whenever a movement of air is required. Common examples include: air conditioning of buildings, air management in manufacturing facilities, appliances such as air conditioners and humidifiers, cooling of electric equipments like computers and projectors.

Noise emitted from the fans used in small electric equipments such as desktop computers is becoming especially problematic in recent years. There is an increasing pressure to use higher speed, thus inevitably noisier fans in order to satisfy the cooling needs of faster, and often more heat-producing computer processors [1]. Since desktop computers are used typically in quiet environments like office spaces, the margin of tolerance against noise emission is especially small. As a consequence, there is much interest in finding effective and efficient ways to reduce the noise emission from fans.

1.1 Proposed Noise Control Approach

In this thesis, a novel approach for controlling the radiation of noise from a fan is proposed and its noise control characteristics are studied both analytically and experimentally. The approach is to enclose a fan in a carefully designed compact finite-length duct, which possesses both passive and active noise reduction functions. Passive noise reduction is attributed, as it shall be shown later in the study, to the inherent property of a short finite duct and also to the sound-absorptive passive liner installed in the duct. Active noise reduction is obtained by a specially designed active noise control system integrated into the duct. As it will be apparent in the literature review following this section, there has been little work done in the past investigating this "active-passive

noise control fan duct" approach, including the acoustical impact of adding a short duct to a fan, and its implication to the overall noise control performance.

1.2 Literature Review

A literature review on the control of noise emitted from a fan is presented. Attention is given particularly to those research works addressing active control of fan noise emission. Subsequently, a review is provided on those literatures, which may not directly deal with the control of fan noise, but are nevertheless highly relevant to the present study. These include literatures on analytical modeling of ducts and various methods of active noise control of in-duct sound propagation.

1.2.1 Control of Global Fan Noise Emission

Generally, there are two approaches to the reduction of noise emission from a fan. One approach is to redesign the geometry of the fan itself to make it quieter. However, this is apparently not a straightforward task, due to the complexity involved in the mechanisms of fan noise generations, which is evident from a long history of research in this area [2]. The other approach is to apply some kind of external silencing devices. The approach described in this thesis belongs to the latter.

Active control of global fan noise emission has been the topic of many research studies. Especially numerous are the studies on active control of BPF (Blade Passing Frequency) fan noise tones. BPF noise is a type of periodic fan noise originated from aerodynamic interactions between rotating fan blades and stationary objects like struts and stators. Quinlan [3] analyzed an approach where an active dipole representing a control speaker is placed close to a fan as a dipole source. He has shown that this results in the alteration of acoustic radiation impedance seen by the fan dipole, which in turn results in the reduction of total fan noise power. In his accompanying experiment, a fan and a control speaker were placed side by side in a baffle, and this arrangement resulted in the elimination of the first two BPF tones. A feedforward controller based on the FXLMS algorithm was used in conjunction with a rotational sensor installed in the fan hub to produce the required reference signal. Lauchle and others [4] investigated the

utilization of a fan itself as an active acoustic source for active noise control. The fan unit was forced to oscillate in the direction of the fan axis by using a shaker to produce control sounds. Their experimental results also showed elimination of the first two BPF tones. Gee and Sommerfeldt [5] investigated the use of multiple speakers in conjunction with a multi-channel feedforward controller for the reduction of BPF noise from a fan. Their experimental results indicated improvement in global noise control performance as a result of multiple actuator usage. Similar feedforward active noise control schemes have been applied to control BPF tones emitted from a variety of fans, such as automotive engine cooling fan [6], jet fan for freeway tunnel ventilation [7], centrifugal fan [8, 9] and aircraft turbofan engine [10].

In contrast, studies addressing global active control of the other important noise component, broadband fan noise, have been limited in number. O'Brien and others [11] have used an optimal feedback control approach for reducing broadband noise from a centrifugal fan in a duct. The research was somewhat unique in that a novel magnetic bearing actuator was utilized. However, only a limited reduction performance (a few Hz in bandwidth) was reported. Minogue and others [12] experimented with active control of broadband noise emitted from a fan installed in a network server. Their work involved a finite duct (about 20-30 cm) with a feedforward active noise control system positioned at an air outlet opening of a server. Though a good local reduction of broadband noise was indicated, there were no results on overall global fan noise reduction effect.

1.2.2 Control of In-Duct Sound Propagation

In the present approach, a fan is installed into a finite-length duct. As a consequence, the problem may be treated in the framework of the theory of sound propagating in ducts. Doak presented a comprehensive theory of sound in rectangular ducts in his 100-plus paged, double paper [13, 14]: one paper on infinite duct and the other on finite-length duct. Much of the second paper [14] analyzed the modal wave scattering (or modal impedance, alternatively) associated with a duct open end, which is important for the determination of both interior and exterior sound field of a finite-length duct. Wang and Tszeng [15] used a modeling approach similar to Doak for analyzing a finite duct of circular cross-section. They too have focused on the modal impedance of open ends,

which was in this case, circular. Osborne [16] studied the modal wave scattering characteristics of a curved bend, a type of discontinuity, in a rectangular duct. Redmore and Mulholland [17] used a modal coupling approach in order to determine the modal wave scattering characteristics of a side branch in a rectangular duct. A modal coupling approach was also used by Muehleisen and Swanson [18] to study the modal wave scattering characteristics of a planer discontinuity (e.g. a sudden cross-sectional area change). Muehleisen investigated the modal wave scattering characteristics of various discontinuities in his Ph.D. thesis [19]. Muheilsen also proposed, in his thesis, a concept of modeling a discontinuity as a "junction" which joins multiple simple duct segments. Junctions were characterized in term of modal impedance or modal scattering matrix, which were obtained by applying the Green's function method. In the present thesis, this modeling approach is extended to include ducts with multiple discontinuities, such as duct open ends, acoustic sources and segmentations.

Sounds propagating in a duct can be controlled by traditional noise control approaches, such as sound absorptive liner, turned resonators or duct discontinuities (e.g. expansion chamber). These conventional noise control methods could certainly be effective. However, in certain applications, the implementation of these conventional methods can be difficult due to size, cost and other constraints. For example, in small electric equipment cooling applications (like desktop computers), a successful utilization of conventional noise control methods, such as passive liner, is difficult due to generally tight volume and airflow constraints. Furthermore, the applicable frequency range of a conventional method tends to be limited. For example, passive liners tend to be only effective at high frequencies. A tuned resonator is only effective in a relatively narrow frequency band around its tuning frequency and its size has to increase as the target frequency decreases.

The shortcomings of the conventional noise control methods can be compensated by the use of active noise control. Active noise control achieves noise reduction by introducing secondary sounds, which destructively interfere with disturbance sounds. It is especially suited for the control of low frequency sound propagated in a duct. For example, by incorporating an active control system with a conventional passive liner in a

duct, noise can be reduced over a wider frequency range, thereby enhancing the overall noise control effect.

Many researchers have investigated the active control of sound in a duct. Nelson and Elliott carried out much work on the fundamental mechanisms of active noise control for one-dimensional ducts [20]. Trinder and Nelson [21] used a higher order finite duct model and studied the sound field in the vicinity of a control speaker in detail. Stell and Bernhard [22, 23] analytically investigated active control of multi-modal sound in a duct. They studied the effect of different factors on the performance of active noise control, including wave reflections at duct terminations, presence of evanescent modes and different control objectives. Other researchers have also investigated the active control of multi-modal sound [24, 26, 26, 27].

The active noise control in a finite duct is actively researched in the field of aircraft turbofan engine noise control. Joseph [28] and others investigated the active control of harmonic sound radiated from a finite-length circular duct using an analytical model. Risi and Burdisso [29] also presented an analytical model, which was based on an infinite duct model, to predict the radiated sound from a duct inlet. Burdisso and others [30] presented a model with more realistic representation of fan noise. Hutcheson [31] studied the turbofan engine active noise control problem using a comprehensive analytical model of a finite duct and a fan including the duct open end reflections, the effect of air mean flow, and the interactions of inlet and outlet sounds.

All investigations described above, except for one by Hutcheson [31], used simplified models for the duct open-ends in a finite-length duct, neglecting the cross modal coupling effect. In the present thesis, the cross modal coupling effect is naturally included into the matrix-based duct model. This was done by incorporating a full modal impedance matrix of the duct opening, which was pre-calculated by a numerical method. Investigations of in-duct active noise control using finite duct models with this level of detail have been limited and this thesis also contributes in that aspect.

As for the methods of active noise control, there are basically two distinct control strategies: feedforward and feedback. For a single channel feedforward active noise control, a microphone is typically positioned upstream of an active source in order to obtain the reference signal which contains an advanced information about the incoming

disturbance. Then, based on this reference signal, the controller "predicts" the effect of the incoming disturbance sensed at an error microphone positioned downstream and produces appropriate control sound to counteract the disturbance. A 1936 patent by Paul Lueg [32] is considered to be the origin of this feedforward active control concept. On the other hand, for a single-channel feedback active noise control, a controller is driven only by the signal from an error microphone placed directly in front of an active source. Unlike the feedforward control, which utilizes "future" disturbance information, the feedback active noise control uses only the current information on disturbance. A 1953 work by Olson and May [33] is considered to be the earliest work on this feedback active noise control.

The first practical implementations of the feedforward active control using digital processing techniques and hardware were carried out first by Kido [34] and Chaplin [35] in the 1970's. Chaplin proposed a type of feedforward control strategy called "waveform synthesis". In this strategy, a tachometer signal from a rotating machine was used to synthesize the control signal waveform for the reduction of the periodic noise. This strategy can alternatively be implemented by using FIR filters driven by the reference signal consisting of periodic impulses [20]. In the experimental studies of Chapter 4 in the present thesis, the latter approach is utilized to control tonal fan noise.

Other researchers have studied and implemented the feedback active noise control in ducts. Hong and others [36] proposed the so called "tight-coupled monopole" for reducing broadband noise transmitted inside duct systems. The device consisted of a microphone and a speaker connected in a simple negative feedback arrangement. Trider and Nelson [21] studied a similar device in conjunction with a higher order finite duct model and investigated the optimal position of the microphone with respect to the speaker. Clark and Frampton [37] used phase compensating filters in a feedback loop to enhance the noise reduction performance. Some researchers have applied more sophisticated techniques in designing feedback controllers. Hong and others [38] used the LQG (Liner Quadratic Gaussian) optimal control technique. O'Brien [11] used the H^{∞} optimal control design method for the feedback control of centrifugal fan noise in a duct.

A feedforward and a feedback control system can be combined to obtain a hybrid control system. For the experimental studies in Chapter 4 of the present thesis, a hybrid active noise control system is implemented. In this system, the feedforward control part is configured to reduce BPF tones while the feedback control part is designed to reduce broadband fan noise. The idea of the hybrid control approach is not new and it has been applied in different applications [39-43]. However, to the best of author's knowledge, the application of the BPF feedforward-broadband feedback control approach to the control of fan noise emission has not been reported in literature.

1.3 Thesis Scope and Contributions

The overall objective of this thesis is to investigate the noise control characteristics of the proposed active-passive control fan duct approach. There are two major components to the investigation; one is theoretical and the other is experimental.

The purpose of the analytical investigation is to determine the potential noise control performance achievable by the proposed approach. In order to facilitate the analytical studies, a general matrix-based methodology for modeling ducts with multiple discontinuities is formulated. Then, comprehensive analytical models of finite-length, active-passive ducts are developed in order to obtain insights into the noise attenuation characteristics. Two alternate designs of the active-passive control fan duct are considered. The first design is a simple, passively-lined, finite-length duct combined with a two-actuators-two-sensors (2x2) active noise control. The second design is a finite duct with the same outer dimensions as the first one, but with its inner space segmented into small duct segments. An 8x8 active noise control is used in conjunction with the second design. Passive and active noise control characteristics are calculated with respect to each of these two design cases and compared. Furthermore, both feedforward and feedback approaches are considered for the active noise control. The influence of different error microphone positions to the global active noise control performance is also investigated.

The second major component in this thesis is the experimental validation of the active-passive fan duct approach. The design and the implementation of an experimental active-passive control fan duct unit are performed. The constructed active-passive fan

duct incorporates the segmented duct design, which is found to be preferable based on the results from the analytical studies. A hybrid feedforward-feedback active noise control approach is utilized in order to achieve simultaneous control of both BPF and broadband fan noise content. The active control effects are measured with respect to each of the feedforward and the feedback control individually as well as the hybrid control in order to examine the performance advantages of the hybrid control approach. Furthermore, the effect of change in the fan operating condition to the active-passive noise control performance is also investigated. Finally, the practical utility of the active-passive approach is demonstrated by applying it to control the noise emitted from a fan in an actual desktop computer chassis.

The original contributions of the present thesis are as follows:

- **The development of a new compact active-passive approach to the control of noise radiated from axial fans:** The proposed approach is unique in that it aims to reduce the *global noise emission level of a fan as a noise source* by utilizing both the passive acoustic characteristics of a short duct and the active control elements tightly integrated in a compact package.

- **The formulation of a methodology for the systematic modeling of ducts with multiple discontinuities:** The methodology is based on the method utilized by Muheilsen [20] for the determination of multi-modal scattering characteristics of various duct discontinuities. The present work extends his approach to handle the modeling of a duct with complex geometries.

- **The development and the use of high-fidelity theoretical models for the study of finite-duct active-passive noise control:** The proposed matrix-based modeling approach is especially suited for the development of comprehensive analytical models of finite-length ducts with active and passive elements. One notable feature of the developed duct is the use of full modal impedance matrices with the cross-coupling terms, which have been typically omitted in the previous work on active noise control in finite ducts.

- **Exploration of potential noise control performance achievable by the active-passive fan duct approach:** Using the developed analytical models, the potential performances of the active-passive fan duct are studied. A novel, segmented duct design with an 8x8 control configuration is studied and its performance is compared against a simple, non-segmented duct with a 2x2 control. Much attention is also paid to the effect of error microphone positions to the local and global noise reduction performances. Furthermore, theoretical performances of both feedforward and feedback active noise control are considered.

- **The use of a hybrid feedforward/feedback control approach for the simultaneous reduction of both BPF and broadband noise emission from an axial fan:** In contrast to the previous work on active control of fan noise which mostly focused on the reduction of harmonic BPF fan noise, the present thesis addresses the active control of both BPF and broadband fan noise components simultaneously. This is achieved by the use of a combination of BPF feedforward and broadband feedback active noise control.

1.4 Thesis Outline

After the introduction in this chapter, Chapter 2 discusses the matrix method used in the modeling of the fan ducts. A fan model is also presented, which is followed by the results from a model validation experiment. Then, in the later part of the chapter, the modeling approaches to simulate the performances of the active noise control are presented and discussed. Chapter 3 presents the analytical studies on the noise control characteristics of the active-passive noise control fan duct approach. The analytical models of the two alternate designs of the active-passive fan duct are presented first. Then, the active-passive noise control performances for the two designs are calculated and compared. Some experimental results are also provided in order to validate the analytical models. Chapter 4 presents the experimental validation of the active-passive control fan duct approach. The chapter starts with the descriptions of the developed experimental unit of an active-passive control fan duct and the implementation of the hybrid feedforward-feedback active noise control system. The experimental apparatus for measuring the global noise control performances of the fan duct is also described. The experimental active-passive noise control performance results are presented and the features are discussed in relation to the findings obtained from the analytical studies in Chapter 3. Overall conclusions of the present thesis are presented in Chapter 5 along with the suggestions for future work.

Chapter 2

Analytical Modeling Approach

Approaches for developing the analytical models of the active-passive noise control fan duct are described in this chapter. A review of the theory of sound propagation in a rectangular duct is presented. Then, a general description of the method used for modeling a complex duct system with multiple discontinuities is provided. The method described here is applied for modeling active-passive noise control fan ducts in Chapter 3. Furthermore, the approach used for modeling the fan noise source is presented along with some experimental validations. Lastly, the descriptions of active noise control approaches, including feedforward and feedback control, are presented.

2.1 Sound Propagation in a Duct

Pressure fluctuation, p, or sound is characterized by the wave equation,

$$\nabla^2 p(x,y,z,t) = \frac{1}{c^2}\frac{\partial^2}{\partial t^2} p(x,y,z,t) \tag{2.1}$$

where c is the speed of sound. Acoustic pressure, p, is related to particle velocity, u, by

$$\rho \frac{\partial \vec{u}(x,y,z,t)}{\partial t} = -\nabla p(x,y,z,t) \tag{2.2}$$

where ρ is the air density.

The Fourier transform is defined as

$$F(x,y,z,\omega) = \int_{-\infty}^{+\infty} f(x,y,z,t) e^{-j\omega t} dt \tag{2.3}$$

which can be used to obtain the Frequency domain equivalent of the wave equation (the Helmholtz equation),

$$(\nabla^2 + k^2)p(x,y,z,\omega) = 0 \tag{2.4}$$

where the wave number, k, is ω/c. The Frequency domain equivalent of Equation (2.2) is

$$\vec{u}(x,y,z,\omega) = \frac{j}{k\rho c}\nabla p(x,y,z,\omega) \tag{2.5}$$

which is called the Euler's equation

For an infinite duct with rigid sidewalls, a solution of Equation (2.4) is given by

$$p(x,y,z) = \sum_M (a_M e^{-jk_M z} + b_M e^{+jk_M z})\psi_M(x,y) \tag{2.6}$$

where a_M and b_M are the complex amplitudes of the modal wave components, k_M is the wave number of the M-th mode and $\psi_M(x,y)$ is the eigenfunction or the mode-shape function describing the spatial distribution of pressure over the duct cross section. The function, $\psi_M(x,y)$, satisfies the orthogonality condition,

$$\frac{1}{S}\iint_S \psi_M \ \psi_R dS = \begin{cases} 1 & for\ M = R \\ 0 & for\ M \neq R \end{cases} \tag{2.7}$$

where S is the duct cross-sectional area.

The propagation and the decay of a modal wave component (or a mode) is dictated by the value of the modal wave number, k_M,

$$k_M = -j\sqrt{\kappa_M - k} \tag{2.8}$$

where κ_M is the eigenvalue associated with the mode. Note that when $k > \kappa_M$, the modal wave number, k_M, is a positive real value and the mode propagates down the duct without amplitude decay. A mode in this condition is commonly referred to as, "cut-on". On the other hand, when $k < \kappa_M$, the wave number, k_M, becomes a negative imaginary value and the mode decays exponentially with z. Then, the mode is said to be "cut-off" or "evanescent". Contributions from these decaying cut-off modes to the total pressure field are called "near field" effects since these are present in the locality of sound sources (or discontinuities).

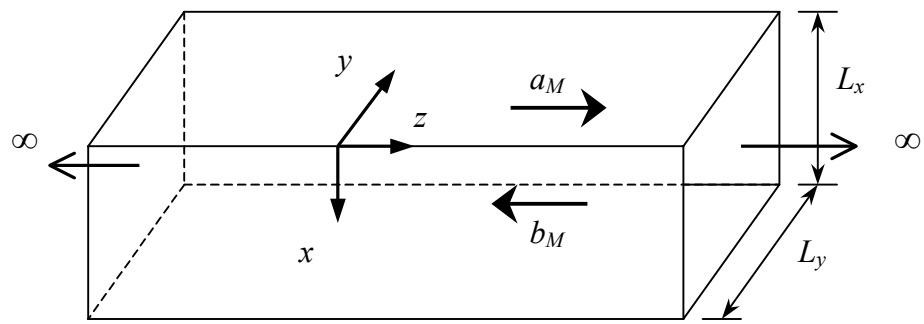

Figure 2.1. Sound propagating in an infinite duct (rectangular)

For a rectangular duct with sides, *Lx* and *Ly*, as shown in Figure 2.1, the mode shape function, $\psi_M(x,y)$, becomes

$$\psi_M(x,y) = \frac{\cos(\frac{m_x\pi}{L_x}x)\cos(\frac{m_y\pi}{L_y}y)}{\sqrt{\Lambda_{m_x}\Lambda_{m_y}}} \tag{2.9}$$

where m_x and m_y are the x and the y mode indices (i.e. $M = (m_x, m_y)$). The quantities, Λ_{mx} and Λ_{my}, are the normalization constants and given by

$$\Lambda_{m_x} = \begin{cases} 1 & for \quad m_x = 0 \\ \frac{1}{2} & for \quad m_x \neq 0 \end{cases} \tag{2.10}$$

The modal wave number, k_M, for a rectangular duct is

$$k_M = k_{m_x m_y} = -j\sqrt{(\frac{m_x\pi}{L_x})^2 + (\frac{m_y\pi}{L_y})^2 - k} \tag{2.11}$$

Substituting Equation (2.5) into (2.6), the z component (normal to the duct cross section) of particle velocity becomes

$$u_z(x,y,z) = \sum_M Y_M(a_M e^{-jk_M z} - b_M e^{+jk_M z})\psi_M(x,y) \tag{2.12}$$

where Y_M is the specific modal admittance of the duct and given by

$$Y_M = \frac{k_M}{k\rho c} \tag{2.13}$$

2.2 Modeling of Duct with Multiple Discontinuities

Equations presented so far describe sound in a simple infinite duct. Here, a modeling method is introduced which enables the modeling of more complex ducts with multiple discontinuities. The method is based on the concept called, "General Junction Theory", described in a thesis by Muehleisen [19] where it was used in investigating the scattering characteristics of modal waves at relatively simple duct discontinuities, such as bend and duct open ends. In the present study, this concept is extended and systematically applied to model ducts with multiple discontinuities.

2.2.1 Duct-Junction System Model

In this modeling approach, a duct with complex internal geometry is considered to be composed of multiple duct segments connected at, so called, "Junctions" which represent regions of discontinuity. An illustration of this duct-junction system is illustrated in Figure 2.2 below.

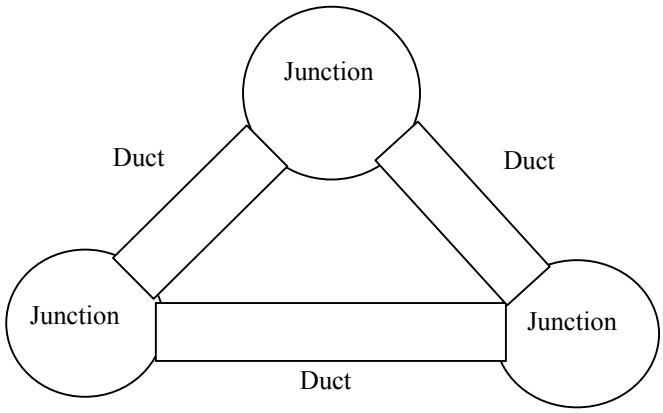

Figure 2.2. A duct-junction system

Pressure and particle velocity in each duct segment are described by Equations (2.6) and (2.12), respectively. By including only a finite number of modes, M, these equations can be re-written into a matrix format as

$$
\begin{aligned}
p(x,y,z) &= \begin{bmatrix} a_1 e^{-jk_1 z} + b_1 e^{+jk_1 z} \\ a_2 e^{-jk_2 z} + b_2 e^{+jk_2 z} \\ \vdots \end{bmatrix}^T \cdot \begin{bmatrix} \psi_1(x,y) \\ \psi_2(x,y) \\ \vdots \end{bmatrix} \\
&= \left[a_M e^{-jk_M z} + b_M e^{+jk_M z}\right]^T \cdot \left[\psi_M(x,y)\right] \\
&= \mathbf{p_M}^T \cdot \boldsymbol{\psi}_\mathbf{M}
\end{aligned}
\tag{2.14}
$$

where $\mathbf{p_M}$ is a vector containing all modal pressures in a duct segment and $\boldsymbol{\psi}_\mathbf{M}$ is a vector of corresponding mode shape functions. The modal pressure vector, $\mathbf{p_M}$, may further be written as

$$
\begin{aligned}
\mathbf{p_M} &= \left[a_M e^{-jk_M z} + b_M e^{+jk_M z}\right] \\
&= \left[e^{-jk_M z}\right]_{diag} \cdot \left[a_M\right] + \left[e^{+jk_M z}\right]_{diag} \cdot \left[b_M\right] \\
&= \mathbf{e}^- \cdot \mathbf{a_M} + \mathbf{e}^+ \cdot \mathbf{b_M}
\end{aligned}
\tag{2.15}
$$

where the designation, $[\ ]_{diag,}$ signifies a diagonal matrix.

Similarly for particle velocity,

$$
\begin{aligned}
u(x,y,z) &= \begin{bmatrix} y_1\left(a_1 e^{-jk_1 z} + b_1 e^{+jk_1 z}\right) \\ y_2\left(a_2 e^{-jk_2 z} + b_2 e^{+jk_2 z}\right) \\ \vdots \end{bmatrix}^T \cdot \begin{bmatrix} \psi_1(x,y) \\ \psi_2(x,y) \\ \vdots \end{bmatrix} \\
&= \left[y_M\left(a_M e^{-jk_M z} + b_M e^{+jk_M z}\right)\right]^T \cdot \left[\psi_M(x,y)\right] \\
&= \mathbf{u_M}^T \cdot \boldsymbol{\psi}_\mathbf{M}
\end{aligned}
\tag{2.16}
$$

where $\mathbf{u_M}$ is the modal velocity vector and

$$
\begin{aligned}
\mathbf{u_M} &= \left[y_M\left(a_M e^{-jk_M z} - b_M e^{+jk_M z}\right)\right] \\
&= \left[y_M\right]_{diag} \cdot \left(\left[e^{-jk_M z}\right]_{diag}\left[a_M\right] - \left[e^{+jk_M z}\right]_{diag} \cdot \left[b_M\right]\right) \\
&= \mathbf{y_M}\left(\mathbf{a_M} \cdot \mathbf{e}^- - \mathbf{b_M} \cdot \mathbf{e}^+\right)
\end{aligned}
\tag{2.17}
$$

On the other hand, the junctions which join the duct segments are characterized in terms of relationships between the modal pressure vector, $\mathbf{p}_\mathbf{R}^l$, at the *l*-th duct-junction interface and the modal velocity vector, $\mathbf{u}_\mathbf{M}^i$,at the *i*-th interface for each junction. This is expressed in a matrix form as

$$
\begin{bmatrix} \mathbf{p}_\mathbf{R}^1 \\ \mathbf{p}_\mathbf{R}^2 \\ \vdots \end{bmatrix} = \begin{bmatrix} \mathbf{z}_\mathbf{RM}^{11} & \mathbf{z}_\mathbf{RM}^{12} & \cdots \\ \mathbf{z}_\mathbf{RM}^{21} & \mathbf{z}_\mathbf{RM}^{22} & \cdots \\ \vdots & \vdots & \ddots \end{bmatrix} \cdot \begin{bmatrix} \mathbf{u}_\mathbf{M}^1 \\ \mathbf{u}_\mathbf{M}^2 \\ \vdots \end{bmatrix}
\tag{2.18}
$$

or

$$
\mathbf{P_R} = \mathbf{Z_{RM}} \cdot \mathbf{U_M}
\tag{2.19}
$$

where $\mathbf{Z_{RM}}$ is the modal impedance matrix relating the modal pressures and the modal velocities for all the combinations of the interfaces (*l* ,*i*), and the duct modes, (*R*, *M*) in a particular junction. The matrix, $\mathbf{Z_{RM}}$, shall be referred as, "junction modal impedance matrix", from this point on.

Equation (2.18)can be written in terms of modal wave amplitudes, a_M and b_M in the adjacent duct segments by substituting Equation (2.15) and Equation (2.17) into Equation (2.18) as

$$
\begin{bmatrix} \mathbf{e}^-{}_1 \cdot \mathbf{a}_{\mathbf{M}1} + \mathbf{e}^+{}_1 \cdot \mathbf{b}_{\mathbf{M}1} \cdot \\ \mathbf{e}^-{}_2 \cdot \mathbf{a}_{\mathbf{M}2} + \mathbf{e}^+{}_2 \cdot \mathbf{b}_{\mathbf{M}2} \\ \vdots \end{bmatrix} = \begin{bmatrix} \mathbf{z}_\mathbf{RM}^{11} & \mathbf{z}_\mathbf{RM}^{12} & \cdots \\ \mathbf{z}_\mathbf{RM}^{21} & \mathbf{z}_\mathbf{RM}^{22} & \cdots \\ \vdots & \vdots & \ddots \end{bmatrix} \cdot \begin{bmatrix} \mathbf{y}_{\mathbf{M}1}\left(\mathbf{e}^-{}_1 \cdot \mathbf{a}_{\mathbf{M}1} - \mathbf{e}^+{}_1 \cdot \mathbf{b}_{\mathbf{M}1}\right) \\ y_{\mathbf{M}2}\left(\mathbf{e}^-{}_2 \cdot \mathbf{a}_{\mathbf{M}2} \cdot - \mathbf{e}^+{}_2 \cdot \mathbf{b}_{\mathbf{M}2}\right) \\ \vdots \end{bmatrix}
\tag{2.20}
$$

Further rearrangement yields

$$\mathbf{E}^{-}\left(\mathbf{I}-\mathbf{Z}_{\mathbf{RM}}\mathbf{Y}\right)\mathbf{A}_{\mathbf{M}}+\mathbf{E}^{+}\left(\mathbf{I}+\mathbf{Z}_{\mathbf{RM}}\mathbf{Y}\right)\mathbf{B}_{\mathbf{M}}=\mathbf{0} \tag{2.21}$$

where

$$\mathbf{A}_{\mathbf{M}}=\begin{bmatrix}\mathbf{a}_{\mathbf{M}1}\\ \mathbf{a}_{\mathbf{M}2}\\ \vdots\end{bmatrix},\qquad \mathbf{B}_{\mathbf{M}}=\begin{bmatrix}\mathbf{b}_{\mathbf{M}1}\\ \mathbf{b}_{\mathbf{M}2}\\ \vdots\end{bmatrix}$$

$$\mathbf{E}^{-}=\begin{bmatrix}\mathbf{e}^{-}{}_{1} & \mathbf{0} & \cdots\\ \mathbf{0} & \mathbf{e}^{-}{}_{2} & \cdots\\ \vdots & \vdots & \ddots\end{bmatrix},\qquad \mathbf{E}^{+}=\begin{bmatrix}\mathbf{e}^{+}{}_{1} & \mathbf{0} & \cdots\\ \mathbf{0} & \mathbf{e}^{+}{}_{2} & \cdots\\ \vdots & \vdots & \ddots\end{bmatrix} \tag{2.22}$$

$$\mathbf{Y}_{M}=\begin{bmatrix}\mathbf{y}_{\mathbf{M}1} & \mathbf{0} & \cdots\\ \mathbf{0} & \mathbf{y}_{\mathbf{M}2} & \cdots\\ \vdots & \vdots & \ddots\end{bmatrix}$$

Equation (2.21) can be further rearranged to obtain

$$\left[\,\mathbf{E}^{-}\left(\mathbf{I}-\mathbf{Z}_{\mathbf{RM}}\mathbf{Y}\right)\quad \mathbf{E}^{+}\left(\mathbf{I}+\mathbf{Z}_{\mathbf{RM}}\mathbf{Y}\right)\,\right]\cdot\begin{bmatrix}\mathbf{A}_{\mathbf{M}}\\ \mathbf{B}_{\mathbf{M}}\end{bmatrix}=\mathbf{0} \tag{2.23}$$

which shall be designated as

$$\mathbf{S}_{J}\cdot\begin{bmatrix}\mathbf{A}_{\mathbf{M}}\\ \mathbf{B}_{\mathbf{M}}\end{bmatrix}_{J}=\mathbf{0} \tag{2.24}$$

The matrix, $\mathbf{S}_J$, represents the scattering characteristics of the particular junction, J, relating the modal wave amplitudes, a_M and b_M, in the adjacent duct segments. The matrix, $\mathbf{S}_J$, shall be called, "junction modal scattering matrix". The junction modal scattering matrix, $\mathbf{S}_J$, needs to be determined for each of the junctions present in the duct system.

In the present modeling approach, the acoustic sources, such as speakers or a fan, are to be located at junctions. For a junction containing one or more acoustic sources, the modal scattering matrix equation becomes

$$\mathbf{S}_J \cdot \begin{bmatrix} \mathbf{A_M} \\ \mathbf{B_M} \end{bmatrix}_J = \mathbf{F}_J \tag{2.25}$$

where the right hand side contains a vector, $\mathbf{F}_J$, which represents the source excitations.

Once the modal scattering matrix equations are obtained with respect to all the junctions present in the system, the equations can be assembled into a single matrix equation as

$$\mathbf{S}_{global} \cdot \begin{bmatrix} \mathbf{A_M} \\ \mathbf{B_M} \end{bmatrix}_{global} = \mathbf{F}_{global} \tag{2.26}$$

where

$$\mathbf{S}_{global} = \begin{bmatrix} \mathbf{S}_{J_1} \\ \mathbf{S}_{J_2} \\ \vdots \end{bmatrix}, \qquad \mathbf{F}_{global} = \begin{bmatrix} \mathbf{F}_{J_1} \\ \mathbf{F}_{J_2} \\ \vdots \end{bmatrix} \tag{2.27}$$

It should be noted that the junction modal scattering matrix equations can be assembled only after appropriate manipulations are performed to ensure compatibility.

Finally, Equation (2.26) can be solved for the unknown global modal wave amplitude vector by

$$\begin{bmatrix} \mathbf{A_M} \\ \mathbf{B_M} \end{bmatrix}_{global} = \mathbf{S}_{global}^{-1} \cdot \mathbf{F}_{global} \tag{2.28}$$

which contains the modal wave amplitudes, a_M and b_M, in all the duct segments.

2.2.2 Junction Modal Impedance Matrix

In discussions so far, the junction modal impedance matrices, $\mathbf{Z_{RM}}$, are assumed to be available. Now, the explanation on how to actually obtain the junction modal impedance matrix is presented as follows.

For the determination of the junction modal impedance matrices, $\mathbf{Z_{RM}}$, the Green's function approach is used. The pressure field inside a junction due to a distribution of the normal components of the particle velocity, $u_n(\mathbf{r_0})$, over a duct-junction interface with an area, S_o, is given by

$$p(\mathbf{r}) = jk\rho c \int_{S_o} G_J(\mathbf{r}|\mathbf{r_o}) \cdot u_n(\mathbf{r_o}) dS_o \tag{2.29}$$

where G_J is the Green's function associated with the particular geometry of the junction, $\mathbf{r}$ and $\mathbf{r_o}$ are the position vectors designating the observation and the source location, respectively.

The Green's function, G_J, for an enclosed space is

$$G_J(\mathbf{r}|\mathbf{r_o}) = \frac{1}{V} \sum_N \frac{\phi_N(\mathbf{r})\phi_N(\mathbf{r_o})}{\kappa_N{}^2 - k^2} \tag{2.30}$$

where V is the volume of the enclosed space, Φ_N is the associated N-th mode-shape function and κ_N is the eigenvalue. For an enclosed space with sides, Lx, Ly and Lz, the mode-shape function and the eigenvalue are

$$\phi_N(\mathbf{r}) = \frac{cos(\frac{n_x\pi}{L_x}x)\, cos(\frac{n_y\pi}{L_y}y)\, cos(\frac{n_z\pi}{L_z}z)}{\sqrt{\Lambda_{m_x}\Lambda_{m_y}\Lambda_{m_z}}} \tag{2.31}$$

and

$$\kappa_N = (\frac{n_x\pi}{L_x})^2 + (\frac{n_y\pi}{L_y})^2 + (\frac{n_z\pi}{L_z})^2 \tag{2.32}$$

Pressure field at the l-th duct-junction interface is calculated by summing the contributions from the particle velocities, u_n, at all the other interfaces. That is,

$$p(\mathbf{r})^l = jk\rho c \sum_i \int_{S_i} G_J(\mathbf{r} \mid \mathbf{r_o}) \cdot u_n(\mathbf{r_o}) dS_i \tag{2.33}$$

The modal expansions of the pressure at the l-th interface and the velocity at the i-th interface are

$$p(\mathbf{r})^l = \sum_M p_M{}^l \cdot \Psi_M(\mathbf{r})^l \tag{2.34}$$

and

$$u_n(\mathbf{r_o})^i = \sum_M u_M{}^i \cdot \Psi_M(\mathbf{r_o})^i \tag{2.35}$$

where p_M, u_M and $\psi_M(x,y)$ are the modal pressure, the modal velocity and the mode-shape function associated with the interface, respectively. Substituting Equations (2.34) and (2.35) into (2.33),

$$\sum_M p_M{}^l \cdot \Psi_M(\mathbf{r})^l = jk\rho c \sum_i \int_{S_i} G_J(\mathbf{r} \mid \mathbf{r_o}) \cdot (\sum_M u_M{}^i \cdot \Psi_M{}^i(\mathbf{r_o})) dS_i \quad . \tag{2.36}$$

that is,

$$\sum_M p_M{}^l \cdot \Psi_M(\mathbf{r})^l = jk\rho c \sum_i \sum_M u_M{}^i \int_{S_i} G_J(\mathbf{r} \mid \mathbf{r_o}) \cdot \Psi_M{}^i(\mathbf{r_o}) dS_i \tag{2.37}$$

Multiplying both sides by $\psi_R{}^l(x,y)/S_l$, integrating over S_l, and applying the orthogonality condition of (2.7), the right hand side becomes

$$\sum_M p_M{}^l \frac{1}{S_l} \int_{S_l} \Psi_R{}^l \cdot \Psi_M{}^l dS^l = p_R{}^l \tag{2.38}$$

and thus Equation (2.36) becomes

$$p_R{}^l = jk\rho c \sum_i \sum_M u_M{}^i \frac{1}{S_l} \int_{S_l} \int_{S_i} G_J(\mathbf{r}|\mathbf{r_o}) \cdot \Psi_R{}^l(\mathbf{r}) \Psi_M{}^i(\mathbf{r_o}) dS_l dS_i \tag{2.39}$$

Denoting

$$z_{RM}{}^{li} = \frac{jk\rho c}{S_l} \int_{S_l} \int_{S_i} G_J(\mathbf{r}|\ \mathbf{r_o}) \cdot \Psi_R{}^l(\mathbf{r}) \Psi_M{}^i(\mathbf{r_o}) dS_l dS_i \tag{2.40}$$

Equation (2.40) finally becomes

$$p_R{}^l = \sum_i \sum_M z_{RM}{}^{li} \cdot u_M{}^i \tag{2.41}$$

where the quantity, $z_{RM}{}^{li}$, is the modal impedance between the M-th particle velocity at the i-the duct-junction interface to the R-th modal pressure at the l-th interface. The matrix form of this equation is given by Equation (2.18). Equation (2.40) is extensively used in this thesis to determine the junction modal impedance matrix.

2.2.3 Junction Interior Pressure Field

In the discussions above, the pressure and the velocity in the duct segments are determined. The pressure field in the remaining regions, namely within the junctions, can be determined as follows.

The pressure field inside a junction can be determined by summing the contributions of the particle velocities, u_n, at all duct-junction interfaces as

$$p(\mathbf{r}) = jk\rho c \sum_i \int_{S_i} G_J(\mathbf{r}|\ \mathbf{r_o}) \cdot u_n(\mathbf{r_o}) dS_i \tag{2.42}$$

Now, modally expanding the junction pressure field, $p(\mathbf{r})$,

$$p(\mathbf{r}) = \sum_M p_M \cdot \phi_M(\mathbf{r}) \tag{2.43}$$

where the mode-shape function, $\Phi_M(\mathbf{r})$, associated with the junction *volume* is Equation (2.31). The particle velocity, u_n, normal to the duct-junction interface is expanded in

terms of mode associated with the interface *surface* as shown in (2.35). Then, Equation (2.42) becomes,

$$\sum_M p_M \cdot \phi_M(\mathbf{r}) = jk\rho c \sum_i \int_{S_i} G_J(\mathbf{r}|\mathbf{r_o}) \cdot (\sum_M u_M{}^i \cdot \Psi_M{}^i(\mathbf{r_o}))dS_i \tag{2.44}$$

Multiplying both sides by $\Phi_R(\mathbf{r})/V$ and integrating over the junction volume, V, yield

$$\begin{aligned} &\sum_M p_M (\frac{1}{V}\int_V \phi_R(\mathbf{r}) \cdot \phi_M(\mathbf{r})dV) \\ &= jk\rho c \sum_i \sum_M u_M{}^i \frac{1}{V}\int_V \int_{S_i} G_J(\mathbf{r}|\mathbf{r_o}) \cdot \phi_R(\mathbf{r})\Psi_M(\mathbf{r_o})dS_i dV \end{aligned} \tag{2.45}$$

Substituting Equation (2.30) and further rearranging the right hand side gives

$$\begin{aligned} &\sum_M p_M (\frac{1}{V}\int_V \phi_R(\mathbf{r}) \cdot \phi_M(\mathbf{r})dV) \\ &= jk\rho c \sum_i \sum_M u_M{}^i \sum_N \left(\frac{1}{V}\int_V \cdot \phi_N(\mathbf{r})\phi_R(\mathbf{r})dV \right) \frac{1}{\kappa_R{}^2 - k^2} \int_{S_i} \cdot \phi_N(\mathbf{r_0})\psi_M(\mathbf{r_0})dS_i \end{aligned} \tag{2.46}$$

Applying the orthogonality condition, which is in this case,

$$\frac{1}{V}\iint_V \phi_M \ \phi_R dV = \begin{cases} 1 & for\ M = R \\ 0 & for\ M \neq R \end{cases} \tag{2.47}$$

Equation (2.46) becomes

$$p_R = \sum_i \sum_M \left(\frac{jk\rho c}{V} \frac{1}{\kappa_R{}^2 - k^2} \int_{S_i} \cdot \phi_R(\mathbf{r_o})\psi_M(\mathbf{r_o})dS_i \right) \cdot u_M{}^i \tag{2.48}$$

It should be noted that the summation over M in the left hand side and the summation over N on the right hand side of Equation (2.46) have been eliminated as a consequence of applying the othogonality condition.

The quantity enclosed by the parenthesis in Equation (2.48) is essentially the impedance between the M-th *surface* modal velocity at the i-th duct-junction interface and the R-th *volume* modal pressure of the junction. This quantity is designated as

$$z_{I\,RM}{}^{i} = \frac{jk\rho c}{V}\frac{1}{\kappa_R{}^2 - k^2}\int_{S_i} \cdot \phi_R(\mathbf{r_0})\psi_M(\mathbf{r_0})dS_i \tag{2.49}$$

in which the subscript, *I*, is given to emphasis that it concerns the "interior" volume of the junction rather than the surface-to-surface impedance of Equation (2.40).

Once the junction interior modal impedance above is determined, the pressure field within the junction is calculated as follows. First, Equation (2.43), which is the modal expansion of the junction interior pressure, is rearranged as

$$\begin{aligned} p(\mathbf{r}) &= \sum_R p_R \cdot \phi_R(x,y,z) \\ &= \sum_{R_{xy}} \left(\sum_{R_z} p_R \cdot \psi_{R_z}(z) \right) \cdot \psi_{R_{xy}}(x,y) \end{aligned} \tag{2.50}$$

where the volume mode-shape function, $\phi_R(x,y,z)$, is written as a product of mode-shape functions, $\psi_{R_z}(z)$ and $\psi_{R_{xy}}(x,y)$. This can be written in a matrix format as

$$\begin{aligned} p(\mathbf{r}) &= \begin{bmatrix} p_{R_{xy}=1} & p_{R_{xy}=2} & \cdots \end{bmatrix} \cdot \begin{bmatrix} \phi_{R_{xy}=1}(x,y) \\ \phi_{R_{xy}=2}(x,y) \\ \vdots \end{bmatrix} \\ &= \left\{ \begin{bmatrix} \begin{bmatrix} p_{R_{xy}=1} \\ p_{R_{xy}=2} \\ \vdots \end{bmatrix}_{R_z=1} & \begin{bmatrix} p_{R_{xy}=1} \\ p_{R_{xy}=2} \\ \vdots \end{bmatrix}_{R_z=2} & \cdots \end{bmatrix} \cdot \begin{bmatrix} \psi_{R_a=1}(z) \\ \psi_{R_a=2}(z) \\ \vdots \end{bmatrix} \right\}^T \cdot \begin{bmatrix} \psi_{R_{xy}=1}(x,y) \\ \psi_{R_{xy}=2}(x,y) \\ \vdots \end{bmatrix} \\ &= \left\{ \begin{bmatrix} \mathbf{p}_{\mathbf{R_{xy}}\,R_z=1} & \mathbf{p}_{\mathbf{R_{xy}}\,R_z=2} & \cdots \end{bmatrix} \cdot \boldsymbol{\psi}_{\mathbf{R_a}}(z) \right\}^T \cdot \boldsymbol{\psi}_{\mathbf{R_{xy}}}(x,y) \end{aligned} \tag{2.51}$$

Each sub-matrix, $\mathbf{p}_{\mathbf{R_{xy}}\,R_z}$, in the equation is evaluated at a particular value of R_z as

$$\mathbf{p}_{\mathbf{R_{xy}}\,R_z} = \begin{bmatrix} \mathbf{z_{IRM}}{}^1 & \mathbf{z_{IRM}}{}^2 & \cdots \end{bmatrix}_{R_z} \cdot \begin{bmatrix} \mathbf{u_M}{}^1 \\ \mathbf{u_M}{}^2 \\ \vdots \end{bmatrix} \tag{2.52}$$

where $\mathbf{z}_{\mathbf{IRM}}{}^{l}$ is an R by M_{xy} modal impedance matrix for the l-th interface given by Equation (2.49), $\mathbf{u}_{\mathbf{M}}{}^{l}$ is the modal velocity vector corresponding to the l-th interface.

2.3 Fan Noise Model

Up to this point, the method for modeling the acoustic duct has been discussed. In this section, the approach used for modeling the source of the noise, which is the axial fan located inside a duct. First, a model of the fan as a noise source is presented. Then, some experimental results are provided in order to validate the model.

2.3.1 Modal Force Excitation Model

An illustration of a fan in a duct is shown in Figure 2.3 below.

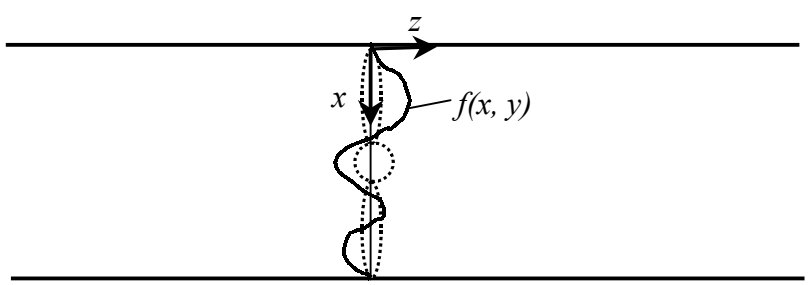

Figure 2.3. Acoustic excitation from a fan represented by a force field

The fan source excitation is modeled as a complex field of force, $f(x,y)$, distributed over the duct cross-sectional area, S, concentrated at the z-position of the fan. This distributed force creates a discontinuity in pressure at the location of the fan as

$$p(x,y,0^{+}) - p(x,y,0^{-}) = \frac{f(x,y)}{S} \tag{2.53}$$

where $p(x,y,0^+)$ and $p(x,y,0^-)$ are the pressure field at the surfaces immediately to the left and right of the fan source positioned at $z = 0$. On the other hand, the particle velocity is assumed to be continuous across the fan source, that is,

$$u(x,y,0^+) - u(x,y,0^-) = 0 \quad . \tag{2.54}$$

Modal expansions of the equations above yield

$$\sum_M p_M(0^+) \cdot \psi_M(x,y) - \sum_M p_M(0^-) \cdot \psi_M(x,y) = \frac{1}{S} \sum_M f_M \cdot \psi_M(x,y) \tag{2.55}$$

where $\psi_M(x,y)$ is the mode-shape function given earlier by Equation (2.9). In a matrix format, the equation becomes

$$\left[p_M(0^+)\right] \cdot \left[\psi_M(x,y)\right] - \left[p_M(0^-)\right] \cdot \left[\psi_M(x,y)\right] = \frac{1}{S}\left[f_M\right] \cdot \left[\psi_M(x,y)\right] \tag{2.56}$$

Canceling out the mode-shape function matrices, $[\psi_M(x,y)]$, one obtains

$$\left[p_M(0^+)\right] - \left[p_M(0^-)\right] = \left[f_M\right]/S$$

or

$$\mathbf{p_M}(0^+) - \mathbf{p_M}(0^-) = \mathbf{f_M}/S \tag{2.57}$$

where $\mathbf{p_M}(0^+)$ and $\mathbf{p_M}(0^-)$ are the modal pressure vectors immediately to the left and to the right of the fan source, $\mathbf{f_M}$ is the complex modal amplitude vector of the source force excitation. Similarly, for the particle velocity,

$$\mathbf{u_M}(0^+) - \mathbf{u_M}(0^-) = \mathbf{0} \tag{2.58}$$

where $\mathbf{u_M}(0^+)$ and $\mathbf{u_M}(0^-)$ are the modal velocity vectors immediately to the left and to the right of the fan source.

2.3.2 Radiation Characteristics

The most notable feature of this fan noise model is that, provided that the duct geometry is symmetric, it results in the asymmetric acoustic radiation, meaning that the pressure fields at the inlet side and the outlet side of the fan source are equal in magnitude but opposite in phase. This is shown by the following example.

Assuming the duct shown in Figure 2.4 is an infinite duct, the pressure field, *p(x, y, z),* for z > 0 and z < 0 are

$$
\begin{aligned}
p(x,y,z) &= \begin{cases} \left[a_M e^{-jk_M z}\right]^T \cdot \left[\psi_M(x,y)\right] & for\ z>0 \\ \left[b_M e^{+jk_M z}\right]^T \cdot \left[\psi_M(x,y)\right] & for\ z<0 \end{cases} \\
&= \begin{cases} \left(\left[e^{-jk_M z}\right]_{diag}\left[a_M\right]\right)^T \cdot \left[\psi_M(x,y)\right] & for\ z>0 \\ \left(\left[e^{+jk_M z}\right]_{diag} \cdot \left[b_M\right]\right)^T \cdot \left[\psi_M(x,y)\right] & for\ z<0 \end{cases} \\
&= \begin{cases} \left(\mathbf{e}^- \cdot \mathbf{a_M}\right)^T \cdot \boldsymbol{\psi}_\mathbf{M} & for\ z>0 \\ \left(\mathbf{e}^+ \cdot \mathbf{b_M}\right)^T \cdot \boldsymbol{\psi}_\mathbf{M} & for\ z<0 \end{cases}
\end{aligned}
\tag{2.59}
$$

Thus, the cross-sectional surface modal pressure amplitudes for $z > 0$ and $z < 0$ are

$$
\mathbf{p_M}(z)_{z>0} = \mathbf{e}^- \cdot \mathbf{a_M} \cdot \qquad \mathbf{p_M}(z)_{z<0} = \mathbf{e}^+ \cdot \mathbf{b_M} \tag{2.60}
$$

For the particle velocity ,

$$
\begin{aligned}
u(x,y,z) &= \begin{cases} \left(\left[y_M\right]_{diag} \cdot \left[a_M\right] \cdot \left[e^{-jk_M z}\right]_{diag}\right)^T \cdot \left[\psi_M(x,y)\right] & for\ z>0 \\ \left(\left[y_M\right]_{diag} \cdot \left[b_M\right] \cdot \left[e^{+jk_M z}\right]_{diag}\right)^T \cdot \left[\psi_M(x,y)\right] & for\ z<0 \end{cases} \\
&= \begin{cases} \left(\mathbf{y_M} \cdot \mathbf{e}^- \cdot \mathbf{a_M} \cdot\right)^T \cdot \boldsymbol{\psi}_\mathbf{M} & for\ z>0 \\ \left(\mathbf{y_M} \cdot \mathbf{e}^+ \cdot \mathbf{b_M}\right)^T \cdot \boldsymbol{\psi}_\mathbf{M} & for\ z<0 \end{cases}
\end{aligned}
\tag{2.61}
$$

where y_M is the specific modal admittance defined in Equation (2.13).

The surface modal amplitudes are

$$
\mathbf{u_M}(z)_{z>0} = \mathbf{y_M} \cdot \mathbf{e}^- \cdot \mathbf{a_M} \qquad \mathbf{u_M}(z)_{z<0} = \mathbf{y_M} \cdot \mathbf{e}^+ \cdot \mathbf{b_M} \tag{2.62}
$$

Substituting Equation (2.62) into (2.58) results in

$$\mathbf{a_M} = -\mathbf{b_M} \tag{2.63}$$

which shows that the magnitudes of the modal waves to the left and the right of the fan are equal in magnitude , but opposite in phase. Furthermore, substituting Equation (2.60) into (2.57) gives

$$\mathbf{a_M} - \mathbf{b_M} = \mathbf{a_M} - (-\mathbf{a_M}) = 2 \cdot \mathbf{a_M} = \mathbf{f_M} / S \tag{2.64}$$

Figure 2.4 below illustrates the conditions of Equations (2.63) and (2.64)

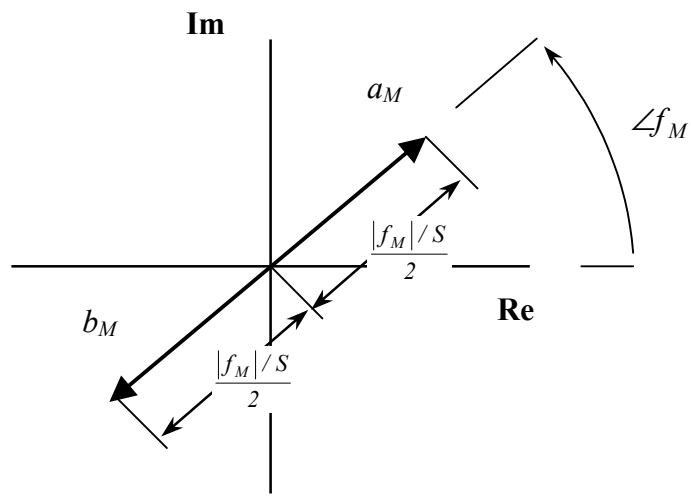

Figure 2.4. The relationship between the modal wave amplitude, a_M and b_M, and the modal fan force excitation, f_M

2.3.3 Model Validating Experiment

An experiment was carried out in order to validate the fan noise model above. The detailed descriptions of the experiment are provided in Appendix A. The objective of the experiment was to observe the condition of Equation (2.63) which suggested that, for an infinite duct, the amplitudes, a_M and b_M, of the waves produced on both side of the fan should be equal in magnitude but 180 degrees out-of-phase.

A rectangular duct was constructed with anechoic wedges installed at both ends to simulate an infinite duct. Then an axial fan was positioned in the middle of this duct. The modal amplitudes, a_M and b_M, were experimentally determined for the first four modes and the relative differences in magnitude and phase were calculated (see Appendix A for details). The following figures show the obtained results.

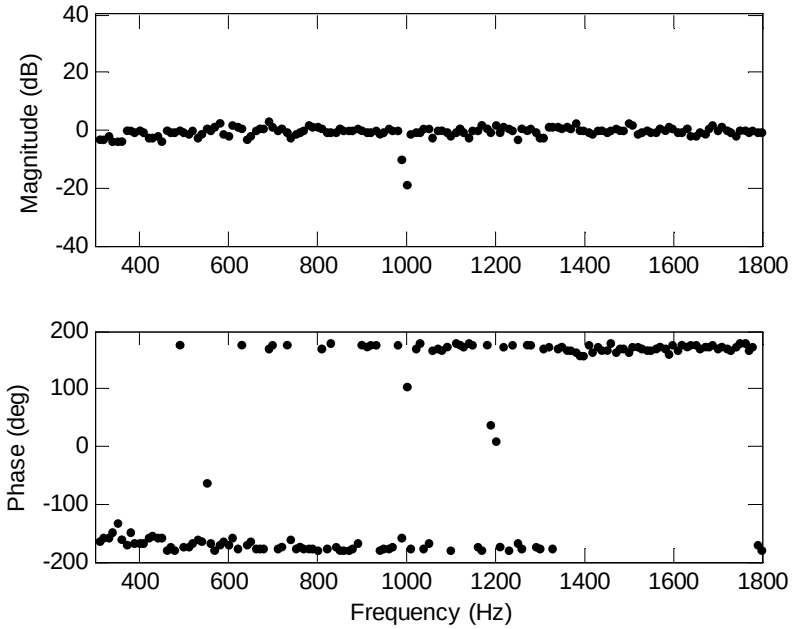

Figure 2.5. Magnitude and phase of a_M / b_M for M=1 (cut-on frequency: 0 Hz)

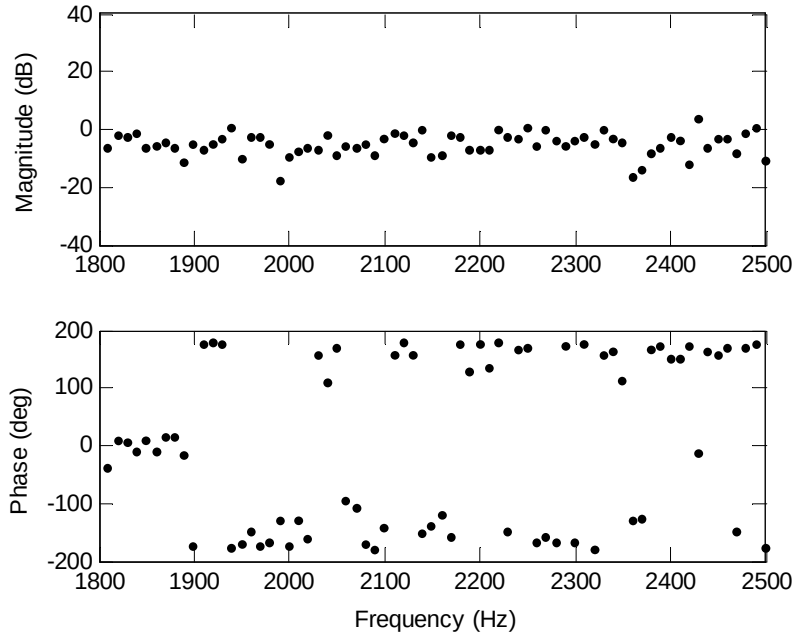

Figure 2.6. Magnitude and phase of a_M/b_M for M=2 (cut-on frequency: 1805 Hz).

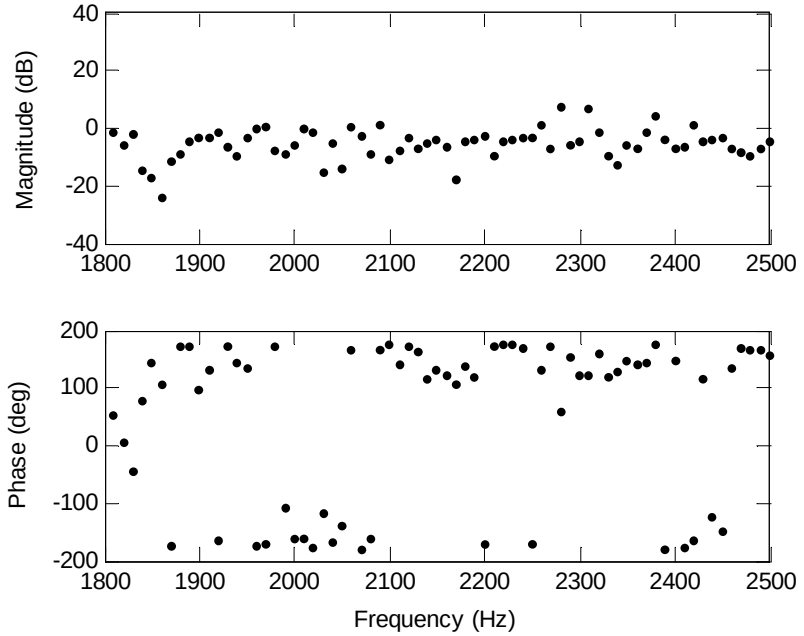

Figure 2.7. Magnitude and phase of a_M/b_M for M=3 (cut-on frequency: 1805 Hz).

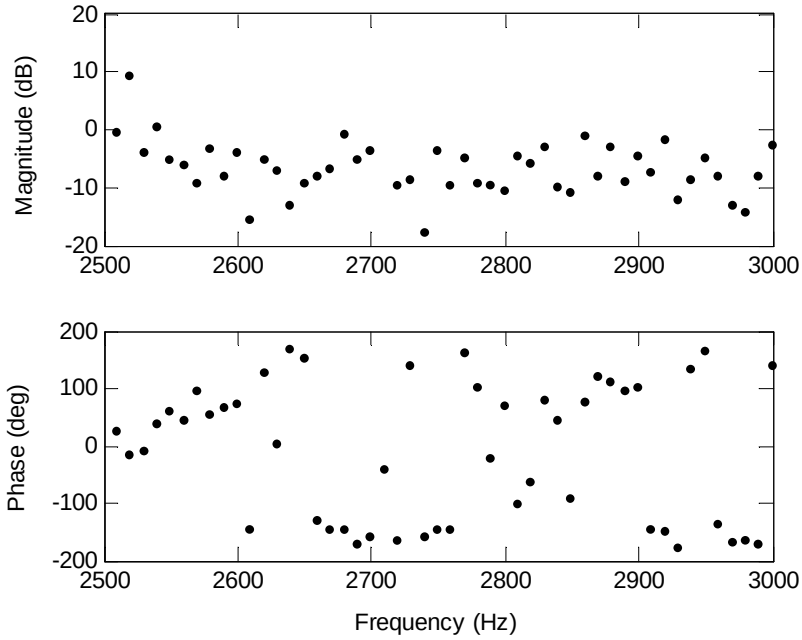

Figure 2.8. Magnitude and phase of a_M/b_M for M=4 (cut-on frequency: 2553 Hz).

Figure 2.5 shows that for the first mode (M = 1) which is the plane wave mode, the difference in the magnitude between the wave amplitudes, a_1 and b_1, are observed to be very small and the relative phase difference is almost nearly 180 degrees. As for the higher order modes (M > 1), though not as distinctively as the case for M=1, similar trend can be observed. More accurate measurements using more number of microphones may improve the results for the higher-order modes. Nevertheless, the results above provide a certain degree of validity to the current fan noise model.

The magnitudes of the excitation force, f_M, for M = 1 to 4 were also estimated from the measurements of a_M and b_M. Figure 2.9 shows the magnitude of, f_M, as a function of frequency for M = 1 to 4. (The data for M = 2, 3 and 4 for frequencies that are lower than their cut-on frequencies are not shown because of low signal to noise ratio.)

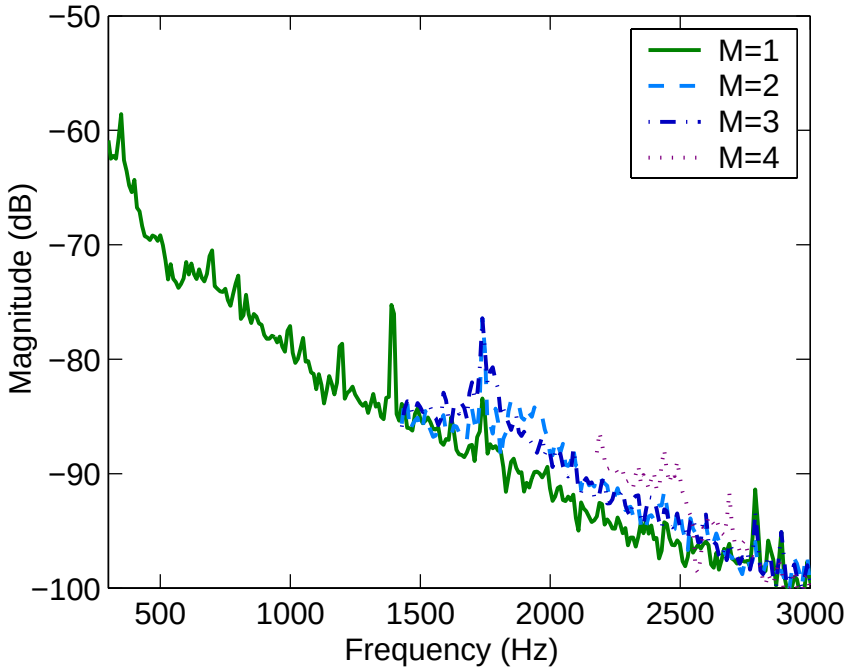

Figure 2.9. Magnitude of complex fan force, f_M, for m=1 to 4.

It is observed in Figure 2.9 that the magnitudes of the estimated modal force excitation, f_M, tend to decrease in frequency. It should be noted here that, for the theoretical studies in Chapter 3, the modal force excitation magnitudes, f_M, are simply assumed to be constant over the frequencies. Thus, the frequency dependency indicated in the experimental data here is not taken into account. This does not affect the results in the following chapter since the focus is on the relative change in magnitudes and not the absolute magnitudes. Furthermore, in Chapter 3, the magnitudes of, f_M, are assumed to be equal among different modes (but with arbitrary phase). This is not an overly simple assumption, based on an observation that the relative differences in the magnitudes between the four modes are indicated to be relatively small for the most part except in the vicinity of respective cut-on frequencies.

2.4 Active Noise Control

Active noise control systems can be classified into two basic categories, namely feedforward control and feedback control. A feedforward control system is a class of control systems that generate control input based on *a priori* information of the disturbance. In other words, this type of control system synthesizes the control inputs based on how the disturbance would look like at some point in the future. Therefore it is also classified as "non-causal control" in some literature. On the other hand, a feedback control system generates control signals based on the current information on the disturbance. It does not predict or anticipate the disturbance change. Therefore, it can be classified as "causal control" approach.

In the present study, the performances of both feedforward and feedback active noise control are investigated. The followings describe the analytical approaches that are used in the simulation studies in Chapter 3 for obtaining the optimal noise reduction performance of the two active control approaches.

2.4.1 Feedforward Control

Figure 2.10 shows a block diagram of a feedforward control system.

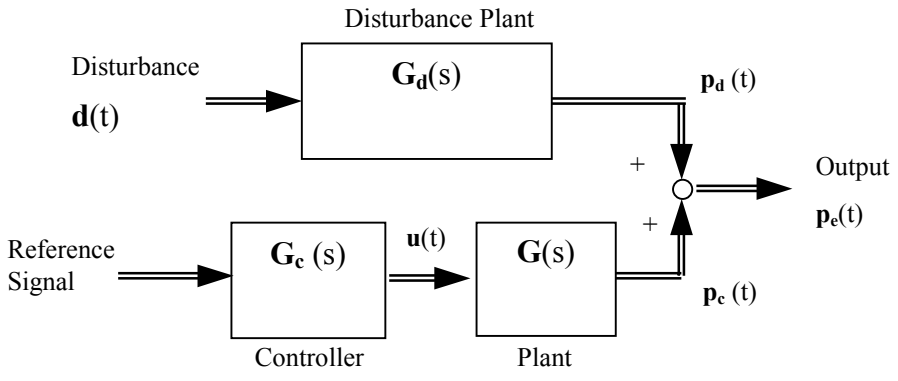

Figure 2.10. Feedforward Control System

In Figure 2.10, the disturbance, **d**(t) is the unwanted noise which is picked up by a microphone as output, $\mathbf{p_d}$(t), after passing through a transfer function, $\mathbf{G_d}$(t). The control sound, $\mathbf{p_c}$(t) is introduced by the control system and superimposed to the output. Given an ideal reference signal, which is completely correlated with the disturbance, the feedforward control yields a maximum noise control performance (at least locally at error microphones) possible for a given system. The analytical method for predicting this ideal performance of the feedforward control is as follows.

The pressures, $\mathbf{p_e}$, sensed by N_e error microphones are the superposition of the contributions from the fan noise (disturbance), $\mathbf{p_d}$, and the control sound, $\mathbf{p_c}$, from N_C active sources (speakers). Thus,

$$\mathbf{p_e} = \mathbf{p_d} + \mathbf{p_c}$$

$$\begin{bmatrix} p_{e1} \\ p_{e2} \\ \vdots \\ p_{eN_e} \end{bmatrix} = \cdot \begin{bmatrix} p_{d1} \\ p_{d2} \\ \vdots \\ p_{N_e} \end{bmatrix} + \begin{bmatrix} p_{c1} \\ p_{c2} \\ \vdots \\ p_{N_c} \end{bmatrix} \tag{2.65}$$

And the control sound, $\mathbf{p_c}$, is

$$\mathbf{p_c} = \mathbf{G} \cdot \mathbf{u}$$

$$\begin{bmatrix} p_{c1} \\ p_{c2} \\ \vdots \\ p_{cN_e} \end{bmatrix} = \begin{bmatrix} g_{c11} & g_{c12} & \cdots & g_{cN_c} \\ g_{c21} & g_{c22} & \cdots & \vdots \\ \vdots & \vdots & \ddots & \vdots \\ g_{cN_c1} & \cdots & \cdots & g_{cli} \end{bmatrix} \cdot \begin{bmatrix} u_1 \\ u_2 \\ \vdots \\ u_{N_c} \end{bmatrix} \tag{2.66}$$

where **G** is the transfer function matrix from the speaker input vector, **u**, and to the control sound vector, $\mathbf{p_c}$. The transfer function matrix, **G**, includes the dynamics of the acoustic duct and also the mechanical dynamics of the speakers.

The feedforward control works to minimize the sum of the square of the error microphone signals,

$$J = \sum_{i}^{N_e} \left| p_{ei} \right|^2 = \mathbf{p_e}^* \cdot \mathbf{p_e} \tag{2.67}$$

Substituting the preceding two equations into (2.67), the quantity, J, becomes

$$
\begin{aligned}
J &= [\mathbf{p_d} + \mathbf{G} \cdot \mathbf{u}]^* \cdot [\mathbf{p_d} + \mathbf{G} \cdot \mathbf{u}] \\
&= \mathbf{u}^* (\mathbf{G}^* \cdot \mathbf{G}) \cdot \mathbf{u} + \mathbf{u}^* \cdot (\mathbf{G}^* \cdot \mathbf{p_d}) + \mathbf{p_d}^* \cdot \mathbf{G} \cdot \mathbf{u} + \mathbf{p_d}^* \cdot \mathbf{p_d} \\
&= \mathbf{u}^* \cdot \mathbf{a} \cdot \mathbf{u} + \mathbf{u}^* \cdot \mathbf{b} + \mathbf{b}^* \cdot \mathbf{u} + c
\end{aligned}
\tag{2.68}
$$

where

$$
\mathbf{a} = \mathbf{G}^* \cdot \mathbf{G}, \qquad \mathbf{b} = \mathbf{G}^* \cdot \mathbf{p_d}, \qquad c = \mathbf{p_d}^* \cdot \mathbf{p_d} \quad . \tag{2.69}
$$

Equation (2.68) shows that the quantity, J, is a quadratic function of the speaker input vector , $\mathbf{u}$.

The control speaker input vector, $\mathbf{u}$, that minimizes J of Equation (2.68) is given by [45],

$$
\mathbf{u}_{opt} = -\mathbf{a}^{-1} \cdot \mathbf{b} = -(\mathbf{G}^* \cdot \mathbf{G})^{-1} \cdot \mathbf{G}^* \cdot \mathbf{p_d}, \tag{2.70}
$$

And the corresponding minimum value of J is

$$
J = \mathbf{p_d}^* \cdot \mathbf{p_d} - \mathbf{p_d}^* \cdot \mathbf{G} \cdot (\mathbf{G}^* \cdot \mathbf{G})^{-1} \mathbf{G}^* \cdot \mathbf{p_d} \tag{2.71}
$$

The action of the feedforward control indicated by Equation (2.70) can be clearly interpreted for a 1x1 system (one error microphone and one speaker). In this case, Equation (2.70) becomes

$$
u_{opt} = -\frac{1}{g} p_d \tag{2.72}
$$

and the quantity, *J, is*

$$
J = \overline{p}_d p_d - \overline{p}_d g \left(\frac{1}{g} p_d \right) = 0 \tag{2.73}
$$

where the notation, $\overline{p}_d$, signifies the conjugate of p_d. This illustrates that, for a simplest case above, the feedforward control works to nullify the plant dynamics, g, and produce the control sound that is 180 degrees out-of-phase with the disturbance.

It should be emphasized that the analysis above gives an idealistic performance of the feedforward control with an assumption that perfectly correlated reference signal is available. In practice, the noise control performance will be limited by the presence of uncorrelated noise component in the reference signal and the error microphones signals.

Furthermore, even though the above analysis could be applicable to both random and periodic disturbances, feedforward control of random disturbance may not be

practical in some applications. The feedforward control of random noise normally requires the reference signal sensor to be placed "upstream" of the propagating disturbance, sufficiently away from the location of the control actuator. This is because the control hardware requires a finite amount of time between the time it obtains the reference signal and the time it produces control output based on the reference signal. The required separation distance between the reference signal sensor and the control actuator depends mainly on how fast (i.e. bandwidth) the controller hardware can react. In applications where this separation distance between the reference sensor and the actuator cannot be made sufficiently large for the given control hardware, the feedforward control of random noise becomes impractical. This is certainly the case for the present application, where the control speakers are required to be near the location of the noise source (fan) due to size constraints. Therefore, the simulation results of the feedforward control performance in Chapter 3 are presented with periodic disturbance in mind. And, for the active control experiments in Chapter 4, the feedforward control is implemented to control only the periodic content of the fan noise.

2.4.2 Feedback Control

The block diagram of a feedback control system is shown in Figure 2.11.

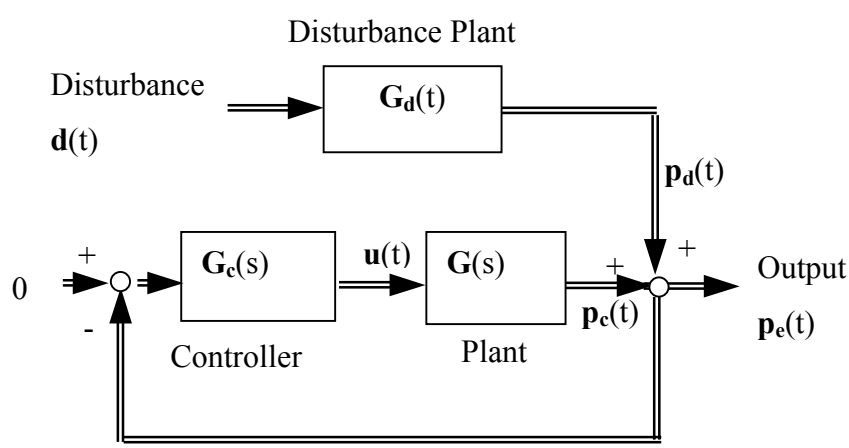

Figure 2.11. Feedback Control System

As shown in the above figure, the feedback control system synthesizes the control input, **u**(t) based solely on the error microphone signal, $\mathbf{p_e}$(t):

$$\mathbf{u} = -\mathbf{G_c} \cdot \mathbf{p_e} \tag{2.74}$$

where **Gc**(s) is the control filter transfer function. Combining this into Equations (2.66) and(2.65) yields

$$\mathbf{p_e} = (\mathbf{I} + \mathbf{G_c}\mathbf{G})^{-1} \cdot \mathbf{p_d} = \mathbf{S} \cdot \mathbf{p_d} \tag{2.75}$$

where $\mathbf{p_e}$ is the error microphone pressure vector, $\mathbf{p_d}$ is the fan noise (disturbance) vector and **S** is commonly referred as the sensitivity transfer function matrix. The noise reduction (or disturbance rejection in control literature) performance of a feedback control system is characterized by this sensitivity transfer function matrix, **S**.

For the purpose of enhancing the noise reduction performance of the feedback control system, a suitable controller, $\mathbf{G_c}$, is chosen in such away that this matrix, **S**, is minimized in the disturbance frequency range without causing closed-loop instability. There are a variety of methodologies available for obtaining the controller, $\mathbf{G_c}$.

For the simulation studies in Chapter 3, an optimal control design methodology called, the Linear Quadratic Gaussian (LQG) method, is used. The LQG control strategy provides a convenient means of designing an optimal MIMO controller. The procedure to determine the controller, $\mathbf{G_c}$(s), based on the LQG control design methodology is explained below.

In order to use the LQG design methodology, a state space model of the dynamics of the plant, **G**(s), is needed. A state space model of the plant is

$$\begin{aligned} \dot{\mathbf{x}}(t) &= \mathbf{A} \cdot \mathbf{x}(t) + \mathbf{B} \cdot \mathbf{u}(t) + \mathbf{w_n}(t) \\ \mathbf{p}(t) &= \mathbf{c} \cdot \mathbf{x}(t) + \mathbf{w_d}(t) \end{aligned} \tag{2.76}$$

where $\mathbf{x}(t)$ and $\dot{\mathbf{x}}(t)$ are the state vector and its derivative, $\mathbf{u}(t)$ is the input vector, $\mathbf{p}(t)$ is the output vector which, in this case, is the vector of microphone pressure signals. The vectors, $\mathbf{w_d}(t)$ and $\mathbf{w_n}(t)$, are white noise inputs to the system with properties

$$E\{\mathbf{w_d}(t)\cdot\mathbf{w_d}(\tau)^T\} = \mathbf{W}\delta(t-\tau)$$
$$E\{\mathbf{w_n}(t)\cdot\mathbf{w_n}(\tau)^T\} = \mathbf{V}\delta(t-\tau) \tag{2.77}$$

where $E\{\ \}$ is the expectation operator, **W** and **V** are the correlation matrices. The vectors, $\mathbf{w_d}(t)$ and $\mathbf{w_n}(t)$ are uncorrelated from each other, that is

$$E\{\mathbf{w_d}(t)\cdot\mathbf{w_n}(\tau)^T\} = \mathbf{0}$$
$$E\{\mathbf{w_n}(t)\cdot\mathbf{w_d}(\tau)^T\} = \mathbf{0} \tag{2.78}$$

In the simulation studies in Chapter 3, the plant state space model is obtained by performing a system identification procedure on the frequency response data obtained from analytical models. In order to facilitate a system identification of MIMO system, a procedure called "Eigensystem Realization Algorithm" or "ERA" [45] was used. The ERA is a time-domain system identification method which operates on the impulse response information of a MIMO plant dynamics. The details of the ERA procedure are provided in Appendix C.

Once the state space model of the plant is obtained, the LQG controller can be designed based on the model as follows. The following diagram shows the internal structure of a LQG controller.

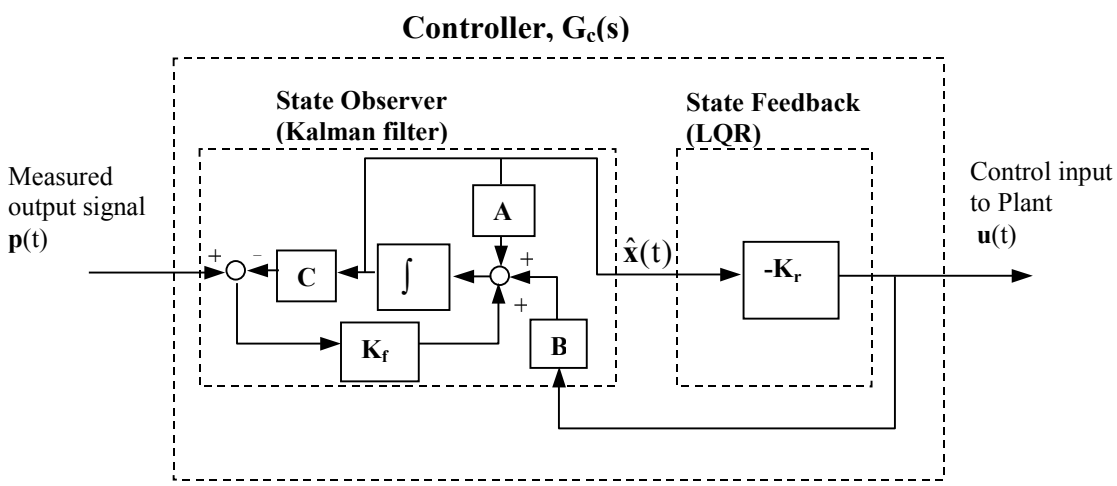

Figure 2.12. Structure of a LQG controller

As shown in the diagram, the controller consists of a state feedback and a state observer. The state feedback part is expressed as

$$\mathbf{u}(t) = -\mathbf{K}_r \cdot \hat{\mathbf{x}}(t) \tag{2.79}$$

where $\mathbf{u}(t)$ is the control input vector and $\mathbf{K_r}$ the constant gain matrix. The vector, $\hat{\mathbf{x}}(t)$ is the state vector estimated by the state observer which is

$$\dot{\hat{\mathbf{x}}}(t) = \mathbf{A} \cdot \hat{\mathbf{x}}(t) + \mathbf{B} \cdot \mathbf{u}(t) + \mathbf{K}_f \left(\mathbf{p}(t) - \mathbf{C} \cdot \hat{\mathbf{x}}(t)\right) \tag{2.80}$$

where $\mathbf{K_f}$ is the observer gain matrix. The matrices, **A**, **B** and **C** are directly obtained from the plant state space model.

There are two design parameters, $\mathbf{K_f}$ and $\mathbf{K_r}$, to be determined and these two parameters can be determined independently (the Separation Theorem [46]). The state feedback gain matrix, $\mathbf{K_f}$, is obtained by solving the LQR (Linear Quadratic Regulator) problem in which the optimal value of the control input, **u**(t), is found by minimizing the cost function

$$J = \lim_{T \to \infty} \int_0^T \mathbf{x}(t)^T \cdot \mathbf{Q} \cdot \mathbf{x}(t) + \mathbf{u}(t)^T \cdot \mathbf{R} \cdot \mathbf{u}(t)\, dt \tag{2.81}$$

where Q ($\mathbf{Q} = \mathbf{Q}^T \geq 0$) and R ($\mathbf{Q} = \mathbf{Q}^T \geq 0$) are the weighting matrices which serve here as design parameters. The cost function, *J*, is minimized by solving the Algebraic Riccati Equation

$$\mathbf{A}^T \cdot \mathbf{X} + \mathbf{X} \cdot \mathbf{A} - \mathbf{A} \cdot \mathbf{B} \cdot \mathbf{R}^{-1} \cdot \mathbf{B}^T \cdot \mathbf{X} + \mathbf{Q} = \mathbf{0} \tag{2.82}$$

for the solution ,**X** ($\mathbf{X} = \mathbf{X}^T \geq 0$). Then the optimal feedback gain matrix, $\mathbf{K_r}$, is given by

$$\mathbf{K}_r = \mathbf{R}^{-1} \cdot \mathbf{B} \cdot \mathbf{X} \tag{2.83}$$

which in turn provides the optimal value of **u**(t) in Equation (2.79).

On the other hand, the state observer gain matrix, $\mathbf{K_f}$, is obtained by minimizing the error in the estimated state vector,

$$E\left\{\left[\mathbf{x}-\hat{\mathbf{x}}\right]^{T}\cdot\left[\mathbf{x}-\hat{\mathbf{x}}\right]\right\} \tag{2.84}$$

The optimal value of $\mathbf{K_f}$ which minimizes this quantity is found by solving another Algebraic Riccati equation

$$\mathbf{Y}\cdot\mathbf{A}^{T}+\mathbf{A}\cdot\mathbf{Y}-\mathbf{T}\cdot\mathbf{C}^{T}\cdot\mathbf{V}^{-1}\cdot\mathbf{C}\cdot\mathbf{Y}+\mathbf{W}=\mathbf{0} \tag{2.85}$$

where $\mathbf{Y}$ is the parameter, $\mathbf{V}$ and $\mathbf{W}$ are the disturbance correlation matrices of (2.77). The observer gain matrix, $\mathbf{K_f}$, is then given by,

$$\mathbf{K}_{f}=\mathbf{Y}\cdot\mathbf{C}^{T}\cdot\mathbf{V}^{-1} \tag{2.86}$$

where $\mathbf{Y}$ is the solution of Equation (2.85). Note that the noise correlation matrices, $\mathbf{V}$ and $\mathbf{W}$, serve as design parameters.

In the actual design process, the design parameter matrices, $\mathbf{Q}$ and $\mathbf{R}$ for the state feedback and the matrices, $\mathbf{V}$ and $\mathbf{W}$, are iteratively adjusted until a desirable control design is achieved.

It should be emphasized here that the LQG design method is used in this thesis for the purpose of determining the theoretical maximum performance achievable by the feedback control approach. The main focus is placed on the effect of different physical design of the active-passive duct rather than the feedback control design itself. The LQG method is used merely as a tool to obtain feedback control filters in a consistent manner.

2.4.3 Feedforward-Feedback Hybrid Control

A feedforward control system and a feedback control system may be combined together to form a hybrid control system. Figure 2.13 shows the block diagram.

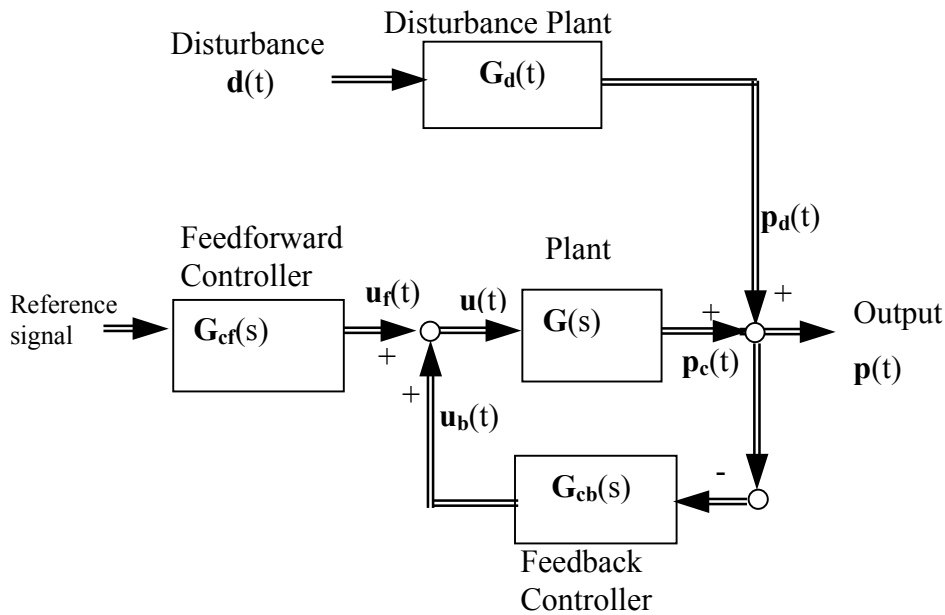

Figure 2.13. Hybrid Feedforward-Feedback Control System

In this control system, the feedforward controller provides the attenuation for those noise content that are correlated with the available reference signal while the feedback controller provides the reduction of the remaining uncorrelated noise content. In Chapter 4, a hybrid feedforward-feedback controller in implemented and tested, where an adaptive digital feedforward controller is combined with an analog feedback controller. The feedforward controller part is designed to reduce only the BPF tones in the fan noise, while the feedback controller part provides the reduction of the remaining broadband fan noise. As it will be shown in the experimental results in Chapter 4, this hybrid control approach offers an efficient and effective way of reducing the total fan noise level, by combining the benefits of both feedforward and feedback control.

2.5 Summary

A matrix approach for the analytical modeling of the active-passive control fan duct was developed and presented in this chapter. The approach was an extension of a modeling concept proposed by Muehleisen [19]. In this proposed approach, a duct is cast as a collection of short duct segments connected at multiple junctions, which represented various discontinuities. As it will be shown in the next chapter, this modeling approach is quite suited for obtaining high-fidelity finite duct models. Using this approach, one can naturally incorporate such complex phenomenon as modal wave cross coupling at duct open ends, which has typically been ignored in previous literature.

An analytical model of a fan was also described in this chapter. A fan was modeled as a force field distributed over a duct cross sectional area and was expressed as a sum of modal force distributions. The validity of this model was checked by experimentally-obtained data of the relative magnitudes and phases between the modal waves propagated away from the front and the back of the fan in a simulated infinite duct. The data indicated, though less clearly for higher-order modes, the expected asymmetric radiation pattern of the fan noise in an infinite duct. The validity of this model will be further demonstrated later in the experimental and analytical result comparisons in Chapter 4.

Lastly, the analytical approaches for the determination of active control performances were also described with respect to both feedforward and feedback control. The analytical approach for the determination of the feedforward control performance implicitly assumed the availability of perfectly correlated reference signal and therefore provided the ideal control performance theoretically obtainable. For the feedback control, the LQG optimal control design approach was adapted. It should be emphasized that, in this thesis, the LQG optimal control design approach was to be used merely as a tool to determine the "optimal" performance theoretically obtainable for feedback control. The hybrid feedforward-feedback control approach was also briefly described. This hybrid active control approach is implemented and investigated in the experimental study later in Chapter 4.

Chapter 3

Analytical Study

In this chapter, the general modeling approach introduced in Chapter 2 is applied to develop analytical models of active-passive noise control fan duct for simulation studies. Two alternate designs of active-passive control fan duct are considered. One is a finite rectangular fan duct in conjunction with 2x2 active control. The other is a finite rectangular duct having the same overall dimensions, but its interior segmented into smaller duct sections in conjunction with 8x8 active control. Potentially achievable passive and active noise control performance are determined with respect to each of these design configurations. Although investigations in this chapter are carried out mainly in the form of simulations, some experimental results are also included in order to validate the analytical models.

3.1 Non-segmented Fan Duct with 2x2 Active Control

A finite rectangular duct with a fan mounted in the middle is shown in Figure 3.1. The duct is open-ended on both sides and assumed to be fitted with infinitely large baffles. There are two active acoustic sources (or control speakers) and two error microphones in the duct for 2x2 active control (one speaker-microphone pair on each side of the fan). The duct interior sidewalls are lined with sound-absorbing material for additional passive noise attenuation.

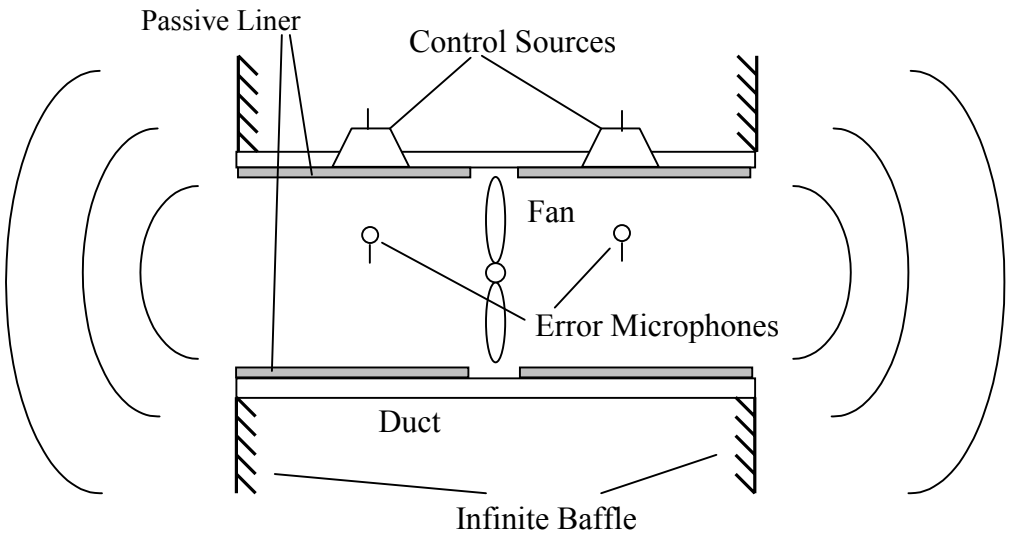

Figure 3.1. Non-segmented fan duct with 2x2 active control

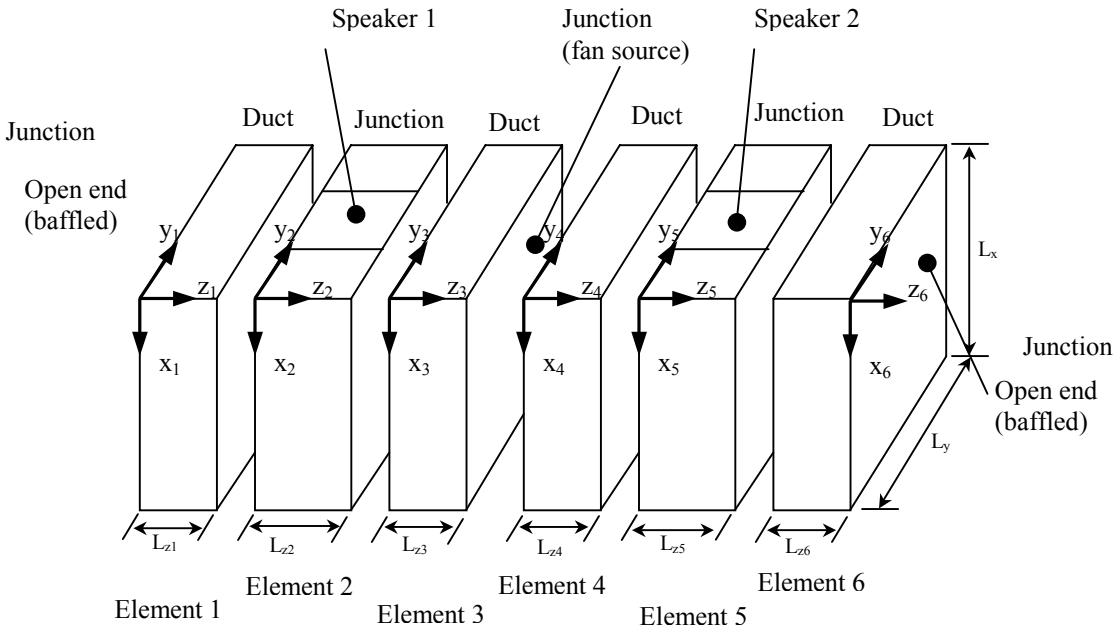

Figure 3.2. Finite rectangular fan duct modeled as a duct-junction system

3.1.1 Model Development

The fan duct of Figure 3.1 can be modeled as a duct-junction system as shown in Figure 3.2. There are four duct segments, which are shown in the figure as Element 1, 3, 4 and 5. These duct segments are connected at junction elements representing the two control speakers and the fan noise source. The figure also shows reference coordinates defined locally in each element.

As explained in Chapter 2, the first step in this modeling approach is to determine modal impedance matrices, $\mathbf{Z_{RM}}$, for all the junctions present in the model. There are three types of junctions in this model: speaker junction, duct open end junction and fan source junction. The modal impedance matrices associated with these junctions can be determined as follows.

Speaker Junction Modal Impedance

The modal impedance matrix, $\mathbf{Z}_{\mathbf{RM}\,2}$, associated with the speaker junction on the left (Element 2), relates the modal velocity vector, $\mathbf{U}_{\mathbf{M}\,2}$, to the modal pressure vector, $\mathbf{P}_{\mathbf{R}\,2}$, at duct-junction interfaces as

$$\mathbf{P}_{\mathbf{R}\,2} = \mathbf{Z}_{\mathbf{RM}\,2} \cdot \mathbf{U}_{\mathbf{M}\,2} \tag{3.1}$$

which is expanded as

$$\begin{bmatrix} \mathbf{p}_{\mathbf{R}}^{1} \\ \mathbf{p}_{\mathbf{R}}^{2} \end{bmatrix}_2 = \begin{bmatrix} \mathbf{z}_{\mathbf{RM}}^{11} & \mathbf{z}_{\mathbf{RM}}^{12} & \mathbf{z}_{\mathbf{RM}}^{13} \\ \mathbf{z}_{\mathbf{RM}}^{21} & \mathbf{z}_{\mathbf{RM}}^{22} & \mathbf{z}_{\mathbf{RM}}^{23} \end{bmatrix}_2 \cdot \begin{bmatrix} \mathbf{u}_{\mathbf{M}}^{1} \\ \mathbf{u}_{\mathbf{M}}^{2} \\ u_{s1} \end{bmatrix}_2 \tag{3.2}$$

where $\mathbf{p}_{\mathbf{R}}^{l}$ is the modal pressure vector at the *l*-th interface, $\mathbf{u}_{\mathbf{R}}^{i}$ is the modal velocity vector at the *i*-th interface in the junction, and u_{s1} the velocity of the square piston representing the left-side speaker (Speaker 1). The subscript, *2*, designates the element number of the junction (Element 2). Figure 3.3 shows a speaker junction.

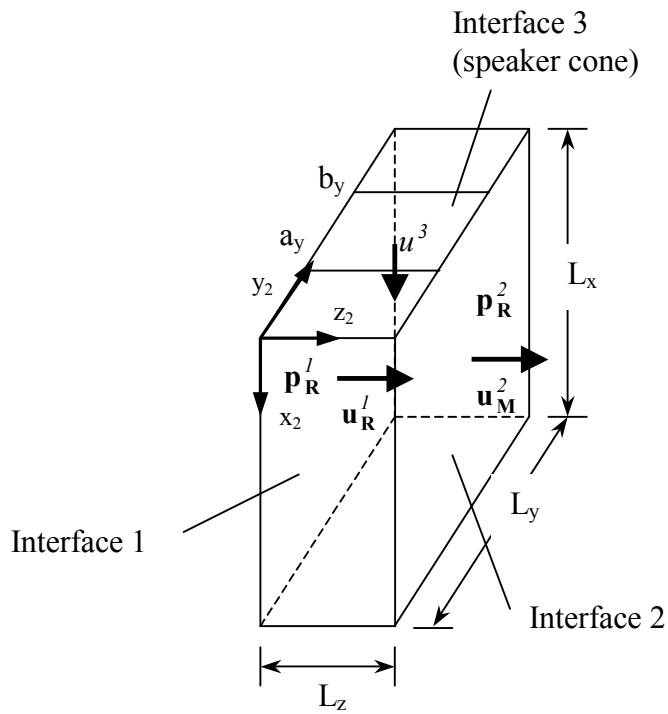

Figure 3.3. Speaker junction element

In Figure 3.3, the positive directions of the modal velocity vectors are defined and indicated by the arrows.

The matrix, $\mathbf{Z_{RM}}_2$, is determined by using an integral expression introduced in Chapter 2 which is repeated here as

$$z_{RM}{}^{li} = \frac{jk\rho c}{S_l} \int_{S_l}\int_{S_i} G_J(\mathbf{r} \mid \mathbf{r_o}) \cdot \Psi_R{}^l(\mathbf{r}) \Psi_M{}^i(\mathbf{r_o}) dS_l dS_i \tag{3.3}$$

where appropriate Green's function, G_J, and mode shape functions, $\Psi_R{}^l(\mathbf{r})$ and $\Psi_M{}^i(\mathbf{r}_o)$, are presented given by Equations (2.30) and (2.9) in Chapter 2.

The integral expression above can be analytically evaluated and simplified. The expressions for the individual sub-matrices of the speaker junction impedance matrix, $\mathbf{Z}_{\mathbf{RM}2}$, are determined as

$$
\begin{aligned}
\mathbf{z}_{\mathbf{RM}}^{11} &= \left[\frac{jk\rho c}{L_z} \sum_{n_z} \frac{1}{\Lambda_{n_z}} \cdot \left(\frac{1}{\left(\frac{m_x \pi}{L_x}\right)^2 + \left(\frac{m_y \pi}{L_y}\right)^2 + \left(\frac{m_z \pi}{L_z}\right)^2 - k^2} \right) \right]_{diag} \\
\mathbf{z}_{\mathbf{RM}}^{22} &= -\mathbf{z}_{\mathbf{RM}}^{11} \\
\mathbf{z}_{\mathbf{RM}}^{21} &= \left[\frac{jk\rho c}{L_z} \sum_{n_z} \frac{(-1)^{n_z}}{\Lambda_{n_z}} \cdot \left(\frac{1}{\left(\frac{m_x \pi}{L_x}\right)^2 + \left(\frac{m_y \pi}{L_y}\right)^2 + \left(\frac{m_z \pi}{L_z}\right)^2 - k^2} \right) \right]_{diag} \\
\mathbf{z}_{\mathbf{RM}}^{12} &= -\mathbf{z}_{\mathbf{RM}}^{21} \\
\mathbf{z}_{\mathbf{RM}}^{23} &= \left[\frac{jk\rho c}{L_x L_y} \cdot \frac{1}{\sqrt{\Lambda_{r_x} \Lambda_{r_y}}} \cdot \left(\frac{1}{\left(\frac{r_x \pi}{L_x}\right)^2 + \left(\frac{r_y \pi}{L_y}\right)^2 - k^2} \right) \right. \\
&\qquad \left. \cdot \left(\frac{\sin\left(\frac{r_y \pi}{L_y} b_y\right)}{\frac{r_y \pi}{L_y}} - \frac{\sin\left(\frac{r_y \pi}{L_y} a_y\right)}{\frac{r_y \pi}{L_y}} \right) \right] \\
\mathbf{z}_{\mathbf{RM}}^{13} &= \mathbf{z}_{\mathbf{RM}}^{23}
\end{aligned}
\tag{3.4}
$$

Equation (3.4) above also apply to the other speaker junction (Element 5).

Open End Junction Modal Impedance

An open end junction is shown in the following figure.

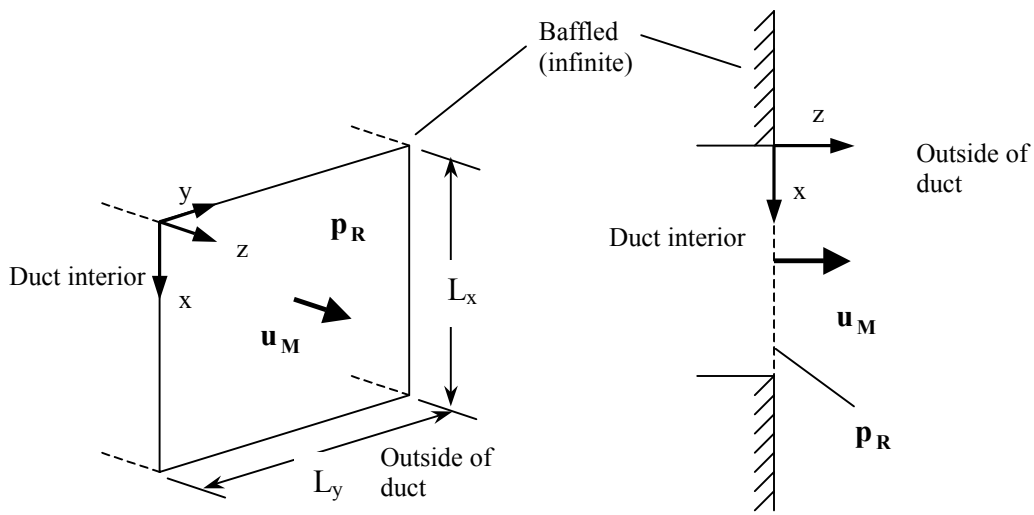

Figure 3.4. Open end junction (right side)

The acoustic characteristics of the duct open end junction is also expressed in term of modal impedance. For the open end at the right side of the duct in Figure 3.2, the modal impedance matrix equation is

$$\mathbf{P}_{\mathbf{R}6} = \mathbf{Z}_{\mathbf{RM}6} \cdot \mathbf{U}_{\mathbf{M}6} \tag{3.5}$$

or

$$\left[\mathbf{p}^{2}_{\mathbf{R}6}\right] = \left[\mathbf{z}^{22}_{\mathbf{RM}6}\right] \cdot \left[\mathbf{u}^{2}_{\mathbf{M}6}\right] \tag{3.6}$$

where $\mathbf{p}^{2}_{\mathbf{R}6}$ and $\mathbf{u}^{2}_{\mathbf{M}6}$ are the modal pressure and the modal velocity vector associated with the duct opening surface (Interface 2 of Element 6).

The integral expression of Equation (3.3) can also be applied for this junction to obtain the modal impedance. The mode-shape functions, $\Psi_R(\mathbf{r})$ and $\Psi_M(\mathbf{r_o})$ are unchanged from those for the speaker junction above. However, the Green's function, G_J,

has to be replaced with that for a free space bounded by an infinite rigid surface and consequently, the equation becomes

$$z_{RM}^{\ li} = \frac{jk\rho c}{2\pi S} \int_S \int_{S_o} \frac{e^{-jk|\mathbf{r}-\mathbf{r_o}|}}{|\mathbf{r}-\mathbf{r_o}|} \cdot \Psi_R(\mathbf{r})\Psi_M(\mathbf{r_o})dSdS_o \tag{3.7}$$

where $|\mathbf{r}-\mathbf{r_o}|$ is the distance between the observation and the source point.

The integral expression in this equation cannot be evaluated in a closed form and thus, numerical integration is required. However, due to singularities at the points where the quantity $|\mathbf{r}-\mathbf{r_o}|$ becomes zero (i.e. where the observation point and the source point coincide), the usual numerical integration method, such as Gaussian quadrature cannot be directly applied. A special numerical integration scheme is needed to circumvent this singularity problem [19]. The method adapted here is commonly used in Boundary Element Methods (BEM) which involves numerical integrations involving the same type of singularity. The description of this numerical integration scheme is provided in Appendix B. The modal impedance matrix for the other duct open end junction is obtained the same way.

Fan Source Junction Modal Impedance

A fan source is to be located between Element 3 and 4 and considered here as a junction. Figure 3.5 shows the fan source junction.

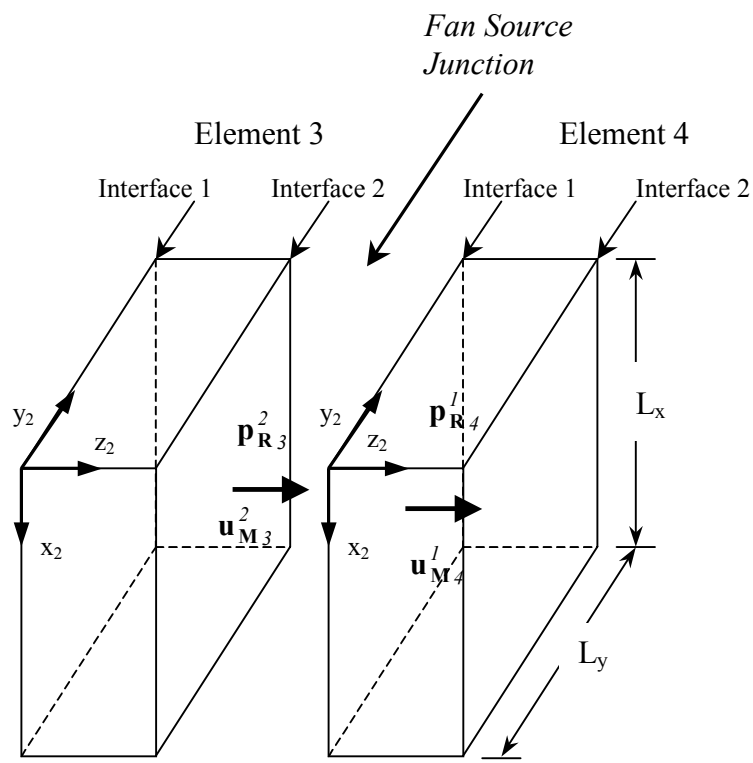

Figure 3.5. Fan source junction

The fan noise source is modeled as a distributed force characterized by a modal force vector, $\mathbf{f_M}$. This gives rise to a discontinuity in pressure at the position of the fan. This is expressed as

$$\mathbf{p}^{1}_{\mathbf{M}4} - \mathbf{p}^{2}_{\mathbf{M}3} = \frac{\mathbf{f_M}}{S} \tag{3.8}$$

where $\mathbf{p}^{1}_{\mathbf{M}4}$ is the modal pressure vector at Interface 1 (left side face) of Element 4, $\mathbf{p}^{2}_{\mathbf{M}3}$ is the modal pressure vector at Interface 2 (right side face) of Element 3 and S is the duct cross-sectional area. On the other hand, the modal velocity at the junction is continuous and therefore,

$$\mathbf{u}^{1}_{\mathbf{M}4} - \mathbf{u}^{2}_{\mathbf{M}3} = \mathbf{0} \tag{3.9}$$

where $\mathbf{u}^{1}_{\mathbf{M}4}$ is the modal velocity vector at Interface 1 of Element 4 and $\mathbf{u}^{2}_{\mathbf{M}3}$ is the modal velocity vector at Interface 2 of Element 3.

In the actual simulations, the force excitation vector, $\mathbf{f_M}$, is assumed to have uniform magnitudes (unity) for all modes, M. This assumption is based on the experimental result presented in Chapter 2 where it was found that the differences in the magnitudes of the fan excitation force for different modes were relatively small. The phases of, $\mathbf{f_M}$, were assigned arbitrary values.

Modal Scattering Matrix Equations

After modal impedance matrix equations are obtained with respect to all the junctions, next step is to convert them into corresponding modal scattering matrix equations. The modal scattering matrix equations describe junction acoustic characteristics in terms of the modal wave amplitudes, a_M and b_M, associated with adjacent duct segments. For example, a modal scattering matrix equation for the left speaker junction (Element 2) is obtained as follows. The modal impedance matrix equation of Equation (3.2) can be written in terms of the modal wave amplitude vectors associated with adjacent duct elements (Element 1 and 3) as

$$\begin{bmatrix} \left[a_{M\,1} e^{-jk_M L_{z1}} + b_{M\,1} e^{+jk_M L_{z1}} \right] \\ \left[a_{M\,3} e^{-jk_M 0} + b_{M\,3} e^{+jk_M 0} \right] \end{bmatrix}$$

$$= \begin{bmatrix} \mathbf{z}_{\mathbf{RM}}^{11} & \mathbf{z}_{\mathbf{RM}}^{12} & \mathbf{z}_{\mathbf{RM}}^{13} \\ \mathbf{z}_{\mathbf{RM}}^{21} & \mathbf{z}_{\mathbf{RM}}^{22} & \mathbf{z}_{\mathbf{RM}}^{23} \end{bmatrix}_2 \cdot \begin{bmatrix} \left[y_{M\,1} \cdot \left(a_{M\,1} e^{-jk_M L_{z1}} - b_{M\,1} e^{+jk_M L_{z1}} \right) \right] \\ \left[y_{M\,3} \cdot \left(a_{M\,3} e^{-jk_M 0} - b_{M\,3} e^{+jk_M 0} \right) \right] \\ u_{s1} \end{bmatrix} \tag{3.10}$$

alternatively,

$$\begin{bmatrix} \mathbf{e}^-_1 \cdot \mathbf{a}_{\mathbf{M}1} + \mathbf{e}^+_1 \cdot \mathbf{b}_{\mathbf{M}1} \\ \mathbf{a}_{\mathbf{M}3} + \mathbf{b}_{\mathbf{M}3} \end{bmatrix} = \begin{bmatrix} \mathbf{z}_{\mathbf{RM}}^{11} & \mathbf{z}_{\mathbf{RM}}^{12} & \mathbf{z}_{\mathbf{RM}}^{13} \\ \mathbf{z}_{\mathbf{RM}}^{21} & \mathbf{z}_{\mathbf{RM}}^{22} & \mathbf{z}_{\mathbf{RM}}^{23} \end{bmatrix}_2 \cdot \begin{bmatrix} \mathbf{y}_{\mathbf{M}1} \cdot \left(\mathbf{e}^-_1 \cdot \mathbf{a}_{\mathbf{M}1} - \mathbf{e}^+_1 \cdot \mathbf{b}_{\mathbf{M}1} \right) \\ \mathbf{y}_{\mathbf{M}3} \cdot \left(\mathbf{e}^-_3 \cdot \mathbf{a}_{\mathbf{M}3} - \mathbf{e}^+_3 \cdot \mathbf{b}_{\mathbf{M}3} \right) \\ u_{s1} \end{bmatrix} \tag{3.11}$$

Further rearrangements yield,

$$\begin{bmatrix} \mathbf{E}^- \left(\mathbf{I} - \mathbf{Z}_{\mathbf{RM}} \mathbf{Y} \right) & \mathbf{E}^+ \left(\mathbf{I} + \mathbf{Z}_{\mathbf{RM}} \mathbf{Y} \right) \end{bmatrix}_2 \cdot \begin{bmatrix} \mathbf{a}_{\mathbf{M}1} \\ \mathbf{a}_{\mathbf{M}3} \\ \mathbf{b}_{\mathbf{M}1} \\ \mathbf{b}_{\mathbf{M}3} \end{bmatrix} = \begin{bmatrix} \mathbf{z}_{\mathbf{RM}}^{13} \\ \mathbf{z}_{\mathbf{RM}}^{23} \end{bmatrix}_2 \cdot u_{s1} \tag{3.12}$$

where

$$\mathbf{E}^- = \begin{bmatrix} \mathbf{e}^-_1 & \mathbf{0} \\ \mathbf{0} & \mathbf{0} \end{bmatrix}, \qquad \mathbf{E}^+ = \begin{bmatrix} \mathbf{e}^+_1 & \mathbf{0} \\ \mathbf{0} & \mathbf{0} \end{bmatrix} \tag{3.13}$$

and

$$\mathbf{Y}_M = \begin{bmatrix} \mathbf{y}_{\mathbf{M}1} & \mathbf{0} \\ \mathbf{0} & \mathbf{y}_{\mathbf{M}3} \end{bmatrix}, \qquad \mathbf{Z}_{\mathbf{RM}} = \begin{bmatrix} \mathbf{z}_{\mathbf{RM}}^{11} & \mathbf{z}_{\mathbf{RM}}^{12} \\ \mathbf{z}_{\mathbf{RM}}^{21} & \mathbf{z}_{\mathbf{RM}}^{22} \end{bmatrix}_2 \tag{3.14}$$

Equation (3.12) above characterizes the scattering of waves at the junction and it shall be compactly designated as

$$\mathbf{S}_2 \cdot \begin{bmatrix} \mathbf{a}_{\mathbf{M}1} \\ \mathbf{a}_{\mathbf{M}3} \\ \mathbf{b}_{\mathbf{M}1} \\ \mathbf{b}_{\mathbf{M}3} \end{bmatrix} = \mathbf{F}_2 \tag{3.15}$$

where $\mathbf{S}_2$ is the scattering matrix, $\mathbf{F}_2$ is the excitation vector for Element 2. Modal scattering matrix equation can be obtained similarly for the rest of the junctions.

Global Modal Scattering Matrix Equation

After the modal scattering matrix equations are obtained with respect to all the junctions, these matrix equations to be assembled into a single global matrix equation. First, the dimensions of the junction modal scattering matrix equations have to be expanded to ensure compatibility. For example, the modal scattering matrix equation of (3.15) is expanded as

$$\begin{bmatrix} \mathbf{S}_2(:,\ 1{:}1N_M) & \mathbf{0} & \mathbf{0} & \mathbf{S}_2(:,\ (1N_M+1){:}2N_M) & \mathbf{0} & \mathbf{0} \end{bmatrix} \cdot \begin{bmatrix} \mathbf{a}_{\mathbf{M}1} \\ \mathbf{a}_{\mathbf{M}3} \\ \mathbf{a}_{\mathbf{M}4} \\ \mathbf{a}_{\mathbf{M}6} \\ \mathbf{b}_{\mathbf{M}1} \\ \mathbf{b}_{\mathbf{M}3} \\ \mathbf{b}_{\mathbf{M}4} \\ \mathbf{b}_{\mathbf{M}6} \end{bmatrix} = \mathbf{F}_2 \tag{3.16}$$

where N_M is the number of included modes, $\mathbf{0}$ is a zero matrix of size N_M by N_M. The notation $\mathbf{S}_2(:,1{:}1N_M)$ designates the column 1 to $1N_M$ of the matrix, $\mathbf{S}_2$, and $\mathbf{S}_2(:,(1N_M+1){:}2N_M)$ designates the column $(1N_M+1)$ to $2N_M$ of the matrix, $\mathbf{S}_2$. Also the columns of the scattering matrices may need to be re-ordered for consistency. Note that the unknown modal wave amplitude vector now contains the modal wave amplitudes in all four duct segments in the system.

Once all the junction modal scattering matrix equations are expanded, the global scattering matrix equation can be obtained as

$$\begin{bmatrix} \hat{\mathbf{S}}_2 \\ \hat{\mathbf{S}}_5 \\ \hat{\mathbf{S}}_{fan_v} \\ \hat{\mathbf{S}}_{fan_p} \\ \hat{\mathbf{S}}_{end_l} \\ \hat{\mathbf{S}}_{end_r} \end{bmatrix} \cdot \begin{bmatrix} \mathbf{a}_{\mathbf{M}1} \\ \mathbf{a}_{\mathbf{M}3} \\ \mathbf{a}_{\mathbf{M}4} \\ \mathbf{a}_{\mathbf{M}6} \\ \mathbf{b}_{\mathbf{M}1} \\ \mathbf{b}_{\mathbf{M}3} \\ \mathbf{b}_{\mathbf{M}4} \\ \mathbf{b}_{\mathbf{M}6} \end{bmatrix} = \begin{bmatrix} \mathbf{F}_2 \\ \mathbf{F}_5 \\ \mathbf{0} \\ \mathbf{F}_{fan_p} \\ \mathbf{0} \\ \mathbf{0} \end{bmatrix} \tag{3.17}$$

where the sub-matrices of the left-hand-side matrix are, beginning from the top, the left and the right speaker junctions, the velocity and the pressure condition at the fan source junction and the left and the right open-end junction. The notation, $\hat{\mathbf{S}}$, signifies that the scattering matrix is appropriately expanded and reordered for compatibility. The sub-vectors of the right-hand -side excitation vector are

$$\mathbf{F}_2 = \begin{bmatrix} \mathbf{z}_{\mathbf{RM}}^{13} \\ \mathbf{z}_{\mathbf{RM}}^{23} \end{bmatrix}_2 \cdot u_{s1}, \qquad \mathbf{F}_5 = \begin{bmatrix} \mathbf{z}_{\mathbf{RM}}^{13} \\ \mathbf{z}_{\mathbf{RM}}^{23} \end{bmatrix}_5 \cdot u_{s2}, \tag{3.18}$$

and

$$\mathbf{F}_{fan_p} = \frac{\mathbf{f}_{\mathbf{M}}}{S} \tag{3.19}$$

where u_{s1} and u_{s2} are the cone velocities of the left and the right speaker, respectively and $\mathbf{f}_{\mathbf{M}}$ is the fan force excitation vector in Equation (3.8).

The global scattering matrix equation of Equation (3.17) above shall be designated as

$$\mathbf{S}_{global} \cdot \begin{bmatrix} \mathbf{A}_{\mathbf{M}} \\ \mathbf{B}_{\mathbf{M}} \end{bmatrix} = \mathbf{F}_{global} \tag{3.20}$$

where $\mathbf{S}_{global}$ is the global modal scattering matrix, $\mathbf{F}_{global}$ is the global excitation matrix. Then, the global scattering matrix equation can be solved as

$$\begin{bmatrix} \mathbf{A_M} \\ \mathbf{B_M} \end{bmatrix} = \mathbf{S}_{global}{}^{-1} \cdot \mathbf{F}_{global} \tag{3.21}$$

which gives the amplitudes of the unknown modal waves in all the duct segments (Element 1, 3, 4, 6). The pressure and the velocity within the duct segments can be obtained from the duct modal wave amplitudes.

Junction Internal Pressure

As described in Chapter 2, the pressure field, $p(\mathbf{r})$, *inside* a junction can be expressed in terms of modal summations as,

$$p(\mathbf{r}) = \left\{ \begin{bmatrix} \mathbf{p}_{\mathbf{R_{xy}}\,R_z=1} & \mathbf{p}_{\mathbf{R_{xy}}\,R_z=2} & \cdots \end{bmatrix} \cdot \boldsymbol{\psi}_{\mathbf{R_a}}(z) \right\}^T \cdot \boldsymbol{\psi}_{\mathbf{R_{xy}}}(x,y) \tag{2.22}$$

where $\boldsymbol{\psi}_{\mathbf{R_{xy}}}(x,y)$ and $\boldsymbol{\psi}_{\mathbf{R_a}}(z)$ are the vectors of mode-shape functions associated with the junction volume. And each sub-matrix of the modal pressure matrix above is given by

$$\mathbf{p}_{\mathbf{R_{xy}}\,R_z} = \begin{bmatrix} \mathbf{z_{IRM}}^1 & \mathbf{z_{IRM}}^2 & \mathbf{z_{IRM}}^3 \end{bmatrix}_{R_z} \cdot \begin{bmatrix} \mathbf{u_M}^1 \\ \mathbf{u_M}^2 \\ \mathbf{u_M}^3 \end{bmatrix} \tag{2.23}$$

where $\mathbf{u}_{\mathbf{M}}^i$ is the modal velocity vector at the i-th duct-junction interface. The values of the modal velocity vectors, $\mathbf{u}_{\mathbf{M}}^i$, are obtained from the already-determined modal wave amplitude vectors of Equation (3.21). The sub-matrices, $\mathbf{z_{IRM}}^i$, represent the impedance between the interface modal velocity vector and the junction internal modal pressure and these are determined by

$$z_{I\,RM}{}^i = \frac{jk\rho c}{V} \frac{1}{\kappa_R{}^2 - k^2} \int_{S_i} \cdot \phi_R(\mathbf{r_0}) \psi_M(\mathbf{r_0}) dS_i \tag{3.24}$$

where $\phi_R(\mathbf{r_0})$ and $\psi_M(\mathbf{r_0})$ are the mode-shape function of the R-th *volume* modal pressure and the M-th *surface* modal velocity, respectively. For example, the application of this equation for the left speaker junction (Element 2) yields

$$\begin{aligned}
\mathbf{z}_{\mathbf{IRM}}^{1} &= \left[-\frac{jk\rho c}{\kappa_R^{\,2} - k^2} \frac{1}{\sqrt{\Lambda_{r_z}}} \frac{(-1)^{r_z}}{L_z} \right]_{diag} \\
\mathbf{z}_{\mathbf{IRM}}^{2} &= \left[\frac{jk\rho c}{\kappa_R^{\,2} - k^2} \frac{1}{\sqrt{\Lambda_{r_z}}} \frac{1}{L_z} \right]_{diag} \\
\mathbf{z}_{\mathbf{IRM}}^{3} &= \left[\frac{jk\rho c}{\kappa_R^{\,2} - k^2} \frac{1}{\sqrt{\Lambda_{r_z}}} \frac{\delta_{r_z 0}}{L_x L_y \sqrt{\Lambda_{r_x} \Lambda_{r_y}}} \left(\frac{\sin\left(\frac{r_y \pi}{L_y} b_y\right)}{\frac{r_y \pi}{L_y}} - \frac{\sin\left(\frac{r_y \pi}{L_y} a_y\right)}{\frac{r_y \pi}{L_y}} \right) \right]
\end{aligned} \tag{3.25}$$

where the factor, $\delta_{r_z 0}$, is given by

$$\delta_{r_z 0} = \begin{Bmatrix} 1 & for & r_z = 0 \\ 0 & for & r_z \neq 0 \end{Bmatrix} \tag{3.26}$$

and the eigenvalue, κ_R, is

$$\kappa_R^{\,2} = \left(\frac{r_x \pi}{L_x}\right)^2 + \left(\frac{r_y \pi}{L_y}\right)^2 + \left(\frac{r_z \pi}{L_z}\right)^2 \tag{3.27}$$

Equation (3.25) also applies to the other speaker junction (Element 5).

As for the determination of the pressure field *outside* the duct (which is considered here as "internal" to the open end junction), the procedure is as follows. Considering the right open end, the pressure field, $p(\mathbf{r})$ in the free space outside of the duct open end is given by

$$p(\mathbf{r}) = \mathbf{z}_{\mathbf{pM}\,end_r} \cdot \mathbf{u}_{\mathbf{M}6}^{2} \tag{3.28}$$

where $\mathbf{u}_{\mathbf{M}6}^{2}$ is the modal velocity vector at the right open end (Element 6, Interface 2). The matrix, $\mathbf{z}_{\mathbf{pM}\,end_r}$, is the given by

$$\mathbf{z}_{\mathbf{pM}end_r} = \left[\frac{jk\rho c}{2\pi} \int_{x_o} \int_{y_o} \frac{e^{-jk\sqrt{(x-x_o)^2+(y-y_o)^2+z^2}}}{\sqrt{(x-x_o)^2+(y-y_o)^2+z^2}} \Psi_M(x_o, y_o) dx_o dy_o \right] \tag{3.29}$$

which may be considered as a modal impedance matrix relating the open-end modal velocity to the pressure at a particular point (x ,y, z) in the free-space. Again, numerical integration is required to evaluate the integral. The equation contains the singularity as encountered earlier in Equation (3.7). However, a normal numerical integration method can be directly applied in this case as long as the domain of integration does not contain $z = 0$. The determination of the pressure field on the left side free space follows the same procedure.

Damping Model for Representing Passive Liner

In the present model, the effect of the passive liner installed on the duct inner walls is modeled as acoustic damping effects associated with the duct inner space. The acoustic damping in the duct is introduced in the model by using a complex value for the speed of sound [47], c, as,

$$c = c_o(1 + j \cdot \eta) \tag{3.30}$$

where c_o is the nominal speed of sound and η is the acoustic loss factor. Using this complex speed of sound has the effect of introducing a complex part to the wave number, $k(=\omega/c)$ which causes the exponential decay of waves propagating in a duct. The complex speed of sound also introduces damping to the junction modal impedances. For the present study, the damping factor, η, is assumed to be constant over frequency, though using frequency-dependant η is likely to result in more accurate representation.

Total Radiated Acoustic Power

The primary quantity of interest in the present study is the total acoustic power emitted out of the duct open ends into the free space. This is calculated as follows.

The acoustic intensity, $I(x, y)$, over a single duct opening is obtained by

$$I(x,y) = \frac{1}{2} Re\left\{p(x,y) \cdot u^*(x,y)\right\} \tag{3.31}$$

where *p(x,y)* and *u*(x,y)* are the pressure and the velocity (conjugate) over duct opening surface. Expressing the pressure and the velocity in terms of mode-shape functions, the expression becomes

$$I(x,y) = \frac{1}{2} Re\left\{\left(\mathbf{p_M}^T \cdot \boldsymbol{\psi}_\mathbf{M}\right) \cdot \left(\mathbf{u_M}^T \cdot \boldsymbol{\psi}_\mathbf{M}\right)^*\right\} \tag{3.32}$$

where the symbol, T, indicates transpose and the symbol,*, indicates a conjugate-transpose operation.

The total acoustic power radiated out from a duct opening is obtained by integrating the intensity over the opening surface area, *S*, as

$$W = \int_S I(x,y)dS = \frac{1}{2} Re\left\{\mathbf{p_M}^T \cdot \left(\int_S \boldsymbol{\psi}_\mathbf{M} \cdot \boldsymbol{\psi}_\mathbf{M}^* dS\right) \cdot \left(\mathbf{u_M}^T\right)^*\right\} \tag{3.33}$$

Eliminating the integral in the middle by applying the orthogonality condition introduced in Chapter 2, the expression becomes

$$W = \frac{S}{2} Re\left\{\mathbf{p_M}^T \cdot \left(\mathbf{u_M}^T\right)^*\right\} \tag{3.34}$$

which represents the total acoustic power emitted from one side of the duct. The power emitted from the other side is obtained the same way. Then, the total acoustic power emitted from both sides of the duct is simply the sum of the power emitted from both ends. This is a consequence of the assumption that the two duct ends are isolated from each other by the infinite baffles.

Model Validation Experiment

For the validation of the model developed above, the frequency responses of the plant dynamics (control speakers to microphones) were obtained experimentally for comparison with analytical model results.

Figure 3.6 shows the experimental setup to measure the plant dynamics of the 2x2 active control fan duct.

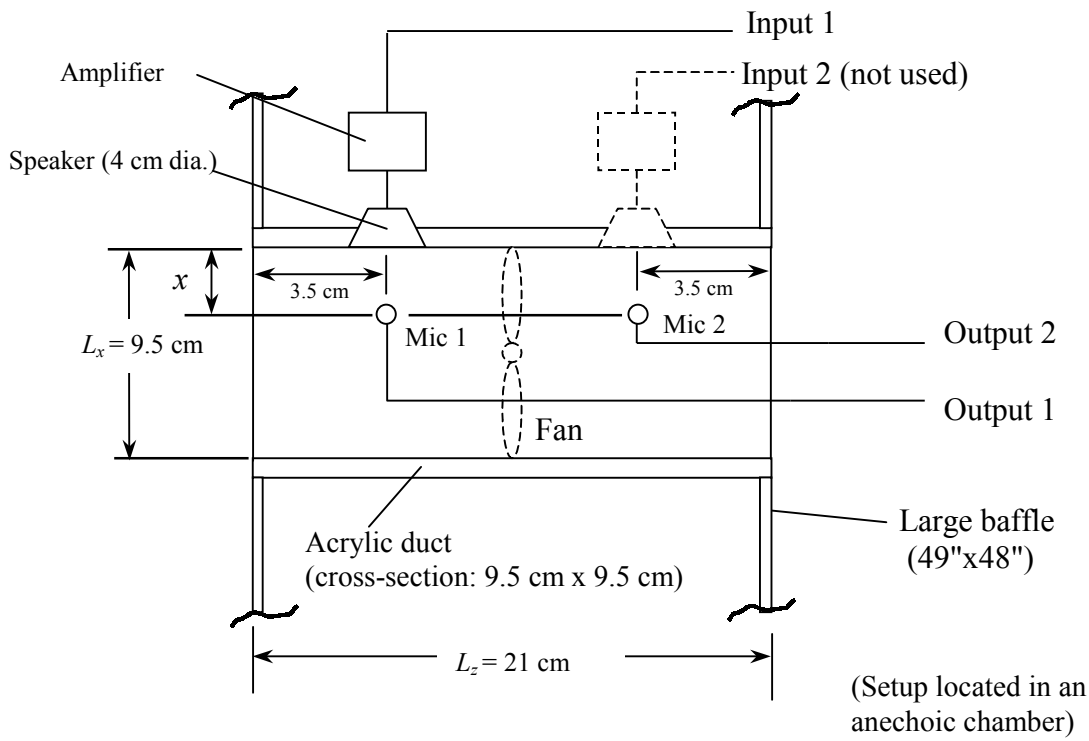

Figure 3.6. 2x2 active control fan duct plant frequency response measurement setup

The duct was constructed from a 1/8" thick, acrylic board. The axial length of the duct was 20.5 cm and the cross-section was 9.5 cm by 9.5 cm. The duct was fitted with large wooden baffles (48 in. by 49 in.) on both ends

As shown in the figure, the plant is a 2x2 system. The inputs to the system are the signals to the two speakers (4 cm diameter) and the outputs are the signals from the two microphones. However, only the frequency responses associated with a single speaker were needed to be measured in this case since the plant is symmetrical. Therefore, only a single speaker was actually used for the experiment together with two microphones.

The dimensions (in meters) of the corresponding analytical model of the fan duct (see Figure 3.2) are shown in Table 3.1 below.

Table 3.1. Non-segmented duct dimensions

Parameter	Value(m)	Parameter	Value(m)	Parameter	Value(m)
L_x	0.095	L_{z3}	0.0495	L_{z5}	0.035
L_y	0.094	L_{z4}	0.0495	L_{z6}	0.0205
L_{z1}	0.038	L_{z5}	0.035	b_y	0.065
L_{z2}	0.035	L_{z6}	0.0205	a_y	0.03

The duct modes and the corresponding cut-on frequencies are summarized in Table 3.2 below. Modes up to the ninth duct mode were included in the model, which was judged to be reasonably accurate as will be shown shortly by the comparisons with the experimental data.

Table 3.2. Non-segmented duct model modes and cut-on frequencies

Mode No.	Mode Index	Cut-on Frequency (Hz)	Mode No.	Mode Index	Cut-on Frequency (Hz)
M	(m_x, m_y)		M	(m_x, m_y)	
1	(0, 0)	0	6	(0, 2)	3649
2	(1, 0)	1805	7	(2, 1)	4045
3	(0, 1)	1825	8	(1, 2)	4071
4	(1, 1)	2567	9	(2, 2)	5133
5	(2, 0)	3611	-	-	-

The plant dynamics contains both the acoustical dynamic of the finite duct and the dynamics associated with the speaker. In the model, the dynamics of the speaker is represented by a second-order transfer function expressed as

$$\frac{K_s \cdot s}{s^2 + 2 \cdot \xi_s \cdot \omega_s + \omega_s^{\ 2}} \tag{3.35}$$

where ω_s is the natural frequency, ξ_s is the damping ratio and K_s is the gain constant. This speaker transfer function was assumed to be connected to the duct acoustical dynamics in series.

Figure 3.7 and Figure 3.8 show experimental and analytical frequency responses for a duct without sound-absorptive liner. The duct was also without a fan installed inside. The two figures show the results for the case of the microphones positioned at the normalized speaker-to-microphone distance, χ, of 0.2 and 0.4 which is defined as

$$\chi = \frac{x}{L_x} \tag{3.36}$$

where x is the x-coordinate of the microphones and L_x is the transverse length of the duct in x (see Figure 3.6). The microphones are positioned directly in from t of the speakers. The magnitudes of the frequency responses shown are normalized by the mean value over the frequency range. The duct acoustic loss factor, η, used for the model was set to 0.001 and the speaker dynamics parameters, ω_s and ξ_s, were set to 180 Hz and 0.3, respectively.

Observing Figure 3.7, a peak in magnitude seen at about 1900 Hz roughly corresponds to the cut-on frequency of the first transverse mode((m_x, m_y) = (1,0)) at 1805 Hz (see Table 3.2). And another peak seen at about 3600 Hz is considered to be due to the cut-on of the (2, 0) duct mode at 3610 Hz. In the frequencies lower than the first cross-mode cut-on frequency of 1805 Hz, the (0, 0) mode (i.e. plane-wave mode) is the only cut-on mode. Therefore, the two peaks seen at around 600 and 1200 Hz are due to the first two axial modes of the duct.

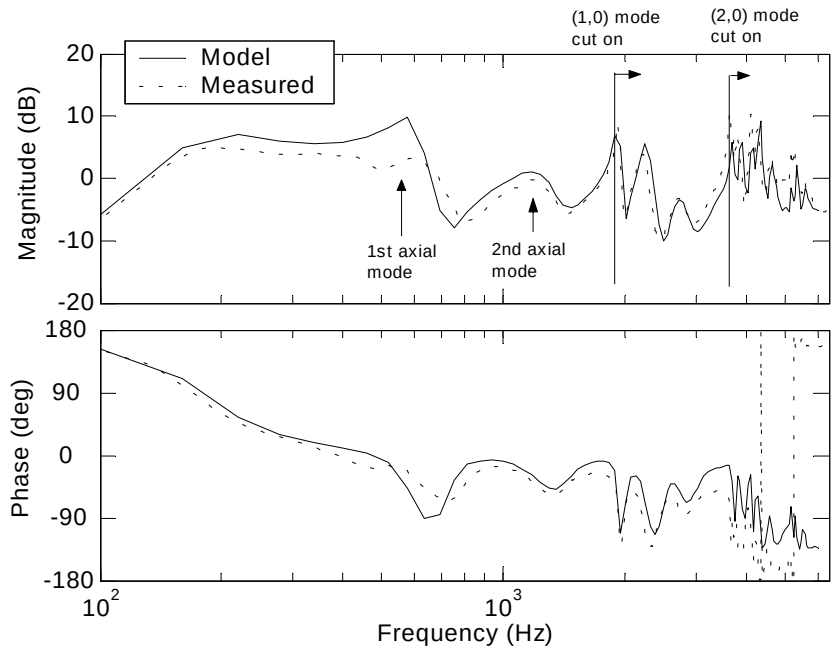

(a) Direct path (Input 1 to Output 1)

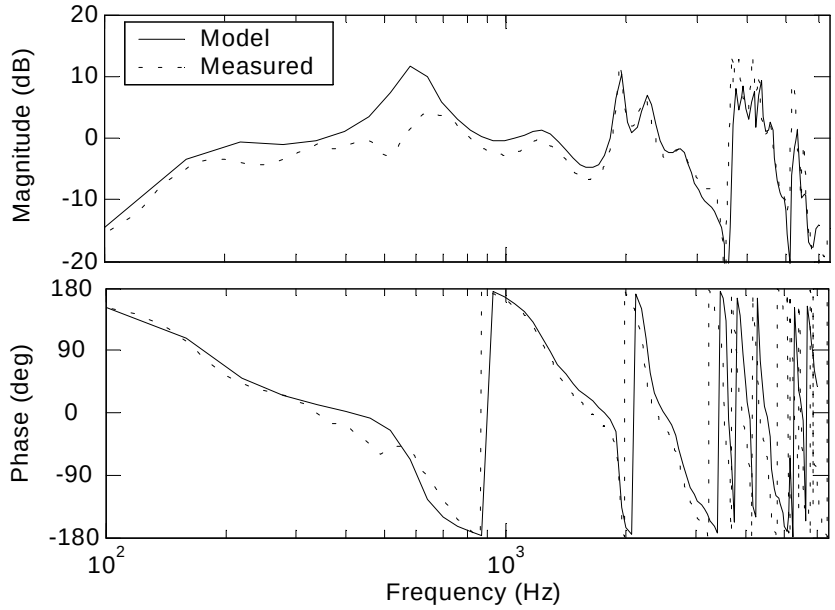

(b) Cross path (Input 1 to Output 2)

Figure 3.7. Plant frequency response, no passive liner, microphone position, $\chi = 0.2$: (a) direct path, (b) cross path

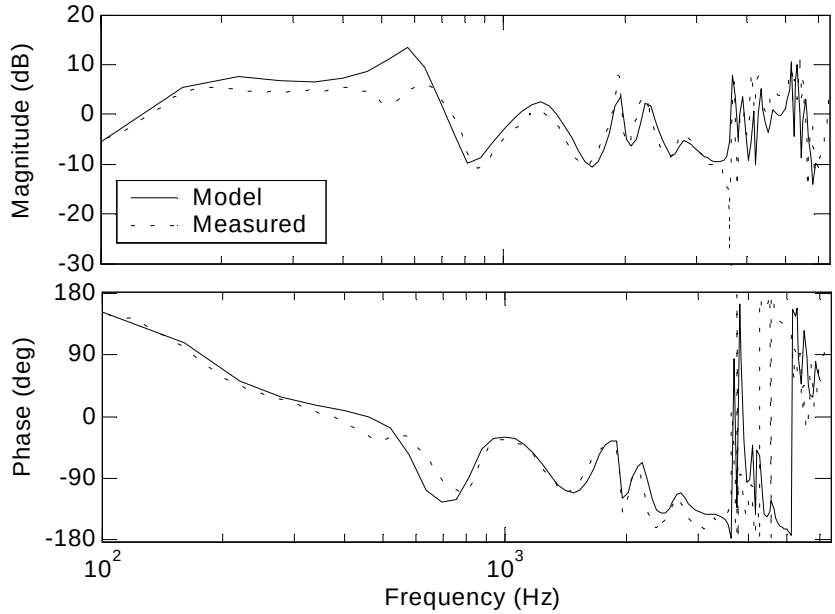

(a) Direct path (Input 1 to Output 1)

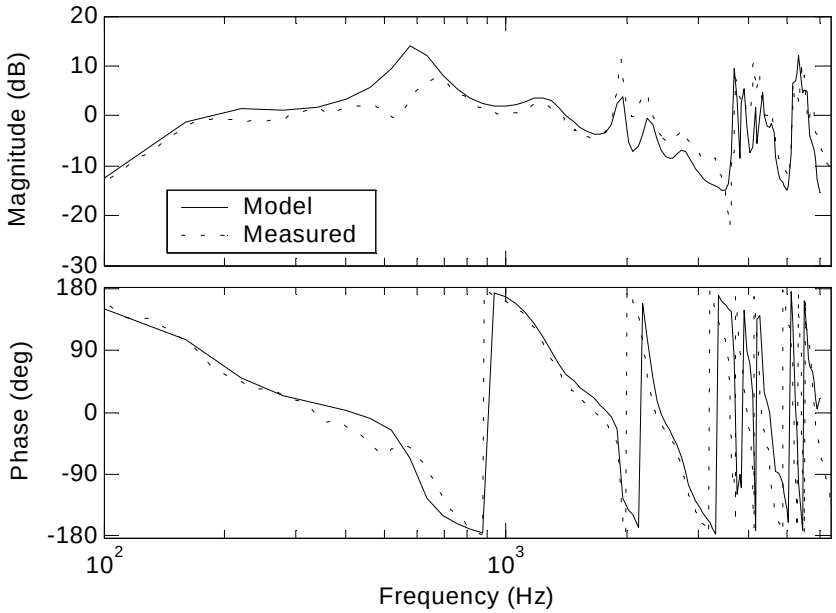

(b) Cross path (Input 1 to Output 2)

Figure 3.8. Plant frequency response, no passive liner, microphone position, $\chi = 0.4$: (a) direct path, (b) cross path

The model and the experimental result show relatively high degree of agreement even in a high frequency range except that there is a noticeable difference around the frequency of the first axial resonance at 600 Hz. It is observed that the measured response seems to have extra zero-like dynamics at this frequency. The source of this behavior in the measured data is unknown at this point. However, judging from the excellent agreement of analytical and experimental data in this frequency range for the segmented duct case, which is discussed in the next section, the cause of this discrepancy is likely to be attributed to some unexpected imperfections in the physical constructions of the experimental duct setup.

Next, the plant frequency responses were measured with some sound absorptive material installed in the inner duct walls as passive liners. The material was melamine with a thickness of 5 mm. The passive liner covered the whole inner duct wall area except around the fan body. The corresponding analytical frequency responses were obtained by simply increasing the duct loss factor, η, to 0.04. Figure 3.9 shows the analytical and the experimental frequency responses.

Figure 3.9 shows a reasonable degree of agreement between the model and experimental frequency responses except again at around the first axial mode peak and also in the high frequency region. Furthermore, the resonant peaks in the experimental data are observed to be somewhat lowered in frequency compared with frequency responses for the duct without the passive liner. This is likely to be originated from the unaccounted effect of the reactive part of the impedance associated with the passive liner. The present model represents the passive liner as purely dissipative damping associated with the duct and therefore does not capture this effect. It is also noticed that the phase lag in the experimental frequency response is slightly larger that that of the model frequency response and the difference increases with frequency. This suggests that there is slightly more time delay in the experimental data than the model.

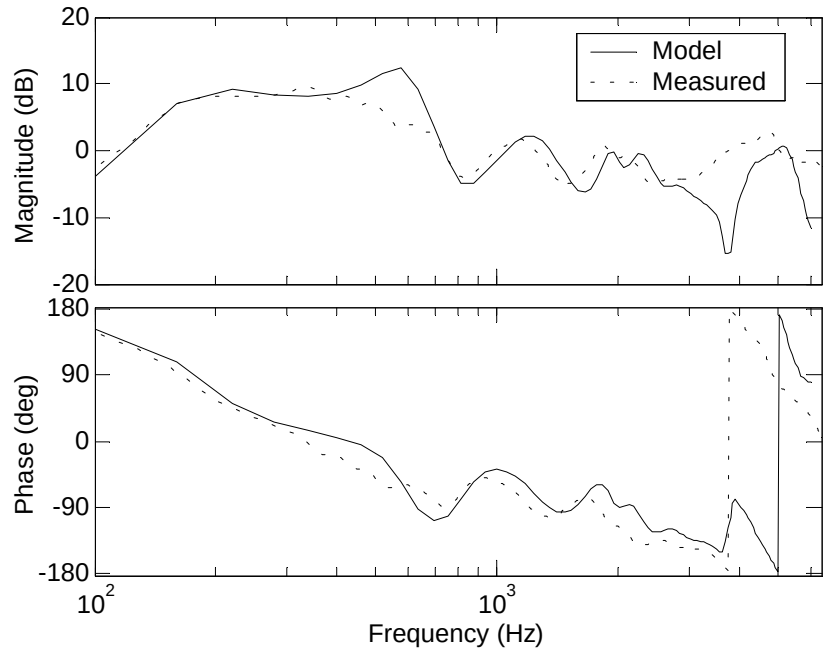

(a) Direct path (Input 1 to Output 1)

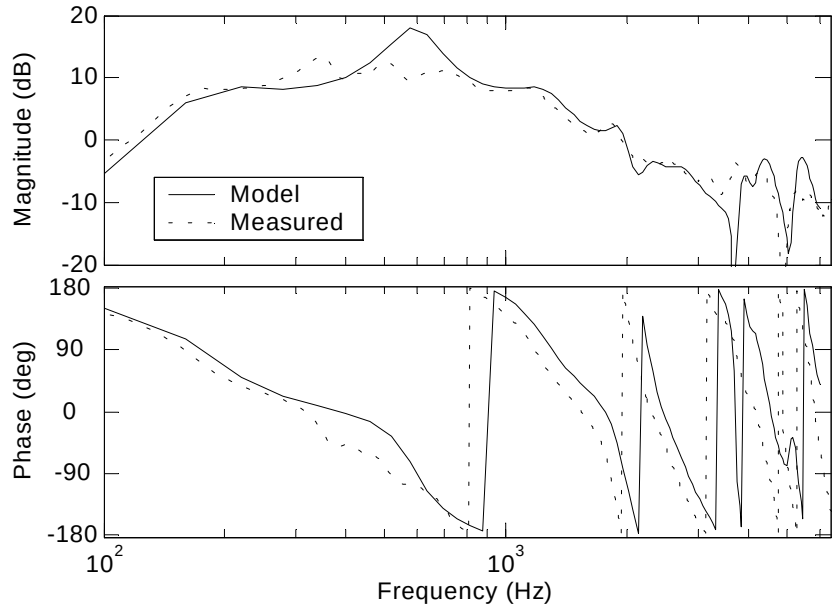

(b) Cross path (Input 1 to Output 2)

Figure 3.9. Plant frequency response, with passive liner (5mm thickness), $\chi = 0.4$: (a) direct path, (b) cross path

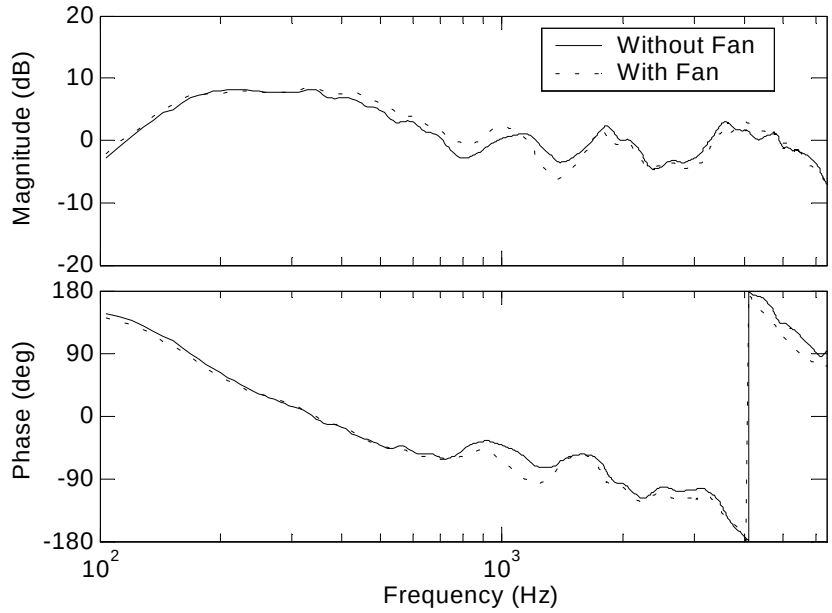

(b) Direct path (Input 1 to Output 1)

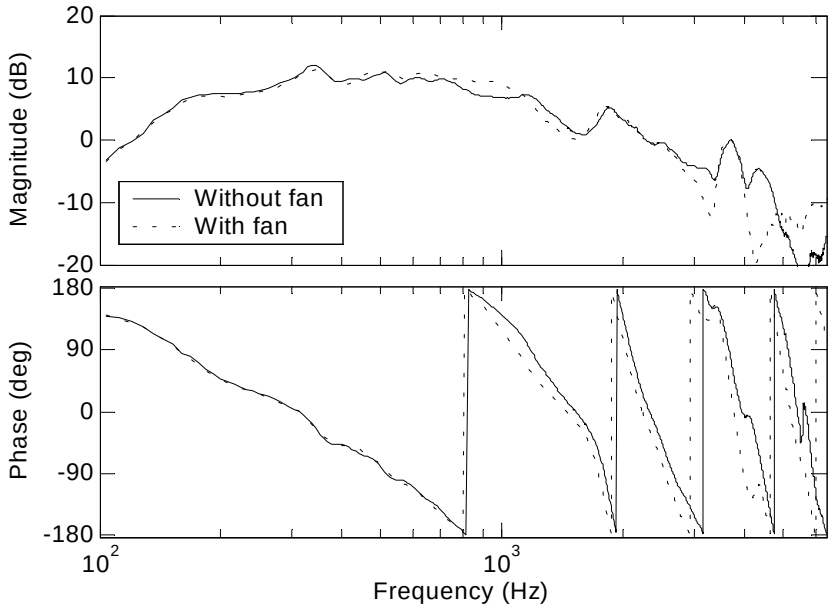

(b) Cross path (Input 1 to Output 2)

Figure 3.10. Plant frequency response with and without a fan (with passive liner , χ = 0.4): (a) direct path (b) cross path

Figure 3.10 shows the experimental plant frequency responses with and without a fan installed in the duct. The purpose of this was to check the effect of the presence of the fan body to the plant frequency responses. It should be recalled that the present model assumes that the potential scattering of sound by the fan body is negligible. As observed in Figure 3.10, the presence of the fan does not significantly alter the frequency responses for the most part, thereby validating the present model.

3.1.2 Passive Control Effect

In this section, the passive noise control effect of the non-segmented fan duct is investigated by using the analytical model. Specifically, the effect of the passively-line fan duct to the level of total emitted fan noise power is investigated.

Baseline Fan Noise Power

First, the baseline fan noise power level has to be determined. The baseline fan noise level is the sound power level of a fan without ducting, which is obtained by making the axial length of the duct infinitely small. In the limit, this is equivalent to having a fan in an infinite baffle as shown in Figure 3.11 below.

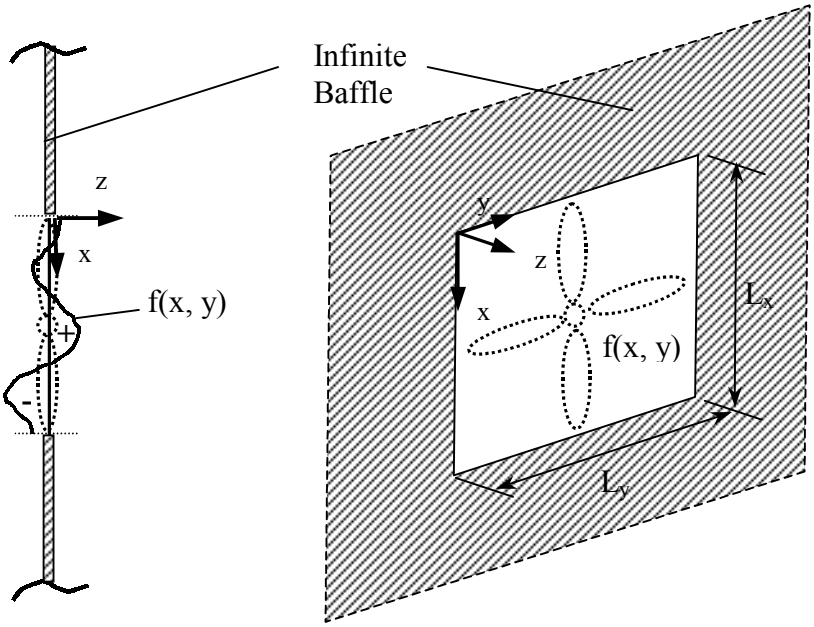

Figure 3.11. Baseline fan model as a force field, *f(x, y)*, in an infinite baffle

As it is done for the ducted fan model, the fan is modeled as a force, *f(x,y)*, distributed over the area the same area as the duct cross-section. From Equation (3.8), the modal pressure vectors, $\mathbf{p}_{\mathbf{M}}^{+}$ and $\mathbf{p}_{\mathbf{M}}^{-}$, immediately to the right and the left of the fan are related to the modal fan force vector, $\mathbf{f}_{\mathbf{M}}$, by

$$\mathbf{p}_{\mathbf{M}}^{+} - \mathbf{p}_{\mathbf{M}}^{-} = \frac{\mathbf{f}_{\mathbf{M}}}{S} \tag{3.37}$$

where S is the area of the fan force field. The velocity is assumed to be continuous across the fan,

$$\mathbf{u}_{\mathbf{M}}^{+} = \mathbf{u}_{\mathbf{M}}^{-} = \mathbf{u}_{\mathbf{M}} \tag{3.38}$$

Now the relationship between the modal pressure vectors, and the modal velocity vector on the two sides of the fan are expressed as

$$\mathbf{p}_{\mathbf{R}}^{+} = \mathbf{z}_{\mathbf{RM}\,right} \cdot \mathbf{u}_{\mathbf{M}}$$
$$\mathbf{p}_{\mathbf{R}}^{-} = \mathbf{z}_{\mathbf{RM}\,left} \cdot \mathbf{u}_{\mathbf{M}} = \left(-\mathbf{z}_{\mathbf{RM}\,right}\right) \cdot \mathbf{u}_{\mathbf{M}} \tag{3.39}$$

where the modal impedance matrices, $\mathbf{z}_{\mathbf{RM}\,right}$ and $\mathbf{z}_{\mathbf{RM}\,left}$ correspond to the duct open end impedance matrices obtained earlier by using Equation (3.7). Substituting Equation (3.37) into (3.39) yields,

$$\mathbf{u}_{\mathbf{M}} = \frac{1}{2}\mathbf{z}_{\mathbf{RM}\,right}^{-1} \cdot \frac{\mathbf{f}_{\mathbf{M}}}{S} \tag{3.40}$$

The acoustic power emitted from one side of the fan, e.g. from the right side, is obtained by using (3.34) as

$$W_{right} = \frac{S}{2} Re\left\{\mathbf{p}_{\mathbf{M}}^{+\,T} \cdot \left(\mathbf{u}_{\mathbf{M}}^{\,T}\right)^{*}\right\} \tag{3.41}$$

Using these equations, it can be shown the total acoustic power emitted from the right side is

$$W_{right} = \frac{1}{8} \cdot \frac{1}{S} Re\left\{\mathbf{f}_{\mathbf{M}} \cdot \mathbf{z}_{\mathbf{RM}\,right} \cdot \mathbf{f}_{\mathbf{M}}^{\,T}\right\} \tag{3.42}$$

which suggests that the emitted power can be calculated only from the modal force excitation vector, $\mathbf{f}_{\mathbf{M}}$, and the modal impedance matrix, $\mathbf{z}_{\mathbf{RM}}$. Due to the symmetry of the model considered here, the acoustic power emitted to the right and the left are equal. Therefore, the total acoustic power emitted the fan is simply twice the amount calculated for each side.

Figure 3.12 shows the fan noise power levels calculated for several cases of modal force vectors, $\mathbf{f}_{\mathbf{M}}$. M = 1 to 9 are used for the calculations. The area of the fan force field is assumed to be 9.5 cm by 9.5 cm. For all the cases, the magnitudes of, $\mathbf{f}_{\mathbf{M}}$, are given uniform values of one for all modes, but the phase directions are given different values:

$$\begin{aligned}\mathbf{f_M}_i &= \begin{bmatrix}|f_1| & |f_2| & \cdots\end{bmatrix}\cdot\begin{bmatrix}e^{j\angle f_1} & e^{j\angle f_2} & \cdots\end{bmatrix}^T \\ &= \begin{bmatrix}|f_M|\end{bmatrix}\cdot\begin{bmatrix}e^{j\theta_M}\end{bmatrix}_i = \begin{bmatrix}1 & 1 & \cdots\end{bmatrix}\cdot\begin{bmatrix}e^{j\theta_1} & e^{j\theta_2} & \cdots\end{bmatrix}_i^T\end{aligned} \tag{3.43}$$

where a set of randomly selected phase angles, $\begin{bmatrix}\theta_1 & \theta_1 & \cdots\end{bmatrix}$ is used for each case of $\mathbf{f_M}$.

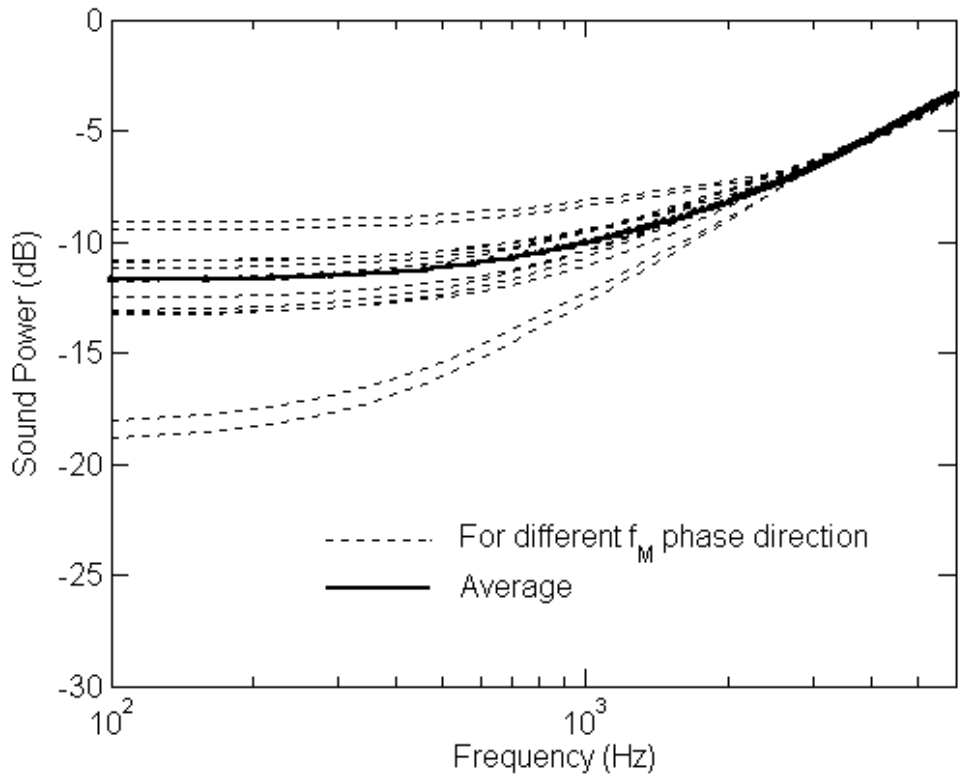

Figure 3.12. Baseline fan noise power level

The result shows some variation in noise power levels depending on the phase angles of $\mathbf{f_M}$. This is due to the modal couplings originated from the presence of some non-diagonal terms in the modal impedance matrix, $\mathbf{z_{RM}}$. For the present study, the average noise power level shown by the solid line in the figure is used as a representative baseline fan noise power. (This is considered to be reasonable since the phase angles of $\mathbf{f_M}$, especially for broadband fan noise, are not consistent.) For the purpose of simulations, a particular set of phase angles of $\mathbf{f_M}$ is consistently used which results in the

average baseline fan noise power level above. It is also noted in the figure that the power levels are increasing with frequency. This is a consequence of assuming constant values for the magnitude of $\mathbf{f_M}$. More realistic representation of $\mathbf{f_M}$ would be to assign magnitudes that decrease with frequency as shown by the experimental data in Chapter 2. However, it is not necessary for the purpose of the present study where only the relative noise power levels are of concern.

Passive Effect of Lined Duct on Fan Noise Power

The effect of a passively-lined duct on the radiated fan noise power is investigated by using the analytical model. The fan duct is 21 cm in length and has 9.5 cm by 9.5 cm square cross-section (See Table 3.1 for exact dimensions). M=1 to 9 are used the calculations. Figure 3.13 shows the calculated total acoustic power levels for the acoustic loss factor, η, of 0.001 and 0.04, which represent a duct without and with a passive liner, respectively. The baseline fan noise power level described above is also shown in the figure.

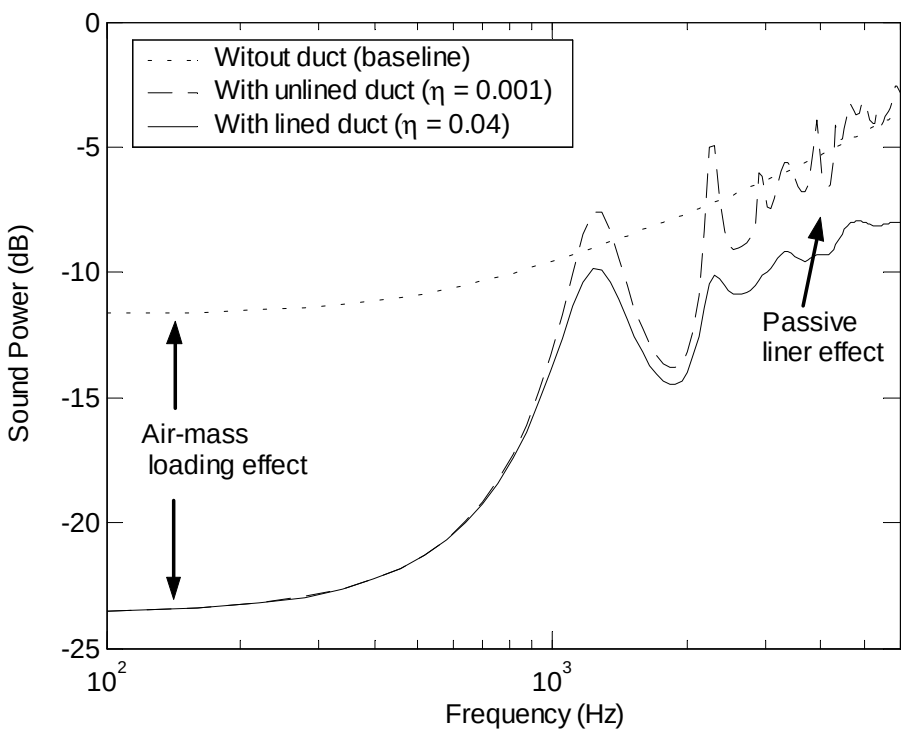

Figure 3.13. Passive effect of non-segmented duct to the global fan noise power level

Figure 13 shows that the passive liner is only effective at reducing noise at relatively high frequencies, in this case, above 1000 Hz. In the low frequency range, the passive liner has little effect. Approximately 5 dB of noise reduction is indicated in the high frequency range for the damping factor of 0.04. The selection of this particular loss factor value is based on the results in Figure 3.9 where it resulted in a good match between the model and the experimental plant frequency responses for the case of a duct with 5 mm thick passive liner.

It is also observed in Figure 3.13 that there is a prominent reduction of about 11 dB in noise power level in the low frequency range. This is due to the mass loading effect of the volume of air in the duct. In the low frequency range where kL<1 (i.e. wavelength is much larger than the duct axial length), the fan source is equivalent to a force exerted on a mass-less piston. It can be shown that the mechanical impedance (force/velocity) experienced by a piston in a finite duct in the low frequency range is

$$z_m = 2 \cdot z_o + j\omega\rho SL \tag{3.44}$$

where Z_o is the impedance associated with the duct opening, ρ is the air density, S is the duct cross-sectional area and L is the duct length. The second term represents the impedance of the mass of air in the duct, ρSL. For a baffled fan without a duct, the corresponding impedance expression is obtained by eliminating this second term since there is no additional duct air mass. Then, the emitted sound power is given by

$$W = \frac{1}{2} u^2 \, Re\{z_m\} = \frac{1}{2} \frac{f^2}{\left|z_m\right|^2} \cdot Re\{z_m\} \tag{3.45}$$

where u is the piston velocity, f is the force exerted on the piston. The two equations above suggest that when a fan is installed in a short duct, the impedance, z_m, is increased by the air mass loading on the piston. Consequently, the piston velocity is decreased and the total emitted power is decreased. For example, this low-frequency mass-loading effect can be calculated easily for the case of a duct with a circular cross-section since the closed form expression for the circular openend impedance, z_o, is readily available and given by,

$$z_o = \frac{\rho\omega^2 S^2}{c2\pi} + \frac{j\omega\rho 8aS}{3\pi} \tag{3.46}$$

Using the above expressions, it can be shown that the ratio of the total emitted acoustic power with the duct, W_w, to the power without the duct, W_{wo}, at low frequencies is

$$\frac{W_w}{W_{wo}} = \left(\frac{16a}{3\pi}\right)^2 \Big/ \left(\frac{16a}{3\pi} + L\right)^2 \tag{3.47}$$

Assuming that the present duct had an equivalent circular cross-section with a radius, $a = \sqrt{S/\pi} = 0.053$ and the length, L, of 0.21, the low frequency power reduction ratio is calculated to be 0.091 or minus 10.4 dB. This is approximately consistent with the value indicated in Figure 3.13 at the low frequency range.

3.1.3 Active Control Effect

The effect of the 2x2 active noise control to the noise emission from the non-segmented fan duct is considered here. The dimensions of the fan duct are unchanged from those listed in Table 3.1. Both feedforward and feedback control are considered.

Feedforward Control

The effect of 2x2 feedforward active noise control is investigated first. The analytical procedure detailed in Section 2.1 in Chapter 2 is used to synthesize the inputs to the two control speakers. Then, the resulting fan noise power levels are calculated with and without the inputs to the control speakers. The results represent the noise control performance of an ideal feedforward control with perfectly correlated reference signals, thereby essentially providing the theoretical upper limit on the global active noise reduction obtainable for the given configuration.

Figure 3.14 shows the noise reduction effects of feedforward control obtained locally at the microphones. The plot shows the dB change in the norm (2-norm) of the error microphone vector, $\mathbf{p_e}$, for several different cases of the normalized microphone-to-speaker distance, χ (defined by Equation (3.36)). The 2-norm or the Euclidean norm of a vector is defined as

$$\|\mathbf{p_e}\|_2 = \sqrt{\mathbf{p_e}^* \cdot \mathbf{p_e}} = \sqrt{\sum_i |p_{ei}|^2} \tag{3.48}$$

Thus, Figure 3.14 can be considered as the average of the reduction levels obtained at individual microphones. All microphones are positioned directly in front of the speakers.

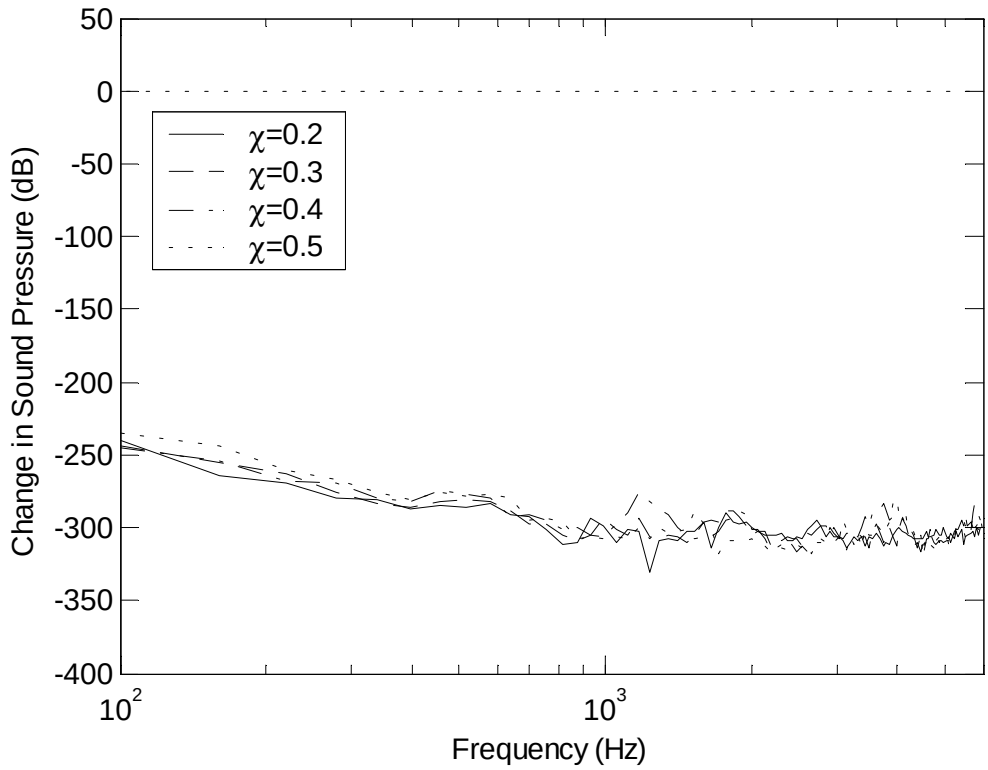

Figure 3.14. Change in error microphone pressure vector norm due to feedforward control

It is shown in Figure 3.14 that noise is reduced to practically zero at the error microphones by feedforward control. This is expected for a system with equal number of inputs and outputs.

Figure 3.15 shows the levels of the total noise power radiated out from the duct with and without feedforward control.

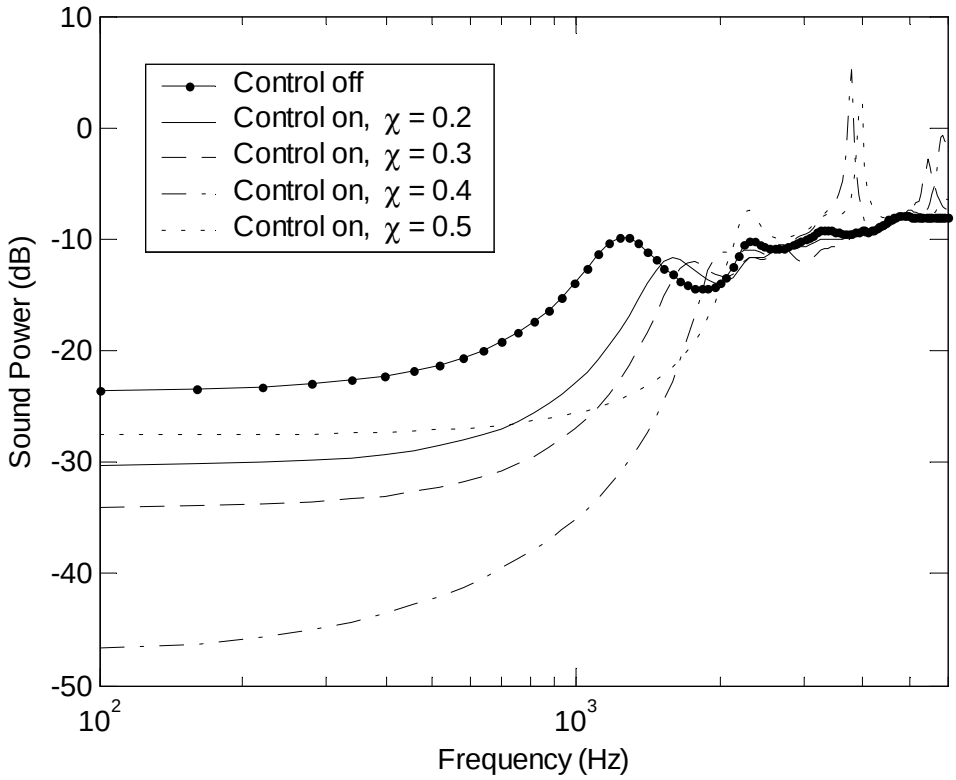

Figure 3.15. Feedforward control effect on global noise power level of non-segmented fan duct for different microphone positions

It is observed in Figure 3.15 that the reductions in global noise power are finite even though noise is reduced practically to zero at error microphones as shown in Figure 3.14. The positioning of microphones is seen to have a significant effect on the global noise power reduction levels obtained by feedforward control. Also observed in Figure 3.14 is that, for all cases, the global noise reductions are obtained only up to around the frequency corresponding to the cut-on of the first cross mode (1,0) at 1805 Hz. In the mid frequency range of 1000 to 1800 Hz, the noise reduction performances are observed to be somewhat better for the cases of $\chi = 0.4$ and 0.5 than $\chi = 0.2$ and 0.3. This result is reasonable since the mode that contributes most to the unwanted evanescent pressure, in this frequency range, is the (1,0) mode which has the cut-on frequency at 1805 Hz. And the (1,0) mode has a pressure node point at $\chi = 0.5$, so the pressure contribution from this evanescent (1,0) mode is relatively small around the middle point.

Figure 3.16 shows the global noise control performance of feedforward control for the case where the two microphones are placed outside of the duct openings. The two microphones are placed at a distance of 3 cm from the duct openings (one on each side). The global sound power level is shown along with the control-off case and also with the in-duct microphone position result ($\chi = 0.4$) from Figure 3.15.

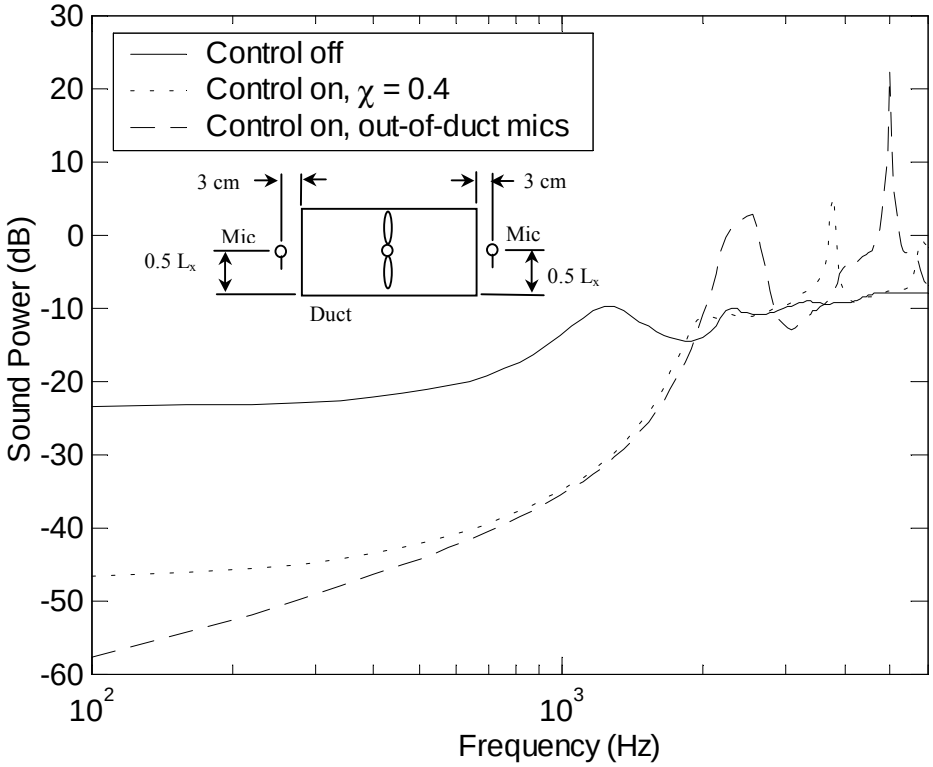

Figure 3.16. Feedforward control effect on global noise power level of finite ducted fan: microphones placed 3 cm out from duct openings

Figure 3.16 indicates a limited improvement in the noise control performance. Prominent high frequency amplifications are also indicated in the figure, but this is not a significant problem in practice since control efforts can be rolled off by using low-pass filters in the case of feedforward control.

The pressure contours of the sound pressure fields in the duct interior and exterior are also obtained and shown in Figure 3.17 to Figure 3.19. The plane of contour is in such a way that it shows the middle section of the duct at $y = 0.5L_y$. Figure 3.17 shows the magnitude and the phase of the sound pressure contour without feedforward control, while Figure 3.18and Figure 3.19 show the cases with feedforward control for the in-duct microphone positions of $\chi = 0.2$ and 0.4, respectively. The frequency is at 1000 Hz.

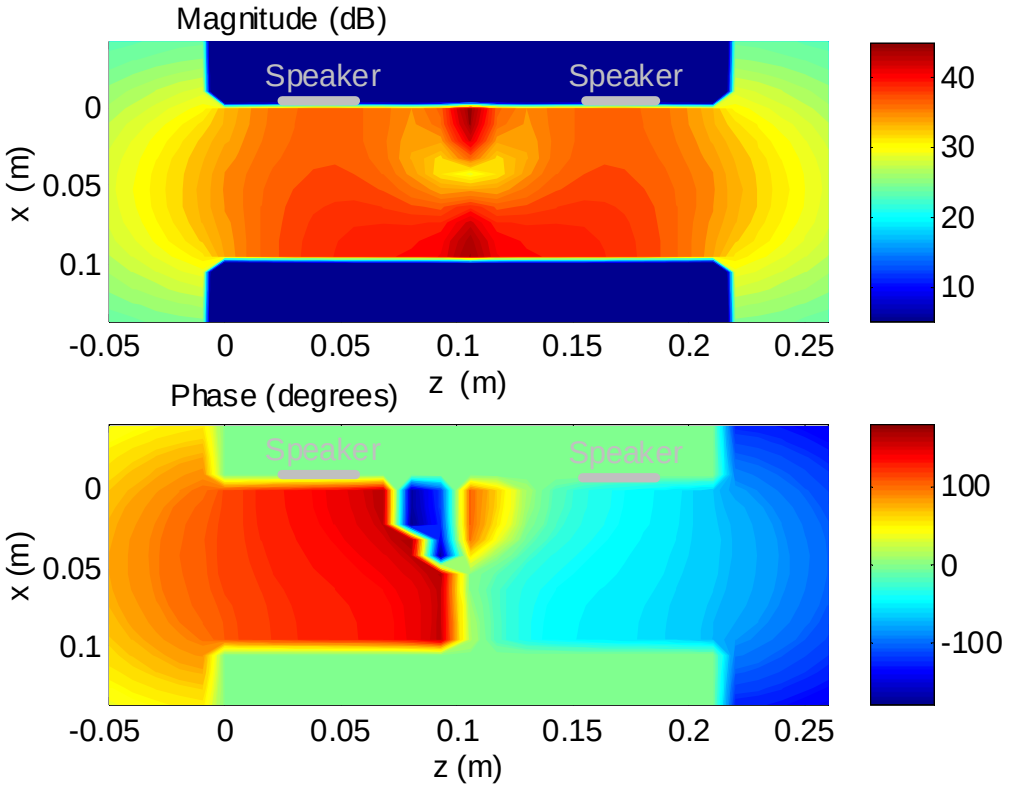

Figure 3.17. Fan noise pressure contour at 1000 Hz: non-segmented fan duct with 2x2 feedforward control inactive

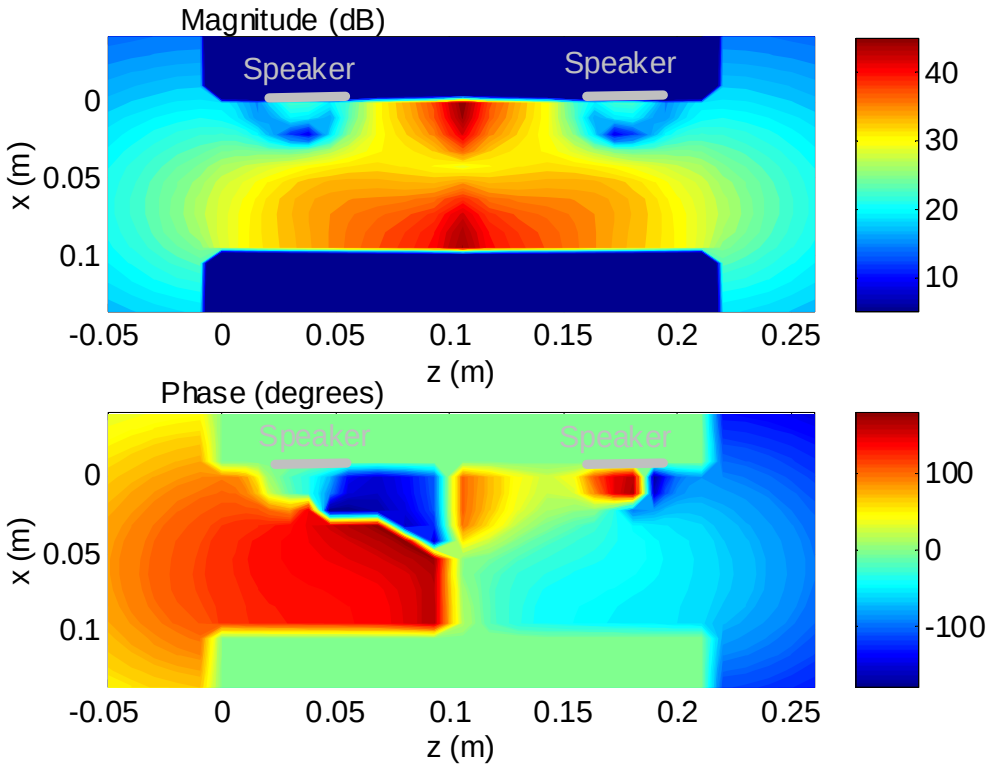

Figure 3.18. Fan noise pressure contour at 1000 Hz: non-segmented fan duct with 2x2 feedforward control active, $\chi = 0.2$

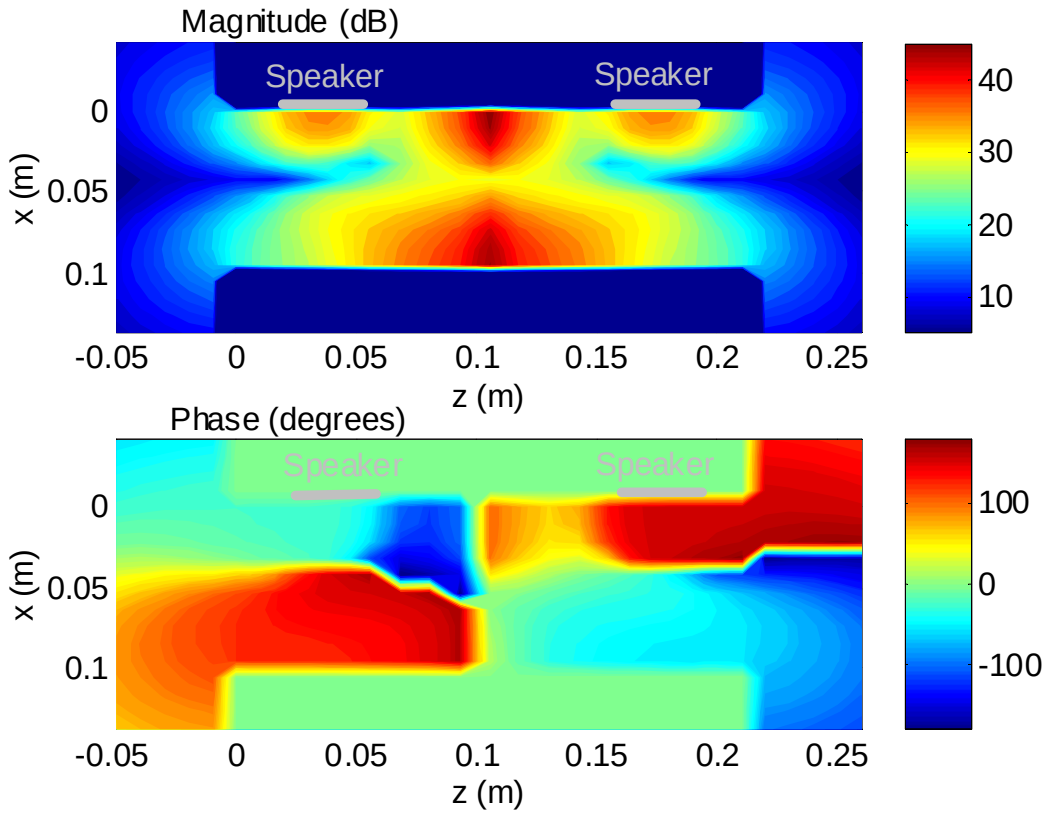

Figure 3.19. Fan noise pressure contour at 1000 Hz: non-segmented fan duct with 2x2 feedforward control active, $\chi = 0.4$

As shown in Figure 3.17, the radiation pattern of the fan noise is anti-symmetric, that is, the pressure fields to the left and to the right of the fan are equal in magnitude but 180 degrees out-of-phase. Comparison of Figure 3.18 and Figure 3.19 clearly show the reductions in the magnitude of the sound radiated out of the duct with the active control turned on. It is also observed that the noise reduction is larger for the case with $\chi = 0.4$ than the case with $\chi = 0.2$ which is in accordance with the results in Figure 3.15. The

results show that placing the microphones too close to the speakers has the adverse effect of allowing the propagating noise power to "leak through" the point of active control.

Feedback Control

The effect of feedback control on the global noise power radiated from the finite ducted fan is considered. The physical configurations (duct geometry, speaker positions, etc) are unchanged from the cases for the feedforward control above.

The LQG optimal control design method described in Section 2.4.2 in Chapter 2 is used to obtain 2x2 feedback controllers. In order to utilize this design method, a state space model of the plant dynamics is required. In the present study, this is achieved by performing a system identification procedure on the frequency response data obtained from the analytical model. A time-domain MIMO system identification method called, "Eigensystem Realization Algorithm" is used.

It should be noted that, for the present theoretical study, the factors associated with the practical implementation of a feedback controller are not considered during the control design process. The order of a designed feedback controller is kept at high without performing any order reduction process. Also minimal stability margins are allocated. The details of the feedback control design process including the system identification procedure are presented in Appendix D.

As it was done for the feedforward control case, the noise control performance of feedback control is investigated for different microphone positions with χ = 0.2, 0.3 and 0.4. A corresponding state space model is obtained for each of the three cases and a separate 2x2 feedback controller is designed using the LQG method. Then, the noise control performance of each the feedback controllers is calculated by incorporating it into the fan duct model. Figure 3.20 shows the noise reduction levels obtained locally at the microphones for the three cases.

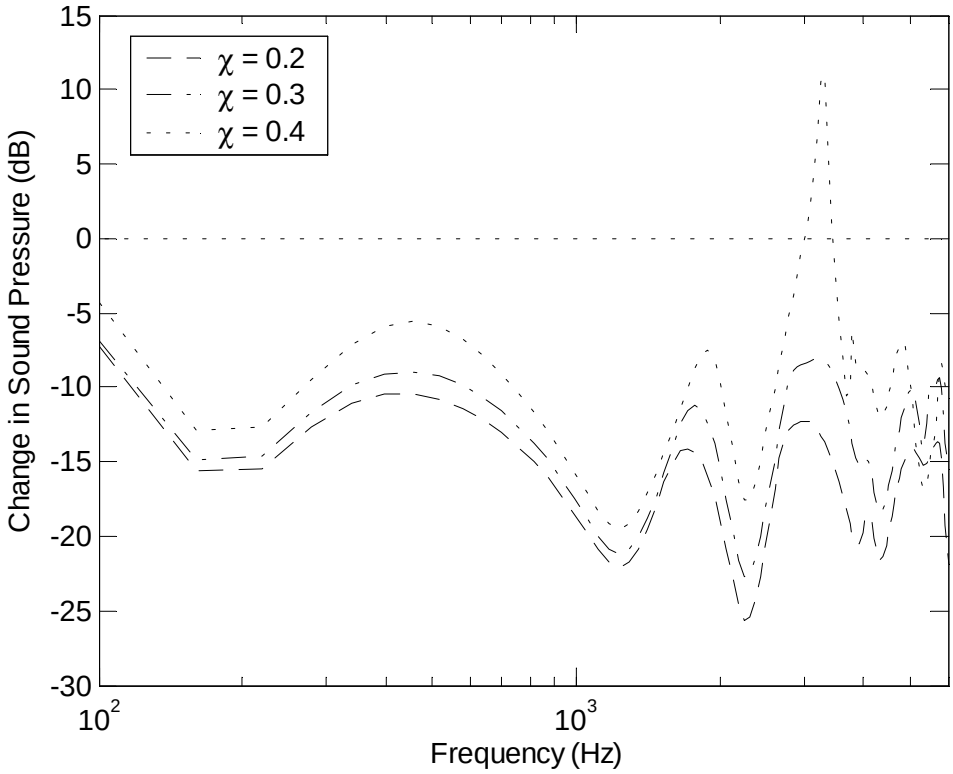

Figure 3.20. Change in the norm of pressure levels at microphones: non-segmented duct with 2x2 feedback control

Figure 3.20 shows the local performance of feedback control in terms of change in the sum-of-square pressures at the two microphones (negative dB means reduced noise). It should be noted that the gains of the corresponding feedback controllers are intentionally selected in such a way that similar local noise reduction performances are obtained for all three cases. However, it can be observed in the figure that there is a significant "spillover" peak at about 3200 Hz for the case of $\chi = 0.4$ even though the noise reduction level at low frequencies is not as different from the other two cases. This is likely attributed to the increased phase lag due to time delay as a result of larger speaker-to-microphone separation distance as seen in the plant frequency responses of Figure 3.7 and Figure 3.8.

Figure 3.21 shows global noise power reduction results. The total emitted sound power levels are shown for the three microphone positions together with the case of the feedback control turned off.

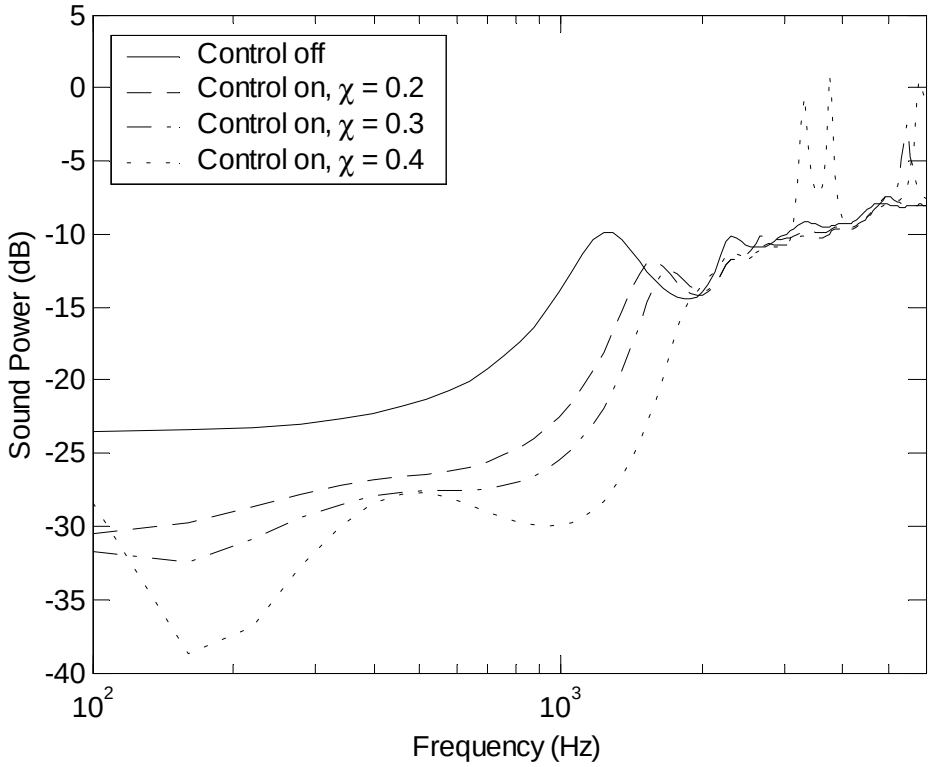

Figure 3.21. Feedback control effect to the global fan noise power emitted from non-segmented fan duct

Comparing the results in Figure 3.20 and Figure 3.21, it is observed that the global reduction in fan noise is only achieved up to the cut-on frequency of the 1st duct cross mode (1,0) at about 1805 Hz despite of the noise being reduced locally at microphones up into higher frequency range. This was also observed in the feedforward control results earlier. It is further observed that, even though the local noise reductions obtained at the microphones are slightly larger for smaller values of χ, the global noise power reduction results show the opposite trend in which reductions are larger for larger values of χ. This

result also suggests that the placing a microphone too close to a speaker has a negative impact on the global control performance even though it tends to improve the local noise reduction performance of the feedback control.

3.1.4 Total Active-Passive Control Effect

Figure 3.22 summarizes the overall effect of the combine active-passive control fan duct. The result clearly shows the advantage of the active-passive noise control approach where the inherent passive noise reduction property of the lined duct is combined with the additional noise reductions provided by the active control. The active control is effective at lower frequencies and especially beneficial in compensating for the mid-frequency duct axial resonance seen at around 1200 Hz. The damping provided by the passive liner installed in the duct provides further noise attenuation at high frequencies. It is also indicated in the figure the noise control potential offered by the feedforward control is much larger than that offered by the feedback control. And the separations between the performances obtained by the feedforward control and those by the feedback control seem to increase as the speaker-to-microphone distance, χ, is increased. This illustrates the performance limiting effect of the time delay increase associated with increase in χ upon the feedback control.

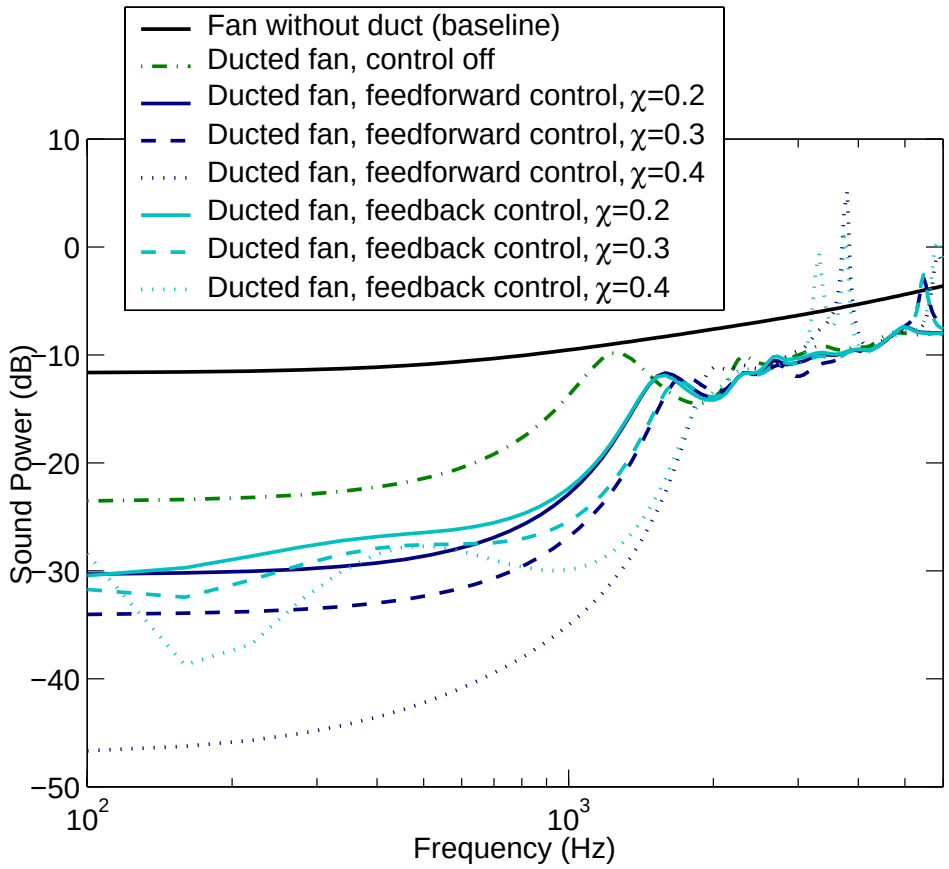

Figure 3.22. Overall active-passive control effect on global noise power levels of non-segmented fan duct

3.2 Segmented Fan Duct with 8x8 Active Control

The second design considered for the active-passive control fan duct is as follows. The overall dimensions of the fan duct are unchanged from the previous design except for the interior of the duct, which is segmented as shown in Figure 3.23.

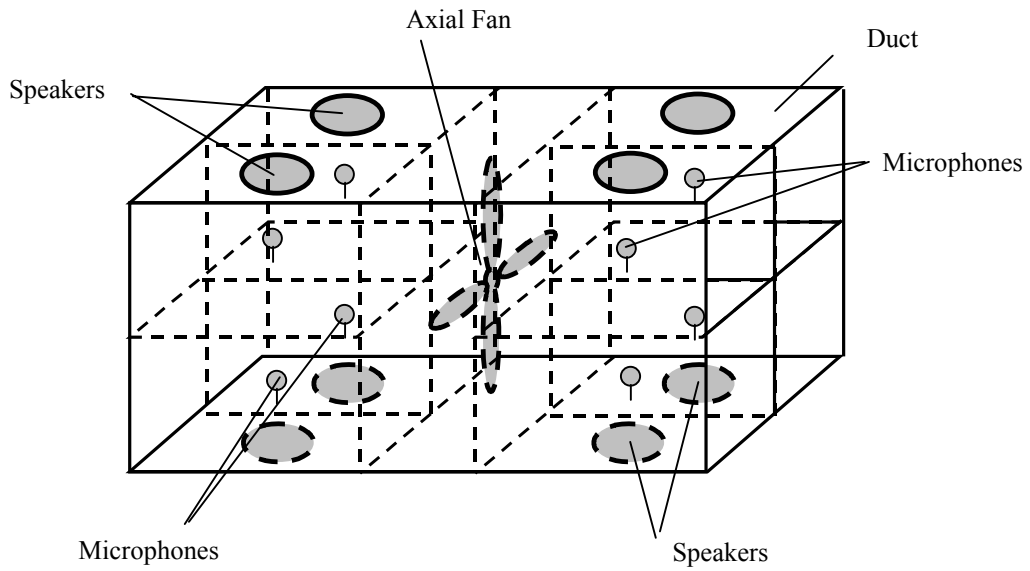

Figure 3.23. Segmented fan duct with eight speakers and eight microphones.

As shown in the figure, each side of the duct is equally partitioned into four smaller duct segments. A pair of a control speaker and a microphone is housed within each duct segment. This amounts to a total of eight control speakers and eight microphones for active control. Passive liner is also to be installed in the duct interior walls.

3.2.1 Model Development

Figure 3.24 shows an illustration of the segmented fan duct, which is modeled as a system of short duct elements joined together at multiple junctions.

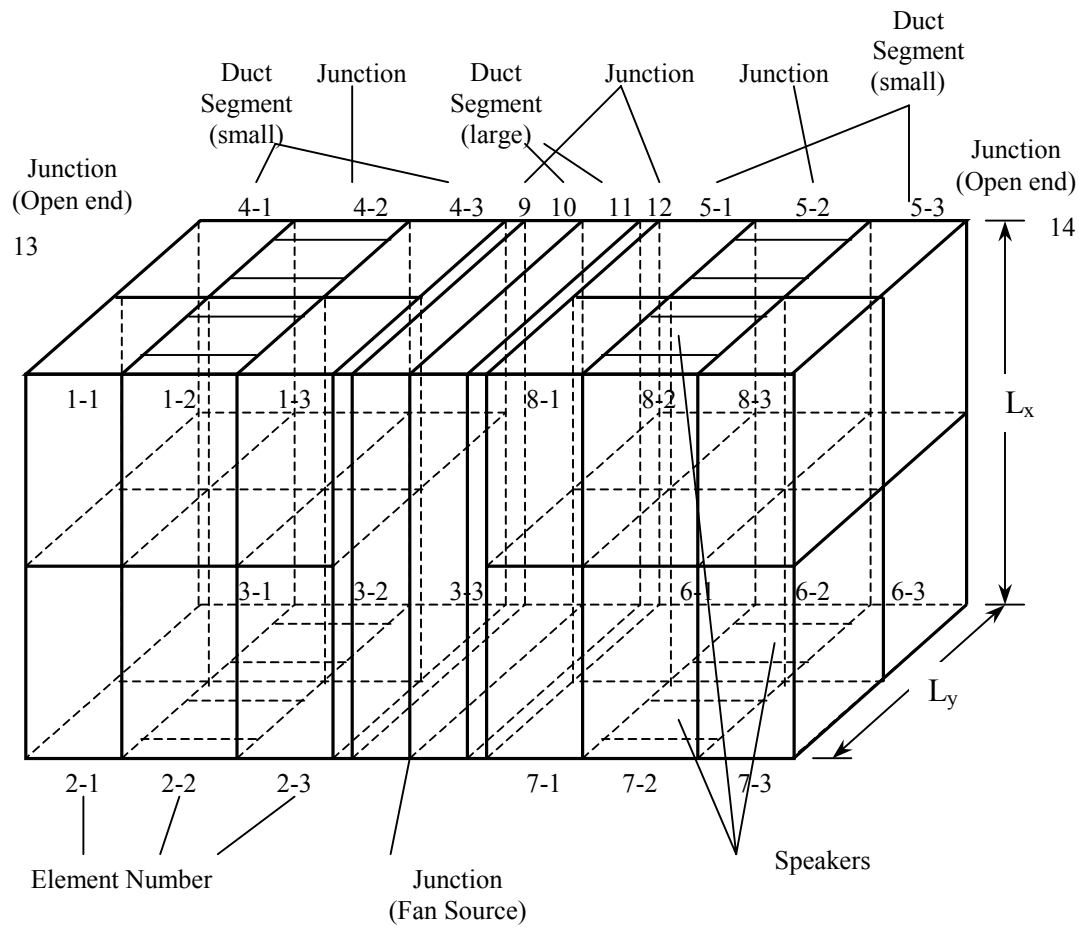

Figure 3.24. Segmented fan duct model

Both ends of the duct are assumed to be fitted with infinite baffles. The control speakers are modeled as square pistons as shown in the figure.

Following the modeling approach described in Chapter 1, the first task is to obtain modal impedance matrices for all the junctions in the model. There are four types of junctions in this model. The speaker junction and the fan source junction are already discussed in the last section. The other two are new in this model. One is the junction associated with the region where the large duct meets the smaller duct segments. This junction shall be referred as, "splitter junction". The other is associated with the segmented duct opening, which shall be referred as, "segmented open end junction". The descriptions of the two new junctions are presented below.

Splitter Junction Modal Impedance

A splitter junction is shown in Figure 3.25.

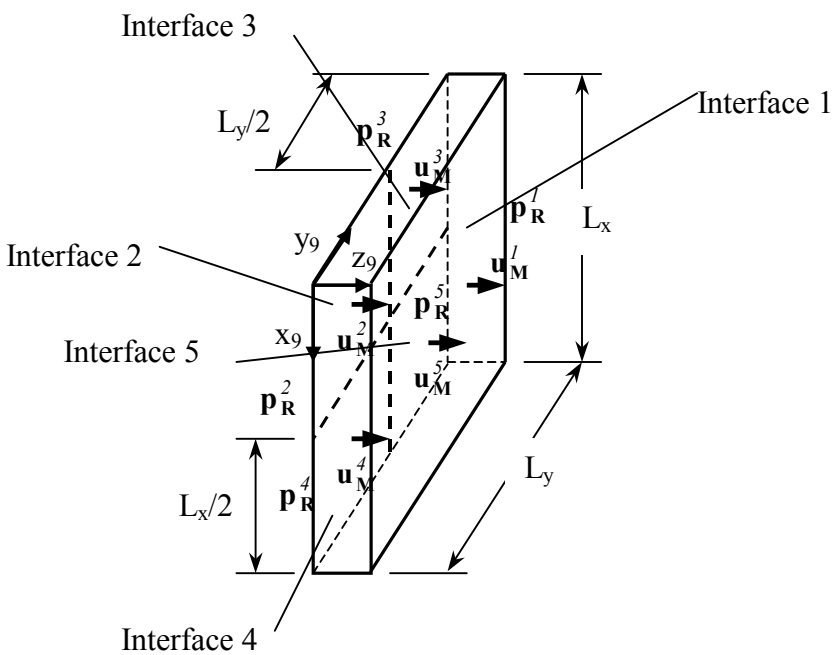

Figure 3.25. Splitter junction, left side (Element 9)

The figure shows the splitter junction at the left side of the duct. The duct-junction interfaces are numbered from 1 to 5. The associated modal impedance matrix equation for this junction is

$$\mathbf{P}_{\mathbf{R}\,9} = \mathbf{Z}_{\mathbf{RM}\,9} \cdot \mathbf{U}_{\mathbf{M}\,9} \tag{3.49}$$

that is

$$\begin{bmatrix} \mathbf{p}_{\mathbf{R}}^{1} \\ \mathbf{p}_{\mathbf{R}}^{2} \\ \mathbf{p}_{\mathbf{R}}^{3} \\ \mathbf{p}_{\mathbf{R}}^{4} \\ \mathbf{p}_{\mathbf{R}}^{5} \end{bmatrix}_{9} = \begin{bmatrix} \mathbf{z}_{\mathbf{RM}}^{11} & \mathbf{z}_{\mathbf{RM}}^{12} & \cdots & \cdots & \mathbf{z}_{\mathbf{RM}}^{15} \\ \mathbf{z}_{\mathbf{RM}}^{21} & \mathbf{z}_{\mathbf{RM}}^{22} & \cdots & \cdots & \vdots \\ \vdots & \vdots & \ddots & \cdots & \vdots \\ \vdots & \vdots & \vdots & \ddots & \vdots \\ \mathbf{z}_{\mathbf{RM}}^{51} & \cdots & \cdots & \cdots & \mathbf{z}_{\mathbf{RM}}^{55} \end{bmatrix}_{9} \cdot \begin{bmatrix} \mathbf{u}_{\mathbf{M}}^{1} \\ \mathbf{u}_{\mathbf{M}}^{2} \\ \mathbf{u}_{\mathbf{M}}^{3} \\ \mathbf{u}_{\mathbf{M}}^{4} \\ \mathbf{u}_{\mathbf{M}}^{5} \end{bmatrix}_{9} \tag{3.50}$$

where $\mathbf{p}_{\mathbf{R}}^{l}$ is the modal pressure vector at the l-th interface, $\mathbf{u}_{\mathbf{M}}^{l}$ is the modal velocity vector at the i-th interface. The subscript, 9, designates Element 9.

The modal impedance matrix, $\mathbf{Z}_{\mathbf{RM}}$, is obtained by using the integral equation of Equation (3.3), which was used in the earlier section for the speaker junction. The sub-matrices, $\mathbf{z}_{\mathbf{RM}}^{li}$, are determined to be

$$\mathbf{z}_{\mathbf{RM}}^{11} = \left[-\frac{jk\rho c}{L_z} \sum_{n_z} \frac{1}{\Lambda_{n_s}} \cdot \left(\frac{1}{(m_x\pi/L_x)^2 + (m_y\pi/L_y)^2 + (m_z\pi/L_z)^2 - k^2} \right) \right]_{diag}$$

$$\mathbf{z}_{\mathbf{RM}}^{li}\Big|_{\substack{l=1 \\ i=2,3,4,5}} = \left[\begin{array}{c} \dfrac{jk\rho c}{4L_z} \displaystyle\sum_{n_z} \frac{(-1)^{n_z}}{\Lambda_{n_s}} \cdot \left(\frac{1}{(r_x\pi/L_x)^2 + (r_y\pi/L_y)^2 + (n_z\pi/L_z)^2 - k^2} \right) \\ \cdot I(L_x, \alpha_i, r_x, m_x) \cdot I(L_y, \beta_i, r_y, m_y) \end{array} \right] \tag{3.51}$$

$$\mathbf{z}_{\mathbf{RM}}^{li}\Big|_{\substack{l=2,3,4,5 \\ i=1}} = \left[\begin{array}{c} \dfrac{jk\rho c}{L_z} \displaystyle\sum_{n_z} \frac{(-1)^{n_z}}{\Lambda_{n_s}} \cdot \left(\frac{1}{(m_x\pi/L_x)^2 + (m_y\pi/L_y)^2 + (n_z\pi/L_z)^2 - k^2} \right) \\ \cdot I(L_x, \alpha_l, m_x, r_x) \cdot I(L_y, \beta_l, m_y, r_y) \end{array} \right]$$

$$\mathbf{z}_{\mathbf{RM}}^{li}\Big|_{\substack{l=2,3,4,5\\ i=2,3,4,5}} = \left[\begin{array}{c} \dfrac{jk\rho c}{4L_z}\sum_{n_x}\sum_{n_y}\sum_{n_z}\dfrac{1}{\Lambda_{n_s}}\cdot\left(\dfrac{1}{(m_x\pi/L_x)^2+(m_y\pi/L_y)^2+(m_z\pi/L_z)^2-k^2}\right) \\ \cdot I(L_x,\alpha_l,n_x,r_x)\cdot I(L_y,\beta_l,n_y,r_y) \\ \cdot I(L_x,\alpha_i,n_x,m_x)\cdot I(L_y,\beta_i,n_y,m_y) \end{array}\right]$$

where

$$\alpha_{l(i)} = \begin{cases} 0 & for \quad l(i)=1,2 \\ L_x/2 & for \quad l(i)=3,4 \end{cases} \qquad \beta_{l(i)} = \begin{cases} 0 & for \quad l(i)=1,3 \\ L_y/2 & for \quad l(i)=2,4 \end{cases} \tag{3.52}$$

and the factor, *I(a, b, m, n)*, has a common form as

$$\begin{aligned} & I(a,b,m,n) \\ & = \frac{1}{a\sqrt{\Lambda_m}\sqrt{\Lambda_n}}\left\{ \cos\left(\frac{n\pi}{a/2}b\right)\left(\frac{\sin\left(\frac{m\pi}{a}+\frac{n\pi}{a/2}\right)x}{\frac{m\pi}{a}+\frac{n\pi}{a/2}}+\frac{\sin\left(\frac{m\pi}{a}-\frac{n\pi}{a/2}\right)x}{\frac{m\pi}{a}-\frac{n\pi}{a/2}}\right)\right. \\ & \qquad \left. -\sin\left(\frac{n\pi}{a/2}b\right)\left(\frac{\cos\left(\frac{m\pi}{a}+\frac{n\pi}{a/2}\right)x}{\frac{m\pi}{a}+\frac{n\pi}{a/2}}+\frac{\cos\left(\frac{m\pi}{a}-\frac{n\pi}{a/2}\right)x}{\frac{m\pi}{a}-\frac{n\pi}{a/2}}\right)\right\} \end{aligned} \tag{3.53}$$

The modal impedance matrix for the other splitter junction (Element 12) on the right side of the duct is also obtained the same way.

Segmented Open End Junction Modal Impedance

Figure 3.26 shows the junction at the right duct open end.

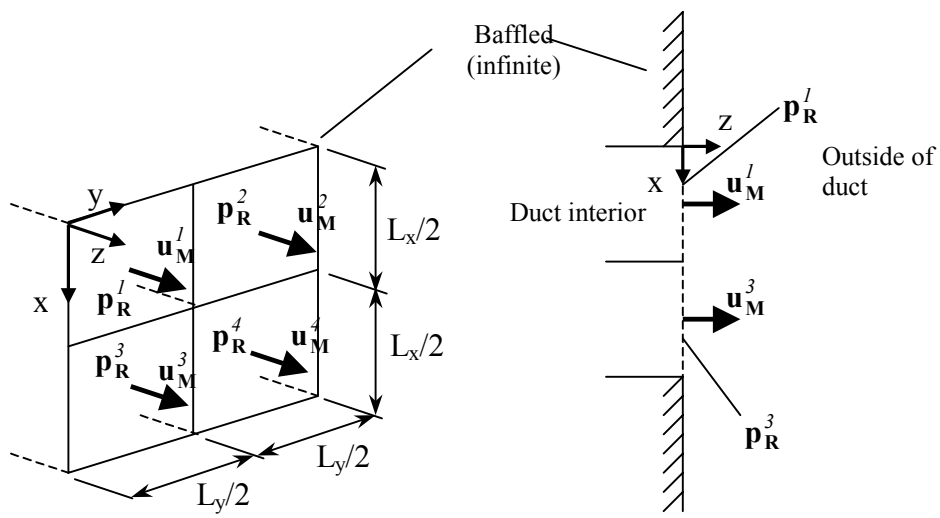

Figure 3.26. Segmented open end junction (right side)

The modal impedance matrix equation for this junction (Element 14) is written as

$$\mathbf{P}_{\mathbf{R}\,14} = \mathbf{Z}_{\mathbf{RM}\,14} \cdot \mathbf{U}_{\mathbf{M}\,14} \tag{3.54}$$

which is

$$\begin{bmatrix} \mathbf{p}_\mathbf{R}^1 \\ \mathbf{p}_\mathbf{R}^2 \\ \mathbf{p}_\mathbf{R}^3 \\ \mathbf{p}_\mathbf{R}^4 \end{bmatrix}_{14} = \begin{bmatrix} \mathbf{z}_\mathbf{RM}^{11} & \mathbf{z}_\mathbf{RM}^{12} & \cdots & \mathbf{z}_\mathbf{RM}^{14} \\ \mathbf{z}_\mathbf{RM}^{21} & \mathbf{z}_\mathbf{RM}^{22} & \cdots & \vdots \\ \vdots & \vdots & \ddots & \vdots \\ \mathbf{z}_\mathbf{RM}^{41} & \cdots & \cdots & \mathbf{z}_\mathbf{RM}^{44} \end{bmatrix}_{14} \cdot \begin{bmatrix} \mathbf{u}_\mathbf{M}^1 \\ \mathbf{u}_\mathbf{M}^2 \\ \mathbf{u}_\mathbf{M}^3 \\ \mathbf{u}_\mathbf{M}^4 \end{bmatrix}_{14} \tag{3.55}$$

where $\mathbf{p}_\mathbf{R}^l$ is the modal pressure vector at the *l*-th interface, $\mathbf{u}_\mathbf{M}^l$ is the modal velocity vector at the *i*-th interface. The interfaces numbered 1 to 4 correspond to the right edge surfaces of Element 8-3, 5-3, 7-3 and 2-3, respectively. The associated modal impedance matrix is obtained by applying the same integral equation, which was used to obtain the

non-segmented duct open end junction in the earlier section. The sub-matrices of the modal impedance matrix are determined to be

$$\mathbf{z}_{\mathbf{RM}}^{li} = [\ \frac{jk\rho c}{2\pi\left(\frac{L_x}{2}\right)\left(\frac{L_y}{2}\right)} \int_{\alpha_l}^{\frac{L_x}{2}+\alpha_l} \int_{\beta_l}^{\frac{L_y}{2}+\beta_l} \int_{\alpha_i}^{\frac{L_x}{2}+\alpha_i} \int_{\beta_i}^{\frac{L_y}{2}+\beta_i} \frac{e^{-jk\sqrt{(x-x_o)^2+(y-y_o)^2}}}{\sqrt{(x-x_o)^2+(y-y_o)^2}}$$

$$\cdot cos(\frac{\frac{r_x\pi}{L_x/2}(x-\alpha_l)}{\sqrt{\Lambda_{r_x}}}) \cdot cos(\frac{\frac{r_y\pi}{L_y/2}(y-\beta_l)}{\sqrt{\Lambda_{r_x}}}) \tag{3.56}$$

$$\cdot cos(\frac{\frac{m_x\pi}{L_x/2}(x_o-\alpha_i)}{\sqrt{\Lambda_{m_x}}}) cos(\frac{\frac{m_y\pi}{L_y/2}(y_o-\beta_i)}{\sqrt{\Lambda_{m_y}}})\ dx\,dy\,dx_o\,dy_o\ ]$$

where the factors, α and β, are given by

$$a_{l(i)} = \begin{cases} 0 & for \quad l(i) = 1, 2 \\ L_x/2 & for \quad l(i) = 3, 4 \end{cases} \qquad \beta_{l(i)} = \begin{cases} 0 & for \quad l(i) = 1, 3 \\ L_y/2 & for \quad l(i) = 2, 4 \end{cases} \tag{3.57}$$

The integral expression above cannot be evaluated analytically and numerical integration is required. As is the case of the non-segmented open end in the previous section, the integrand contains a singularity which arises whenever $x = x_o$ and $y = y_o$. The special numerical integration scheme used in the last section is applied (see Appendix B). It should be noted that the singularity occurs only when the source and the observation interfaces are the same ($l = i$). For those cases where two separate interfaces are involved ($l \neq i$), the singularity condition does not occur and therefore the usual Gaussian Quadrature method is used directly to lighten the computational load.

The determination of the modal impedance matrix for the other segmented open end junction follows the same procedure.

Global Modal Scattering Matrix Equation

After the modal impedance matrices are determined with respect to all junctions in the model, the next step is to convert the modal impedance matrix equations into modal scattering matrix equations which are described in terms of the modal wave amplitudes in

the duct segments. Then, these matrix equations can be assembled into a single global scattering matrix equation (after the junction scattering matrices are appropriately re-sized and re-ordered for compatibility). For the segmented duct model, the global modal scattering matrix equation is

$$\begin{bmatrix} \hat{\mathbf{S}}_{fan_v} \\ \hat{\mathbf{S}}_{fan_p} \\ \hat{\mathbf{S}}_{9} \\ \hat{\mathbf{S}}_{12} \\ \hat{\mathbf{S}}_{13} \\ \hat{\mathbf{S}}_{14} \\ \hat{\mathbf{S}}_{1-2} \\ \hat{\mathbf{S}}_{2-2} \\ \hat{\mathbf{S}}_{3-2} \\ \vdots \\ \hat{\mathbf{S}}_{8-2} \end{bmatrix} \cdot \begin{bmatrix} \mathbf{a}_{\mathbf{M}\,1-1} \\ \mathbf{a}_{\mathbf{M}\,1-3} \\ \mathbf{a}_{\mathbf{M}\,2-1} \\ \mathbf{a}_{\mathbf{M}\,2-3} \\ \vdots \\ \mathbf{a}_{\mathbf{M}\,8-3} \\ \mathbf{b}_{\mathbf{M}\,1-1} \\ \mathbf{b}_{\mathbf{M}\,1-3} \\ \mathbf{b}_{\mathbf{M}\,2-1} \\ \mathbf{b}_{\mathbf{M}\,2-3} \\ \vdots \\ \mathbf{b}_{\mathbf{M}\,8-3} \end{bmatrix} = \begin{bmatrix} \mathbf{0} \\ \mathbf{F}_{fan_p} \\ \mathbf{0} \\ \mathbf{0} \\ \vdots \\ \mathbf{0} \\ \mathbf{F}_{1-2} \\ \mathbf{F}_{2-2} \\ \mathbf{F}_{3-2} \\ \vdots \\ \mathbf{F}_{8-2} \end{bmatrix} \tag{3.58}$$

where the sub-matrices of the global scattering matrix on the right hand side are,

$\hat{\mathbf{S}}_{fan_v}$: Fan source junction, velocity continuity condition

$\hat{\mathbf{S}}_{fan_v}$: Fan source junction, pressure compatibility condition

$\hat{\mathbf{S}}_{9}$: Left splitter junction (Element 9)

$\hat{\mathbf{S}}_{12}$: Right splitter junction (Element 12)

$\hat{\mathbf{S}}_{13}$: Left segmented open end junction (Element 13)

$\hat{\mathbf{S}}_{14}$: Right segmented open end junction (Element 14)

$\hat{\mathbf{S}}_{1-2} \cdots \hat{\mathbf{S}}_{8-2}$: Speaker junction 1 to 8 (Element 1-2 to 8-2)

The fan source excitation is represented by a sub-vector

$$\mathbf{F}_{fan_p} = \frac{\mathbf{f}_{\mathbf{M}}}{S} \tag{3.59}$$

where $\mathbf{f_M}$ is the modal fan force excitation vector. The excitation from i-th speaker with cone velocity, u_{si}, is represented by

$$\mathbf{F}_i = \begin{bmatrix} \mathbf{z}_{\mathbf{RM}}^{13} \\ \mathbf{z}_{\mathbf{RM}}^{23} \end{bmatrix}_{i-2} \cdot u_{si} \tag{3.60}$$

where $\mathbf{z}_{\mathbf{RM}}^{13}$ and $\mathbf{z}_{\mathbf{RM}}^{23}$ are the modal impedance vectors between the speaker cone velocity (Interface 3) to the modal pressure vectors at the edge surfaces (Interface 1 and 2) of the speaker junction, respectively.

Finally, the modal wave amplitudes in all the duct segments in the system can be obtained by solving Equation (3.58). From the modal wave amplitudes, the pressure and the velocity in the duct segments can be determined.

Junction Internal Pressure Field

The procedure to determine the internal pressure field of a speaker junction is already described in the last section. As for the determination of the pressure fields outside of the segmented duct ends (which are considered here as "internal" to the segmented open-end junctions), it follows basically the same procedure except that the associated modal impedance expression has to account for the four openings of the duct segments. For example, the pressure, $p(\mathbf{r})$, at a point, $\mathbf{r}$, in the free space on the right side (Element 14) is given by,

$$p(\mathbf{r}) = \begin{bmatrix} \mathbf{z}_{\mathbf{pM}}^{1} & \mathbf{z}_{\mathbf{pM}}^{2} & \mathbf{z}_{\mathbf{pM}}^{3} & \mathbf{z}_{\mathbf{pM}}^{4} \end{bmatrix} \cdot \begin{bmatrix} \mathbf{u}_{\mathbf{M}}^{1} \\ \mathbf{u}_{\mathbf{M}}^{2} \\ \mathbf{u}_{\mathbf{M}}^{3} \\ \mathbf{u}_{\mathbf{M}}^{4} \end{bmatrix}_{14} \tag{3.61}$$

where the sub-matrix, $\mathbf{z}_{\mathbf{pM}}^{i}$, is the impedance relating the modal velocity vector $\mathbf{u}_{\mathbf{M}}^{i}$ at the i-th duct opening to the free space pressure. The sub-matrix, $\mathbf{z}_{\mathbf{pM}}^{i}$, is obtained by applying Equation (3.7) with the mode-shape functions properly selected for the small duct segments. The pressure field in the left side free-space (Element 13) is determined the same way.

The pressure field inside the splitter junction is not required to be determined since the width of the junction is intentionally set to negligibly small relative to other elements.

Total Radiated Acoustic Power

The acoustic power, W, radiated out from a segmented duct open end is calculated by

$$W = \frac{S}{2} Re\left\{ \begin{bmatrix} \mathbf{p}_{\mathbf{M}}^{1\,T} & \mathbf{p}_{\mathbf{M}}^{2\,T} & \mathbf{p}_{\mathbf{M}}^{3\,T} & \mathbf{p}_{\mathbf{M}}^{4\,T} \end{bmatrix} \cdot \begin{bmatrix} \overline{\mathbf{u}}_{\mathbf{M}}^{1} \\ \overline{\mathbf{u}}_{\mathbf{M}}^{2} \\ \overline{\mathbf{u}}_{\mathbf{M}}^{3} \\ \overline{\mathbf{u}}_{\mathbf{M}}^{4} \end{bmatrix} \right\} \tag{3.62}$$

where $\mathbf{p}_{\mathbf{M}}^{l\,T}$ is the transpose of the modal pressure vector at the l-th duct opening, $\overline{\mathbf{u}}_{\mathbf{M}}^{i}$ is the conjugate of the modal velocity vector at the i-th duct opening and S is the total surface area of the open end. The total acoustic power radiated out from the duct is obtained by summing the power calculated for each open end.

Model Validation Experiment

The frequency responses of the corresponding 2x2 plant were experimentally obtained in order to verify the segmented duct model. The plant frequency response measurements also provided model parameters, such as the duct damping factor and the speaker dynamics parameters. Figure 3.27 shows the experimental setup. The experimental fan duct was constructed with 2.5 mm thick acrylic material. The both duct ends were fitted with large wooden baffles (124 cm x 124 cm). The dimensions of the duct are also shown in the figure. It should be noted that the outer dimensions of the duct was unchanged from those of the previous non-segmented fan duct (9.5 cm x 9.5 cm x 21 cm). A speaker unit with a 4cm diameter diaphragm was used.

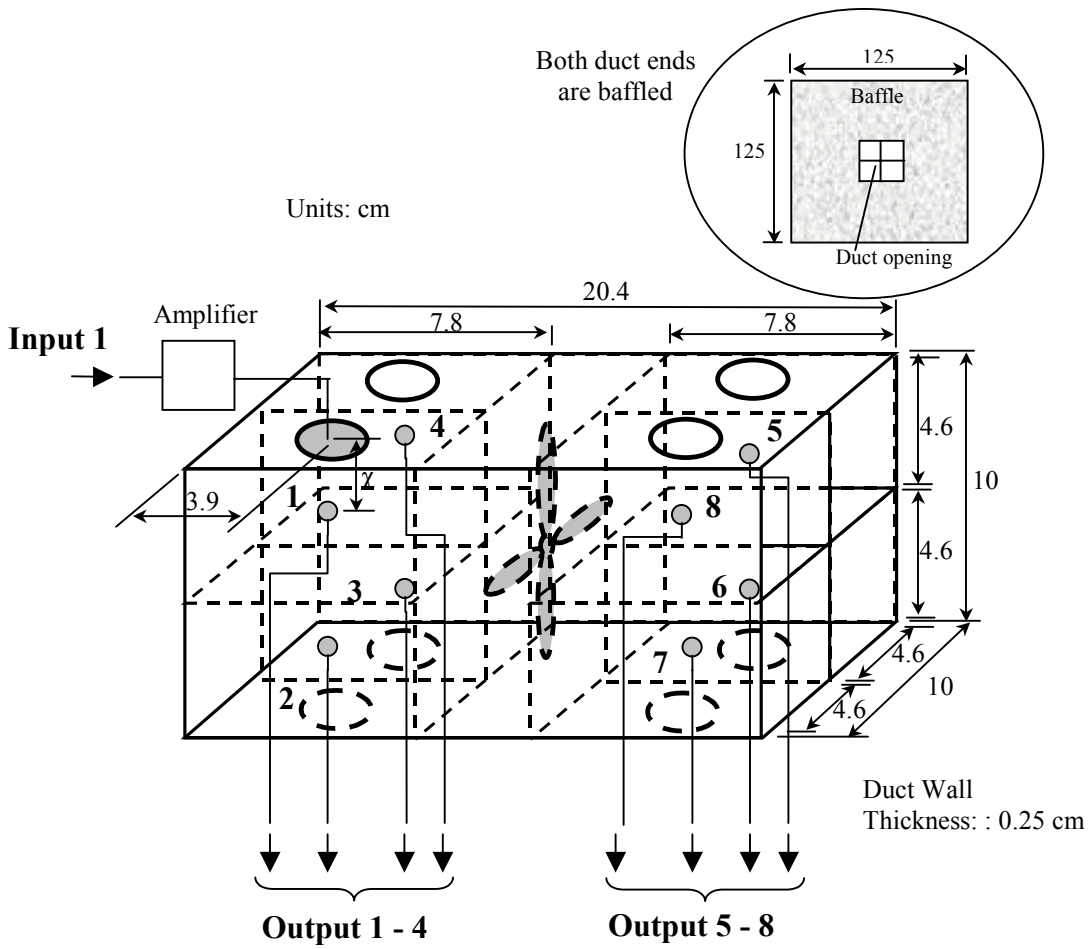

Figure 3.27. Segmented duct plant frequency response measurement setup

The plant was an 8x8 system. However, only the frequency responses between one of the eight speakers and the eight microphones (Input 1 and Output 1 to 8) were actually measured. The rest of the frequency responses associated with the other speakers were the mirror images of those measured due to symmetry. It should be noted that the plant also included the dynamics of the speakers in addition to the acoustic dynamics of the duct.

Figure 3.28 shows the dimensions used for the corresponding analytical model of the segmented duct. A coordinate system is also given in the figure to be used as a point of reference in subsequent discussions.

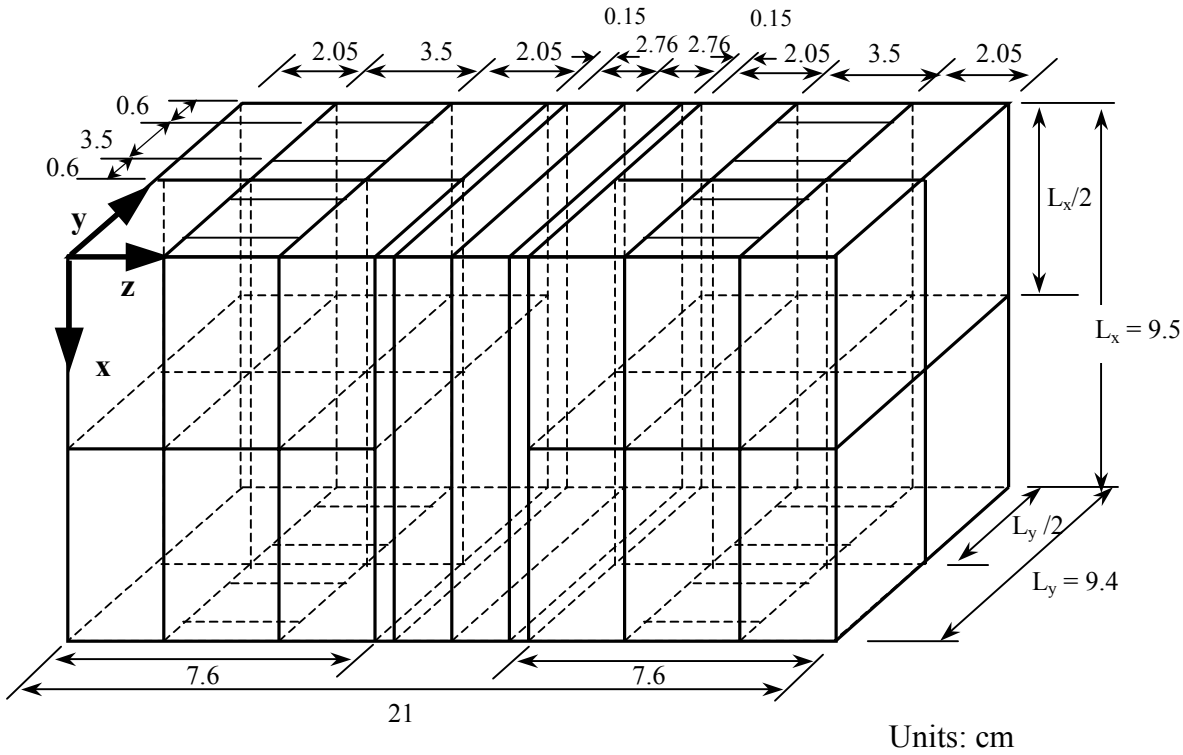

Figure 3.28. Segmented fan duct model dimensions

The duct cross-sectional modes included in the analytical model and associated cut-on frequencies are listed in Table 3.3 below. A total of 16 modes (M=1 to 16) were assumed for the larger duct section in the middle, while 4 modes (M=1 to 4) were assumed for the smaller duct sections.

Table 3.3. Segmented duct model modes and cut-on frequencies

Mode No.	Mode Index	Cut-on Frequency (Hz)		Mode No.	Mode Index	Cut-on Frequency (Hz)	
M	(m_x, m_y)	Large Duct	Small Duct	M	(m_x, m_y)	Large Duct	Small Duct
1	(0, 0)	0	0	9	(2, 2)	5133	-
2	(1, 0)	1805	3611	10	(3, 0)	5416	-
3	(0, 1)	1825	3649	11	(0, 3)	5473	-
4	(1, 1)	2567	5133	12	(3, 1)	5715	-
5	(2, 0)	3611	-	13	(1, 3)	5763	-
6	(0, 2)	3649	-	14	(3, 2)	6530	-
7	(2, 1)	4045	-	15	(2, 3)	6557	-
8	(1, 2)	4071	-	16	(3, 3)	7700	-

First, plant frequency responses were measured without any passive liner and also without a fan in the duct. The microphones were positioned directly in front of speakers at a normalized distance, χ $(=x/(L_x/2))$, of 0.4. The following figures show the experimental and the analytical frequency responses for the direct (Input 1 to Output 1) path and for selected cross paths. The duct acoustic loss factor, η, of 0.001 was used for the analytical model in this case. The natural frequency and the damping ratio of the speaker were set to 180 Hz and 0.3, respectively.

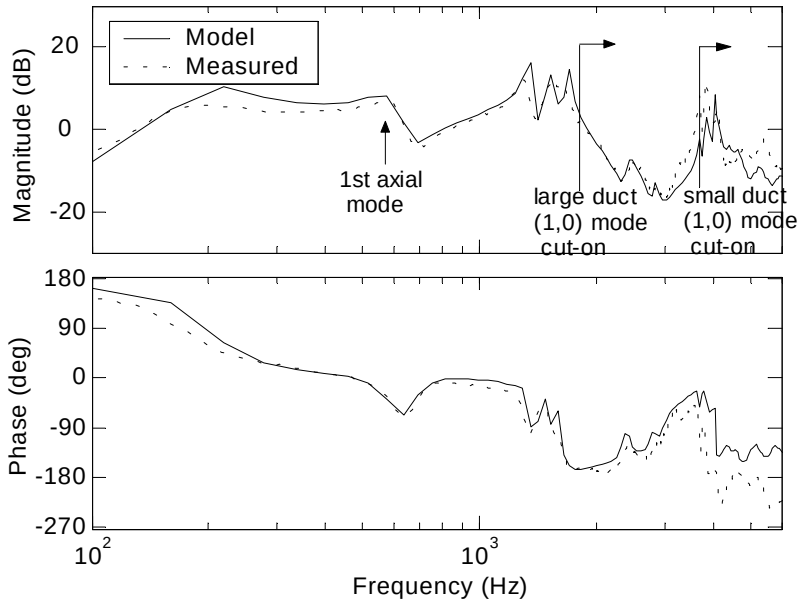

Figure 3.29. Plant frequency response, Input 1 to Output 1: no passive liner

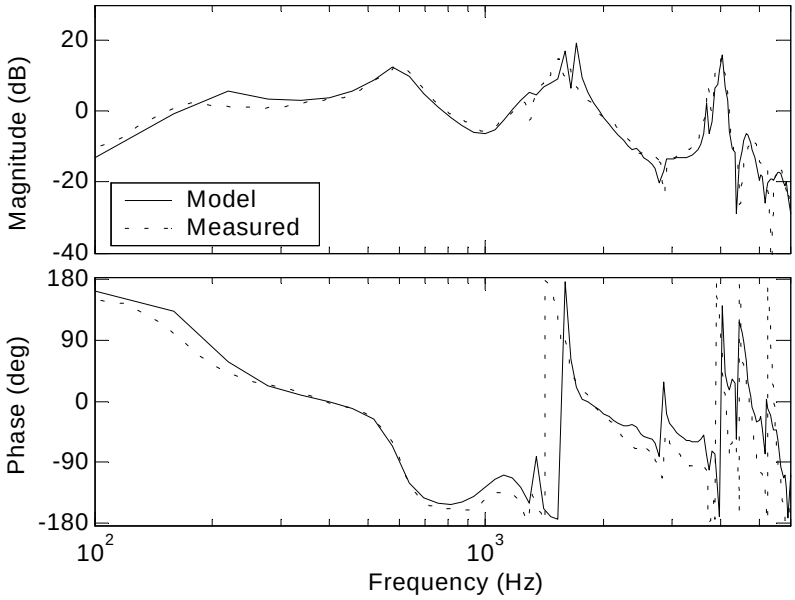

Figure 3.30. Plant frequency response, Input 1 to Output 2: no passive liner

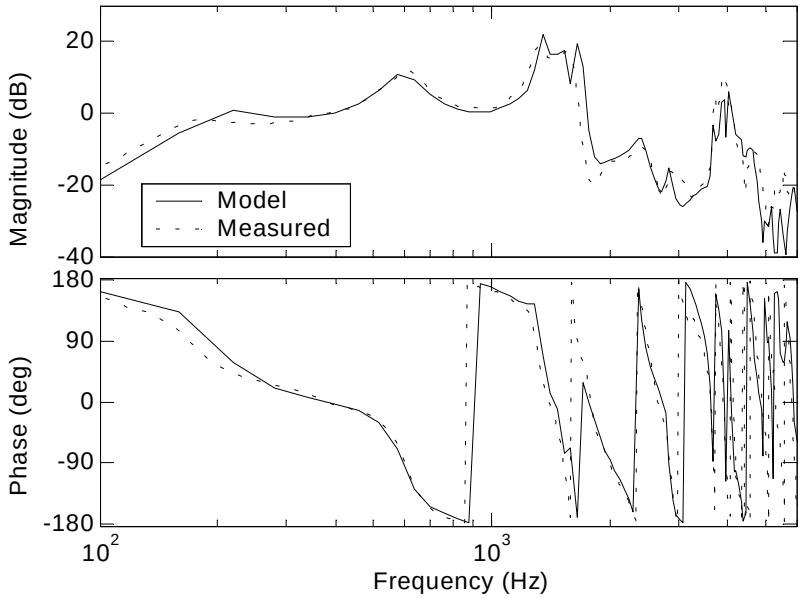

Figure 3.31. Plant frequency response, Input 1 to Output 6, no passive liner

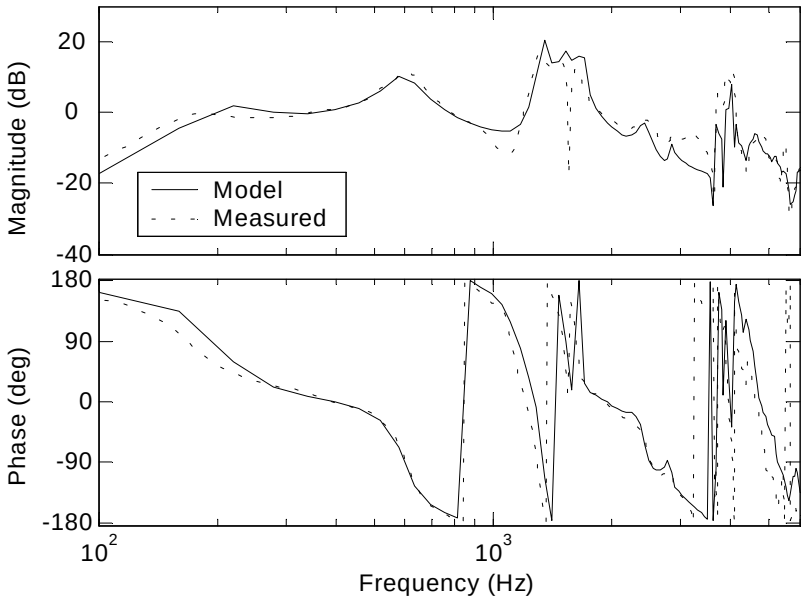

Figure 3.32. Plant frequency response, Input 1 to Output 8, no passive liner

Figure 3.29 to Figure 3.32 show generally good agreements between the experimental and the model frequency responses even at high frequencies. However, as it was the case for the previous non-segmented duct case, there seems to be more time delay in the measured frequency responses than those predicted by the analytical model.

Figure 3.33 to Figure 3.36 show the experimental and the analytical plant frequency responses of the segmented duct with some passive liner material installed. The microphone positions are unchanged (χ = 0.4). The passive liner was made of melamine foam with a thickness of 5mm, and covered the inner sidewalls of the duct. Frequency responses for the direct path and some of the selected cross paths are shown in the figures. The duct loss factor, η, of the analytical model was adjusted to fit the experimental data and resulted to a value of 0.07. The results show reasonable agreements between the experimental and the analytical frequency responses. However, as it was the case for the previous non-segmented duct, the resonant peaks of the plant frequency responses were somewhat shifted lower in frequency as a result of the installation of the passive liner in the duct. This was likely to be attributed to the unaccounted reactive characteristic of the passive material impedance. Further inspections of the *direct* path frequency response of Figure 3.33 show that there was some additional time delay in the experimental plant, which was not fully captured by the model.

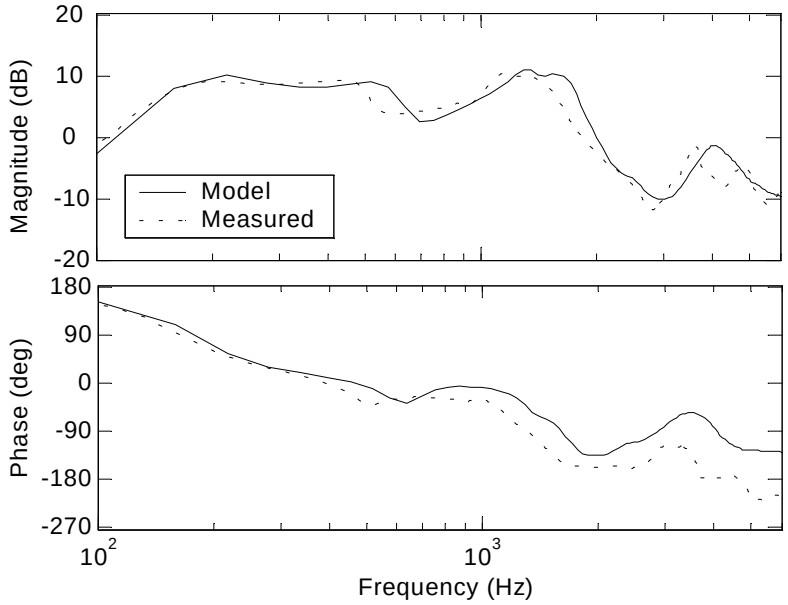

Figure 3.33. Plant frequency response, Input 1 to Output 1: with passive liner.

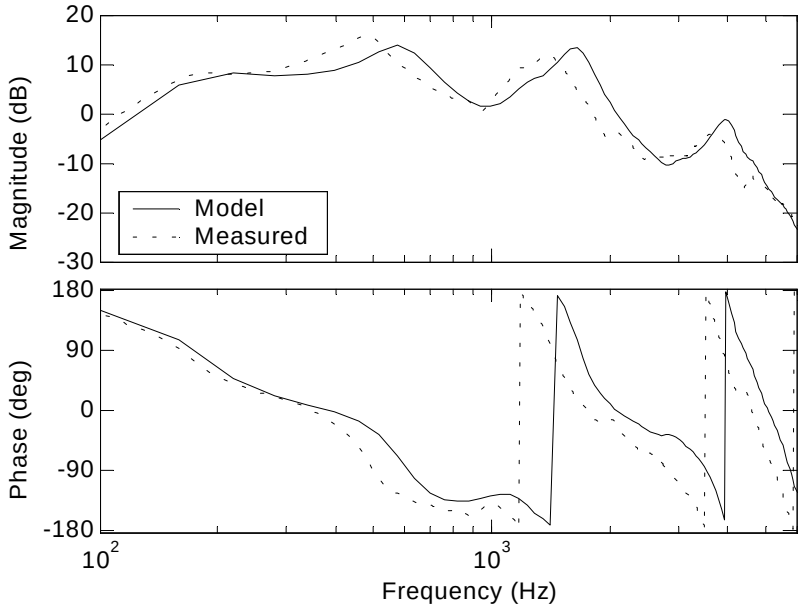

Figure 3.34. Plant frequency response, Input 1 to Output 2: with passive liner.

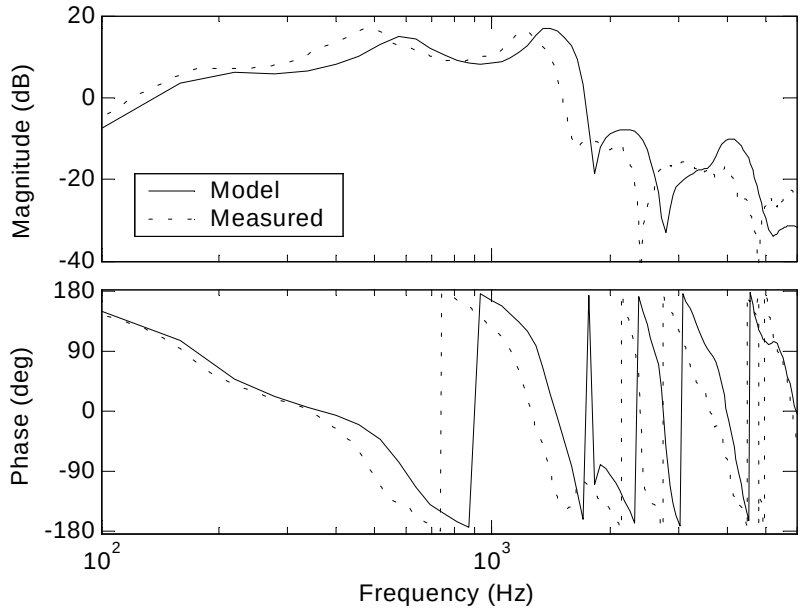

Figure 3.35. Plant frequency response, Input 1 to Output 6: with passive liner.

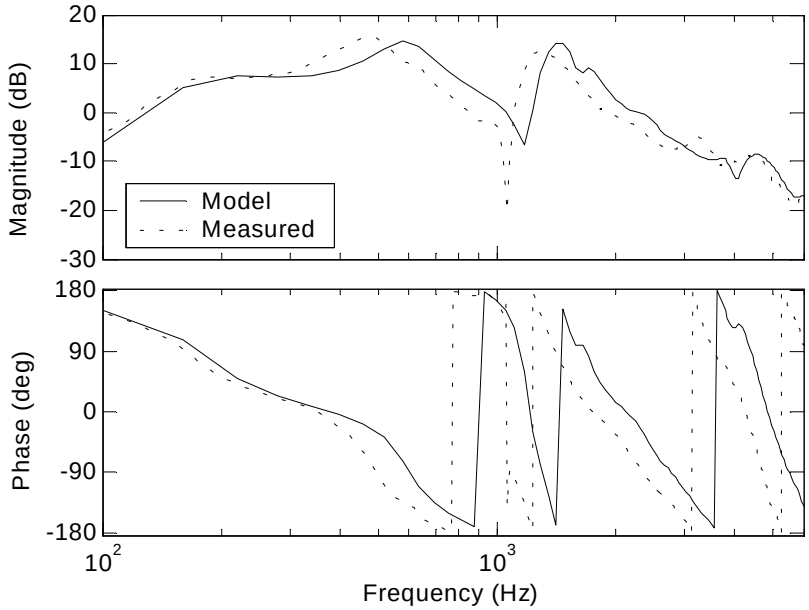

Figure 3.36. Plant frequency response, Input 1 to Output 8: with passive liner.

3.2.2 Passive Control Effect

The passive noise control characteristic of the passively-lined segmented fan duct is investigated by using the analytical model. Figure 3.37 shows the total acoustic power levels calculated for a fan with and without ducting. The case of the fan without a duct is represented by the model of a fan in an infinite baffle (See Section 3.1.2).

The duct acoustic loss factor, η, of 0.04 is used in order to model the effect of the passive liner. This is the same loss factor value used earlier for the non-segmented fan duct.

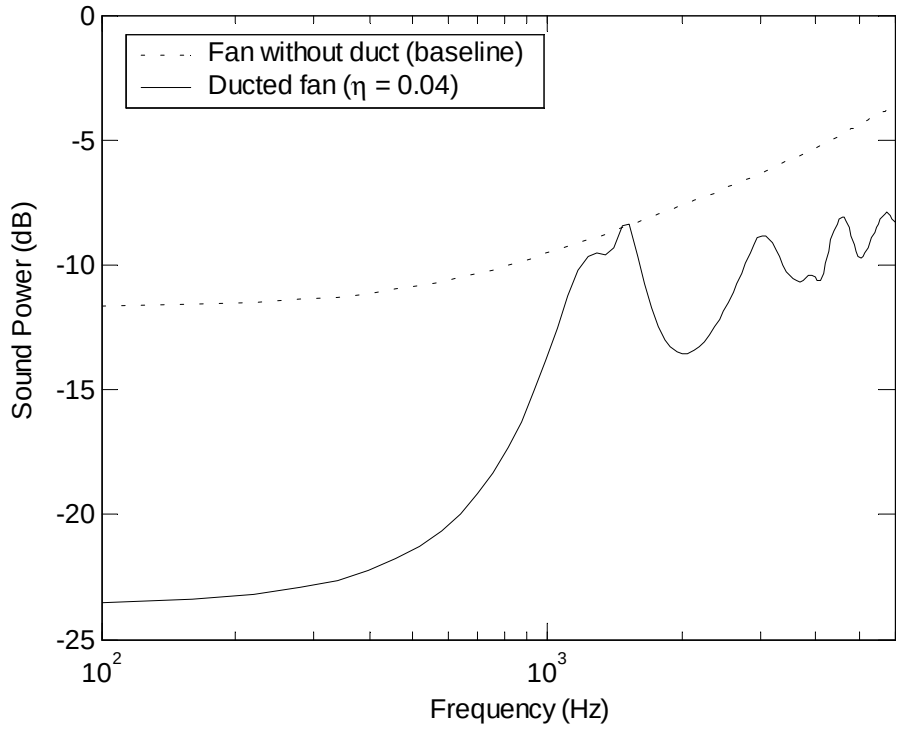

Figure 3.37. Passive effect of a segmented fan duct on global acoustic power

Figure 3.37 shows prominent noise reductions in the low frequency range due to the duct air-mass loading effect, which was also seen for the non-segmented duct case. The moderate noise reductions seen in the high frequency range is the noise-absorbing effect

of the passive liner. It is also observed in the figure that little noise reduction is obtained in the mid frequency range around 1200 to 1300 Hz. This is due to a resonating axial duct mode excited by the fan noise source.

Figure 3.38 shows the comparison of the passive noise control results obtained for the segmented duct and the previous non-segmented duct. Equal duct loss factor of 0.04 is assumed for both cases.

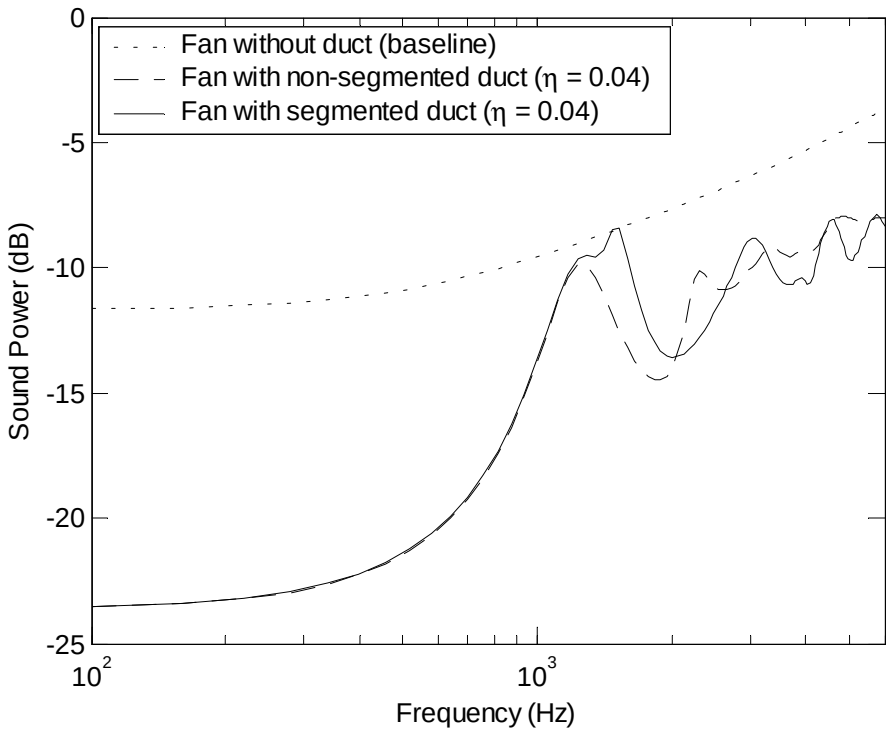

Figure 3.38. Passive control effect on global acoustic power: non-segmented duct and segmented duct

Figure 3.38 shows that there are no significant differences in passive control performance between the two cases. Especially in the low frequency range below 1200 Hz, the curves for the two cases are almost exactly the same. This is reasonable considering that the plane waves are dominant in the low frequency range. The plane waves are little affected by the duct segmentations because the directions of the associated particle velocities run parallel to the partition walls.

3.2.3 Active Control Effect

The active noise reduction performances of both feedforward and feedback control in conjunction with the segmented fan duct are investigated

Feedforward Control

Active noise reduction effect of feedforward control is obtained first. The analytical procedure is unchanged from the corresponding section for the previous non-segmented duct case except that the system here is 8x8 rather than 2x2. The detailed description of the analytical procedure used to determine the control inputs by a feedforward control is provided in Chapter 2, Section 2.4.1.

The local noise reduction effects of the 8x8 feedforward control are shown in Figure 3.39 in terms of the change in the norm of the 8x1 error microphone pressure vector. The error microphones are positioned directly in front of the speakers as indicated in Figure 3.27. The results are obtained for several cases of speaker-to-microphone distances: χ = 0.2, 0.3, 0.4 and 0.5 (= x / (L_x/2)). As shown in Figure 3.39, the fan noise is reduced locally at the microphone to practically zero by the action of the feedforward control, as expected.

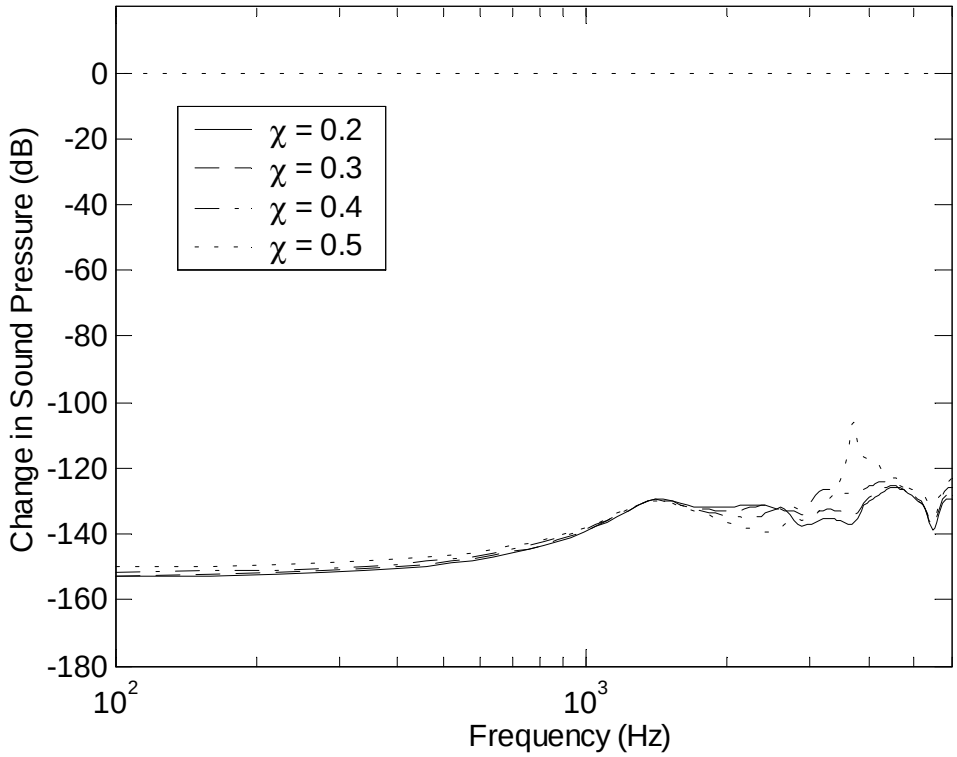

Figure 3.39. Local noise reduction performance of 8x8 feedforward control with segmented fan duct at microphones for χ = 0.2, 0.3, 0.4 and 0.5 (= x / (L_x/2))

Figure 3.40 shows the global noise control performance of the 8x8 feedforward control. The total radiated fan noise power levels with and without the feedforward control are shown for the four microphone position cases.

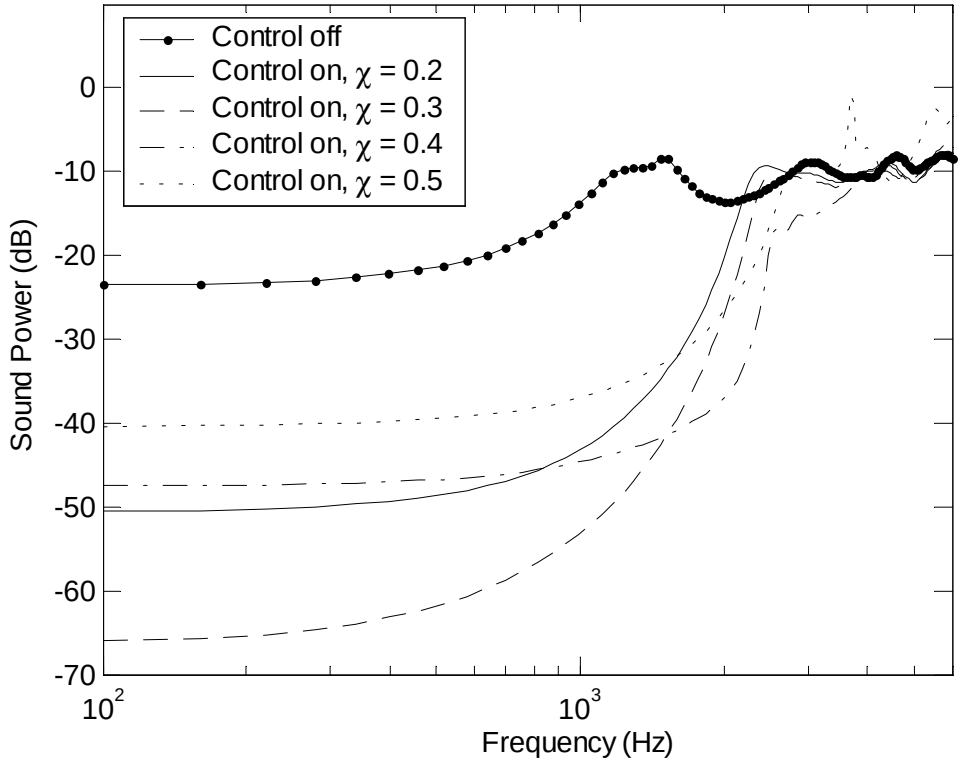

Figure 3.40. Global active noise control performance of 8x8 feedforward control with segmented duct for χ = 0.2, 0.3, 0.4 and 0.5

Figure 3.40 indicates large reductions in global noise power extending up to the frequency of 2000 to 3000 Hz. It is observed that the result for χ = 0.4 indicates higher control frequency range than those for the other three cases, seemingly extending up to the first cross mode cut-on frequency of the small duct segments (3611 Hz). However, the result for χ = 0.3 shows the largest noise reduction level in the low frequency range.

Figure 3.41 compares the global noise control performances obtained for the segmented fan duct with 8x8 feedforward control and the previously presented results for non-segmented fan duct with 2x2 feedforward control.

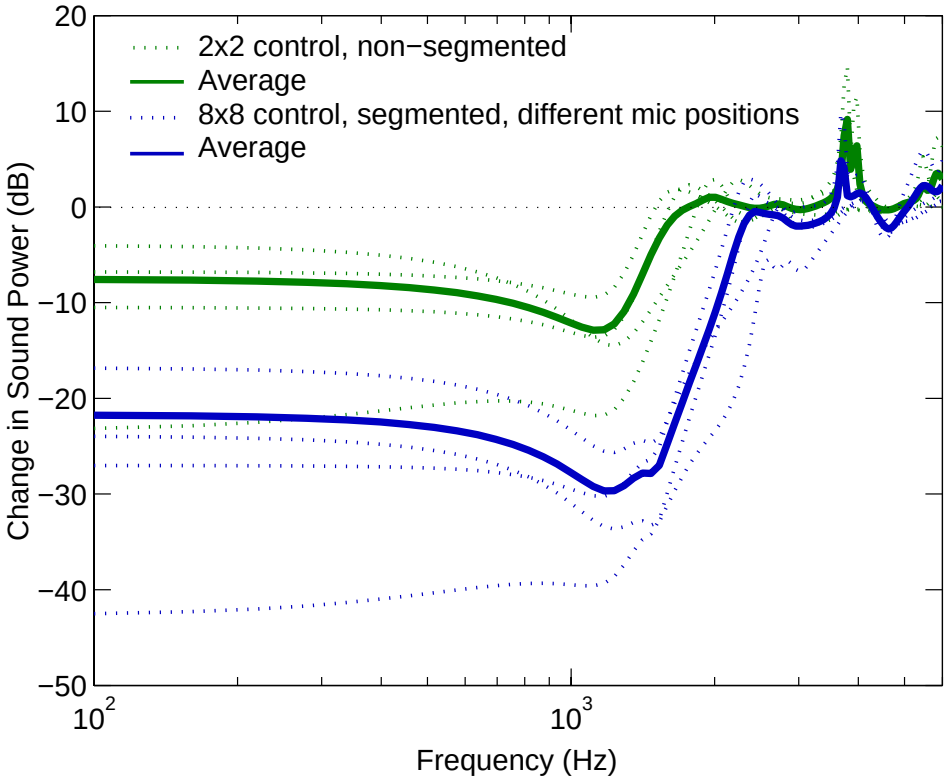

Figure 3.41. Global noise control performance comparison: non-segmented duct with 2x2 feedforward control and segmented duct with 8x8 feedforward control

It is observed in Figure 3.41 that, on average, the segmented fan duct with 8x8 control offers a significantly larger global noise control potential than the non-segmented fan duct with 2x2 control. The average upper frequency limit of global noise reduction is higher by about 1000 Hz. The result clearly indicates that the high-frequency shifting of the effective duct cut-on through the duct segmentation is beneficial in extending the global noise control bandwidth. Furthermore, it is also observed that the average noise reduction level is larger by as much as 15 dB for the segmented duct. This suggests that the segmentation has an effect of reducing the speaker near field (i.e. evanescent modes) contributions, which degrade global active control performance.

The following figures show the pressure contour plots of the interior and the exterior sound field of the segmented duct with and without feedforward control. The selected plane of pressure contour is at $y = L_y/4$ (see Figure 3.28). Figure 3.42 shows the

pressure contour of the fan noise field at 1000 Hz without active control. Figure 3.43 and Figure 3.44 show the noise field with feedforward control for χ = 0.2 and 0.3, respectively.

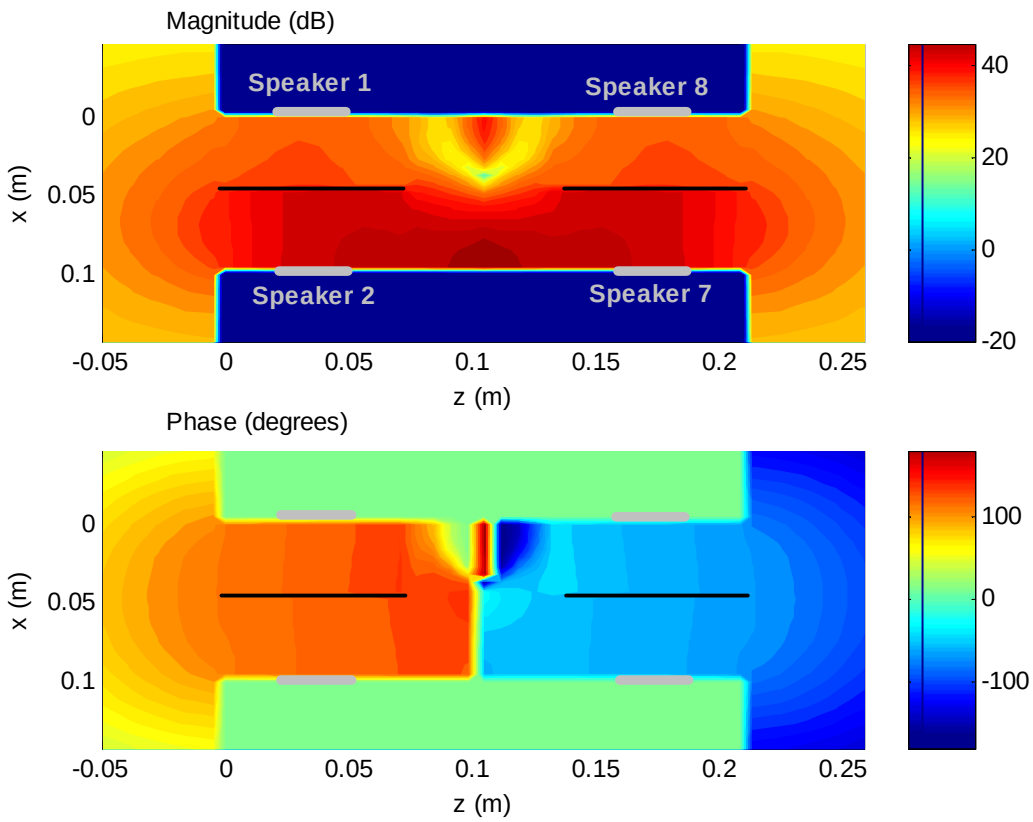

Figure 3.42. Sound pressure contour at 1000 Hz: segmented fan duct, feedforward control off

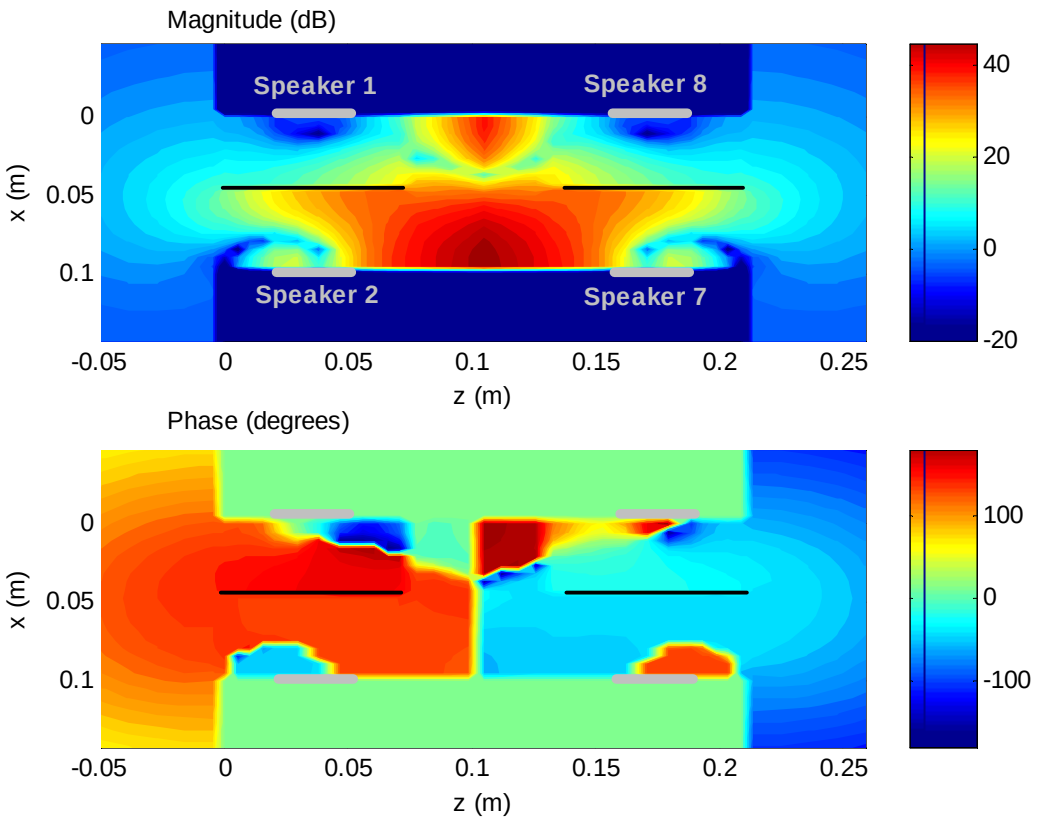

Figure 3.43. Sound pressure contour at 1000 Hz: segmented duct, feedforward control on, $\chi = 0.2$

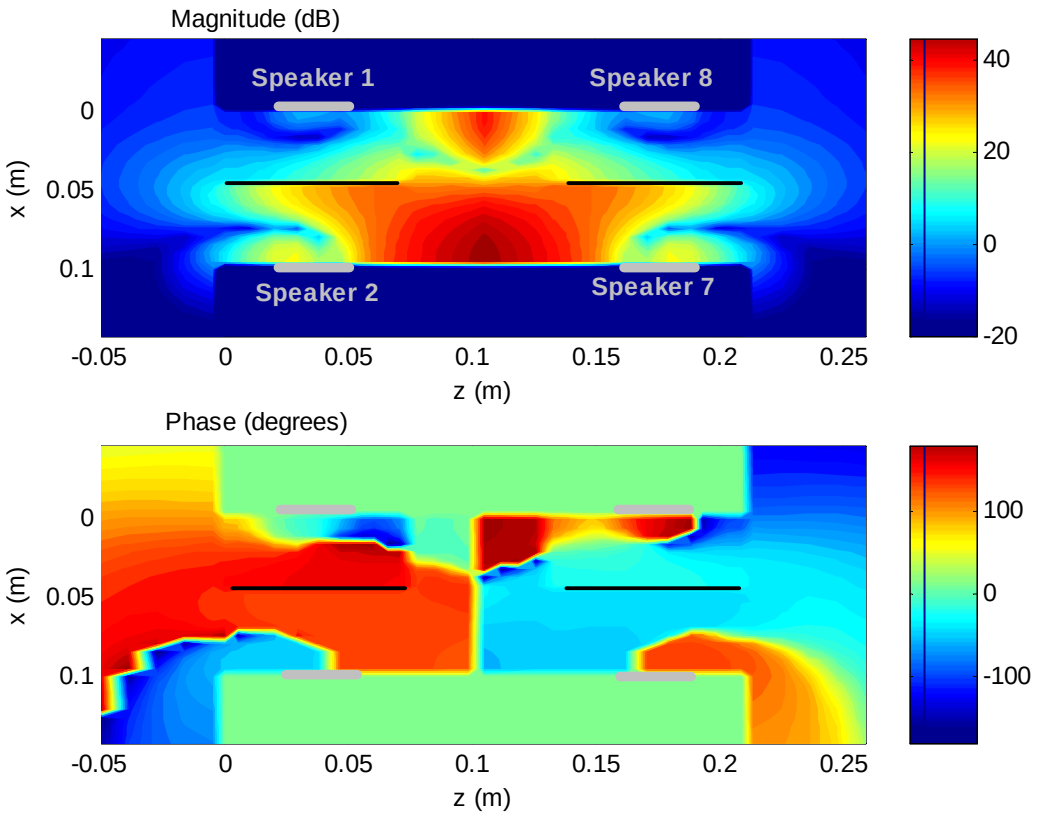

Figure 3.44. Sound pressure contour at 1000 Hz: segmented duct: feedforward control on, $\chi = 0.3$

The pressure contour plots show that the 8x8 feedforward control can effectively reduce the fan noise radiated out from the duct openings. It is also observed from the figures that a better noise control performance is obtained for χ = 0.3 than χ = 0.2, which is consistent with the result shown in Figure 3.40.

Feedback Control

Feedback control is considered next. The dimensions of the segmented duct and the 8x8 active control configuration are unchanged from the feedforward control case above. The same analytical procedure, which was used in the corresponding section for the earlier non-segmented case, is also followed here; the plant state space model is obtained by applying the ERA system identification procedure to the model plant frequency responses and then an MIMO feedback controller is determined using the LQG optimal control design method. The only difference is that now the system under consideration is 8x8 rather than 2x2.

In order to study the effect of microphone positioning to the feedback control performance, three different cases of the normalized microphone position, χ= 0.2, 0.3 and 0.4, are considered. The control design procedure is performed to obtain a separate feedback controller for each of the three cases.

Figure 3.45 shows the local noise reduction performance of the 8x8 feedback controllers obtained for χ= 0.2, 0.3 and 0.4. The results are shown in terms of dB change in the norm of the microphone pressure vector.

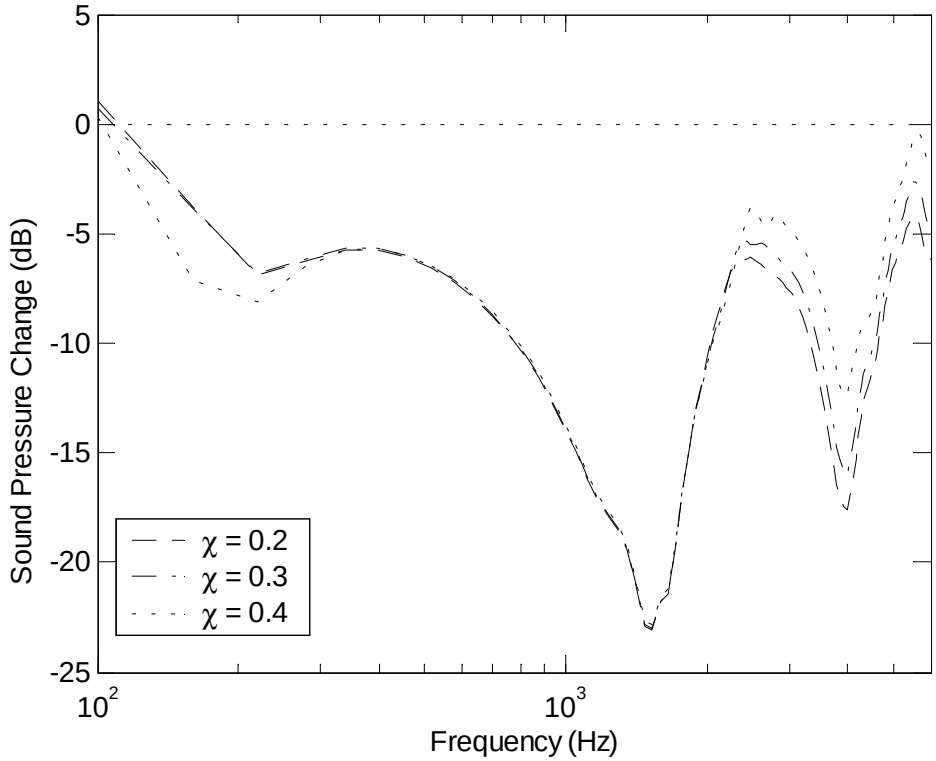

Figure 3.45. Change in the norm of error microphone pressure vector due to feedback control: segmented duct case

As shown in Figure 3.45, similar local noise reduction levels are obtained for all three cases. This is because the parameters of the feedback controllers are intentionally adjusted to yield similar local performances for the three cases. However, it is interesting to note that the reduction performances are being slightly degraded in the high frequency range with increasing χ. This is considered to be the effect of increasing phase lag as a result of the increased speaker-to-microphone distance, χ.

Figure 3.46 shows the global noise reduction performance of 8x8 feedback control for $\chi = 0.2$, 0.3 and 0.4.

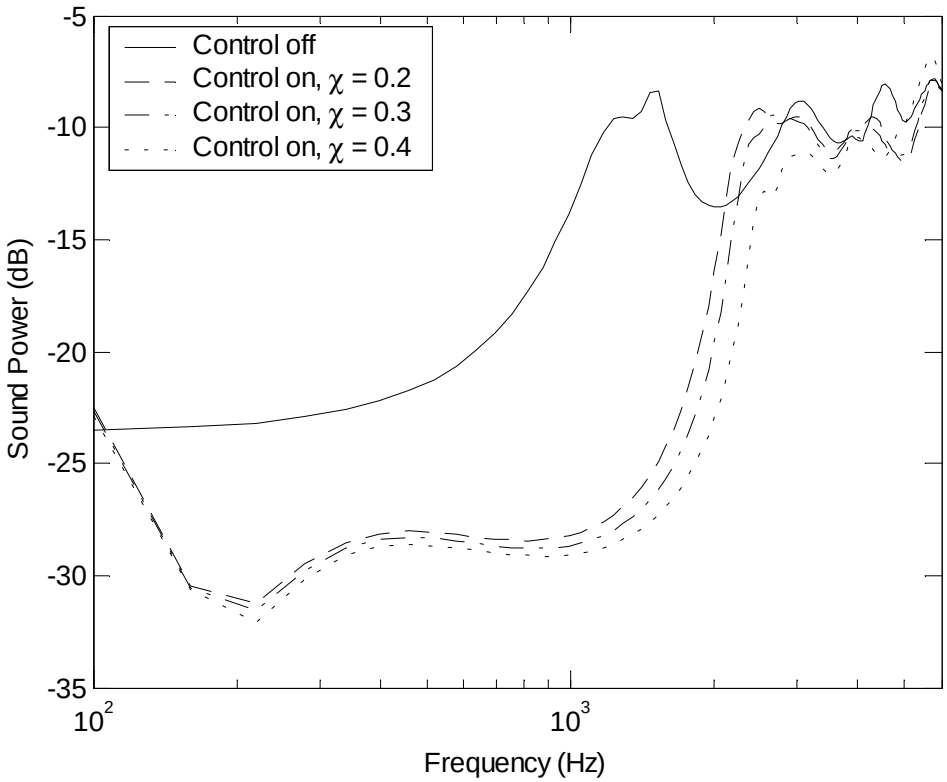

Figure 3.46. Feedback control effect on global noise power level: segmented duct case

It is observed in Figure 3.46 that the feedback control is most effective in reducing the duct axial resonance peak in the mid-frequency range of 1000 to 2000 Hz. It is also observed that slightly better global noise reductions are obtained in the frequency range of 300 to 2000 Hz with increasing χ, despite that there are no significant differences in the local noise reduction levels as shown in Figure 3.45.

Figure 3.47 shows comparison between the results obtained for the segmented duct with 8x8 feedback control and the previously presented results for the non-segmented duct with 2x2 feedback control. The figure shows both local and global noise control performances in the frequency range of 400 to 3000 Hz. It should be noted that the gains of the feedback control loops are intentionally chosen so that the local noise control performances are somewhat comparable between the segmented duct case and the

non-segmented duct case. Even then, it is observed from the figures that the results for the segmented duct with 8x8 feedback control show better global power reduction on average than the results for the non-segmented duct with 2x2 feedback control despite of comparable local noise reduction performances.

Finally, it should be noted that, for the present theoretical study, the feedback control design processes were performed without regard to factors associated with practical controller implementation issues. Therefore, no order reduction procedures were performed on the high-order controllers, which were obtained as a result of the direct application of the ERA system identification and the LQG optimal control design. Also the gain margins are kept minimal. Therefore, the feedback noise control performance results presented here should be treated as rather idealistic theoretical estimates. The actual levels of noise control performance obtained by more practical feedback controllers are likely to be somewhat less than those indicated in the results in this section.

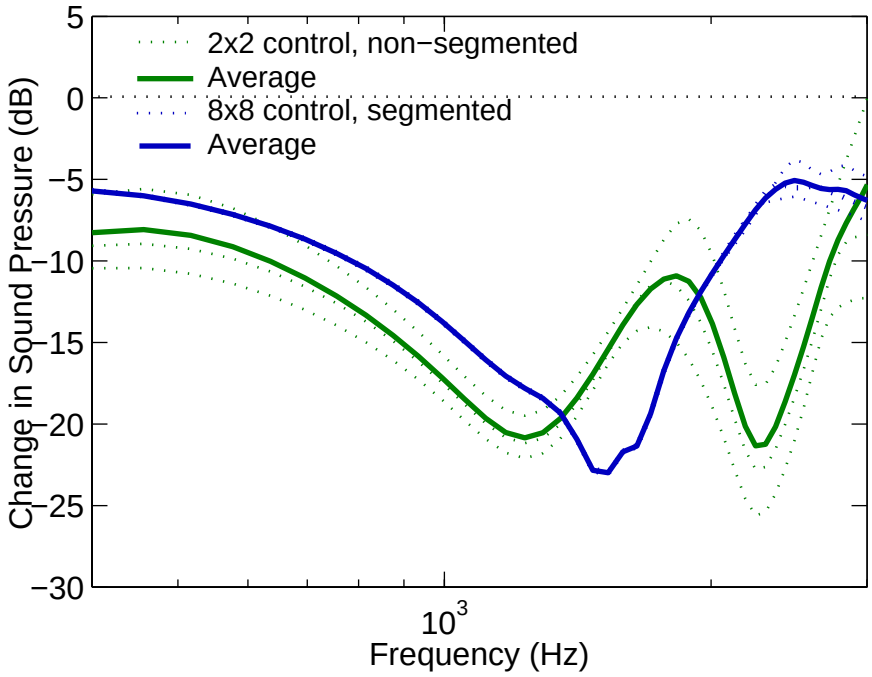

(a) Local control effect

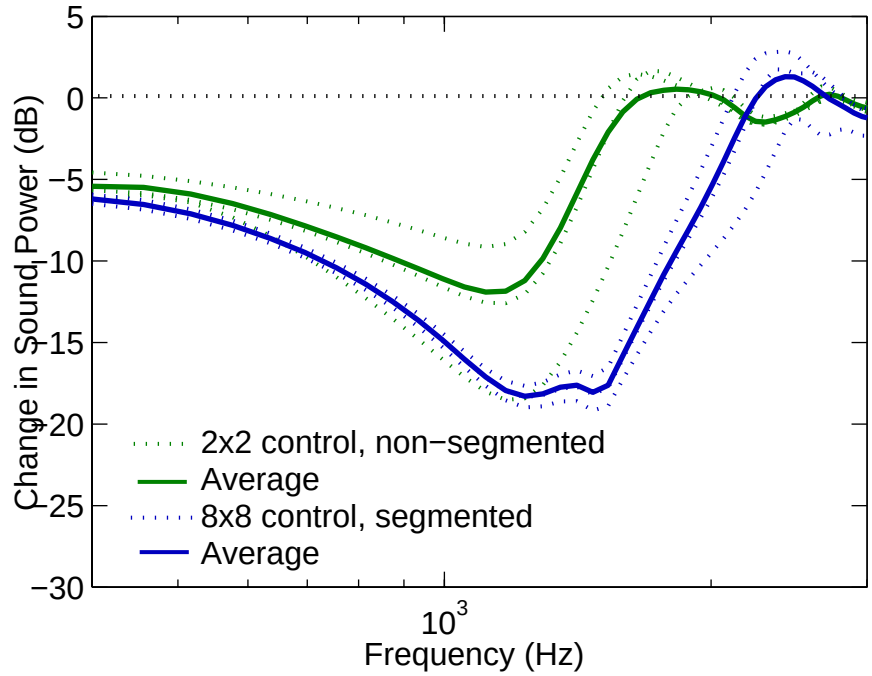

(b) Global control effect

Figure 3.47. Feedback control effect comparison: (a) microphone pressure norm change (b) global sound power change

3.2.4 Total Active-Passive Control Effect

The overall global noise control effect of the active-passive fan duct is summarized in Figure 3.22 below.

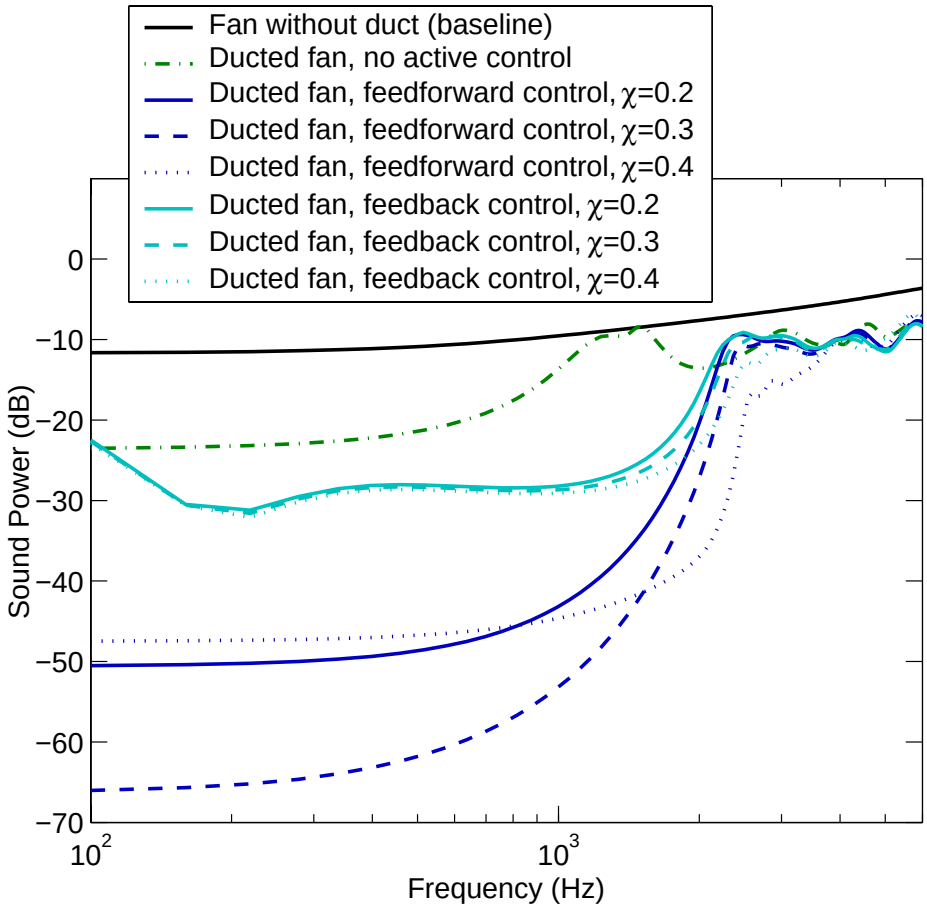

Figure 3.48. Overall effect of active-passive noise control fan duct on global noise power level: segmented duct with 8x8 control

The similar observations, which were made for the previous non-segmented duct case, can also be made for the segmented duct case in Figure 3.22. The passively-lined fan duct itself provides inherent noise reductions in the low frequency range due to the duct air-mass loading effect also in the high frequency range due to the sound absorptive

passive liner. Active control provides additional reductions of noise in the low frequency range. Active noise control is especially observed to be useful in compensating for the adverse effect of the duct axial resonance in the mid-frequency range. Practicality aside, feedforward control offers higher noise reduction potential that offered by feedback control.

3.3 Summary

In this chapter, analytical investigations were carried out in order to gain insights into the noise control characteristics of the active-passive noise control fan duct. Two alternate designs of the active-passive noise control fan duct were considered: one was a simple finite duct with 2x2 active control and the other was an internally segmented fan duct with 8x8x active control. The modeling approach introduced in Chapter 2 (Section 2.2) was used to develop the analytical models for the two design cases.

The analytical models were also verified by comparing analytical and experimental plant frequency responses. The experimental and analytical frequency responses corresponded reasonably well even at relatively high frequencies, except that the experimentally obtained frequency responses indicated slightly more time delay than the analytical frequency responses. It was also observed in the experimental data that the installation of the duct passive liner tended to lower the frequencies of the plant dynamics.

Having developed and validated the analytical models, active and passive noise control characteristics were investigated for each of the two fan duct designs. Non-segmented and segmented fan duct models indicated similar passive noise control performances. Passive noise reduction is obtained at both low (below 1k Hz) and high frequencies (above 2k Hz) due to the mass loading effect of the air in the duct and the passive liner damping, respectively. It was also shown that the overall passive noise control performance is degraded by the presence of a duct axial resonance in the mid-frequency range (from 1k Hz to 2k Hz).

Active noise control effects were examined by using the analytical fan duct models in conjunction with the analytical procedures for the feedforward and feedback control described in Chapter 2. The feedforward control results typically indicated large

active noise reductions, extending at best to the first cut-on frequency of the respective duct (1805 Hz for the non-segmented design with 2x2 control and 3611 Hz for the segmented duct with 8x8 control). Significantly better global noise control performances, in terms of both bandwidth and depth, were observed in the feedforward control results for the segmented duct with 8x8x control than for the non-segmented 2x2 control. It was also observed that the global noise control performance of the feedforward control is significantly affected by the positioning of the error microphones with respect to the control speakers. The feedback control results also indicated the dependence to the error microphone position, though not as dramatically as the feedforward control results. The segmented duct with 8x8 feedback control was also shown to yield better global performances than the non-segmented duct with 2x2 feedback control. It was also observed that the most global noise reduction is obtained in the mid frequency range (1k Hz to 2k Hz), which effectively compensates for the performance degrading effect of the axial duct resonance.

Chapter 4

Active-Passive Control Experiment

Noise control characteristics of the active-passive control fan duct were experimentally investigated. An experimental fan duct unit was constructed based on the segmented fan duct design introduced in the previous chapter. The passive noise control performance of the segmented fan duct is presented first. Then, the design and the implementation of the active noise control system are described. The active control system utilized the hybrid control approach, in which feedforward and feedback control are combined to achieve the simultaneous reduction of both BPF tonal and broadband fan noise. The results of the active noise control experiments using this hybrid active noise control system are presented. Then, the results from the passive and the active control experiments are combined together to show the total noise control benefit of the active-passive control approach. At the end of the chapter, the practical utility of the current fan noise control approach is demonstrated by an experiment using an actual PC chassis, simulating a realistic operating environment of the fan duct.

4.1 Experimental Setup Description

The followings describe the constructed active-passive control fan duct unit and the experimental apparatus used to measure its noise control characteristics.

4.1.1 Active-Passive Control Fan Duct Unit

An experimental unit of active-passive noise control fan duct was designed and constructed. The geometry and the dimensions of the constructed fan duct are shown in Figure 4.1.

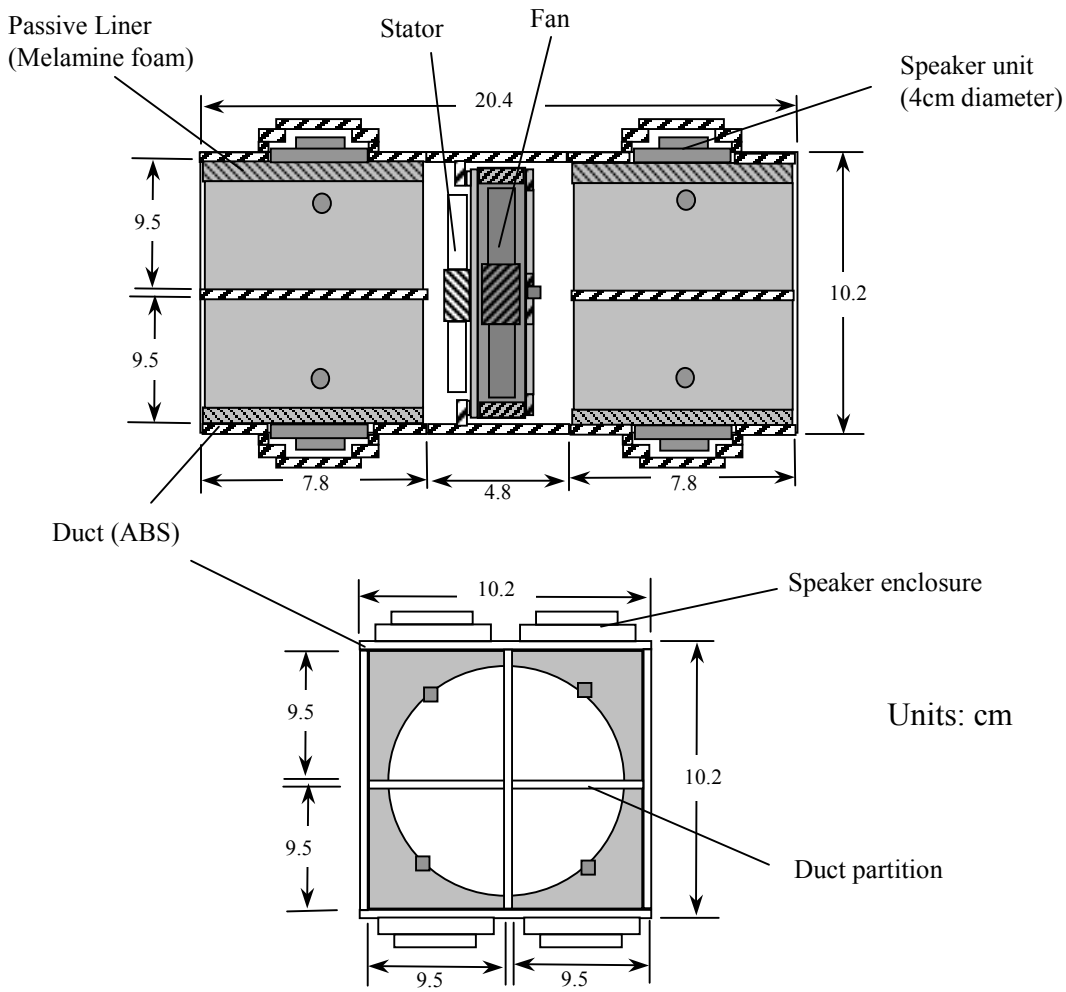

Figure 4.1. Active-passive noise control fan duct dimensions

Figure 4.2 shows the photos of the constructed fan duct.

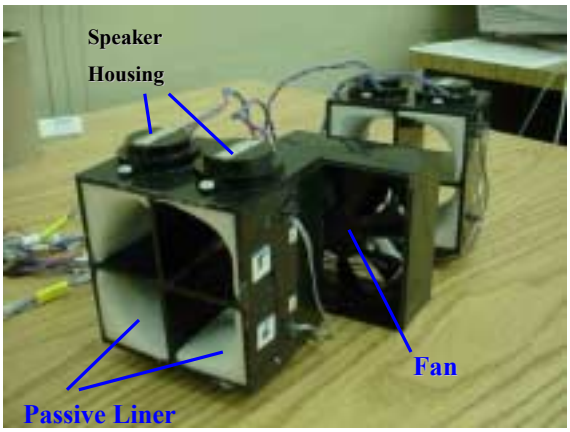

(a)

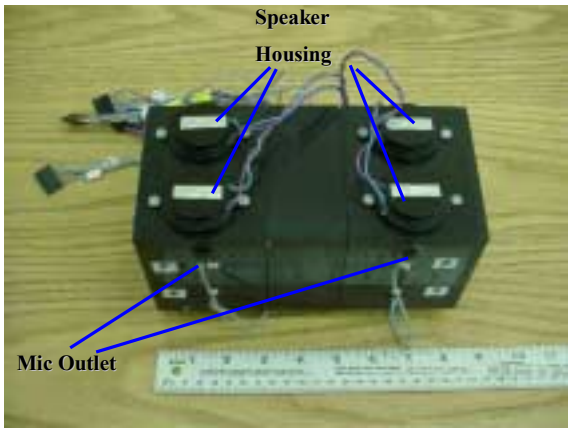

(b)

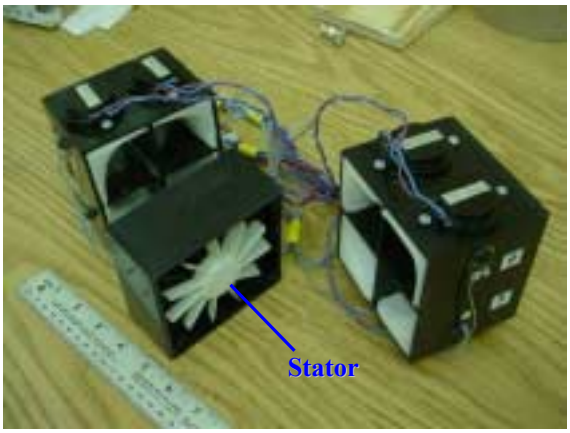

(c)

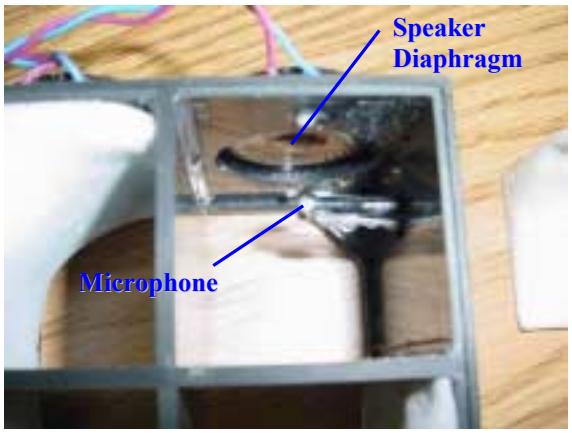

(d)

Figure 4.2. Active-passive noise control fan duct: (a) disassembled duct, (b) assembled duct, (c) stator, (d) speaker & microphone

The design of the fan duct was based on the segmented fan duct studied in Chapter 3, Section 3.2. In this design, both the inlet and the outlet side of the duct were partitioned into four smaller duct segments of equal size. Each small duct segment contained a speaker (diameter: 4 cm) and also some passive lining material (melamine foam) as indicated in Figure 4.2. A small axial fan, which is typically installed into a desktop computer for ventilation, was installed in the middle of the duct. It should be noted in Figure 4.2 that a device called, "stator", was also attached to the exhaust side of the fan in order to increase the airflow performance.

4.1.2 Noise Control Performance Measurement Setup

Global noise control performance of the above active-passive control fan duct was measured by using the following experimental setup. Following figures show the experimental setup.

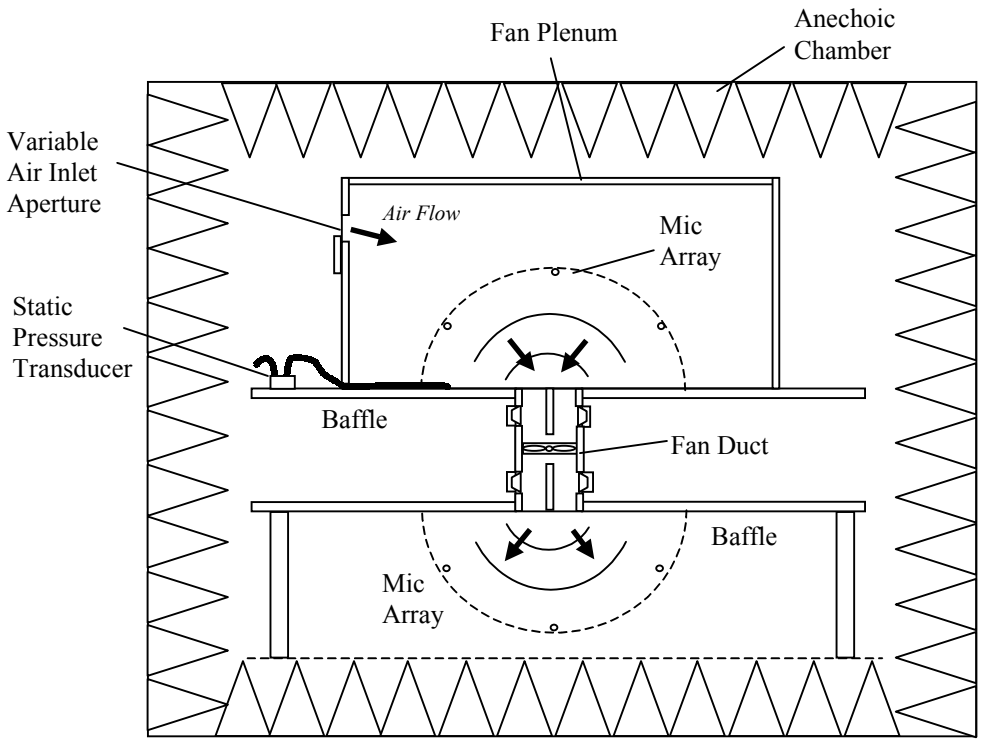

Figure 4.3. Fan noise power measurement setup

(a)

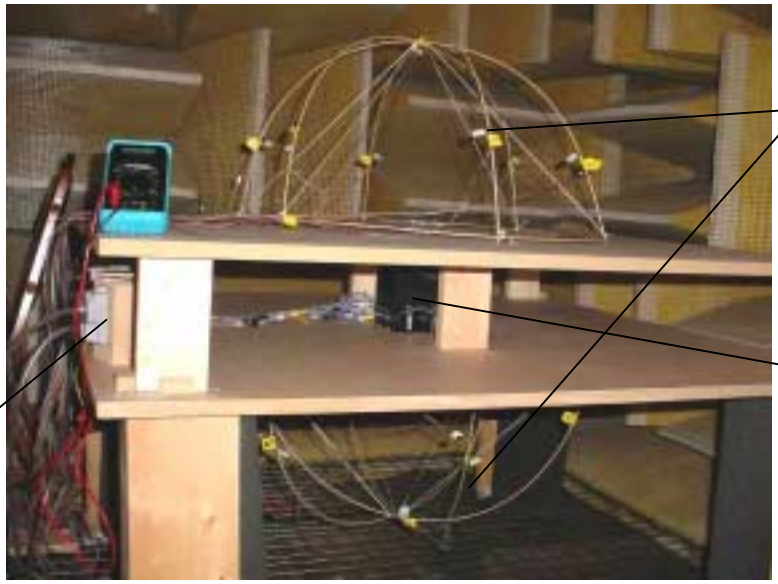

(b)

Figure 4.4. Fan noise power measurement setup images: (a) baffle table with fan plenum, (b) baffle table without fan plenum

The setup consisted of two wooden boards (48 in x 49 in), which were constructed in such a way that the fan duct could be flush-mounted in the middle. These wooden boards served as "infinite" baffles to the duct openings. This was constructed in the form of a table so that it could be positioned horizontally in an anechoic chamber. Total radiated fan noise power was, then, measured by using the two sets of microphones provided at the air inlet and the outlet side of the duct. Each set of microphones formed a hemisphere at the top and the bottom of the baffle table. The radius, *r*, of these hemispherical microphone arrays (hence the distance of the respective opening to the microphones) was chosen so that the microphones were in the far field from the opening. The exact positions of the microphones in a hemispherical array are shown is Figure 4.5.

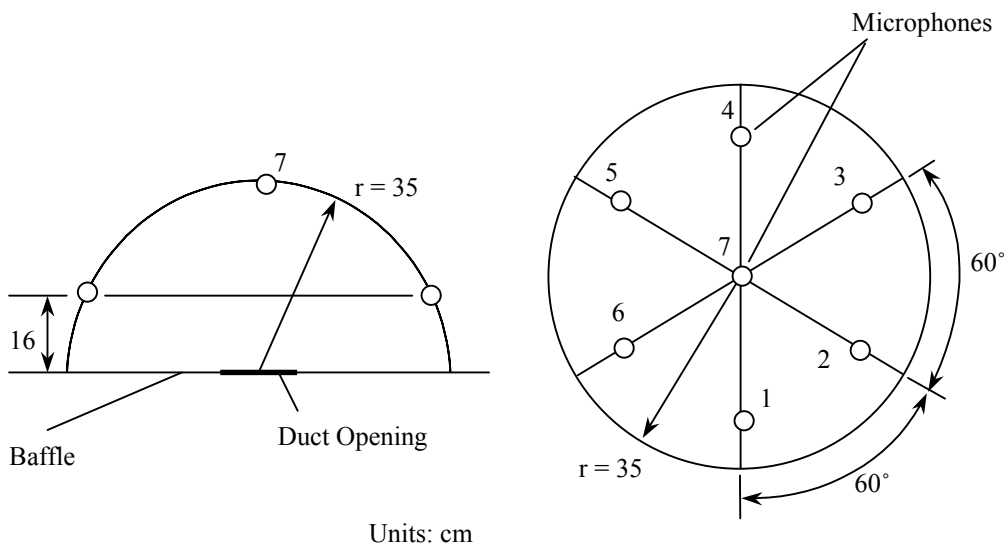

Figure 4.5. Hemispherical microphone array (single side)

Assuming that the top and the bottom hemisphere form a single sphere of radius, r, total fan noise power, W, radiated from the fan duct is calculated as

$$W = \frac{2\pi r^2}{\rho c} \frac{1}{N} \sum_N p_{rms}^{\ 2} \tag{4.1}$$

where N is the total number of microphones (7 x two sides = 14), p_{rms} is the RMS microphone pressure, ρ is the air density and c is the speed of sound. In the present study, $p_{rms}^{\ 2}$ in the equation above is replaced with autospectrum, $p_{xx}(f_i)$, so that W becomes the sound power spectrum, $W(f_i)$, instead. The total sound power value, W, is then obtained by summing all the spectrum components as

$$W = \sum_i W(f_i) \tag{4.2}$$

The experimental setup also included a fan plenum in order to adjust the aerodynamic operating condition of the axial fan. The fan plenum consisted of a wooden frame tightly covered with thin plastic sheets. It was positioned at the inlet side of the duct in order to regulate the airflow. Decrease in airflow rate through the duct is normally accompanied by increase in static pressure that develops across the fan. This static pressure was monitored by a differential pressure sensor and adjusted to a desired level by varying the size of the variable air inlet aperture on the fan plenum.

4.2 Passive Control Effect

Passive noise control characteristics of the segmented fan duct were experimentally determined. This was done by comparing the total sound power spectrum obtained for the fan with and without the duct. The measurement of the sound power level of the fan without the duct (the baseline noise level) was facilitated by removing the top baffle and by installing the fan without the duct into the remaining bottom baffle. Figure 4.6 shows the setup for measuring the baseline fan noise power.

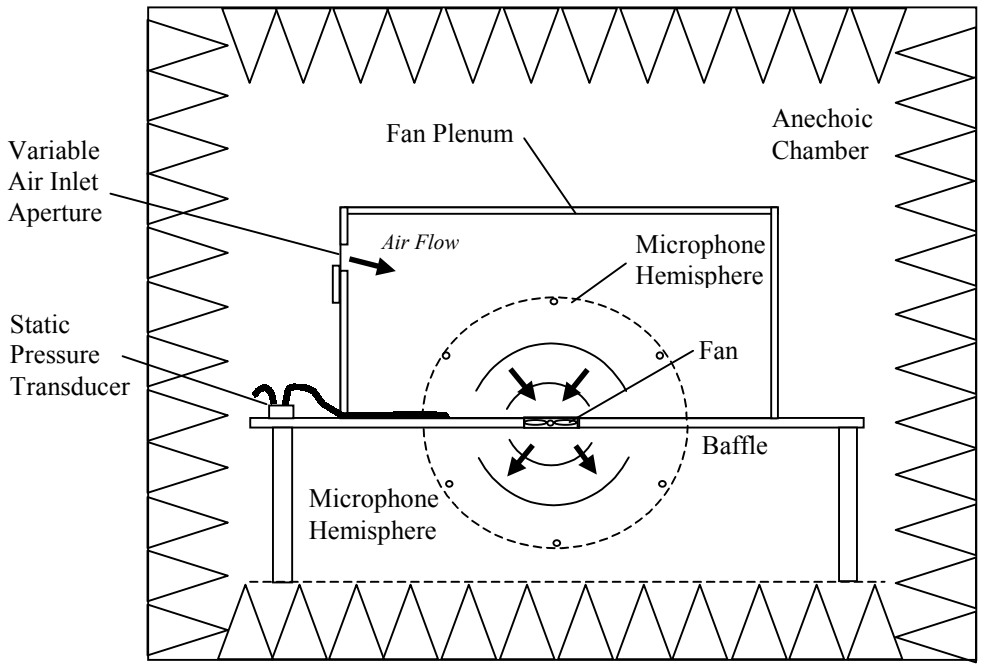

Figure 4.6. Baseline fan noise power level measurement setup

In comparing the fan noise power spectrum for the fan with and without the duct, it was important to maintain a consistent fan operating condition so that a consistent noise source characteristic was obtained between the measurements. The operating condition of a fan is specified by two variables: airflow rate and static pressure. Figure 4.7 shows experimentally obtained airflow rate (units in CFM or cubic feet per minute) versus static pressure, p_{static}, (units in inH_2O or inches of water column) for this particular fan with and without the duct.

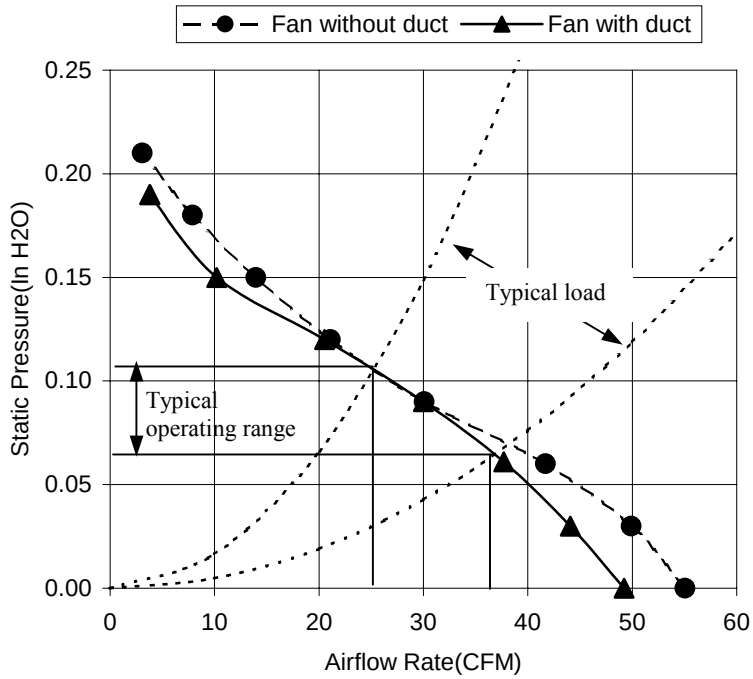

Figure 4.7. Airflow performance data of the fan with and without the duct

As shown in Figure 4.7, the curves are very similar for the two cases. And the difference is observed to be especially small in the typical operating range of the fan (p_{static} = 0.07 - 0.11 inH_2O), indicating that the impact of fan duct to the fan airflow performance would be insignificant in normal operating conditions. This finding was important since it meant that the passive noise reduction effect could be obtained without significantly degrading the airflow performance of the fan. It also implied that a consistent fan operating condition could be maintained during the sound power measurements simply by keeping a consistent fan static pressure, $p_{static,}$ between 0.07 to 0.11 inH_2O.

Figure 4.8 and Figure 4.9 show the measured fan noise power spectrum (A-weighted) with and without the duct for the static pressure, $p_{static,}$ of 0.09 and 0.11 inH_2O, respectively. Figure 4.10 compares these experimental passive noise control results with an analytical result obtained by using the model from Chapter 3 (Figure 3.37). The duct acoustic loss factor, η, of 0.07 was assumed for the model.

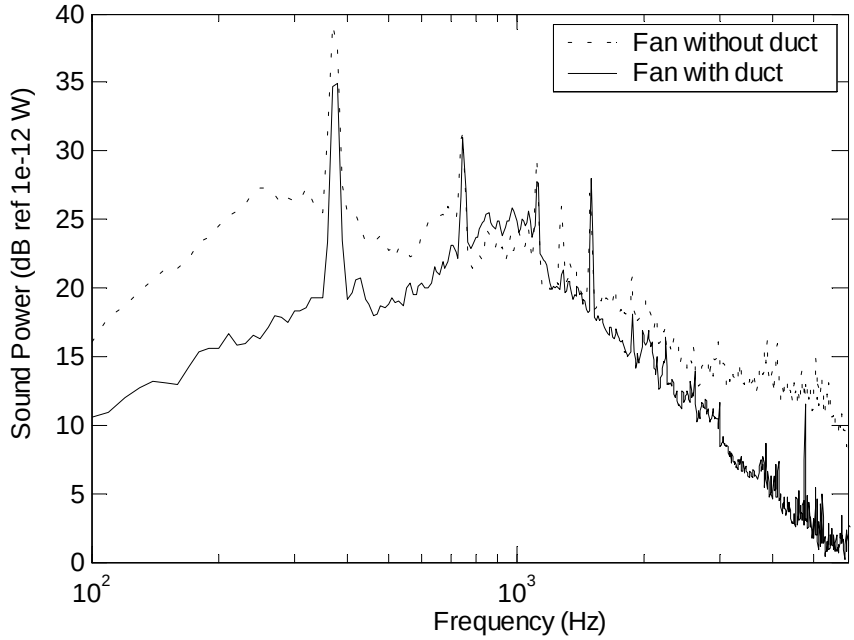

Figure 4.8. Fan noise power level with and without the fan duct: for p_{static} = 0.09 inH_20

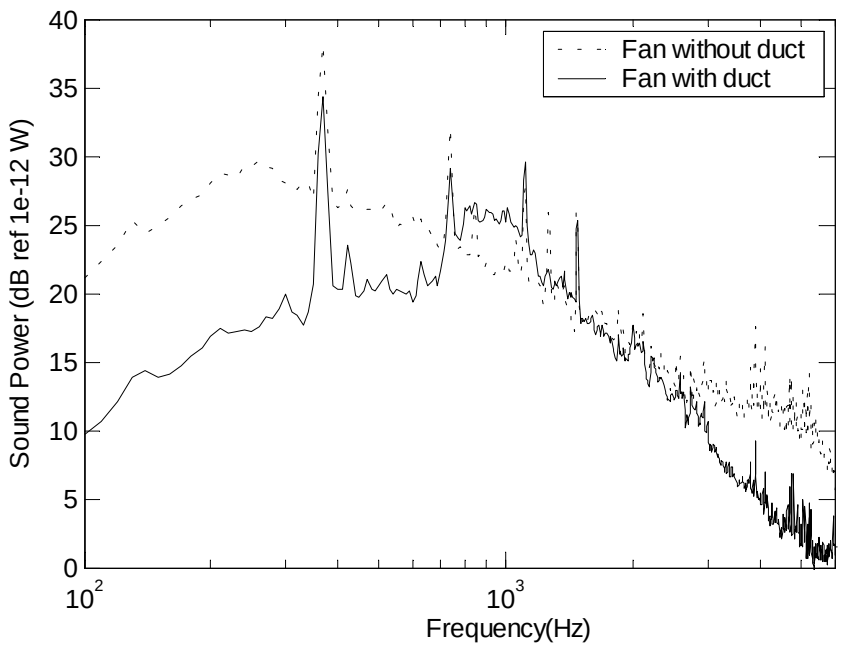

Figure 4.9. Fan noise power level with and without the fan duct: for p_{static} = 0.11 inH_20

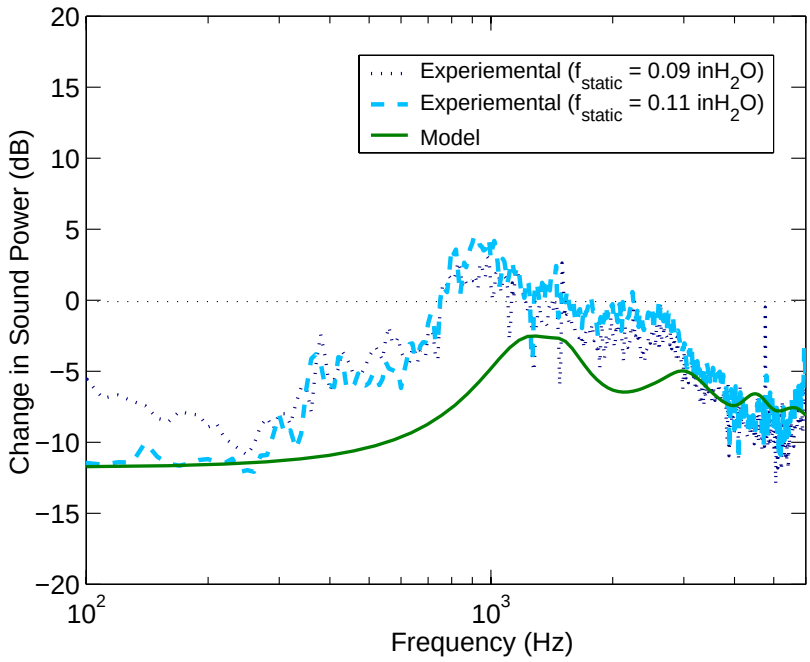

Figure 4.10. Change in fan noise power level due to the fan duct

Although Figure 4.10 seems to indicate a certain degree of bias error between the experimental and analytical result, the experimental data confirms the overall passive noise control characteristics of the fan duct, discussed in the previous chapter. The results clearly show the low frequency noise power reductions due to air-mass loading effect (see Equation 3.44), which was discussed in Chapter 3. The decrease in passive noise control performance in the mid-frequency range due to duct axial resonance is observed around 1000 Hz. The high frequency noise reduction effect of the passive liner is also shown in the figure above 2000 Hz. It is also observed in Figure 4.10 that the experimental passive noise reduction levels were somewhat shifted lower in frequency

compared with the analytical model counterpart. This is likely related to the similar trend observed in the plant frequency response measurements (see Figure 3.33 to Figure 3.36) in Chapter 3, where resonant peaks in the experimental frequency responses were lower in frequency than those exhibited by the analytical frequency responses. This resonant frequency shifting is suspected to be due to the reactive part of the passive liner impedance which is not accounted in the model.

4.3 Active Control Effect

Having determined the passive noise control effect of the fan duct, the next step was to experimentally examine the effect of active noise control on the fan noise emission. The hybrid feedforward-feedback active noise control approach briefly described in Chapter 2, Section 2.4.3, was used for the experiment. The implemented hybrid active control system utilized feedforward control for reducing BPF tones and feedback control for reducing broadband noise. First, a description of this hybrid active noise control system is presented. Then, the results of the active noise control experiments are discussed.

4.3.1 Description of Active Noise Control System

The hybrid active control system considered here is a combination of a two-inputs-two outputs (2x2) adaptive feedforward control system designed to reduce BPF tones and an eight-inputs-eight-outputs (8x8) fixed feedback control system designed to reduce broadband fan noise. Figure 4.11 illustrates this hybrid active noise control system.

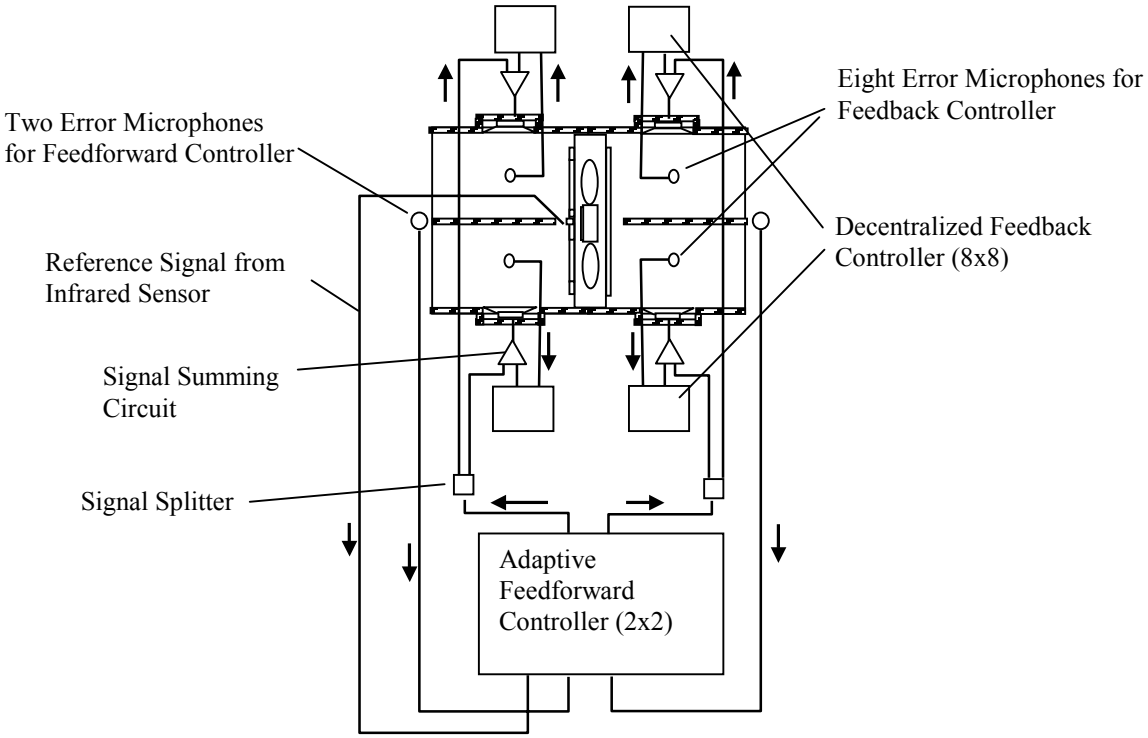

Figure 4.11. Implemented hybrid feedforward-feedback active noise control system

As indicated in Figure 4.11, the feedback controller was implemented as an 8x8 decentralized system, which consisted of eight SISO feedback controllers. Note that the feedback controller used eight in-duct microphones positioned in front of the speakers. Analog components were used to implement the feedback controller. On the other hand, the 2x2 feedforward controller utilized the popular FXLMS algorithm implemented on a Digital Signal Processing (DSP) board. The feedforward control was fully-coupled between the two channels. Inputs were taken from the two microphones positioned just outside the inlet and the outlet duct opening. Note that the separate microphones are used for the feedforward and the feedback controller. And the two outputs were connected to all eight speakers in such a way that four speakers on single side of the duct shared one

output. This feedforward controller was designed to reduce only the BPF tones. An infrared sensor mounted on the hub of the fan provided the reference signal that was only correlated with the BPF tones. Control outputs from the feedforward and the feedback controller were superimposed through signal summing circuits before fed to the power amplifiers that drove the speakers. Features of the feedforward and the feedback controller are discussed individually in detail below.

Feedforward Controller

Figure 4.12 shows the adaptive feedforward controller, isolated from the rest of the control system.

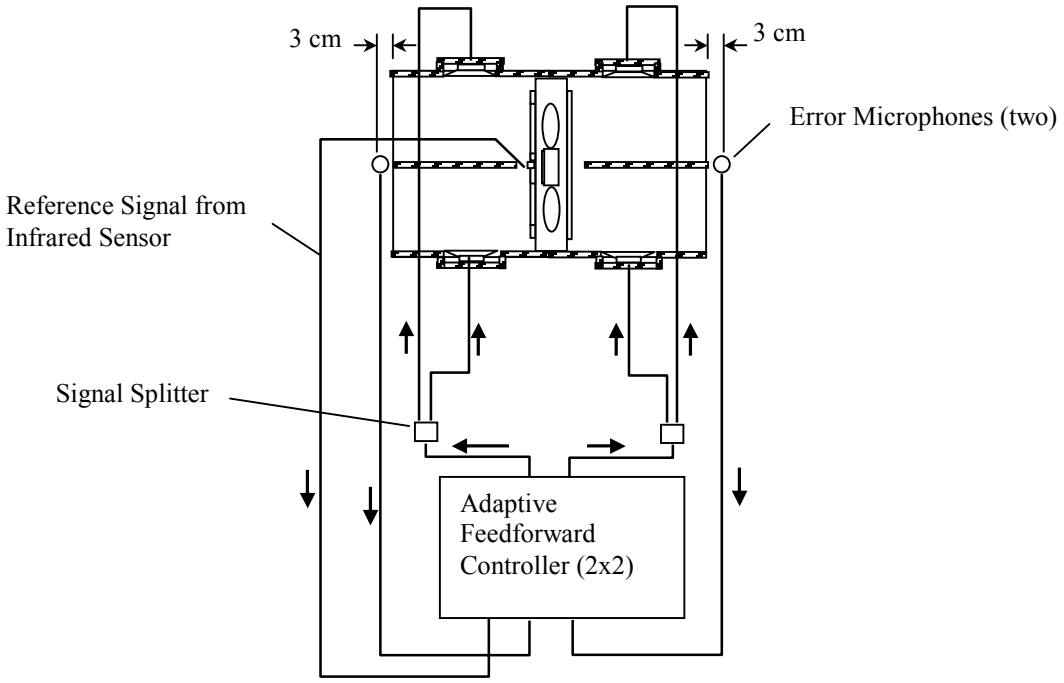

Figure 4.12. 2x2 adaptive feedforward controller

The adaptive feedforward controller was a 2x2 system. The two inputs were taken from the two error microphones positioned just outside of the duct openings at a distance of 3 cm from the duct edge. And the two outputs were used to drive the eight speakers. This was accomplished by driving four speakers on each side of the duct with one control

output. The internal structure of the adaptive feedforward controller is shown in Figure 4.13.

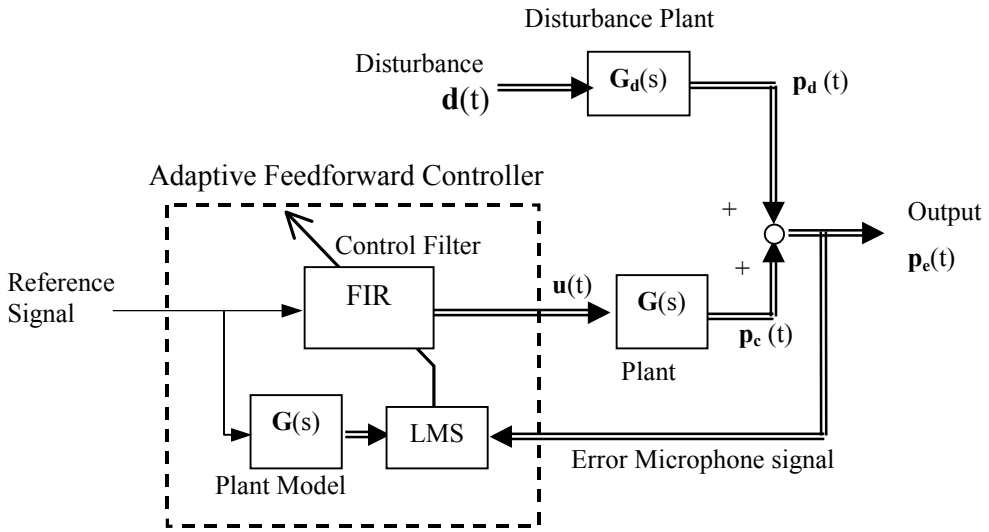

Figure 4.13. Adaptive feedforward controller structure

As shown in Figure 4.13, the control filters were realized by using Finite Impulse Response (FIR) digital filters. And the coefficients of the FIR filters were adjusted adaptively by the Filtered-x LMS (FXLMS) algorithm [21], which is a variant of the common LMS algorithm. The FXLMS algorithm achieves the minimization of the error signals by adjusting the coefficients of the FIR filters based on the reference and the error signals. It is called, "Filtered-x", because the reference signal is filtered through the identified plant model, **G**(s), before fed into the LMS algorithm as indicated in Figure 4.13. The controller based on this algorithm was implemented on a TMS320C30 DSP board installed in a host computer.

The feedforward controller was configured to specifically target the BPF tones. This was achieved by using the reference signal that was correlated only with the BPF tones. Figure 4.14 shows the detail of the reference signal sensor.

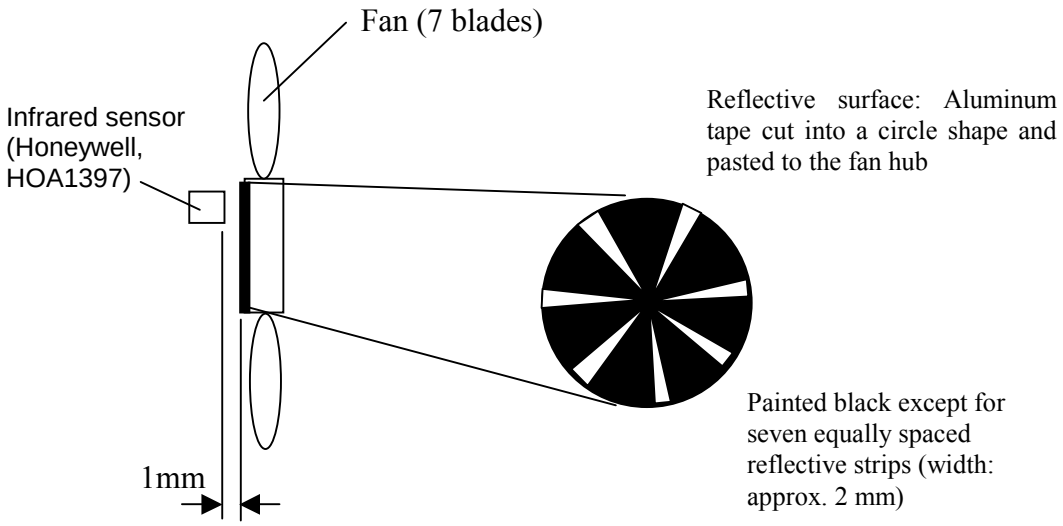

Figure 4.14. Reference signal sensor

As shown in Figure 4.14 an infrared sensor was installed near the fan hub to produce a pulse whenever a reflective strip passed through the sensor's field-of-view. Reflective strips on the fan hub were distributed in such a way that the sensor produced the same number of impulses as the number of the fan blades (seven) for every fan rotation. This resulted in a reference signal that contained the same tonal components as the BPF tones. Figure 4.15 shows the frequency spectrum of this reference signal.

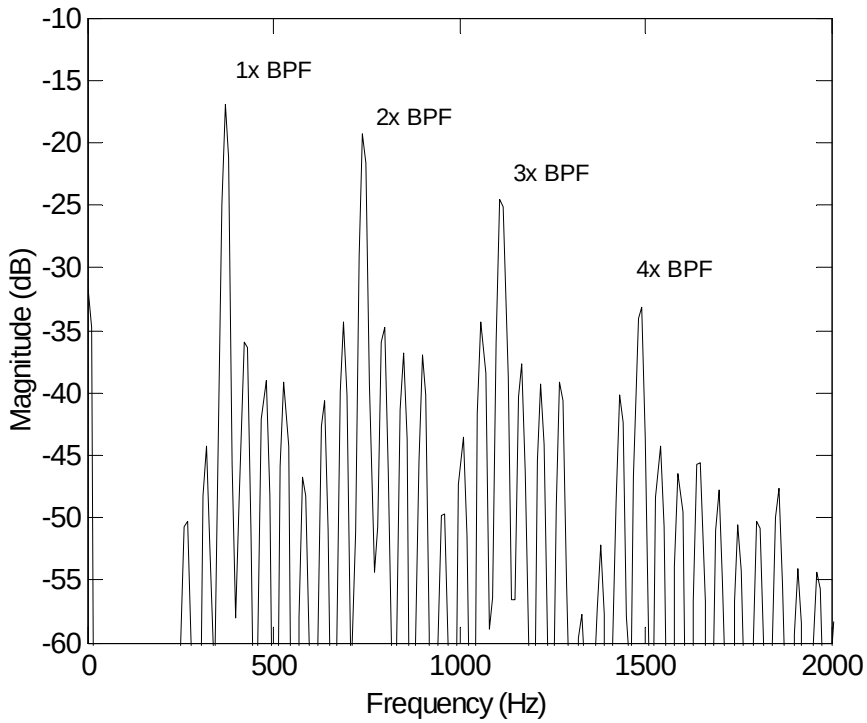

Figure 4.15. Reference signal obtained from the infrared sensor

As shown in Figure 4.15, the reference signal spectrum was dominated by four tonal components at 370, 740, 1110 and 1480 Hz, which corresponded to the frequencies of the first four BPF tones. It should be noted that the fundamental BPF tone frequency of 370 Hz corresponded to the fan rotational speed, 3171 RPM, multiplied by the total number of blades, 7.

The setting of the feedforward controller was as follows. The sampling frequency of the DSP board was set to 6000 Hz. The number of coefficients for the FIR filters in the controller was set to 80. Both the error and the reference signal were conditioned through band-pass filters in order to prevent signal aliasing and also to concentrate the control effort to the frequency range of BPF tones. The filter pass band was set to 315 to 1600 Hz covering the first four BPF tones. Control outputs were also conditioned by low-pass filters with a cut off frequency of 1600 Hz in order to eliminate high frequency

noise generated by digital-to-analog conversion process. Table 4.1 below summarizes the parameter settings of the adaptive feedforward controller.

Table 4.1. Adaptive feedforward controller setting

Parameter	Value
Sampling rate	6000 Hz
Number of FIR filter coefficients (control and plant model filters)	80
Reference signal filtering	Band-pass, 315-1600Hz
Error signal filtering	Band-pass, 315-1600Hz
Control signal filtering	Low-pass, 1600 Hz

Feedback Controller

A feedback control system was designed and implemented for the reduction of the broadband content of the fan noise. Figure 4.16 shows the implemented feedback control system.

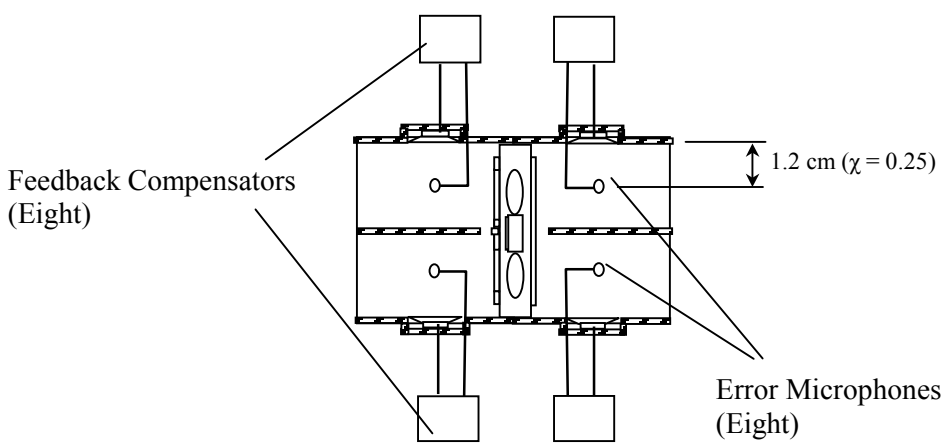

Figure 4.16. 8x8 decentralized feedback controller

The controller was an 8x8 decentralized feedback control system, which consisted of eight SISO feedback control loops formed at the eight microphone-speaker pairs in the duct segments. The controller used a total of eight in-duct error microphones (see Figure 4.2), which were positioned directly in front of the speakers at a distance of 1.2 cm (about 25 % of small duct transverse length, or $\chi = 0.25$).

This decentralized feedback controller was designed by using a classical loop-shaping method based on measured plant frequency responses. The design process was as follows. First, direct-path (e.g. Speaker 1 to Microphone 1) plant frequency responses were measured for all the eight speaker-microphone pairs. Then, a system identification procedure was performed on the average of the eight direct-path frequency responses. Figure 4.17 shows the experimental and the identified plant frequency response. Table 4.2 shows the poles and zeros of the identified direct-path plant model.

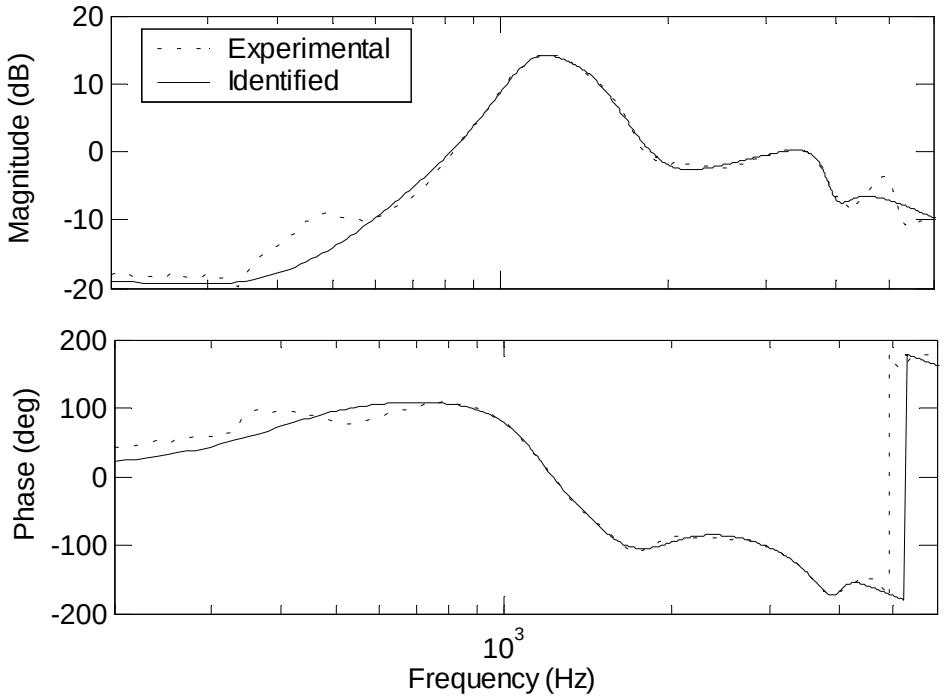

Figure 4.17. Experimental direct-path plant frequency response and identified frequency response

Table 4.2. Poles and zeros of the identified direct-path plant model

Zeros			Poles		
Value	Natural Frequency (Hz)	Damping Ratio	Value	Natural Frequency (Hz)	Damping Ratio
-1.11e3±2.27e3	402	0.44	-1.06e3±7.13e3	1147	0.15
-2.44e3±1.2e4	1944	0.20	-1.71e3±9.19e3	1488	0.18
-1.41e3±2.52e4	4011	0.056	-8.6e3±2.23e4	3807	0.36
7.11e4±1.58e4	11588	-0.98	-2.1e3±2.4e4	3827	0.087

It is observed in Figure 4.17 that there existed a large magnitude peak in the mid-frequency associated with the complex poles identified at 1147 and 1488 Hz. The origin of this behavior became clear when the experimental frequency response was compared against the analytical frequency response obtained by using the analytical model of Chapter 3. Figure 4.18 compares the experimental and the analytical plant frequency response.

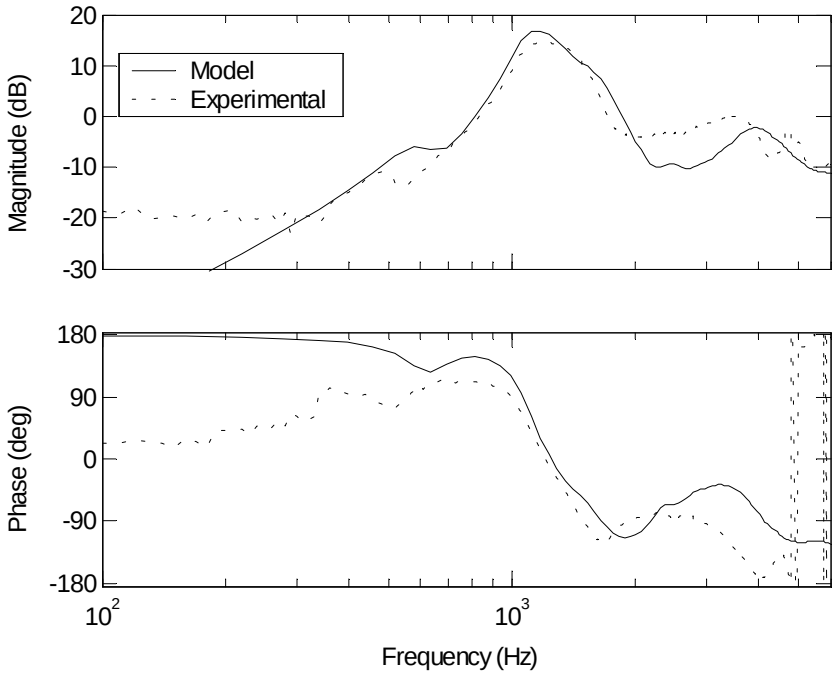

Figure 4.18. Experimental and analytical model plant frequency response (direct path)

It was found that the analytical and the experimental data matched best when the natural frequency and the damping ratio associated with the speaker dynamics were set to1100 Hz and 0.1. This suggested that the identified complex pole at 1146 Hz listed in the table above was originated from the speaker dynamics. It should be recalled that, for the analytical studies in Chapter 3, the speaker natural frequency was determined to be 180 Hz. This shifting in speaker natural frequency was attributed to an increase in the effective "stiffness" of the speaker diaphragm as a result of closing the back of the speakers with relatively small enclosures. However, as it will be demonstrated shortly, the presence of the speaker natural frequency in the mid-frequency range was not necessarily an undesirable feature since it had an effect of concentrating the control effect at the frequency range where the control was needed most. It is also observed in Figure 4.18 that the experimental frequency response exhibited more phase lag than the analytical frequency response. This was already observed earlier in Chapter 3 during the

plant frequency response validation experiment (see Figure 3.33). It is an indication that the actual plant dynamics had more time delay than the analytical counterpart.

Having identified a model of the average direct-path plant transfer function, a compensator transfer function for the individual SISO feedback loops was designed using a classical loop-shaping design. After numerous design iterations to "shape" the associated open-loop transfer function into a desirable form, a compensator transfer function, $g_c(s)$, was obtained:

$$g_c(s) = \frac{s^2 + 1722s + 2.98 \cdot 10^7}{s^2 + 1895s + 1.68 \cdot 10^7} \tag{4.3}$$

Corresponding natural frequency and the damping ratio of poles and zeros were

Complex zero: $\omega_n = 5459$ (868 Hz), $\xi = 0.158$

Complex pole: $\omega_n = 4098$ (652Hz), $\xi = 0.231$

Figure 4.19 shows the frequency response of this compensator. And Figure 4.20 shows the Bode plot of the corresponding open loop response including the compensator dynamics.

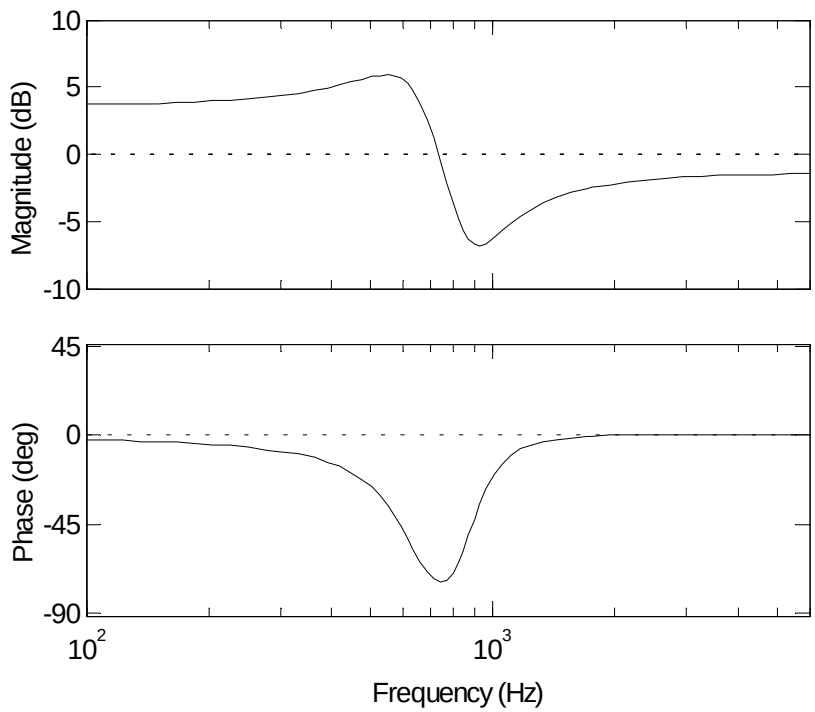

Figure 4.19. Compensator frequency response

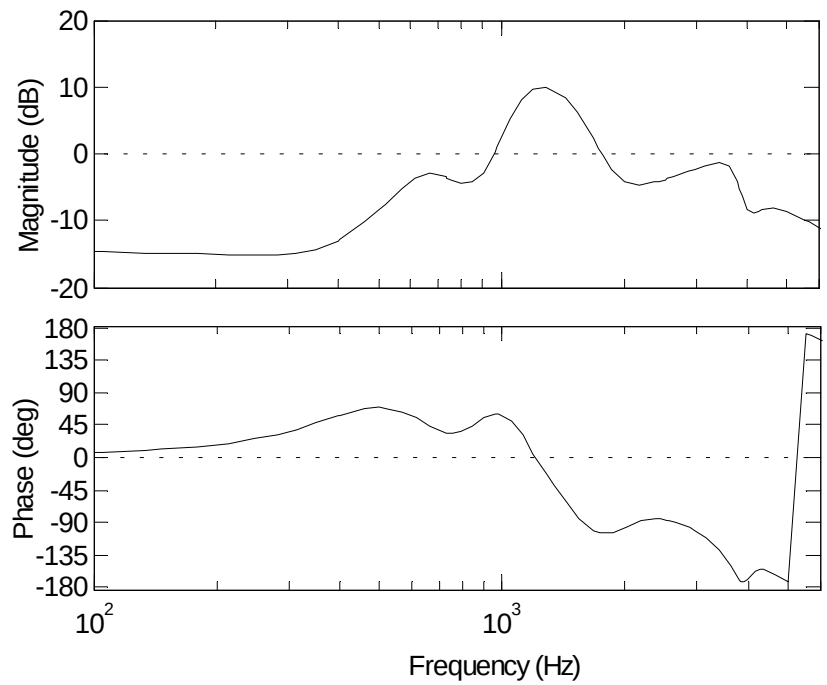

Figure 4.20. Open-loop frequency response including compensator

Figure 4.17 and Figure 4.20 clearly show the effect of the compensator; the excessive phase lead at low frequencies below 1000Hz was reduced and at the same time the magnitude was increased in the low frequency range in order to enhance low frequency performance.

The overall 8x8 decentralized feedback controller, $\mathbf{G_c}(s)$, was obtained by assembling the determined SISO compensator transfer function, $g_c(s)$ as

$$\mathbf{G_c}(s) = \begin{bmatrix} g_c(s) & 0 & \cdots & 0 \\ 0 & g_c(s) & 0 & \vdots \\ \vdots & 0 & \ddots & 0 \\ 0 & \cdots & 0 & g_c(s) \end{bmatrix} \tag{4.4}$$

The noise reduction (i.e. disturbance rejection) performance of this 8x8 decentralized feedback controller was estimated from the 8x8 sensitivity frequency response matrix, $\mathbf{S}(\omega)$. The sensitivity matrix, $\mathbf{S}(\omega)$, is defined as

$$\mathbf{p_e} = \mathbf{S} \cdot \mathbf{p_d} \tag{4.5}$$

where $\mathbf{p_e}$ is the error microphone pressure vector and $\mathbf{p_d}$ is the disturbance (fan noise)vector (see Chapter 2 for a diagram). This matrix, $\mathbf{S}(\omega)$, can be obtained by calculating

$$\mathbf{S} = \left(\mathbf{I} + \mathbf{G_c}\mathbf{G}\right)^{-1} \tag{4.6}$$

where $\mathbf{G}$ is a measured 8x8 plant frequency response matrix, and $\mathbf{G_c}$ is the controller matrix above. The level of noise reduction is expressed by the "gain" of the matrix, **S,**

$$\frac{\|\mathbf{S} \cdot \mathbf{p_d}\|}{\|\mathbf{p_d}\|} = \frac{\|\mathbf{p_e}\|}{\|\mathbf{p_d}\|} \tag{4.7}$$

which is the ratio of the norm of the error microphone pressure vector, $\mathbf{p_e}$, to the norm of the disturbance (fan noise)vector, $\mathbf{p_d}$. This ratio being less than one represents noise reduction, while being more than one represents noise amplification.

It should be noted that the noise reduction level indicated by Equation (4.7) varies with the phase direction of the disturbance vector, $\mathbf{p_d}$. The maximum and the minimum noise reduction levels can be obtained by calculating the maximum and the minimum singular values, σ, of the $\mathbf{S}(\omega)$ matrix:

$$\begin{aligned} max(\sigma(\mathbf{S}(\omega))) &= max(\frac{\|\mathbf{p_e}\|}{\|\mathbf{p_d}\|}) \quad for\ all\ \mathbf{p_d} \\ min(\sigma(\mathbf{S}(\omega))) &= min(\frac{\|\mathbf{p_e}\|}{\|\mathbf{p_d}\|}) \quad for\ all\ \mathbf{p_d} \end{aligned} \tag{4.8}$$

Figure 4.21 shows the singular value plot of the $\mathbf{S}(\omega)$ matrix. The plot indicates the maximum and the minimum singular values of the $\mathbf{S}(\omega)$ matrix (along with intermediate singular values), thereby indicating the possible range of noise reductions for all $\mathbf{p_d}$. Figure 4.21 indicates that the noise reduction would be mainly concentrated in the mid-frequency range of about 800 to 1800 Hz. The stability of the MIMO system can also be evaluated from this plot by observing the maximum level of the high-frequency amplification or the spillover peaks. In Figure 4.21, the maximum of 10 dB of noise amplification is seen at around 3800 Hz, indicating a relatively small stability margin.

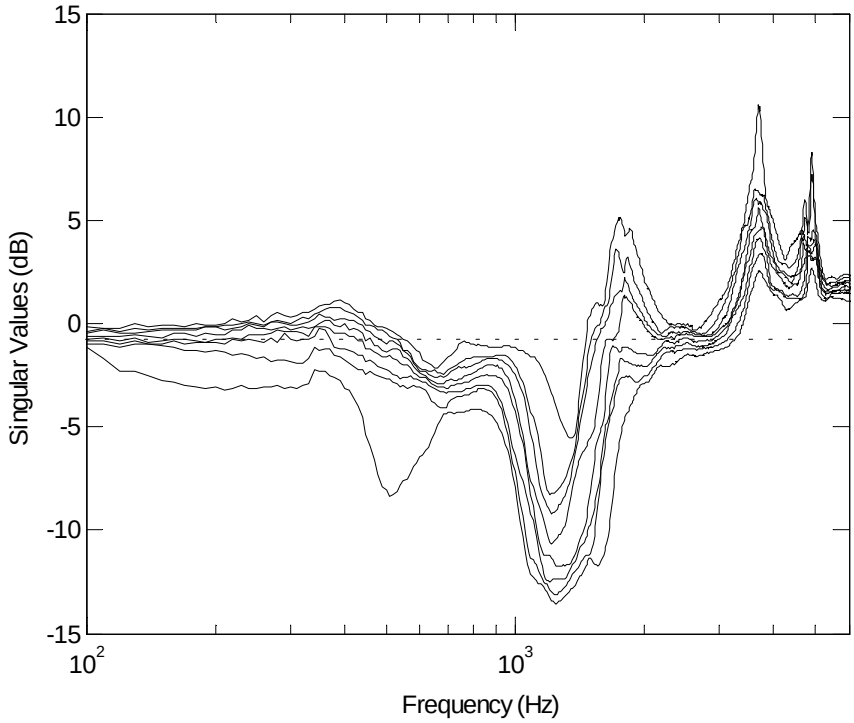

Figure 4.21. Singular values of the sensitivity matrix $\mathbf{S}(\omega)$

In a case where the phase direction of the disturbance vector, $\mathbf{p_d}$, is known, the noise reduction performance can be obtained for that particular disturbance direction. Figure 4.22 shows the noise reduction performance (i.e. Equation (4.7)) obtained for

$$\mathbf{p_d} = [-1 \; -1 \; -1 \; -1 \quad 1 \quad 1 \quad 1]^T \tag{4.9}$$

which represented the disturbances sensed by the four microphones on one side of the duct are 180 degrees out-of-phase with the other four on the other side of the duct. This particular selection of the disturbance vector was based on a finding from the fan noise identification experiment in Chapter 2 that the fan noise was asymmetric and dominantly plane wave in the low frequency range below 1800 Hz (see Figure 2.5). As for the disturbance phase direction above 1800 Hz, Equation (4.9) above was likely not an accurate representation of the actual disturbance. However, the dependency of the noise control performance on the disturbance phase directions was not significant in this frequency range due to weaker cross-couplings between channels, as indicated in Figure

4.21 by the relatively small differences between the maximum and the minimum singular values.

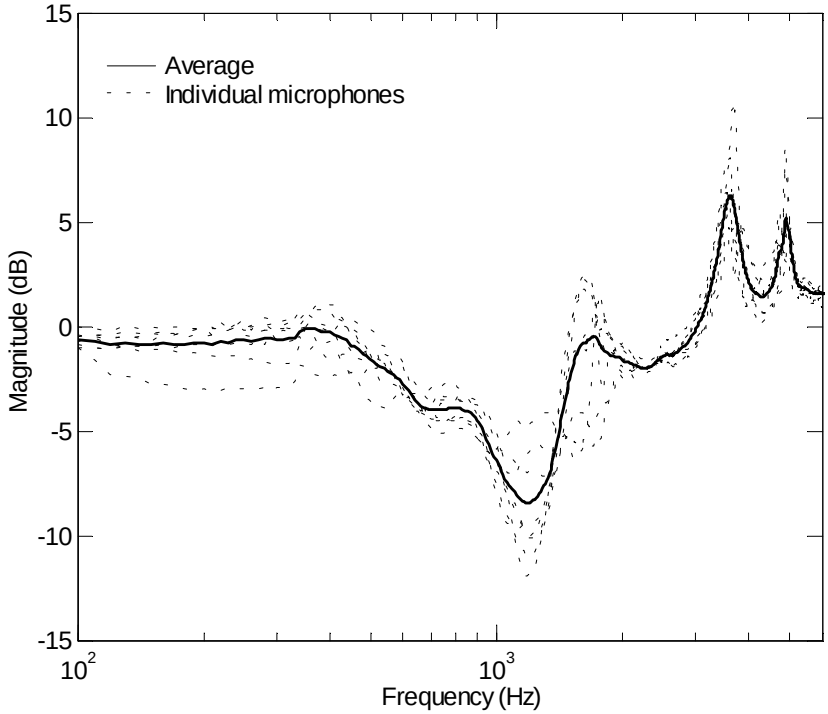

Figure 4.22. Estimated 8x8 decentralized feedback controller performance (local) assuming asymmetric plane wave disturbance.

The estimated performance result in Figure 4.22 indicates that noise reduction effect is mainly obtained in the frequency of about 500 to 1500 Hz with an average peak reduction of 8 dB at 1200 Hz. Small noise reduction of about 2 to 3 dB is also indicated in the frequency range of 1800 to 3000 Hz, followed by spillover peaks at about 3800 and 5000 Hz. By comparing Figure 4.22 with the preceding figures (Figure 4.17 to Figure 4.20), it can be observed that low frequency performance is somewhat improved by the compensator. It is also observed that there is a rather abrupt loss in noise control performance at about 1800 Hz. This is apparently due to the effect of a complex zero

identified at 1944 Hz (see Table 4.2), which is seen as a "dent" in the open-loop frequency response in Figure 4.17.

It is also observed in Figure 4.22 that the indicated noise control performance is rather moderate compared with the level of performance that has been suggested by the theoretical result of Figure 3.45 in Chapter 3. This was to be expected to some extent due to the difference in the way a controller was designed. It should be recalled that, in the simulation studies in Chapter 3, an optimal control design method was used to yield high-order, fully-coupled MIMO controllers, whereas the present decentralized controller was designed by a non-optimal control design approach. However, the most significant performance limiting factor here is suspected to be the additional time delay that was present in the actual experimental plant dynamics as indicated in Figure 4.18. Especially for a present case where a relatively high-frequency control performance is required, time delay could be a significant factor that limits the performance of a feedback system. The reason for the difference in time delay suggested in the analytical and the experimental plant dynamics is unclear at this point. However, one potential reason might have been the use of finite number of duct modes in the analytical model. Another potential reason is that there might have been some unmodeled phenomena in the actual plant dynamics that was not fully included in the analytical model.

The decentralized feedback controller above was implemented with analog components. Detailed descriptions of the controller circuit including the realization of the compensator transfer function are provided in Appendix D.

4.3.2 Active Control Performance Results

The noise control effect of the implemented hybrid active noise control system was experimentally determined. The experimental apparatus presented earlier by Figure 4.3 was used to measure the active control effect on the global fan noise power radiated from the fan duct. In order to clearly identify individual contributions from the feedforward and the feedback control, measurements were taken with respect to the following three cases:

Case 1: Feedforward control is on, while feedback control is off

Case 2: Feedback control is on, while feedforward control is off

Case 3: Both feedforward and feedback control are on (hybrid control)

Case 1: Feedforward control

First, the noise control effect of the 2x2 BPF feedforward control was measured, while the feedback control was kept inactive. Figure 4.23, Figure 4.24 and Figure 4.25 below show the noise control results obtained with the fan static pressure, P_{static}, adjusted to 0.07, 0.09 and 0.11 inH_2O (inches of water column), respectively. Both local and global noise control effect are shown. The local noise control effect is indicated by the change in average error microphone pressure spectrum, while the global noise control effect is indicated by the change in global sound power spectrum. It should be noted that the microphone signals were band-pass filtered from 315 to 1600 Hz, while the global sound power spectrum was A-weighted.

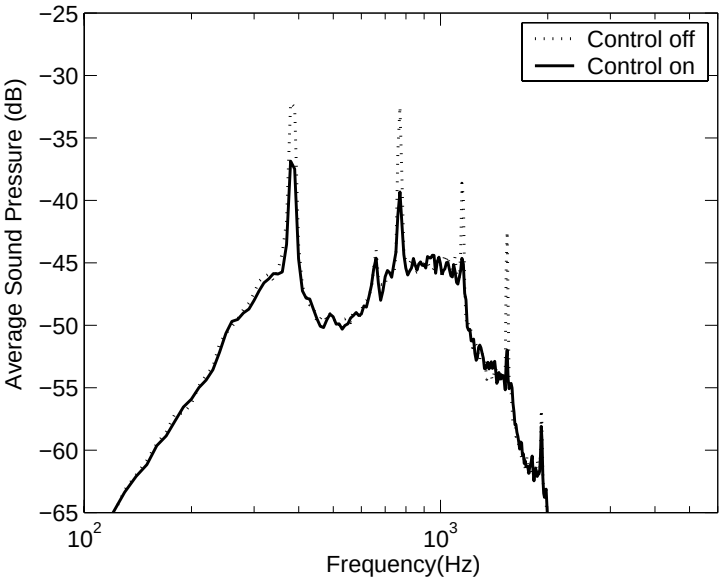

(a) Local

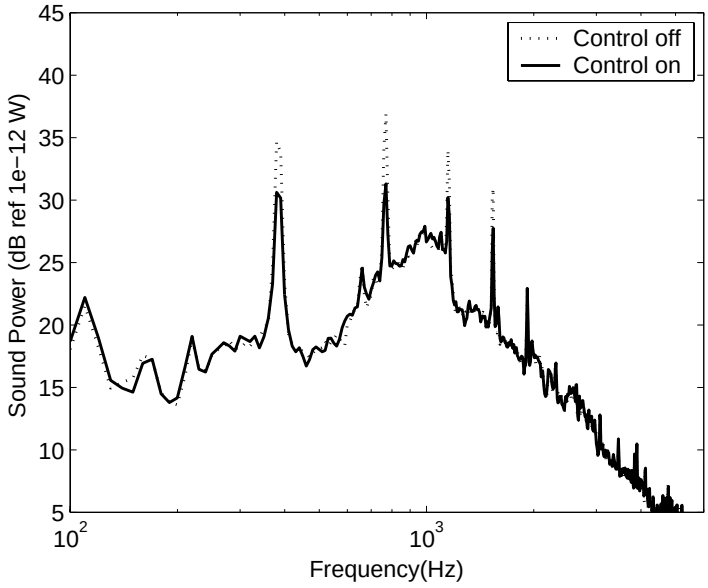

(b) Global

Figure 4.23. BPF feedforward control effect at P_{static} = 0.07 inH_2O: (a) average error microphone sound spectrum, (b) total sound power spectrum (A-weighted)

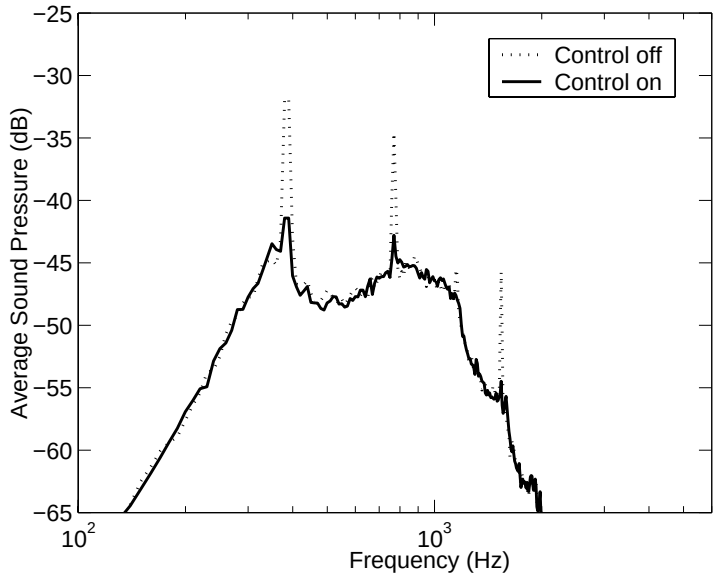

(a) Local

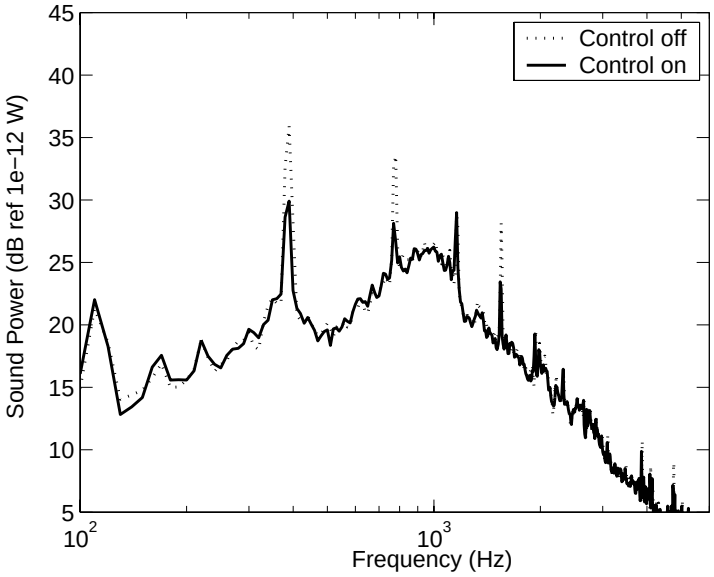

(b) Global

Figure 4.24. BPF feedforward control effect at P_{static} = 0.09 inH_2O: (a) average error microphone sound spectrum, (b) total sound power spectrum (A-weighted)

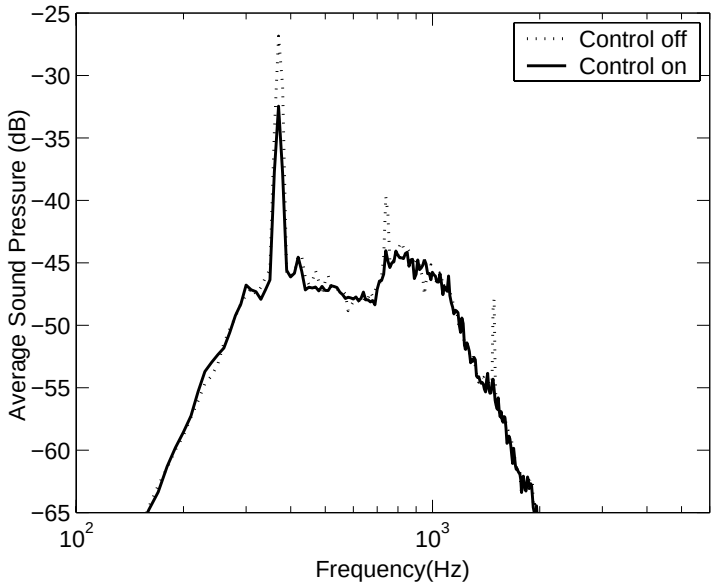

(a) Local

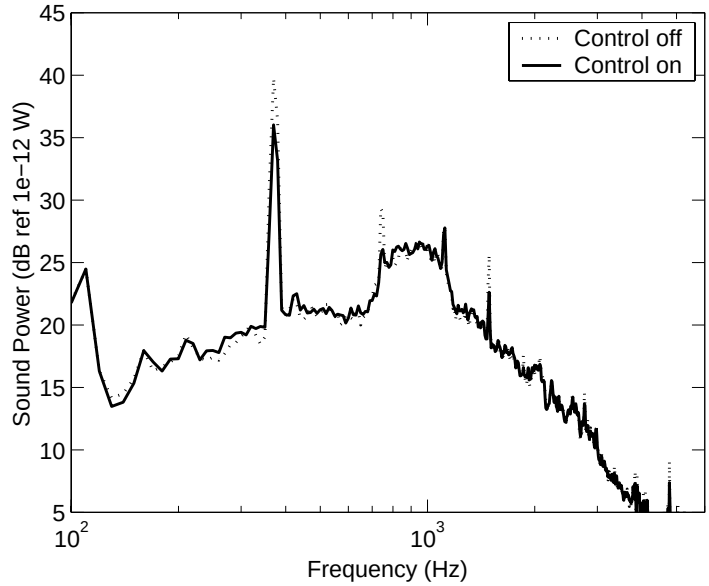

(b) Global

Figure 4.25. BPF feedforward control effect at P_{static} = 0.11 inH_2O: (a) average error microphone sound spectrum, (b) total sound power spectrum (A-weighted)

In Figure 4.23, which represents the lowest fan static pressure case among the three, the first four BPF tones at 370 Hz, 740 Hz, 1110 Hz, and 1480 Hz are clearly visible in the error microphone and the global power spectrum, rising 5 to 12 dB above the broadband noise level. Figure 4.23 (a) shows that the feedforward control has reduced these four BPF tones by about 5 to 10 dB, locally at the error microphones. It is observed that the third and the fourth BPF tones were reduced down to the level of the broadband noise. As for the first two BPF tones, the local reduction performances were not quite as good, indicating some room before the broadband noise limit was reached. The cause for this is not clear at this point. Figure 4.23 (b) shows the corresponding global noise reduction performances where the sound power components associated with the first four BPF tones were reduced by about 4 to 5 dB. It is observed from Figure 4.23 (a) and (b) that the local BPF reduction levels were consistently smaller than the corresponding global noise power reduction levels. This follows the trend observed in the analytical studies in Chapter 3 that the global noise control performances were always less than the associated local noise control performances.

Figure 4.24 and Figure 4.25 show the local and global performances of the feedforward control at increased static pressures, simulating the situations where resistance to airflow is higher due to increase in flow obstructions (e.g. densely-packed electric equipment chassis). One can observe from the figures that the increase in fan static pressure has an effect of reducing the magnitude of the BPF tones relative to the broadband noise. It is observed in Figure 4.24, which represents the medium static pressure case at 0.09 inH_2O, that the third BPF tone was almost disappeared. Consequently, there was no control performance obtained at this BPF tone. The rest of the BPF tones were reduced quite successfully in the error microphone spectrum, down almost to the broadband noise level. Figure 4.24 (b) shows 5 to 6 dB of corresponding global noise power reductions. For the high fan static pressure case (0.11 inH_2O) of Figure 4.25, it is observed that the BPF tones were further reduced, except for the first BPF tone which was somewhat increased in magnitude. In the error microphone spectrum, the second and the fourth BPF tones were only about 5 dB above the broadband noise and the third BPF was not negligible. As a consequence, only moderate local and thus global reductions were obtained at these BPF tones. As for the first BPF

tone, a large BPF tone reduction could have been expected since it was sizably large in magnitude (about 17dB above broadband). However, the actual result obtained was moderate 6 dB in local reduction and 4 dB in global reduction. It is plausible that the inefficiency of the speaker in the low frequency range might have affected the performance. However, this is rather inconclusive since the first BPF was in fact reduced quite successfully in some cases like Figure 4.24 and also in the forthcoming hybrid control performance results in Figure 4.32 and Figure 4.33.

Figure 4.26 shows a summary of the local and the global reduction levels obtained at the first four BPF tones. It clearly shows that the local BPF reduction levels were consistently larger than the corresponding global BPF reduction levels. It also shows that the overall performance of the BPF feedforward control is affected by the level of the fan static pressure, which tends to change the magnitudes of the BPF tones relative to the broadband noise. Figure 4.26 shows a tendency that the BPF feedforward control is most effective when the fan static pressure is low and therefore the BPF tones are relatively prominent against the broadband noise.

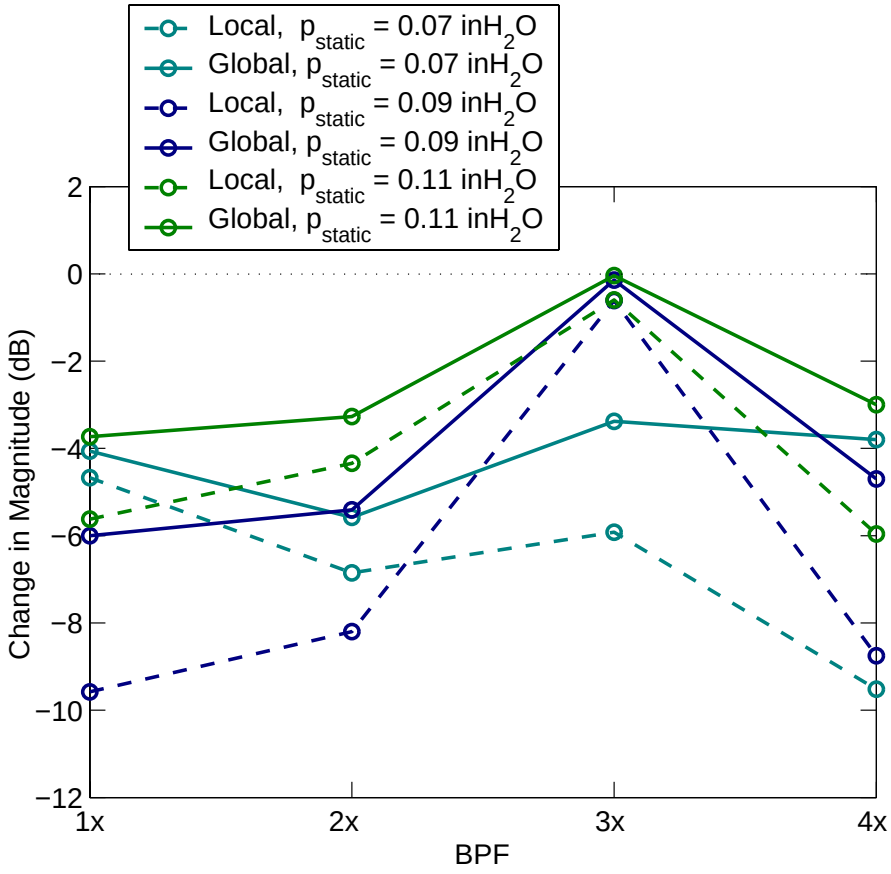

Figure 4.26. BPF feedforward control effect summary

Case 2: Feedback control

Next, the noise reduction effect of the 8x8 decentralized feedback control was measured while the feedforward control was turned off. Figure 4.27, Figure 4.28 and Figure 4.29 show the local and the global noise control effects obtained at P_{static}, = 0.07, 0.09 and 0.11 inH_2O, respectively. It should be noted that the local noise reduction results are shown by the change in the average pressure spectrum from the eight in-duct microphones. Figure 4.30 summarizes the local and the global noise control results in terms of change in spectrum.

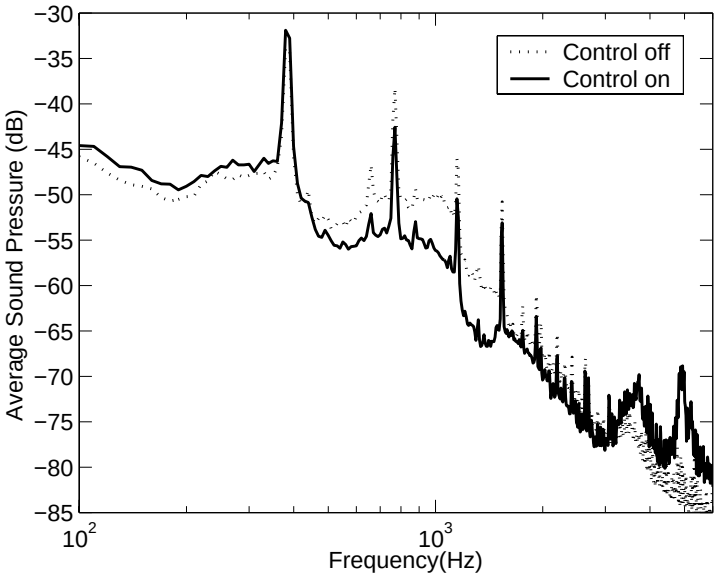

(a)

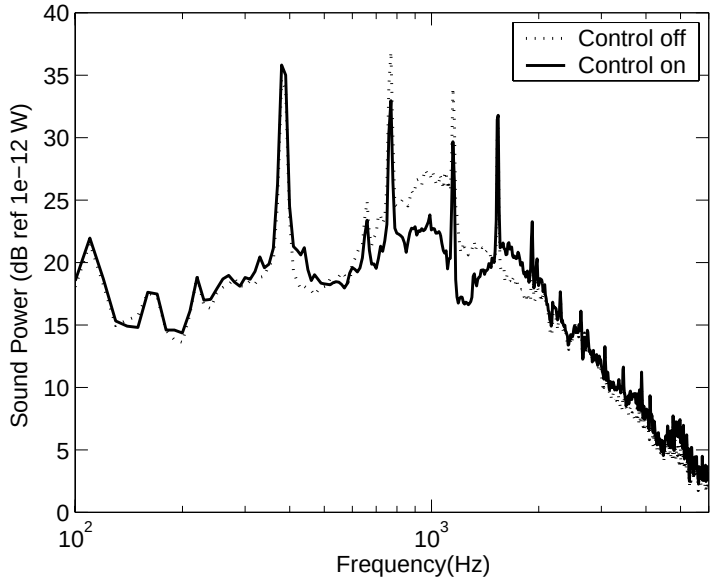

(b)

Figure 4.27. Feedback control effect at P_{static} = 0.07 inH_2O: (a) average error microphone sound spectrum, (b) total sound power spectrum(A-weighted)

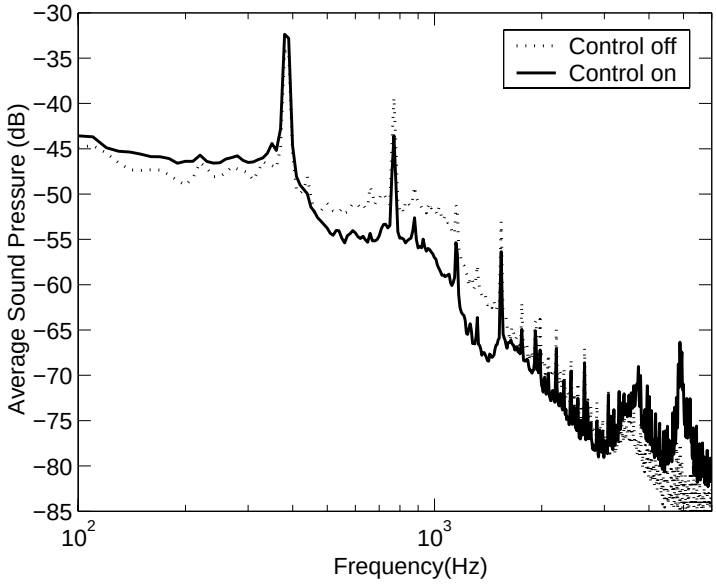

(a)

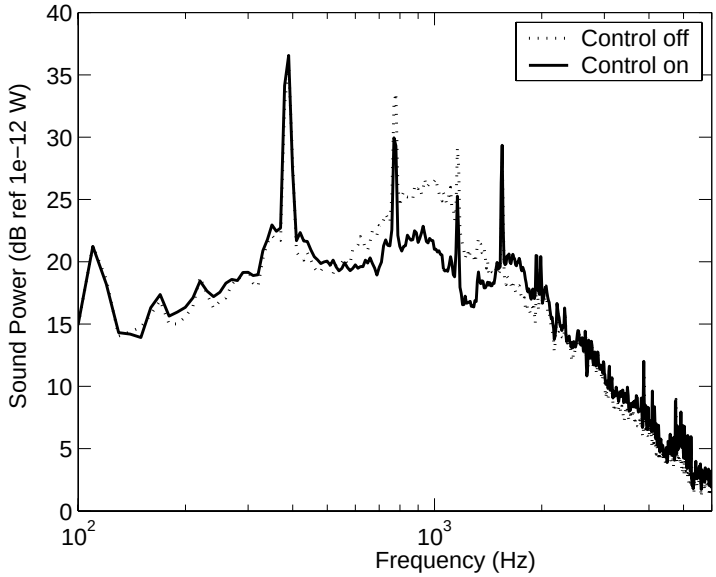

(b)

Figure 4.28. Feedback control effect at P_{static} = 0.09 inH_2 : (a) average error microphone sound spectrum, (b) total sound power spectrum(A-weighted)

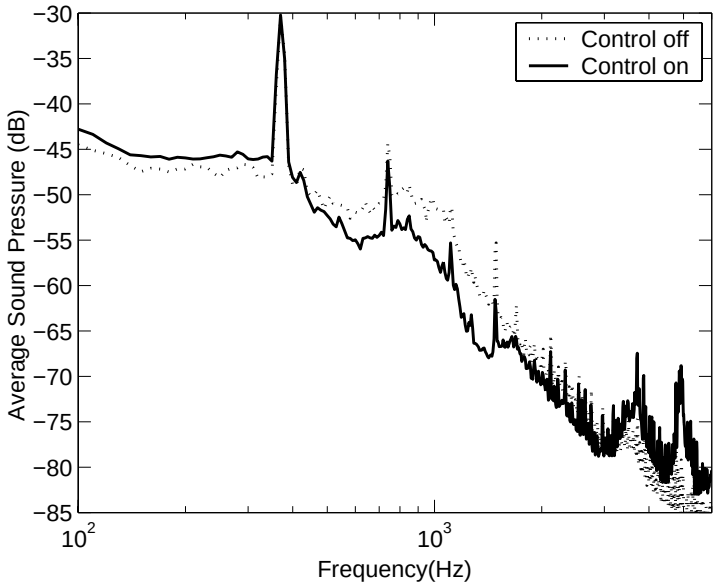

(a)

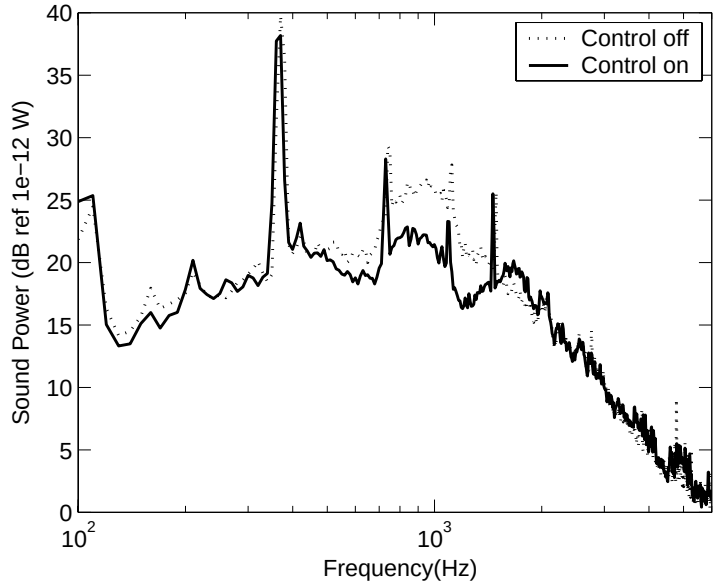

(b)

Figure 4.29. Feedback control effect at P_{static} = 0.11 inH_2O: (a) average error microphone sound spectrum, (b) total sound power spectrum(A-weighted)

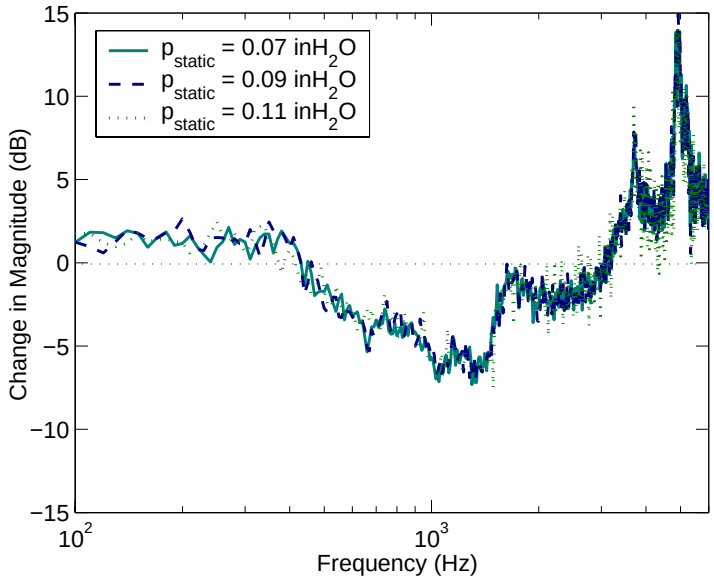

(a) Local effect

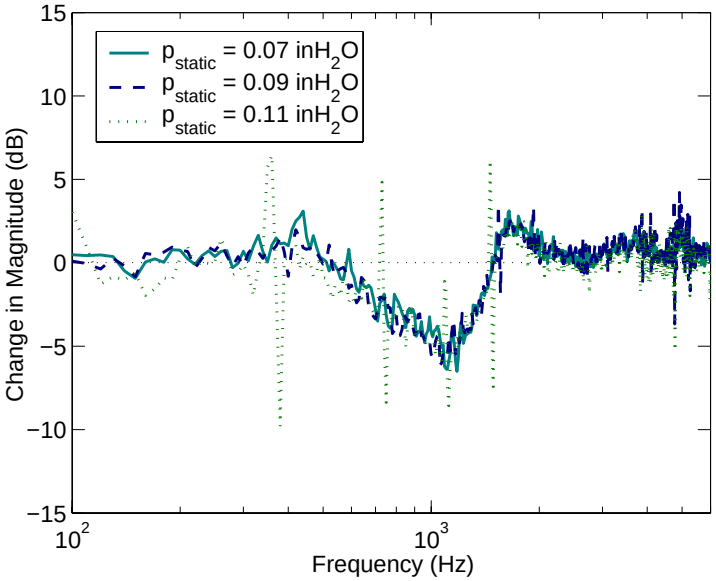

(b) Global effect

Figure 4.30. Feedback control effect summary: (a) change in average error microphone spectrum, (b) change in total sound power spectrum

Figure 4.30 shows that essentially identical performance results were obtained for the three fan static pressure cases. This shows that the performance of the feedback control is not affected by the change in noise spectrum due to the static pressure variation. This is in contrast to the case of the BPF feedforward control, whose performance is affected by the change in the magnitudes of the BPF tones caused by the static pressure variation.

The local noise reduction performance indicated in Figure 4.30 (a) agrees relatively well with the estimated performance in Figure 4.22. The result indirectly reconfirms that the disturbance phase direction of Equation (4.9) was, in fact, appropriate in estimating the noise reduction performance. Figure 4.30 (a) shows that the local noise reduction was obtained in a relatively broad frequency range from 500 to 1700 Hz, with a maximum reduction of 7 dB.

Two spillover peaks are observed in Figure 4.30 (a) at about 3500 Hz and 5000 Hz. Recall that these two spillover peaks were also indicated in the performance estimation in Figure 4.22. It is observed that the magnitudes of the spillover peaks were relatively large. Especially the peak at 5000 Hz was large, indicating that the stability margin was small. This was because the gains of the feedback compensators were adjusted to the maximum levels allowed before causing instability. However, it is observed from the corresponding error microphone spectrum in Figure 4.27 to Figure 4.29 that the impact of these high frequency amplifications was limited since they were in the high frequency range where the noise level was small.

Figure 4.30 (b) shows that the global noise power reduction was obtained in the frequency of 500 to 1500 Hz with a maximum reduction of 6 dB. The corresponding global sound power spectrum in Figure 4.27 to Figure 4.29 show that this corresponds to the reduction of the major broadband noise peak at about 1000 Hz, which was attributed to the axial duct mode resonance. This is consistent with the analytical results in Chapter 3 (see Figure 3.45 and Figure 3.46), where it was found that the feedback control is most effective in reducing the mid-frequency noise peak caused by the undesirable axial duct mode resonance. It is also observed that the global noise control performance corresponded relatively well with the local noise control performance, except in the high frequency range above 1500 Hz. In the high frequency range, especially above 2000 Hz, the active control shows little influence on the global performance; and the total radiate

fan noise power level is seen to be neither significantly reduced or amplified, despite of the change in local noise level. It should be recalled that similar behavior was also observed in Figure 3.45 and Figure 3.46.

Case 3: Hybrid feedforward-feedback control

The BPF feedforward and the feedback control were simultaneously operated and its noise control effect was measured. The configurations and the settings of the feedforward and the feedback controller were unchanged from the individual experiments above. Figure 4.31, Figure 4.32 and Figure 4.33 show the measured noise reduction levels obtained by the hybrid control for fan static pressure of 0.07, 0.09 and 0.11 inH_2O, respectively. Again, both local and global control results are presented. It should be noted that there are two error microphone spectrum plots for the local control result: one corresponding to the out-of-duct microphones for the feedforward control and the other corresponding to the in-duct microphones for the feedback control (see Figure 4.11).

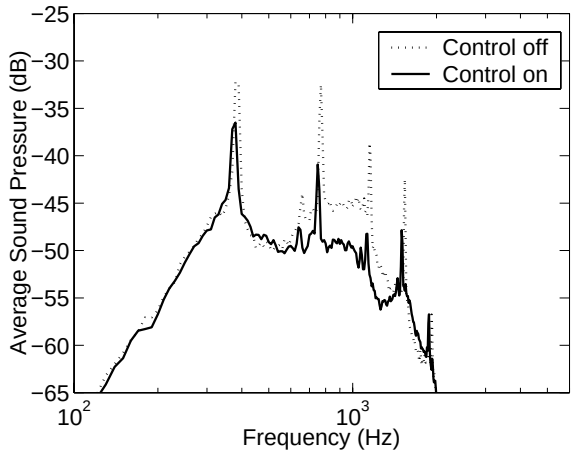

(a) Out-of-duct microphone average

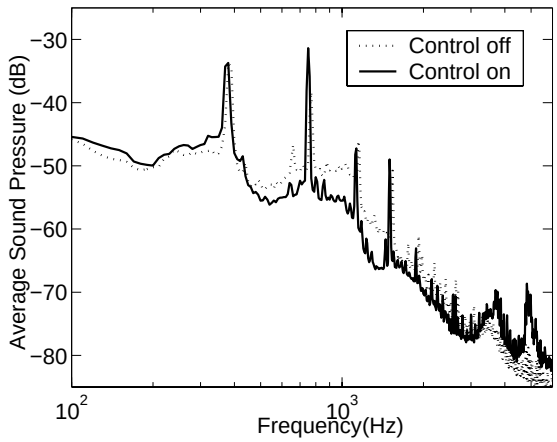

(b) In-duct microphone average

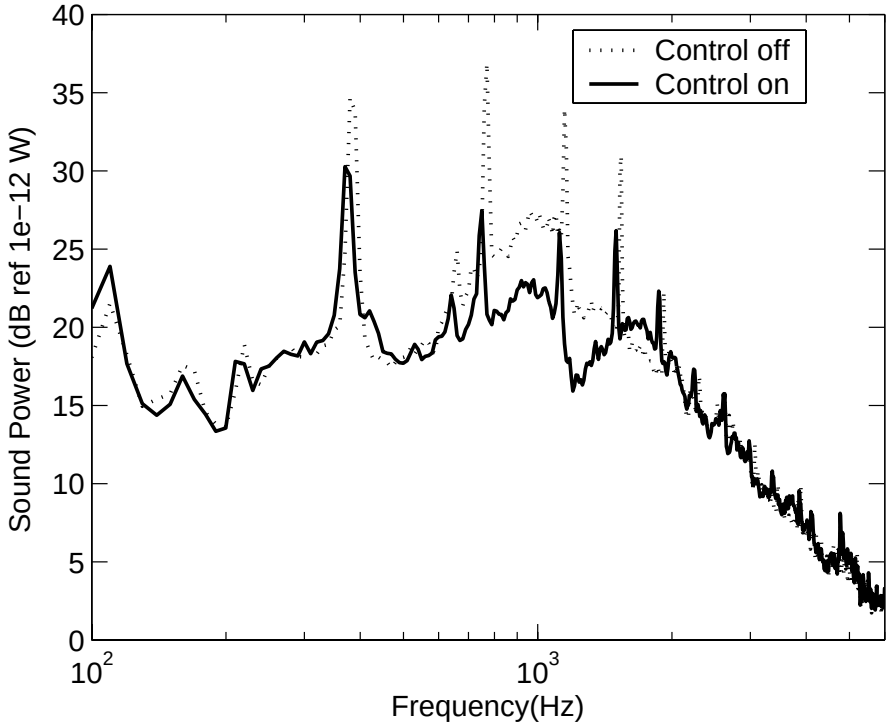

(c) Total sound power

Figure 4.31. Hybrid control effect at P_{static} = 0.07 inH_2O: (a) Out-of-duct microphone average, (b) In-duct microphone average, (c) total sound power spectrum (A-weighted)

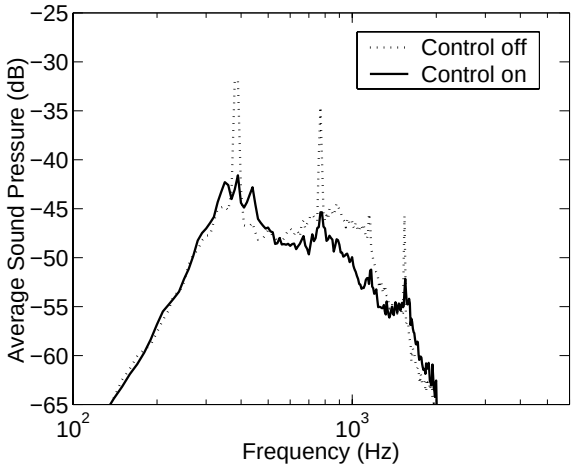

(a) Out-of-duct microphone average

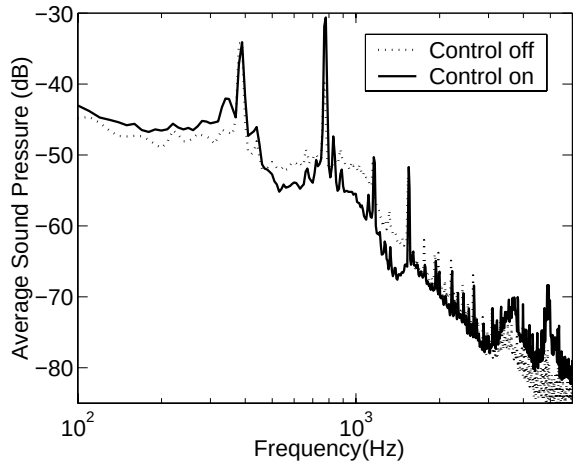

(b) In-duct microphone average

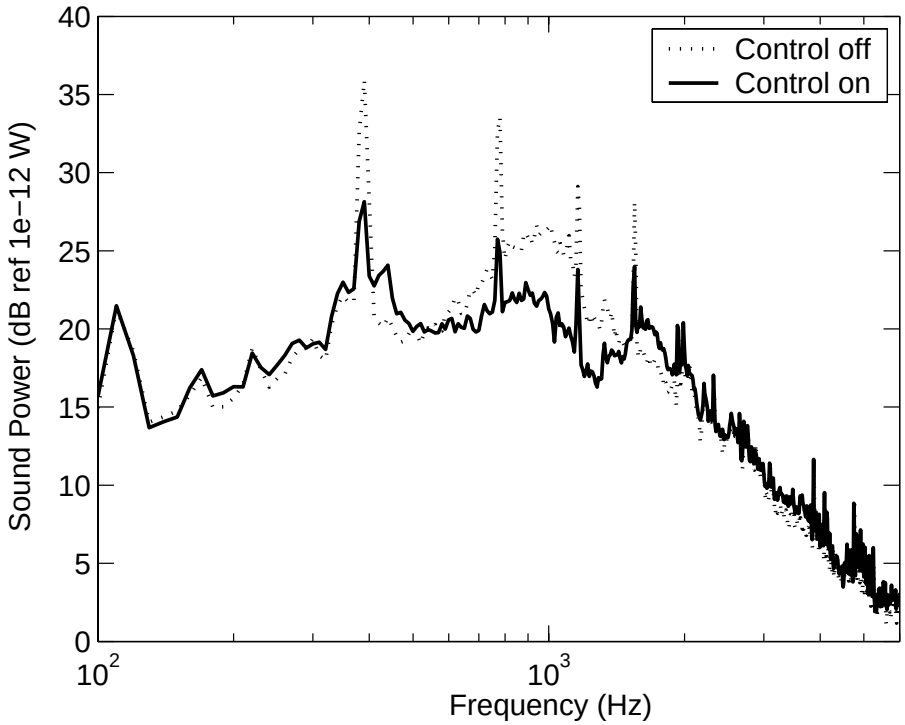

(c) Total sound power

Figure 4.32. Hybrid control effect at P_{static} = 0.09 inH_2O : : (a) Out-of-duct microphone average, (b) In-duct microphone average, (c) total sound power spectrum (A-weighted)

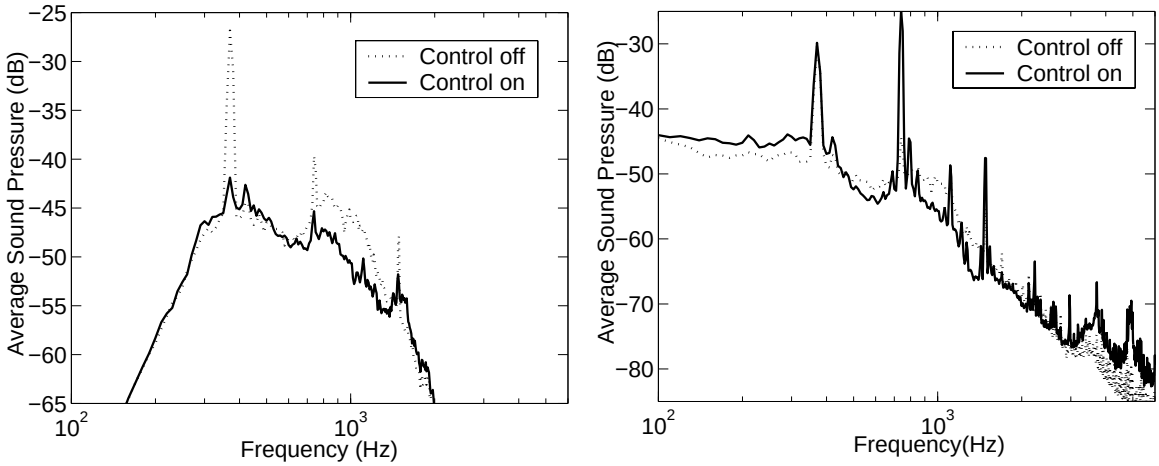

(a) Out-of-duct microphone average (b) In-duct microphone average

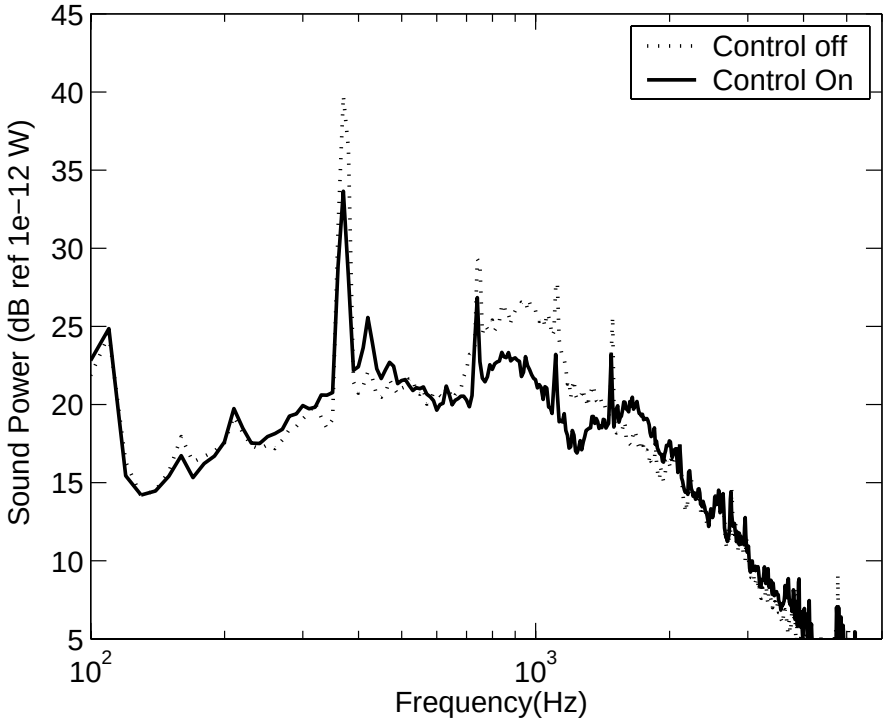

(c) Total sound power

Figure 4.33. Hybrid control effect at P_{static} = 0.11 inH_2O : : (a) Out-of-duct microphone average, (b) In-duct microphone average, (c) total sound power spectrum (A-weighted)

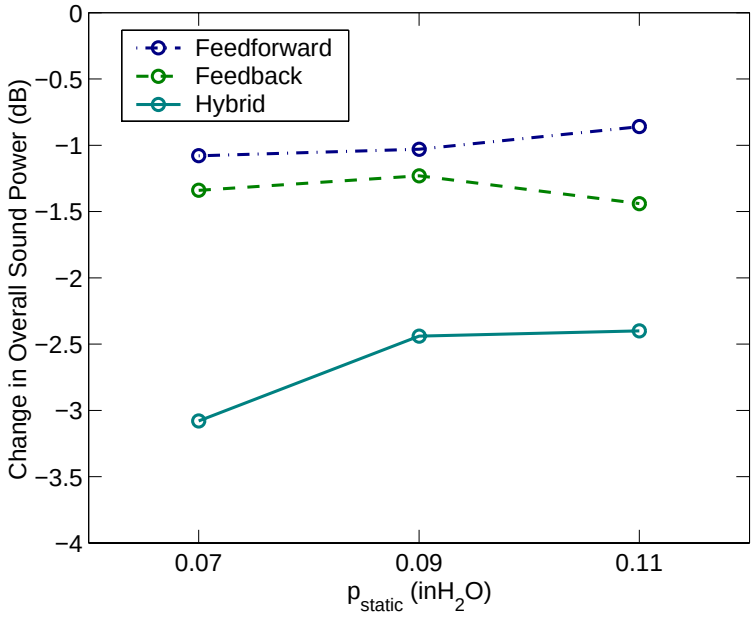

(a) 10-6400 Hz

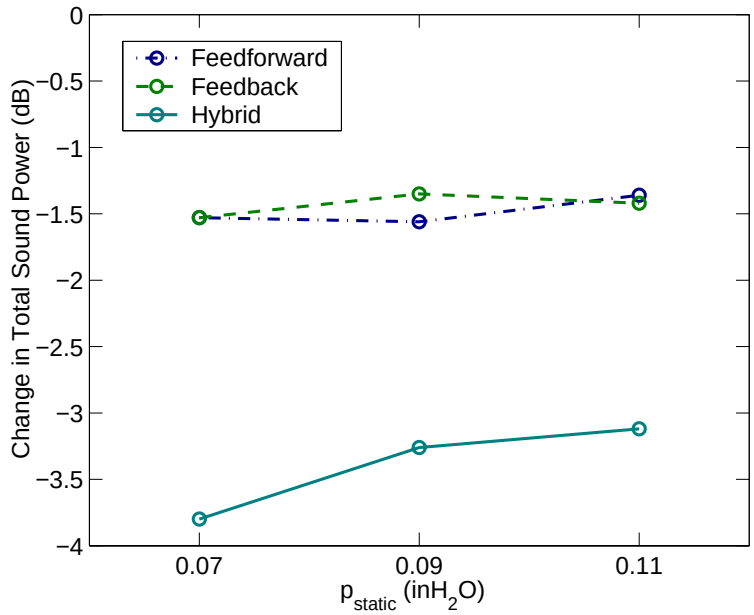

(b) 100-2000 Hz

Figure 4.34. Overall sound power reduction effect of hybrid control: (a) 10 - 6400 Hz, (b) 100 - 2000 Hz

It is observed from the above figures that both BPF tones and the broadband fan noise were reduced by the hybrid control. The first four BPF tones at 370, 740, 1100 and 1480 Hz were reduced mainly by the feedforward control, while the broadband noise in the mid-frequency range of 500 to 1500 Hz was reduced by the feedback control. Comparison of the hybrid control results in Figure 4.31, Figure 4.32 and Figure 4.33 with the results from the individual feedforward and feedback control experiments shows that the noise reduction performance of the hybrid control was essentially the superposition of the individual performances obtained by the BPF feedforward control and the feedback control. It suggests that the BPF feedforward control and the feedback control can be combined and operated simultaneously without adversely affecting each other's performance.

Figure 4.34 summarizes the hybrid control performance results in terms of the overall reduction in radiated fan noise power over the frequency range of 10 to 6400 Hz and 100 to 2000 Hz. Note that the figure includes the overall noise reduction levels calculated for each of the feedforward and the feedback control, based on the individual performance results presented earlier. It is observed from Figure 4.34 (a) that the overall fan noise power was reduced by about 2.5 to 3 dB by the hybrid control. And it is further observed that the amount of total noise reduction obtained by the hybrid control was approximately equal to the summation of the noise reductions obtained solely from the feedforward and the feedback control. Closer observations reveal that the total noise control level obtained by the hybrid control performance slightly exceeded the sum of the individual performances of the feedforward and the feedback control. This is suspected to due to small improvement in the BPF feedforward control performance, which was possibly attributed to the reduction in the duct acoustic resonance by the feedback control. It has been reported in literature [42, 44] that the additional damping provided by the feedback control has a positive effect on the performance of an adaptive feedforward controller in that it reduces the length of the plant impulse response, which results in a faster convergence time for the adaptive algorithm.

4.4 Total Active-Passive Control Effect

This section summarizes the overall global noise reduction effect of the active-passive control fan duct approach. Figure 4.35 and Figure 4.36 show the fan noise power spectrum measured for the following three cases:

1. Fan without duct (baseline)
2. Ducted fan, hybrid active control off
3. Ducted fan, hybrid active control on

The difference in sound power spectrum between the first and the second case above represents the passive control effect of the fan duct, which was previously presented in Section 4.2. The active noise control effect is represented by the difference between the second and the third case. The results were obtained for fan static pressure of 0.09 and 0.11 in H_2O.

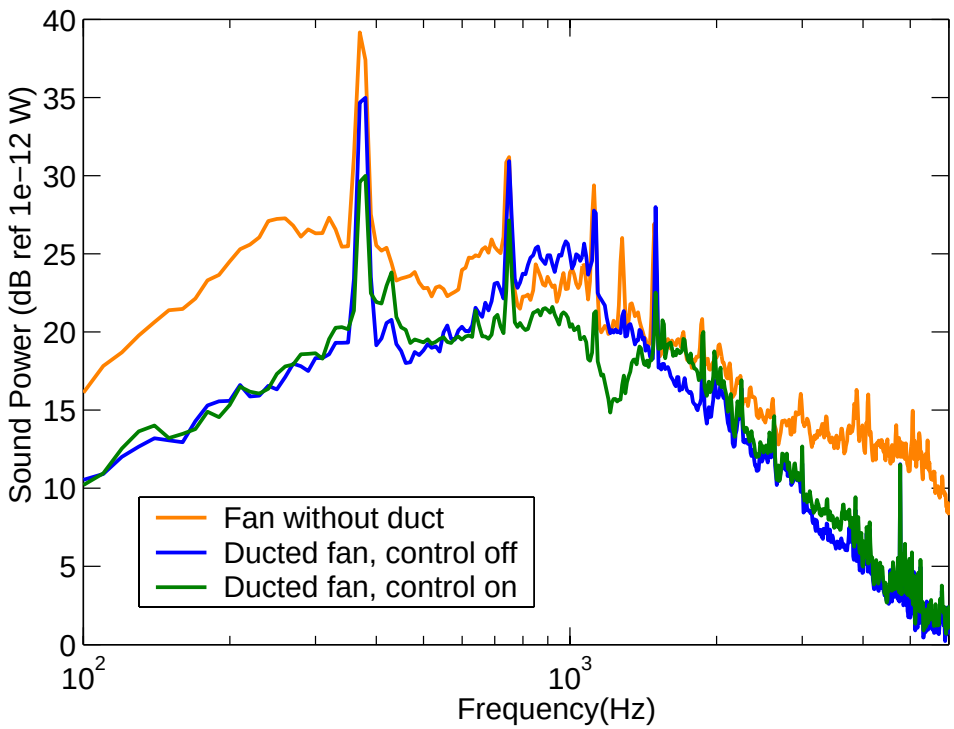

Figure 4.35. Overall active-passive control effect at P_{static} = 0.09 inH_2O

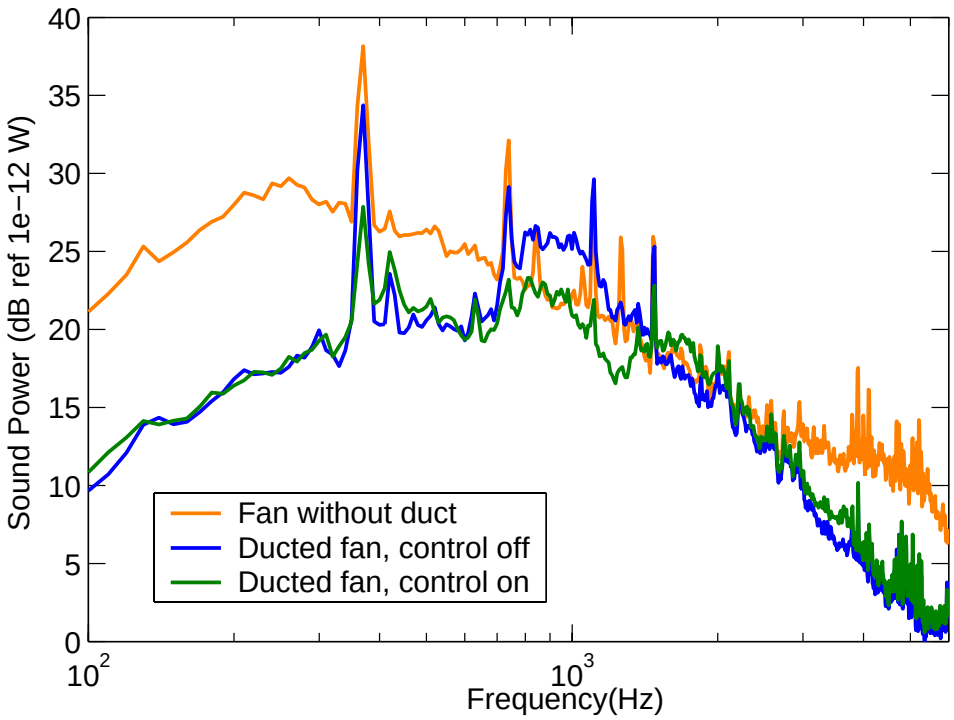

Figure 4.36. Overall active-passive control effect at P_{static} = 0.11 inH_2O

The above results clearly show the overall noise control characteristics of the active-passive control fan duct. The fan duct provided the passive noise reduction in the low frequency range by the duct air-mass loading effect and also in the high frequency range by the sound absorption effect of the passive liner. Then, the hybrid active noise control provided further noise reductions of both BPF tones and the broadband fan noise in the mid frequency range.

Table 4.3 summarizes the total sound power reduction levels obtained by the active-passive control. Two sets of noise reduction values are presented in the table: one for a frequency range of 10-6400 Hz and the other for 100 to 2000 Hz. The former essentially covers most of the fan noise frequency spectrum, while the latter focuses on the range where the fan noise power is most concentrated. It should be also noted that the sound power spectrum is A-weighted.

Table 4.3. Active-passive control effect summary

p_{static} (inH_2O)	0.09		0.11	
Frequency Range (Hz)	10-6400	100-2000	10-6400	100-2000
Passive Control (dB)	-2.60	-2.28	-2.43	-2.27
Active Control (dB)	-2.09	-2.48	-1.96	-2.33
Active-Passive Control (dB)	-4.70	-4.76	-4.39	-4.61

Table 4.3 shows that, for p_{static} = 0.09 inH_2O, the overall fan noise power was reduced by 4.7 dB by the active-passive control in the frequency range of 10-6400 Hz, in which 2.1 dB was from the active control effect, and 2.6 dB was from the passive control effect. Similar performances were also obtained for the case of p_{static} = 0.11 inH_2O. It is observed that, for the frequency range of 100 to 2000 Hz, where the fan noise was most prominent, the impact of the active noise control effect became more significant. It is also observed that passive noise reduction levels are only slightly smaller for 100-2000 Hz than for 10-6400 Hz. This suggests that the passive noise reduction effect was mostly due to the low frequency noise reduction of the duct air-mass loading and not to the high frequency reduction effect of the passive liner.

4.5 Application: PC Case Fan Noise Control

In order to evaluate the practical utility of the current approach, the same active-passive control fan duct was installed into a typical desktop computer chassis to control the noise emitted from a chassis fan. A chassis fan is typically installed at an air outlet or an inlet of a computer chassis for ventilation and it is often a dominant source of noise emitted from a computer. In this experiment, the global noise control performance of the active-passive control fan duct was evaluated by measuring the total radiated fan noise power using a hemispherical array of microphones surrounding the computer chassis in an anechoic chamber. Figure 4.37 and Figure 4.38 illustrate the experimental setup.

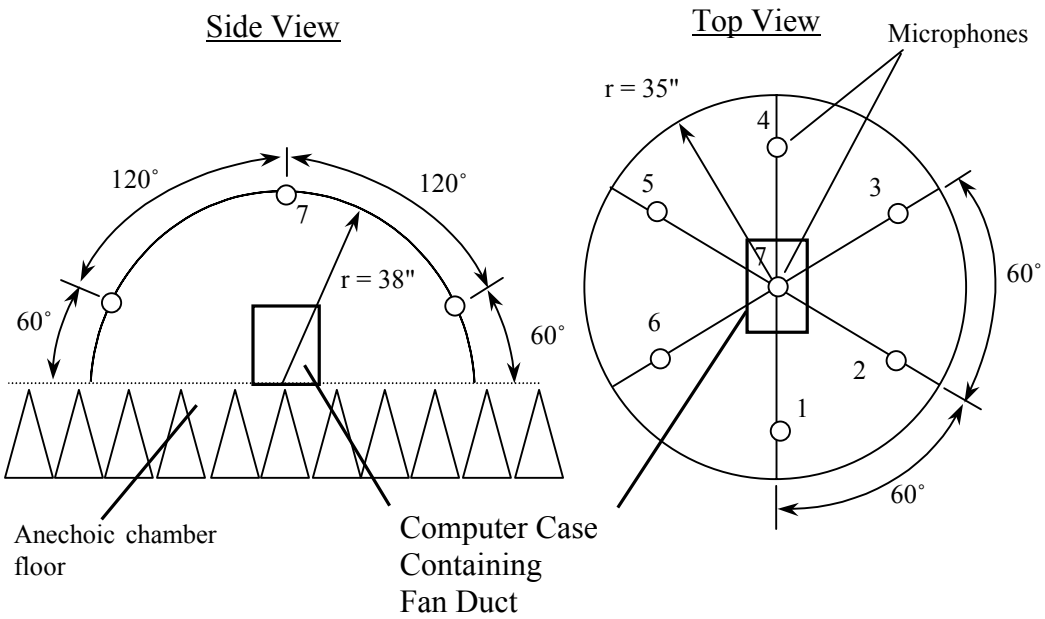

Figure 4.37. Computer fan active-passive noise control experiment setup

(a)

(b)

Figure 4.38. Computer fan active-passive noise control experiment setup images: (a) active-passive control fan duct installation, (b) sound power measurement setup

It should be noted that the hemispherical microphone array shown in the figures above measured only half of the total sound power emitted from the computer chassis. The total

sound power emitted from the computer chassis was estimated by doubling the half sound power with an assumption that the same amount of power is emitted above and below the chassis.

As shown in Figure 4.38, the active-passive control fan duct with a chassis fan contained inside was installed at the back of the computer chassis in such a way that the fan forced the air out from the chassis. It should be noted that the only noise source in this experiment was the chassis fan running within the fan duct. Other noise sources typically present in a computer, such as hard disk drives, optical drives and CPU fans, were not included.

The configuration of the hybrid active noise control system used in this experiment was unchanged from the previous sections. In order to evaluate the overall active-passive noise control performance, the sound power measurements were performed for the following cases:

1. Chassis fan without the fan duct
2. Chassis fan without the fan duct, with the hybrid active noise control turned off
3. Chassis fan without the fan duct, with the hybrid active noise control turned on

Note that the first case represented the original condition of the computer and constituted the baseline noise level. The passive noise control effect was observed from the difference between the first and the second case, while the active noise control effect was observed from the difference between the second and the third case. And, the total active-passive noise control effect of the fan duct was observed from the difference between the first and the third case.

In measuring the total sound power, especially for the first and the second case above, care was taken to maintain a consistent fan static pressure, in this case, of 0.09 inH_2O in order to minimize a potential bias due to the variation in sound power with the fan operating condition. This particular fan static pressure was selected since the impact of the fan ducting to the airflow rate was found to be insignificant at this pressure as shown in Figure 4.7. Fan static pressure was monitored by a differential static pressure transducer, which indicated the level of static pressure developed in the chassis relative to the atmospheric pressure.

Figure 4.39 shows the result of the sound power measurements.

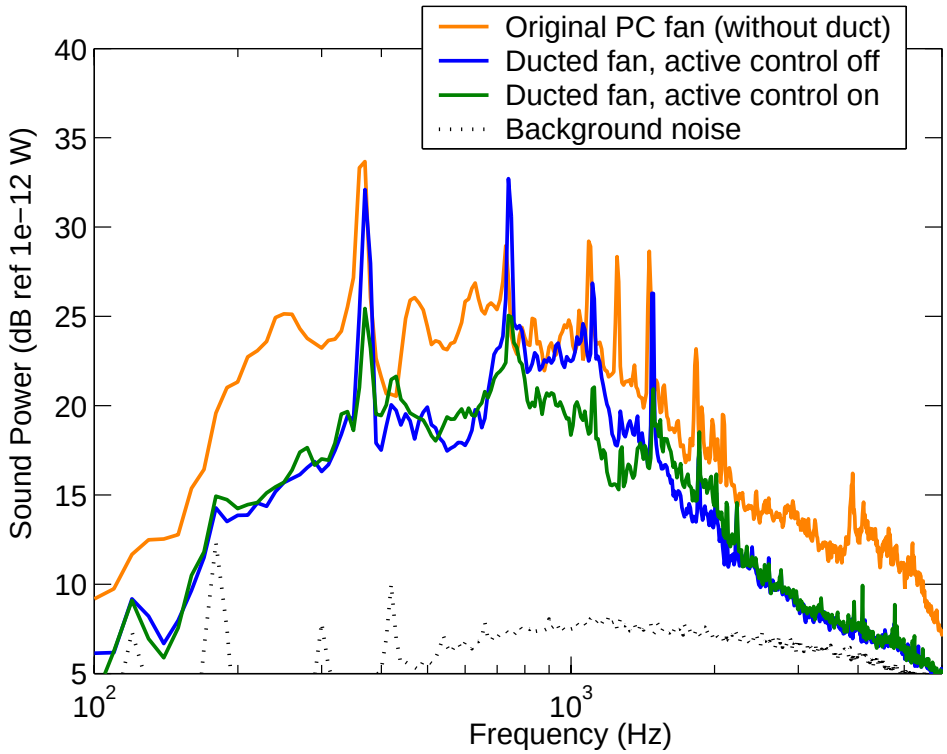

Figure 4.39. Computer fan noise control experiment, active-passive control result

As shown in Figure 4.39, the performance result was very similar to the results obtained earlier by the double-baffle table experiment. Passive noise reductions were obtained by the air-mass loading effect of the fan duct in the low frequency range and also by the sound absorption effect of the passive liner in the high frequency range. Then, the hybrid active noise control system provided further reductions of both BPF tones and the broadband fan noise in the mid frequency range. The result also reconfirms the validity of the double-baffle table setup in the earlier experiments in this Chapter and also the assumption of the infinite-baffled duct in the analytical studies in Chapter 3.

Table 4.4 below summarizes the overall active-passive noise reduction values calculated in the frequency range of 100 to 2000 Hz. (Spectrum components above 2000 Hz were excluded in the calculation due to the presence of high background noise in the measured signal as shown in Figure 4.39). The overall active-passive noise reduction in this frequency range was calculated to be 4.9 dB where 2.6 dB was from the passive effect and 2.3 dB was from the active effect. The noise reduction effect was clearly audible.

Table 4.4. Overall active-passive noise reduction obtained from the computer chassis test

Frequency Range (Hz)	100-2000
Passive Control (dB)	-2.6
Active (Hybrid) Control (dB)	-2.3
Active-Passive Control (dB)	-4.9

4.6 Summary

Experimental investigations were carried out to study the noise control characteristics of the active-passive control fan duct. An experimental fan duct unit utilized the segmented fan duct design introduced in Chapter 3.

Experimental passive noise control results confirmed the trend observed in the analytical studies in the previous chapter. The results showed that, by housing a fan into a lined short duct, global radiated fan noise power can be reduced at both low and high frequency frequencies. The low frequency noise reduction is obtained by the mass-loading effect of the air volume in the duct, while the high frequency noise reduction is obtained by the sound absorption effect of the passive liner. The experimental result also showed the expected control performance degradation in the mid frequency range due to a duct axial resonance effect.

A hybrid feedforward-feedback active noise control system was implemented and its performance was determined. The system was a combination of a feedforward controller designed for BPF noise reduction and a feedback controller for broadband noise reduction. The feedforward controller significantly reduced the global emission of all the major BPF fan tones, whose frequencies were typically at 370 740 1100 and 1480 Hz. It was observed that the feedforward control performance was influenced by the prominence of the BPF tones relative to uncorrelated broadband noise. As a result, feedforward control was found to be more effective for low fan static pressure conditions, in which the relative magnitudes of the BPF tones were larger. In contrast, the performance of the feedback controller was independent of the fan static pressure. The implemented feedback controller significantly reduced the broadband content of fan noise in the frequency range of 500 to 1500 Hz. The main performance-limiting factor for the feedback controller was considered to be the time delay, which was somewhat more than the level predicted by the analytical plant model. The global noise control performance of the hybrid feedforward-feedback controller was observed to be essentially the superposition of the individual performances of the feedforward and the feedback controller.

The total noise control performance of the active-passive fan duct was observed to be in accordance with the trend shown in the analytical studies in Chapter 3. The passive control reduced fan noise at both low and high frequencies. Then, the active control enhanced the overall noise reduction performance by compensating for the undesirable effect of duct axial resonance in the mid frequency range and also further reducing BPF tones. The total reduction in radiated fan noise power was determined, for instance, to be 4.7 dB, in which 2.7 dB was from the passive control and 2.0 dB was from the active control. It should be emphasized that this was obtained without significant degradation of fan airflow performance.

In order to demonstrate the practical utility of the noise control approach, the active-passive noise control fan duct was applied to reduce the global noise emission from a fan installed in an actual PC chassis. The noise control performance result was similar to that obtained by the baffle table setup, thereby validating the experimental and the analytical methodologies of the thesis. The total fan noise power reduction of 4.9 dB was achieved, in which 2.6 dB was from passive control and 2.3 dB was from active control.

Chapter 5

Conclusions and Recommendations

A new active-passive approach for controlling the global noise emission from a small axial fan has been investigated in this thesis. The approach involved the installation of a fan in a compact duct with both passive and active noise control functions. There were two major components to the investigation. The first part of the thesis concentrated on the theoretical investigations into the potential noise control performance of such approach. Then, the second part of the thesis involved the design, implementation and testing of an active-passive noise control fan duct.

In order to obtain analytical models of the proposed fan noise control approach, a general analytical modeling methodology was formulated first. The formulation was based on the approach utilized by Muehleisen who has investigated modal scattering at various duct discontinuities [20]. This modeling method enabled the systematic development of the comprehensive analytical models of the ducts with multiple discontinuities.

By extensively applying the proposed modeling approach, high-fidelity analytical models of the fan ducts were developed. The matrix-based modeling method allowed one to naturally incorporate full modal impedance matrices in the models including cross-mode coupling terms at duct open ends, which have typically been ignored in previous studies on active control of noise in ducts. Then, an axial fan as a noise source was modeled as a distributed force, which was represented as a sum of modal forces. This fan model was validated experimentally by observing the characteristic noise radiation pattern.

Two alternate designs of active-passive fan duct were considered for analytical investigations. The first was a simple, passively-lined, short duct with a 2x2 active control. The second was an internally segmented, passively-lined, short duct with an

8x8 active control. Analytical models for the two cases were validated experimentally by comparing analytical and experimental plant frequency responses. The acoustic loss factors, which represented the effect of foam passive liner, were also estimated from the experimental frequency responses. Then, passive and active noise control performances for these two designs were determined and compared. For active control, both feedforward and feedback control were considered. Attention was paid particularly to the effect of different error microphone positions to the local and the global active noise control performance.

An experimental unit of an active-passive fan duct was designed and implemented. The segmented fan duct design with eight-speaker configuration was adapted. A hybrid feedforward-feedback active control system was designed and implemented. The feedforward control part was designed specifically for the reduction of harmonic BPF tones, while the feedback control part was designed to reduce broadband fan noise content. Passive noise control effect of the fan duct was determined by measuring the difference in global fan noise power with and without the fan duct in an anechoic chamber. Both local and global noise power reduction effect of the active noise control system was determined at several different fan operating conditions. The results were summarized to show the overall passive-active noise reduction performance of the fan duct. Furthermore, the performance of the fan duct was measured in a more realistic setup using an actual personal computer chassis in order to demonstrate the utility of the noise control approach.

Major findings of the thesis are summarized as follows:

- It has been shown both analytically and experimentally that by housing a fan in a short passively-lined duct, the global fan noise emission can be reduced by two distinct mechanisms. The mass-loading effect of the bulk air volume in the duct provided noise reductions at low frequencies, while the passive liner provided the reduction of high frequency noise. It has been shown that these noise attenuation effects are also accompanied by an undesirable duct axial resonance in the mid-frequency range, which negatively impacts the overall passive control performance.

- Analytical and experimental investigations have shown that the global noise control performance of a compact, passively-lined fan duct can be enhanced further by incorporating an active noise control. It was found that the active control can further reduce the global fan noise emission in the low-to-mid frequency range. Active control is shown to be particularly effective in compensating for the undesirable mid-frequency duct resonance, thereby enhancing the overall noise reduction effect of the fan duct.

- Analytical results have shown that global noise control potential of the segmented fan duct with an 8x8x control is significantly higher than that of the non-segmented fan duct with a 2x2 control with respect to both control bandwidth and attenuation depth. The increase in control bandwidth is attributed to the shifting of the first cross duct mode cut-on to a higher frequency. The segmented duct with an 8x8 control configuration was observed to be beneficial for both feedforward and feedback control.

- It was shown experimentally that both harmonic and broadband content of global fan noise radiation can be reduced simultaneously by using a hybrid feedforward/feedback control. The feedforward control part was effective in reducing global fan noise power associated with the first four BPF tones, while the feedback control part was effective in reducing the broadband global nose radiation in the frequencies starting from 500 to 1500 Hz. While the performance of the feedback control part was not affected by the variations in the fan operating condition, the BPF feedforward control part did change significantly due to change in the relative prominence of BPF tones against broadband noise floor. It was observed that the BPF feedforward control was more beneficial when the static pressure across the fan was relatively low and consequently BPF tones were more prominent.

- The total global active-passive noise control effect of the implemented active-passive fan duct was measured to be 4.7 dB in which 2.7 dB was from passive control and 2.0 dB was from active control. This was achieved without significant degradations of the airflow performance of the fan. Similar global noise control performance results were obtained also in a realistic experimental setup using an actual PC chassis, thereby demonstrated the robustness and the utility of the current noise control approach.

The followings are recommended for future investigations.

- Regarding the analytical modeling of the fan duct, the followings may be considered.
  - Consider the effect of reactive impedance of the passive liner
  - Introduce the frequency-dependent acoustic loss factor for the passive liner
  - Use of non-uniform modal force terms for the fan source
  - Include the noises emitted from the fan exhaust vortices

- Further explorations may be carried out in order to optimize the design of the active-passive noise control fan duct, possibly with respect to the geometry of the duct and/or configurations of the active control systems.

- With respect to the active noise control experiments, the broadband feedback noise control performance may further be improved, if the time delay can be reduced to the level indicated by the analytical model, which predicted better feedback control performances.

- The use of novel actuators may be considered in order to replace the conventional electromagnetic speakers. Actuators using piezoelectric films or electro-active polymers may be considered.

References

[1] Quinlan, D.A. (1997). Future trend in acoustic noise emission for telecommunications and information technology. In *Proceedings of Noise-Con 97*. Institute of Noise Control Engineering, 65-70.

[2] Maling, G.C., Jr. (1994). Historical developments in the control of noise generated by small air-moving devices. *Noise Control Engineering Journal*. 42(5), 159-169.

[3] Quinlan, D.A. (1992). Application of active control to axial flow fans. *Noise Control Engineering Journal*. 39(3), 95-101.

[4] Lauchle, G.C., MacGillivray, J.R. and Swanson, D.C. (1997). Active control of axial flow fan noise. *Journal of Acoustical Society of America*. 101(1), 341-349.

[5] Gee, K.L. and Sommerfeldt, S.D. (2002). Multi-channel active control of axial cooling fan noise. In *Proceedings of Inter-Noise 2002*. Institute of Noise Control Engineering.

[6] Berry, A., Gerard, A. and Masson, P. (2003). Active control of multi-harmonic noise of engine cooling fan. In *Proceedings of Noise-Con 2003*. Institute of Noise Control Engineering.

[7] Watanabe, M., Takano, Y., Koodu, T., Terasaka, H. and Ise, S. (2002). Active noise control of jet fan. In *Proceedings of Inter-Noise 2002*. Institute of Noise Control Engineering.

[8] Wu, J.D. and Bai, M.R. (2001). Application of feedforward adaptive active-noise control for reducing blade passing noise in centrifugal fans. *Journal of Sound and Vibration*. 239(5), 1051-1062.

[9] Koopman, G.H., Neise, W. and Chen, W. (1988). Active noise control to reduce the blade tone noise of centrifugal fans. Journal of vibration, acoustics, stress, and reliability in design. 110, 377-383.

[10] Thomas, R.H., Burdisso, R.A., Fuller, C.R. and O'Brien, W.F. (1993). Preliminary experiments on active control of fan noise from a turbofan engine. *Journal of Sound and Vibration*. 161(3), 532-537.

[11] O'Brien, Jr., R.T., Watkins, J.M., Piper, G.E., Baumann, D.C. (2000). H_∞ active noise control of fan noise in an acoustic duct. In *Proceedings of the American Control Conference*. 3028-3032.

[12] Minogue, P., Rankin, N. and Ryan, J. (1999). Short duct server fan noise cancellation. In *Proceedings of Active '99*. 539-550.

[13] Doak, P.E. (1973). Excitation, transmission and radiation of sound from source distributions in hard-walled ducts of finite length (I): the effects of duct corss-section geometry and source distribution space-time pattern. *Journal of Sound and Vibration*. 31(1), 1-72.

[14] Doak, P.E. (1973). Excitation, transmission and radiation of sound from source distributions in hard-walled ducts of finite length (II): the effects of duct length. *Journal of Sound and Vibration*. 31(2), 137-174.

[15] Wang, K.S. and Tszeng, T.C. (1984). Propagation and radiation of sound in a finite length duct. *Journal of Sound and Vibration*. 93(1), 57-79.

[16] Osborne, W.C. (1976). Higher mode propagation of sound in short curved bends of rectangular cross-section. *Journal of Sound and Vibration*. 45(1), 39-52.

[17] Redmore, T.L. and Mulholland, K.A. (1982). The application of mode coupling theory to the transmission of sound in the side branch of a rectangular duct system. *Journal of Sound and Vibration*. 85(3), 323-331.

[18] Muehleisen, R.T. and Swanson, D.C. (2002). Modal coupling in acoustic waveguides: planer discontinuities. *Applied Acoustics*, 63, 1375-1392.

[19] Muehleisen, R.T. (1996). Reflection, radiation and coupling of higher order modes at discontinuities in finite length rigid walled rectangular ducts. PhD thesis. Pennsylvania State University, University Park, PA.

[20] Nelson, P.A. and Elliott, S. J. (1992). *Active Control of* Sound. Academic Press, London.

[21] Trinder, M.C.J. and Nelson, P.A. (1983). Active Noise Control in Finite Length Ducts. *Journal of Sound and Vibration*. 89(1), 95-105.

[22] Stell, J.D., Bernhard, R.J. (1993). Active control of sound in acoustic waveguides, part I: Theory. *Journal of Sound and Vibration*. 173(2), 179-196.

[23] Stell, J.D., Bernhard, R.J. (1993). Active control of sound in acoustic waveguides, part II: Theory. *Journal of Sound and Vibration*. 173(2), 197-215.

[24] Zander, A.C., Hansen, C.H. (1992). Active control of higher order acoustic modes in ducts. *Journal of the Acoustical Society of America*, 92, 244-257.

[25] Zander, A.C., Hansen, C.H. (1993). A comparison of error sensor strategies for the active control of duct noise. *Journal of the Acoustical Society of America*, 94, 841-848.

[26] Laugesen, S. (1996). Active control of multi-modal propagation of tonal noise ducts. *Journal of Sound and Vibration*. 195(1), 33-56.

[27] Kim, I. and Kim, K. (1994). Active control cross mode waves in rectangular ducts. *Mechanical Systems and Signal Processing*. 8(1), 93-107.

[28] Joseph, P., Nelson P.A. and Fisher, M.J. (1995). Active control of harmonic sound radiated from finite length flow ducts. In *Proceedings of Active '95*. 451-462.

[29] Risi, J.D. and Burdisso, R.A. (1994). Analytical investigation of adaptive control of inlet noise from turbofan engines, In *Proceedings of Noise-Con '94*. 395-402.

[30] Burdisso, R.A., Fuller, C.R., Glegg, S.S. (1995). Analytical study of active control of narrow-band turbofan inlet noise. In *Proceedings of the 16th AIAA Aeroacoustics Conference*. 231-238.

[31] Hutcheson, F.V. (1999). Advanced modeling of active control of fan noise for ultra high bypass turbofan engines. PhD thesis. Virginia Polytechnic Institute and State University, Blacksburg, VA.

[32] Lueg, P. (1936). Process of silencing sound oscillations. US Patent no. 2043416.

[33] Olsen, H.L. and May, E.G. (1953). Electronic sound absorber. *Journal of the Acoustical Society of America*. 25(6), 1130-1136.

[34] Kido, K. (1975). Reduction of noise by use of additional sound sources. In *Proceedings of Inter-Noise '75*. 231-238.

[35] Chaplin, G.B.B. and Smith, R.A. (1976). Active methods of canceling repetitive vibrations. U.K. Patent 19717/76.

[36] Hong, W.K.W., Eghtesadi, Kh. and Leventhall, H.G. (1987). The tight-coupled monopole (TCM) and tight-coupled tandem (TCT) attenuators: theoretical aspects and experimental attenuation in an air duct. *Journal of the Acoustical Society of America*. 81(2), 376-388.

[37] Clark, R.L. and Frampton, K.D. (1996). Phase compensation for feedback control of enclosed sound field. *Journal of Sound and Vibration*. 195(5), 701-718.

[38] Hong, J.H., Akers, J.C., Ravinder, V., Lee, M., Sparks, A.G. Washabaugh, P.D. and Bernstein, D.S. (1996). Modeling, identification, and feedback control of noise in an acoustic duct. *IEEE Transactions on Control Systems Technology*. 4(3), 283-291.

[39] Saunders, W.R., Robertshaw, H.H. and Burdisso, R.A. (1993). An evaluation of feedback, adaptive feedforward and hybrid controller designs for active structural control of a lightly-damped structure. In *Proceedings of Recent Advances in Active Control of Sound and Vibration*, 339-354.

[40] Carme, C., Derrien, D. and De Man, P. (1997). A new generation of ANC headsets. In *Proceedings of Active '97*, 373-380.

[41] Carme, C., Derrien, D. and De Man, P. (1997). A new generation of ANC headsets. In *Proceedings of Active '97*, 373-380.

[42] Adachi, S. and Sano, H. (1996). Application of two-degree-of-freedom type active noise control using IMC to road noise inside automobiles. In *proceedings of the 35th Conference on Decision and Control*, 2794-2795.

[43] Ho, Y., Kim, I., Chen, W. and Koopman, G.H. (1997). Active control of broadband sound transmission using feedback and feedforward techniques. In *Proceedings of Noise-Con '97*, 161-171.

[44] Sigurd, S and Postlethwaite, I. (1996). *Multivariable Feedback Control: Analysis and Design*. Wiley, Chichester.

[45] Juang, J. (1994). *Applied System Identification*. Prentice Hall, Englewood Cliffs, N.J.

[46] Hansen, C.H., Snyder, S. (1996). *Active Control of Noise and Vibration*. E&FN Spon.

[47] Skudrzyk, E. (1971). *The Fundamentals of Acoustics.* Springer-Verlag.

Appendix A

Fan Noise Model Validation Experiment

Detailed descriptions are given here for the experiment carried out to validate the modal force fan model presented in Chapter 1. The approach was to install a fan in a simulated infinite duct and to observe the expected asymmetric fan noise radiation. Figure A.1 below shows the experimental setup.

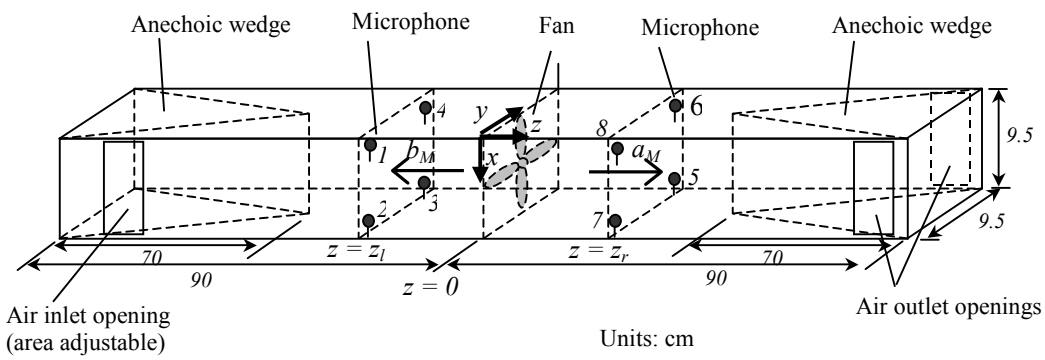

Figure A.1. Experimental setup

The pressure fields, p, over the cross-sectional planes at $z = z_r$ and $z = z_l$ to the right and the left side of the fan respectively are

$$\begin{aligned} p(x,y,z_r) &= \sum_M a_M e^{-jk_M z_r} \psi_M(x,y) \\ p(x,y,z_l) &= \sum_M b_M e^{+jk_M z_l} \psi_M(x,y) \end{aligned} \tag{A.1}$$

where a_M and b_M are the modal wave amplitudes and $\psi_M(x, y)$ is the mode shape function. For the fan model presented in Chapter 2, it is expected that the pressure field to the right

and to the left be asymmetric with respect to the fan source position at $z = 0$. This means that, for a given mode, M, the modal amplitudes, a_M and b_M, should be equal in magnitude but 180 degrees out of phase from each other.

In order to determine the modal amplitudes, a_M and b_M, four microphones were positioned at the four corners of each measurement plane as shown in Figure A.1. With the four microphones, one can determine modes up to $M = 4$ as follows.

With respect to the right side cross section at $z = z_r$, Equation (A.1) above can be written into a matrix format as

$$\begin{aligned} p(x,y,z_r) &= \begin{bmatrix} a_1 \\ a_2 \\ a_3 \\ a_4 \end{bmatrix}^T \cdot \begin{bmatrix} e^{-jk_1 z_r} & 0 & 0 & 0 \\ 0 & e^{-jk_2 z_r} & 0 & 0 \\ 0 & 0 & e^{-jk_3 z_r} & 0 \\ 0 & 0 & 0 & e^{-jk_4 z_r} \end{bmatrix} \cdot \begin{bmatrix} \psi_1(x,y) \\ \psi_2(x,y) \\ \psi_3(x,y) \\ \psi_4(x,y) \end{bmatrix} \\ &= \left[a_M\right] \cdot \left[e^{-jk_M z_r}\right]_{diag} \cdot \left[\psi_M(x,y)\right] \\ &= \mathbf{a_M} \cdot \mathbf{e}^{-} \cdot \boldsymbol{\psi}_{\mathbf{M}}(x,y) \end{aligned} \tag{A.2}$$

Given the measured pressures, p_1 to p_4, at the four microphone locations in the plane along with Equation (A.2), one obtains

$$\begin{bmatrix} p_1 & p_2 & p_3 & p_4 \end{bmatrix} = \mathbf{a_M} \cdot \mathbf{e}^{-} \cdot \begin{bmatrix} \boldsymbol{\psi}_{\mathbf{M}1} & \boldsymbol{\psi}_{\mathbf{M}2} & \boldsymbol{\psi}_{\mathbf{M}3} & \boldsymbol{\psi}_{\mathbf{M}4} \end{bmatrix} \tag{A.3}$$

where $\boldsymbol{\psi}_{\mathbf{M}i}$ is a 4x1 vector for the i-th microphone position. Then the 1x4 modal amplitude vector, $\mathbf{a_M}$, is obtained as

$$\mathbf{a_M} = \begin{bmatrix} p_1 & p_2 & p_3 & p_4 \end{bmatrix} \cdot \left(\mathbf{e}^{-} \cdot \begin{bmatrix} \boldsymbol{\psi}_{\mathbf{M}1} & \boldsymbol{\psi}_{\mathbf{M}2} & \boldsymbol{\psi}_{\mathbf{M}3} & \boldsymbol{\psi}_{\mathbf{M}4} \end{bmatrix} \right)^{-1} \tag{A.4}$$

The modal wave amplitudes, b_M, on the other side are also obtained similarly from the microphone pressures, p_5 to p_8.

The complex pressures for the all eight microphones, p_1 to p_8, were determined by measuring the transfer functions, H_{i1}, between the 1st microphone to the rest of the microphones. That is, the 1st microphone served as a reference. Then, the complex pressure at the i-th microphone, p_i, was determined by

$$p_i = H_{i1} \cdot p_1 \tag{A.5}$$

And the complex pressure at the 1st microphone, p_1, was obtained by

$$p_1 = |p_1| \cdot e^{j0} = \sqrt{2} \cdot \sqrt{G_{xx1}} \tag{A.6}$$

where G_{xx1} is the measured autospectrum of the 1st microphone pressure.

During the actual measurements of the transfer functions, H_{i1}, it was necessary to avoid the spectrum averaging process, which is usually utilized for transfer function estimations. This is because of the observations that the obtained coherence values were high (close to 1) only in the low frequency range up to about 1800 Hz blew the cut-on frequencies of the cross-modes ($M=2, 3$). At frequencies higher than 1800 Hz, the coherence values dropped abruptly and significantly (less than 0.2), indicating the associated transfer functions data were unreliable at these frequencies. This behavior was an indication that there was no consistency in relative phase relations between the modes, (i.e. not correlated).

In order to circumvent this problem, *instantaneous* transfer function values, H_{i1k}, were obtained from a single sampling of time data (say, k-th), and then, based on this data, the *instantaneous* modal wave vectors, $\mathbf{a}_{\mathbf{M}k}$ and $\mathbf{b}_{\mathbf{M}k}$ were determined. Then, after repeating this for N samples, the averages were taken for the relative magnitudes and the relative phases of each corresponding entry (i.e. mode) of the two modal vectors, $\mathbf{a}_{\mathbf{M}k}$ and $\mathbf{b}_{\mathbf{M}k}$. That is,

$$E\left[\left|\frac{a_M}{b_M}\right|\right] = \frac{1}{N}\sum_k^N \left|\frac{a_{Mk}}{b_{Mk}}\right| \quad , \quad E\left[\angle\frac{a_M}{b_M}\right] = \frac{1}{N}\sum_k^N \angle\frac{a_{Mk}}{b_{Mk}} \tag{A.7}$$

where $E[\ ]$ signifies the expected value. The calculated values of Equation (A.7) obtained for N=30 are provided in Figures 2.5 to 2.8 in Chapter 2, showing the relative magnitudes and the relative phases of the wave amplitudes, a_M and b_M, for M = 1 to 4. The expected asymmetric radiation characteristics can be observed clearly in the figure for M=1. The results are not as clear for higher-order modes (M=2 to 4) but the overall asymmetric trend can still be observed especially for M=2 and 3. It is possible that the further increase in the number of microphones may improve the results for the higher order modes. Nonetheless, the result gives a good degree of validation for the fan model.

Figure 2.9 in Chapter 2 shows the magnitudes of the estimated fan modal forces for M=1 to 4. These values were estimated from the average magnitudes of the modal wave amplitudes as

$$f_M = (a_M - b_M) \cdot S \approx (|a_M| + |b_M|) \cdot S \tag{A.8}$$

with an assumption that the wave amplitudes, a_M and b_M, are perfectly out-of phase (S is the duct cross-sectional area).

Appendix B

Numerical Determination of Duct Open End Modal Impedance Matrix

A method to numerically calculate the modal impedance of a rectangular open end is described here. An open end of a rectangular duct is shown below.

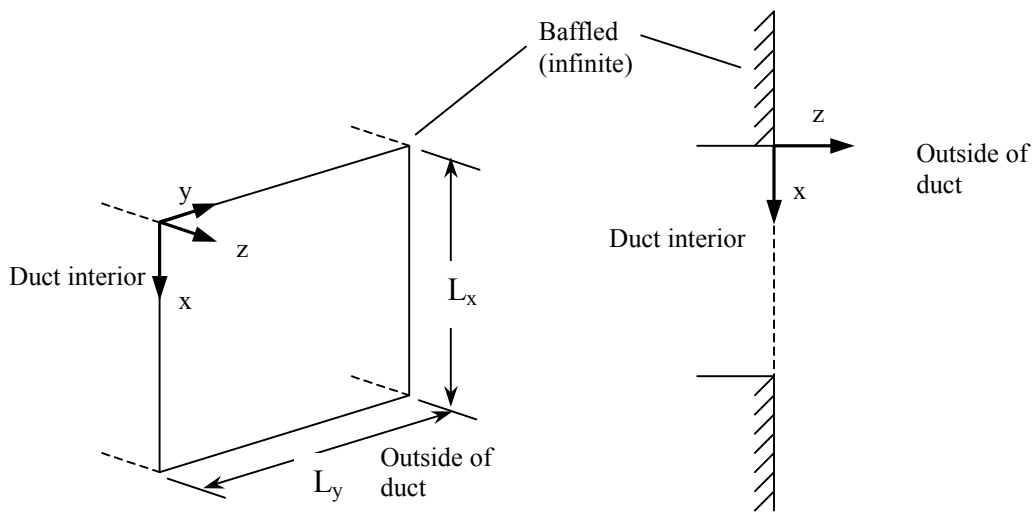

Figure B.1. Rectangular duct open end

The modal impedance from the *M*-th modal velocity to the *R*-th modal pressure is calculated by

$$z_{RM} = \frac{jk\rho c}{2\pi S} \int_S \int_{S_o} \frac{e^{-jk|\mathbf{r}-\mathbf{r_o}|}}{|\mathbf{r}-\mathbf{r_o}|} \cdot \Psi_R(\mathbf{r})\Psi_M(\mathbf{r_o})\, dS dS_o \tag{B.1}$$

where $|\mathbf{r}-\mathbf{r_o}|$ is the distance between the observation point (x, y) and the source point, point (x_o, y_o). For a rectangular open end shown in Figure B.1 above, the expression becomes

$$z_{RM} = \frac{jk\rho c}{2\pi L_x L_x} \int_0^{L_x}\int_0^{L_y}\int_0^{L_x}\int_0^{L_y} \frac{e^{-jk\sqrt{(x-x_o)^2+(y-y_o)^2}}}{\sqrt{(x-x_o)^2+(y-y_o)^2}} \Psi_R(x,y)\Psi_M(x_o,y_o)\,dxdydx_o dy \tag{B.2}$$

where

$$\Psi_R(x,y) = \frac{\cos(\frac{r_x\pi}{L_x}x)}{\sqrt{\Lambda_{r_x}}} \cdot \frac{\cos(\frac{r_y\pi}{L_y}y)}{\sqrt{\Lambda_{r_y}}}$$

$$\Psi_M(x_o,y_o) = \frac{\cos(\frac{m_x\pi}{L_x}x_o)}{\sqrt{\Lambda_{m_x}}} \cdot \frac{\cos(\frac{m_y\pi}{L_y}y_o)}{\sqrt{\Lambda_{m_y}}} \tag{B.3}$$

The usual numerical integration schemes, such as the Gaussian quadrature, cannot be applied directly due to the singularities that arise whenever (x, y)=(x_o, y_o). In order to circumvent the singularities, the following special integration scheme is used.

First, denote the integral as

$$I = \int_0^{L_x}\int_0^{L_y}\int_0^{L_x}\int_0^{L_y} \frac{e^{-jk\sqrt{(x-x_o)^2+(y-y_o)^2}}}{\sqrt{(x-x_o)^2+(y-y_o)^2}} \Psi_R(x,y)\Psi_M(x_o,y_o)\,dxdydx_o dy_o \tag{B.4}$$

Subdividing the domain of integration over the open end surface into smaller rectangular elements, the quantity, I, is then calculated by

$$I = \sum_u \sum_v I_{uv} \tag{B.5}$$

where I_{uv} is

$$I_{uv} = \int_{S_u}\int_{S_v} \frac{e^{-jk\sqrt{(x_u - x_v)^2 + (y_u - y_v)^2}}}{\sqrt{(x_u - x_v)^2 + (y_u - y_v)^2}} \Psi_R(x_u, y_u)\Psi_M(x_v, y_v)dx_u dy_u dx_v dy_v \tag{B.4}$$

which is calculated for all combinations of the v-th source element and the u-th observation element. The observation and the source coordinates, (x, y) and (x_o, y_o), are respectively denoted as (x_u, y_u) and (x_v, y_v) for the purpose of subsequent discussions. When the source element and the observation element are the same (i.e. $u = v$), then the integration of the quantity, I_{uv}, is carried out by directly applying Gaussian quadrature since there are no singularities in that case.

As a review of Gaussian Quadrature method, an integration over a rectangular area bounded by $x = [a_x, b_x]$ and $y = [a_y, b_y]$, for example, is calculated by first transforming the coordinate as

$$I = \int_{a_x}^{b_x}\int_{a_y}^{b_y} F(x, y)dxdy = \int_{-1}^{1}\int_{-1}^{1} F(\xi, \eta)J\, d\xi d\eta \tag{B.5}$$

where J is the determinant of a Jacobian matrix, which is a constant for this particular case and given by

$$J = \frac{1}{4}(b_x - a_x)(b_y - a_y) \tag{B.6}$$

And the mapping between the original rectangular domain and the square-shaped domain which is bounded by $\xi = [-1, 1]$ and $\eta = [-1, 1]$, is

$$x = \frac{(\xi + 1)b_x + (1 - \xi)a_x}{2} \quad , \quad y = \frac{(\eta + 1)b_y + (1 - \eta)a_y}{2} \tag{B.7}$$

Then, the integration of Equation (B.5) is calculated by

$$I = \sum_{j=1}^{4}\sum_{i=1}^{4} w_i w_j F(\xi_i, \eta_j)J = [w_i]^T \cdot [F(\xi_i, \eta_j)] \cdot [w_j]J \tag{B.6}$$

where w_i and w_j are the pre-determined weights corresponding to Gaussian points, (ξ_i, η_j).

For the case of Equation (B.4), Gaussian quadrature is applied as

$$\begin{aligned} I_{uv} &= \int_{S_v}\left(\int_{S_u} F(x_u, y_u, x_v, y_v)dx_u dy_u\right)dx_v dy_v = \int_{S_v} \hat{I}_{uv}(x_v, y_v)dx_v dy_v \\ &\approx [w]^T \cdot \left[\hat{I}_{uv}(x_{vi}, y_{vj})\right]\cdot[w]\cdot\left(0.25\cdot(b_{xv}-a_{xv})\cdot(b_{yv}-a_{yv})\right) \end{aligned} \tag{B.7}$$

where, $[w]$ is a 4x1 vector of weights, the quantity in parentasis is the determinant of the corresponding Jacobian matrix and $[\hat{I}_{uv}(x_{vi}, y_{vj})]$ is a 4x4 matrix containing the values of the inner integral for 4x4 Gaussian points, (x_{vi}, y_{vj}), over a source element, and obtained by

$$\left[\hat{I}_{uv}(x_{vi}, y_{vj})\right] = [w]\cdot\left[F(x_{ui}, y_{uj}, x_{vi}, y_{vj})\right]\cdot[w]\cdot\left(0.25\cdot(b_{xu}-a_{xu})\cdot(b_{yu}-a_{yu})\right) \tag{B.8}$$

where $[F]$ is a 4x4 matrix containing the values of the integrand of Equation (B.4) evaluated at the locations, (x_{ui}, y_{uj}) corresponding to Gaussian points, (ξ_i, η_j) over an observation element for a given source point, (x_{vi}, y_{vj}).

On the other hand, for $u \neq v$, the following procedure is carried out. As illustrated in Figure B.2, the observation element, u, is further subdivided into four triangular regions with the focal point of the triangles being a given source point, (x_{vi}, y_{vj}).

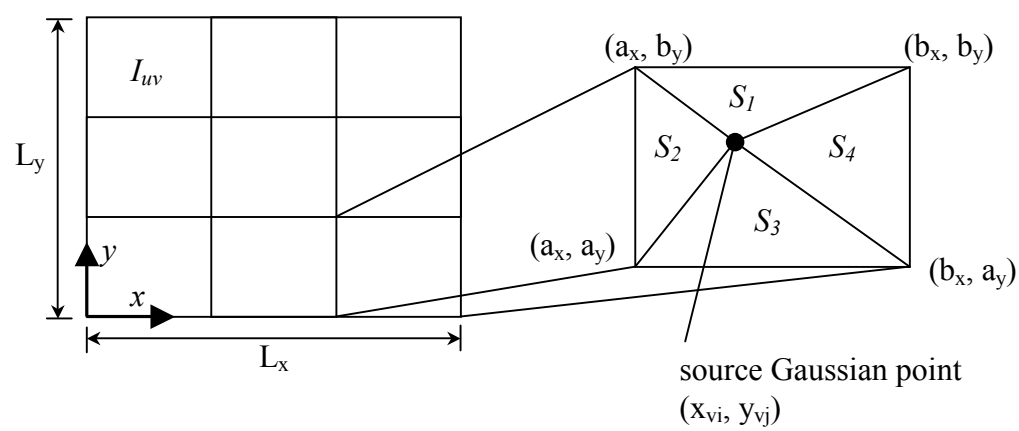

Figure B.2. Domain subdivisions

Then, the integral over the observation element, u, with respect to a given source Gaussian point is calculated by

$$\hat{I}_{uv}(x_{vi}, y_{vj}) = \int_{S_1} F(x_u, y_u, x_v, y_v)dx_u dy_u + \int_{S_2} F(x_u, y_u, x_v, y_v)dx_u dy_u$$
$$+ \int_{S_3} F(x_u, y_u, x_v, y_v)dx_u dy_u + \int_{S_4} F(x_u, y_u, x_v, y_v)dx_u dy_u \tag{B.9}$$

Utilizing Gaussian quadrature, this becomes

$$\hat{I}_{uv}(x_{vi}, y_{vj}) = \sum_{n=1}^{4} \left([w]^T \cdot \left[F(x_{ui}, y_{uj}, x_{vi}, y_{vj}) \cdot \left| \mathbf{J}(x_{ui}, y_{uj}, x_{vi}, y_{vj}) \right| \right] \cdot [w] \right) \tag{B.10}$$

where $[w]$ is a 4x1 vector of Gaussian weights and the quantity in the middle is a 4x4 matrix of the integrand in Equation (B.4) evaluated at 16 observation Gaussian points, (x_{ui}, y_{uj}), for a given source Gaussian point, (x_{vi}, y_{vj}).

The integrations are again carried out in a square domain bounded by ξ = [-1, 1] and η = [-1, 1]. However, the mapping between the original *triangular* domain and the square domain is given, in this case, as

$$\begin{bmatrix} x \\ y \end{bmatrix} = \begin{bmatrix} x_{vi} & x_{vj} & b_x & a_x \\ y_{vj} & y_{vj} & b_y & b_y \end{bmatrix} \cdot \begin{bmatrix} \psi_1(\xi,\eta) \\ \psi_2(\xi,\eta) \\ \psi_3(\xi,\eta) \\ \psi_4(\xi,\eta) \end{bmatrix} \quad \text{for } S_1$$

$$\begin{bmatrix} x \\ y \end{bmatrix} = \begin{bmatrix} a_x & x_{vi} & x_{vi} & a_x \\ a_y & y_{vj} & y_{vj} & b_y \end{bmatrix} \cdot \begin{bmatrix} \psi_1(\xi,\eta) \\ \psi_2(\xi,\eta) \\ \psi_3(\xi,\eta) \\ \psi_4(\xi,\eta) \end{bmatrix} \quad \text{for } S_2 \tag{B.11}$$

$$\begin{bmatrix} x \\ y \end{bmatrix} = \begin{bmatrix} a_x & b_x & x_{vi} & x_{vi} \\ a_y & a_y & y_{vj} & y_{vj} \end{bmatrix} \cdot \begin{bmatrix} \psi_1(\xi,\eta) \\ \psi_2(\xi,\eta) \\ \psi_3(\xi,\eta) \\ \psi_4(\xi,\eta) \end{bmatrix} \quad \text{for } S_3$$

$$\begin{bmatrix} x \\ y \end{bmatrix} = \begin{bmatrix} x_{vi} & b_x & b_x & x_{vi} \\ y_{vj} & a_y & b_y & y_{vj} \end{bmatrix} \cdot \begin{bmatrix} \psi_1(\xi,\eta) \\ \psi_2(\xi,\eta) \\ \psi_3(\xi,\eta) \\ \psi_4(\xi,\eta) \end{bmatrix} \quad \text{for } S_4$$

and

$$\begin{aligned} \psi_1(x,y) &= \frac{1}{4}(1-\xi)(1-\eta) \quad , \quad \psi_2(x,y) = \frac{1}{4}(1+\xi)(1-\eta) \\ \psi_3(x,y) &= \frac{1}{4}(1+\xi)(1+\eta) \quad , \quad \psi_4(x,y) = \frac{1}{4}(1-\xi)(1+\eta) \end{aligned} \tag{B.12}$$

The determinant of Jacobian matrix, $|\mathbf{J}|$ is

$$|\mathbf{J}| = \left\{ \sum_{n=1}^{4} x_{cn} \frac{\partial \psi_n}{\partial \xi} \right\} \left\{ \sum_{n=1}^{4} y_{cn} \frac{\partial \psi_n}{\partial \eta} \right\} - \left\{ \sum_{n=1}^{4} x_{cn} \frac{\partial \psi_n}{\partial \eta} \right\} \left\{ \sum_{n=1}^{4} y_{cn} \frac{\partial \psi_n}{\partial \xi} \right\} \tag{B.13}$$

where (x_{cn}, y_{cn}) are the x-y coordinate corresponding to the four corners of the square domain. It should be noted that, this time, $|\mathbf{J}|$, varies with the coordinate, (x, y), for a given source point (x_{vi} , y_{vj}). And it can be shown that the quantity, $|\mathbf{J}|$, becomes zero at the source point, (x_{vi} , y_{vj}). This effectively removes the singularity in Equation (10), which is the main reason for the procedure. Then, after determining Equation (B.10) this way for all source Gaussian points (x_{vi} , y_{vj}), the final quantity, I_{uv}, is determined by Equation (B.7).

The following figures show the calculated values of *normalized* modal impedances, $Z_{RM}/\rho c$, for some selective modes (R, M) with L_x = 9.5 and L_y = 9.4 cm.

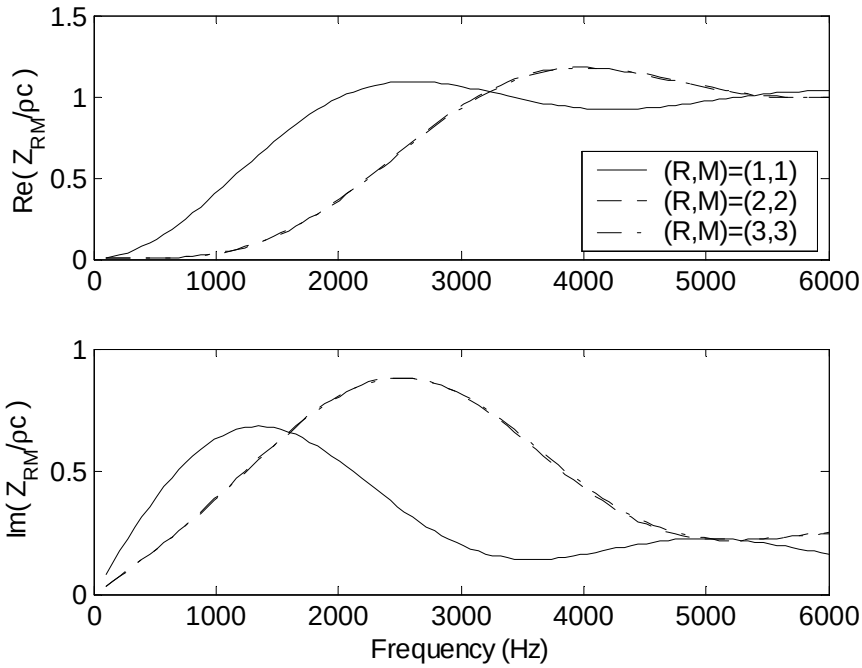

(a)

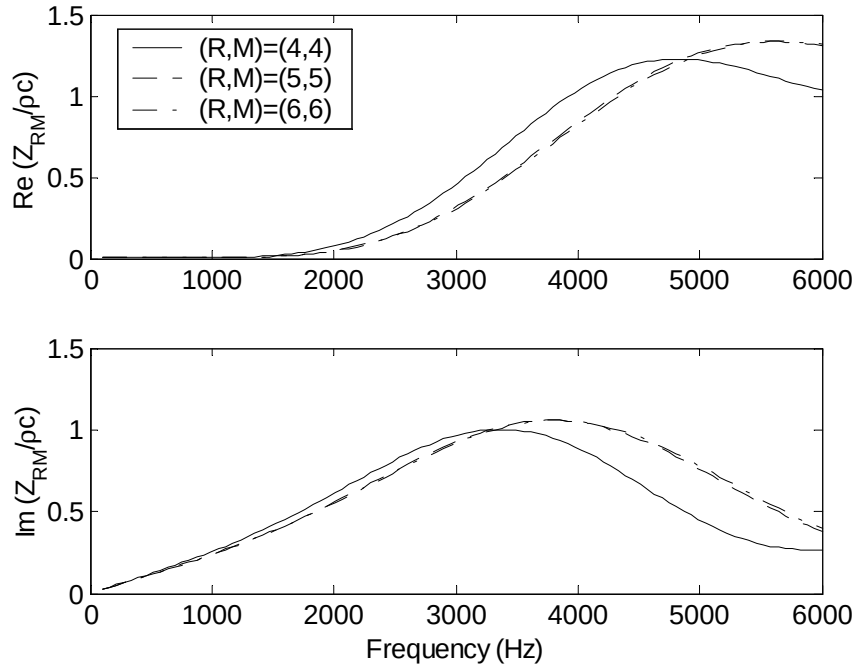

(b)

Figure B.3. Calculated open end modal impedance, Z_{RM}, for selected direct modes

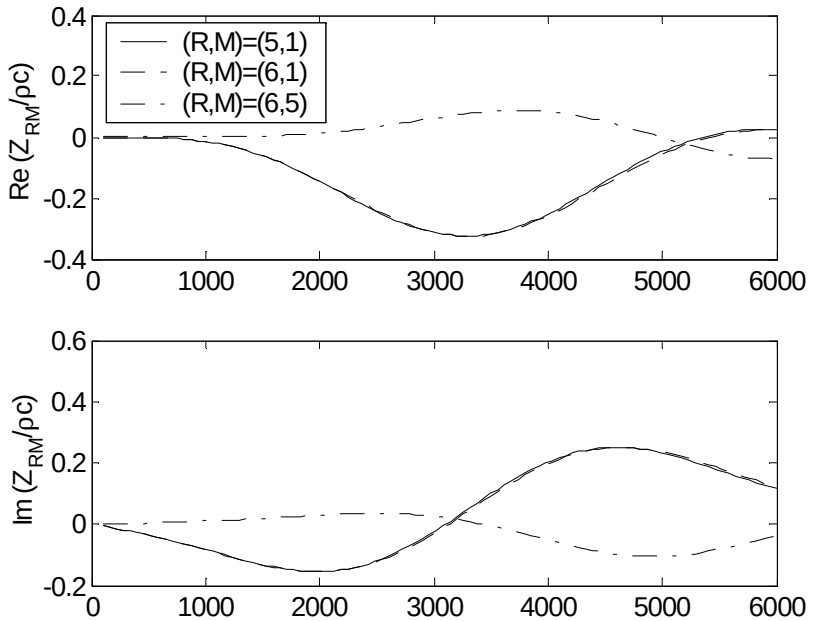

(a)

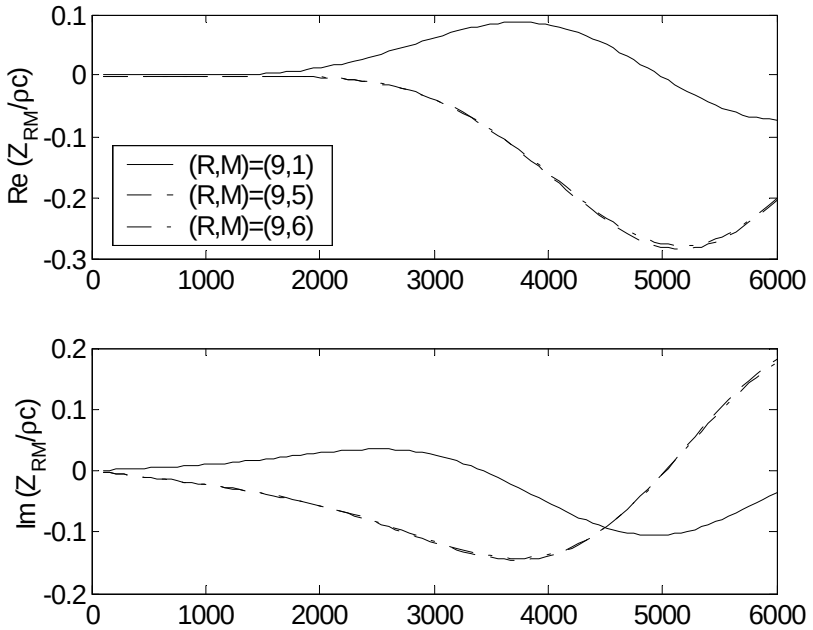

(b)

Figure B.4. Calculated open end modal impedance, Z_{RM}, for selected cross modes

Appendix C

Eigensystem Realization Algorithm

The Eigensystem Realization Algorithm (ERA) was used in Chapter 3 in order to obtain plant state space models based on analytical plant frequency responses. The ERA procedure is described here in detail.

First, an array of unit impulse response matrices is obtained by performing Fourier transform on the plant frequency response matrices, $\mathbf{G}(f_i)$. The number of the columns and the rows of the matrix, $\mathbf{Y}(t_i)$, are m and n for m-output-n-input plant. The unit impulse response matrices, $\mathbf{Y}(t_i)$, are also called Markov parameters and have the following properties.

$$\begin{aligned}
&\mathbf{Y}(t_0) = \mathbf{Y}_0 = \mathbf{D} \\
&\mathbf{Y}(t_1) = \mathbf{Y}_1 = \mathbf{CB} \\
&\mathbf{Y}(t_2) = \mathbf{Y}_2 = \mathbf{CAB} \\
&\vdots \\
&\mathbf{Y}(t_k) = \mathbf{Y}_k = \mathbf{CA}^{k-1}\mathbf{B}
\end{aligned} \tag{C.1}$$

where the set of matrices, (**A**, **B**, **C**, **D**) constitute a discrete state space plant model. Note that **D** matrix is directly obtained from $\mathbf{Y_o}$, and the remaining task is to identify the matrices, **A**, **B** and **C**. This is achieved as follows.

A generalized Hankel matrix, **H(0),** is formed by

$$\mathbf{H(0)} = \begin{bmatrix} \mathbf{Y}_1 & \mathbf{Y}_2 & \cdots & \mathbf{Y}_q \\ \mathbf{Y}_2 & \mathbf{Y}_3 & & \\ \vdots & & \ddots & \\ \mathbf{Y}_p & & & \mathbf{Y}_{p+q-1} \end{bmatrix} \tag{C.2}$$

where is pm-by-qn for m outputs and n inputs and p and q are chosen such that $qr \geq pm$. Combining Equation (C.2) and (C.1),

$$\mathbf{H(0)} = \begin{bmatrix} \mathbf{CB} & \mathbf{CAB} & \cdots & \mathbf{CA}^{q-1}\mathbf{B} \\ \mathbf{CAB} & \mathbf{CA}^{2}\mathbf{B} & & \vdots \\ \vdots & & \ddots & \vdots \\ \mathbf{CA}^{p-1}\mathbf{B} & \cdots & \cdots & \mathbf{CA}^{p+q-2}\mathbf{B} \end{bmatrix} \tag{C.3}$$

which can then be decomposed as

$$\mathbf{H(0)} = \mathbf{P}_p \cdot \mathbf{Q}_q = \begin{bmatrix} \mathbf{C} \\ \mathbf{CA} \\ \mathbf{CA}^{2} \\ \vdots \\ \mathbf{CA}^{p-1} \end{bmatrix} \cdot \begin{bmatrix} \mathbf{B} & \mathbf{AB} & \mathbf{A}^{2}\mathbf{B} & \cdots & \mathbf{A}^{q-1}\mathbf{B} \end{bmatrix} \tag{C.4}$$

where $\mathbf{P}_p$ is the observability matrix and $\mathbf{Q}_q$ is the controllability matrix.. In order to obtain the matrices, $\mathbf{P}_p$ and $\mathbf{Q}_q$, a singular value decomposition can be performed on **H(0)** as

$$\mathbf{H(0)} = \mathbf{R} \cdot \mathbf{\Sigma} \cdot \mathbf{S}^{T} \tag{C.5}$$

where the columns of the matrices, **R** and **S**, are orthonormal and **Σ** is a diagonal matrix with singular values, σ_i,

$$\mathbf{\Sigma} = \begin{bmatrix} \sigma_1 & 0 & 0 \\ 0 & \sigma_2 & 0 \\ 0 & 0 & \ddots \end{bmatrix} \tag{C.6}$$

where singular values are ordered so that, $\sigma_1 \geq \sigma_2 \geq \ldots \geq \sigma_N$. If only the first n singular values and the corresponding column vectors of **R** and **S** are used, then the Hankel matrix **H(0)** becomes

$$\mathbf{H(0)} = \mathbf{R}_n \cdot \mathbf{\Sigma}_n \cdot \mathbf{S}_n^{\ T} \tag{C.7}$$

where

$$\mathbf{R}_n^{\ T}\mathbf{R}_n = \mathbf{I}_n = \mathbf{S}_n^{\ T}\mathbf{S}_n \tag{C.8}$$

where $\mathbf{I}_n$ is an identity matrix. Then the decomposition in the form of Equation (C.4) is then easily obtained from Equation (C.7) by

$$\mathbf{H(0)} = \mathbf{R}_n \cdot \mathbf{\Sigma}_n \cdot \mathbf{S}_n^{\ T} = \left(\mathbf{R}_n \cdot \mathbf{\Sigma}_n^{\ 1/2}\right) \cdot \left(\mathbf{\Sigma}_n^{\ 1/2} \cdot \mathbf{S}_n^{\ T}\right) \tag{C.9}$$

Thus, the observability and the controllability matrix are obtained as

$$\mathbf{P}_p = \left(\mathbf{R}_n \cdot \mathbf{\Sigma}_n^{1/2}\right) \quad , \quad \mathbf{Q}_q = \left(\mathbf{\Sigma}_n^{1/2} \cdot \mathbf{S}_n^T\right) \tag{C.10}$$

Once these matrices are obtained, then from Equation (C.4.), the **B** and **C** matrices of the state space model is obtained by

$$\mathbf{B} = \textit{first n columns of } \mathbf{Q}_r \quad , \quad \mathbf{C} = \textit{first m columns of } \mathbf{P}_p \tag{C.10}$$

The remaining matrix, **A**, is obtained by first forming a shifted Hankel matrix, **H**(1) as

$$\begin{aligned}
\mathbf{H(1)} &= \begin{bmatrix} \mathbf{Y}_2 & \mathbf{Y}_3 & \cdots & \mathbf{Y}_{q+1} \\ \mathbf{Y}_3 & \mathbf{Y}_4 & & \\ \vdots & & \ddots & \\ \mathbf{Y}_{p+1} & & & \mathbf{Y}_{p+q} \end{bmatrix} \\
&= \begin{bmatrix} \mathbf{CAB} & \mathbf{CA}^2\mathbf{B} & \cdots & \mathbf{CA}^q\mathbf{B} \\ \mathbf{CA}^2\mathbf{B} & \mathbf{CA}^3\mathbf{B} & & \vdots \\ \vdots & & \ddots & \vdots \\ \mathbf{CA}^p\mathbf{B} & \cdots & \cdots & \mathbf{CA}^{p+q-1}\mathbf{B} \end{bmatrix} \\
&= \mathbf{P}_p \cdot \mathbf{A} \cdot \mathbf{Q}_r = \left(\mathbf{R}_n \cdot \mathbf{\Sigma}_n^{1/2}\right) \cdot \mathbf{A} \cdot \left(\mathbf{\Sigma}_n^{1/2} \cdot \mathbf{S}_n^T\right)
\end{aligned} \tag{C.11}$$

Thus

$$\mathbf{A} = \left(\mathbf{R}_n \cdot \mathbf{\Sigma}_n^{1/2}\right) \cdot \mathbf{H(1)} \cdot \left(\mathbf{\Sigma}_n^{1/2} \cdot \mathbf{S}_n^T\right) \tag{C.12}$$

The order of the identified state-space model (**A**, **B**, **C**, **D**) is adjusted by choosing the number of singular values, *n*, in Equation (C.7). The equivalent continuous state space model ($\mathbf{A}_c$, $\mathbf{B}_c$, $\mathbf{C}_c$, $\mathbf{D}_c$), then, is obtained by

$$\begin{aligned}
\mathbf{A}_c &= log(\mathbf{A})/\Delta t \quad , \quad \mathbf{B}_c = \mathbf{A}_c(\mathbf{A}-\mathbf{I})^{-1}\mathbf{B} \\
\mathbf{C}_c &= \mathbf{C} \quad , \quad \mathbf{D}_c = \mathbf{D}
\end{aligned} \tag{C.13}$$

where Δt is the sampling time interval.

Appendix D

MIMO Feedback Control Design

More details are provided here on the feedback control design procedure performed in the analytical studies in Chapter 3. The process involved the Eigensystem Realization Algorithm, a MIMO system identification procedure described in the previous Appendix and the LQG optimal control design method described in Chapter 2. The involved steps were as follows:

1. Obtain MIMO plant frequency response matrices from the analytical model of the fan duct (see Chapter 3)
2. Convert the plant frequency response matrices into corresponding impulse response matrices (i.e. Markov parameters)
3. Perform the ERA (Eigensystem Realization Algorithm) system identification procedure (see Appendix C) on the plant impulse response matrices and obtain a plant state space model
4. Use the LQG optimal control design method (see Chapter 2) to determine a feedback controller transfer function based on the plant state space model.
5. The performance of the determined feedback controller is checked by using the original plant frequency responses of Step 1 above.

In Chapter 3, a separate feedback controller was designed for each plant associated with the particular microphone position. Since it is not practical to present all the intermediate results produced by the above steps for all iterations, only the results for a selected plant case are provided below with respect to each of the two fan duct design cases, namely the non-segmented fan duct with 2x2 control and the segmented fan duct with 8x8 control.

D.1. Non-segmented duct with 2x2 control (Chapter 3, Section 3.1)

Figure D.1 to D.7 show the intermediate results produced during the feedback control design process for the non-segmented fan duct with 2x2 control described in Section 3.1 of Chapter 3. The results shown correspond to the case of $\chi = 0.2$. The duct had a total of two microphones and two speakers and therefore the associated plant was a two-input-two-output system.

The first step was to obtain a state space model of the plant. The Eigensystem Realization Algorithm (ERA) was used for this purpose based on the plant impulse responses obtained by converting the frequency responses from the analytical plant model. Figure D.1 and D.2 show the frequency responses of the identified and the original plant for direct (input *i* to output *i*) and cross path (input *i* to output *j*), respectively. The order of the identified plant was 35. Figure D.3 shows the singular value plot of the identified plant model. Figure D.4 shows the singular value plot of the feedback controller (2x2) designed by the LQG design method. The order of this controller was the same as the plant model, which was 35. Figure D.5 shows the singular value plot of the corresponding open-loop transfer function matrix. Figure D.6 shows the singular value plot of the resulting sensitivity transfer function matrix, which indicates the noise reduction performance of the feedback control system. Figure D.7 shows the singular value plot of the sensitivity transfer function matrix obtained based on the original frequency responses (Step 5).

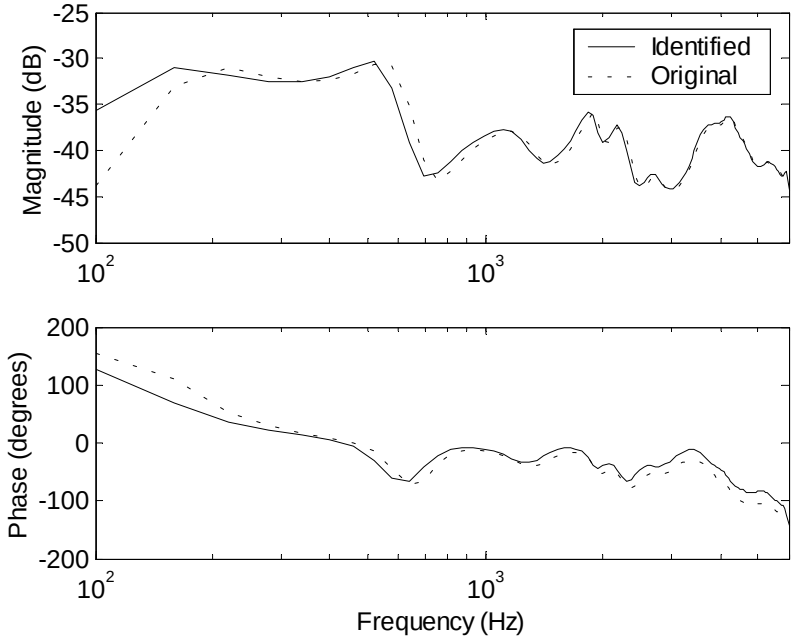

Figure D.1. Identified and original plant (direct path)

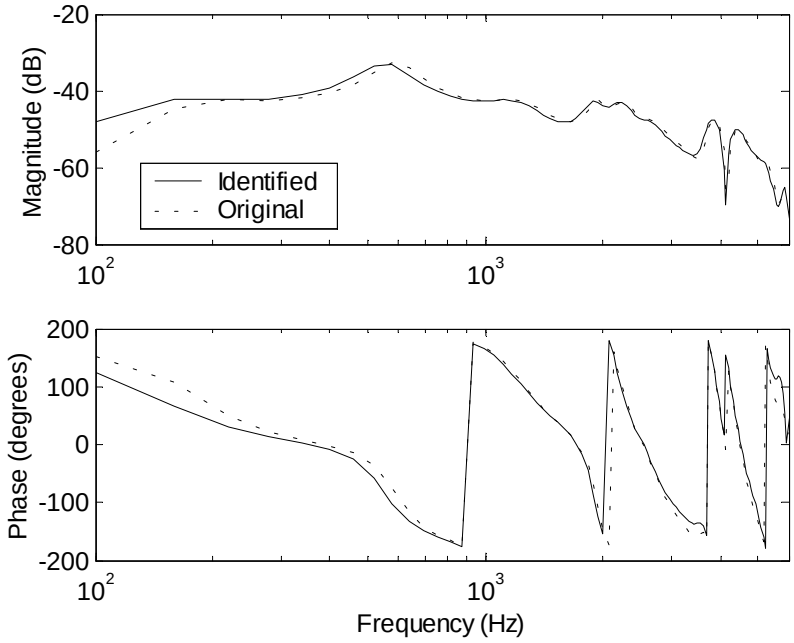

Figure D.2. Identified and original plant (cross path)

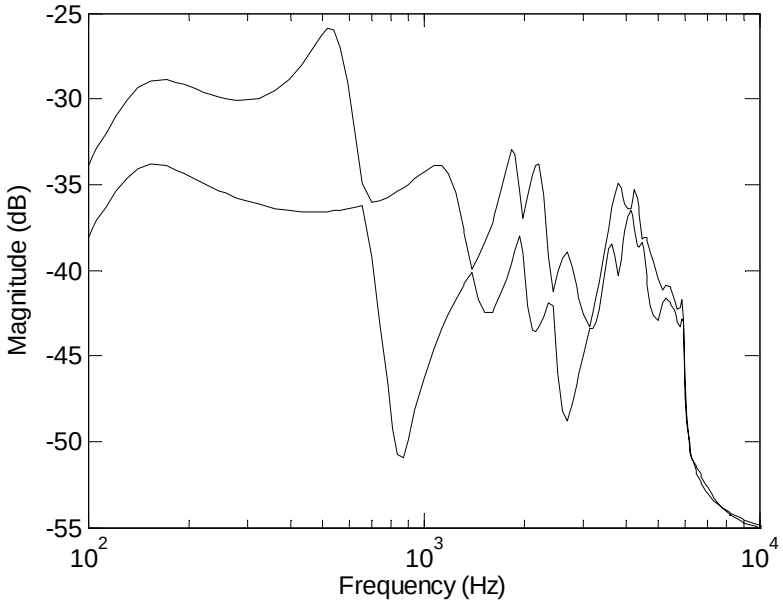

Figure D.3. Plant singular values

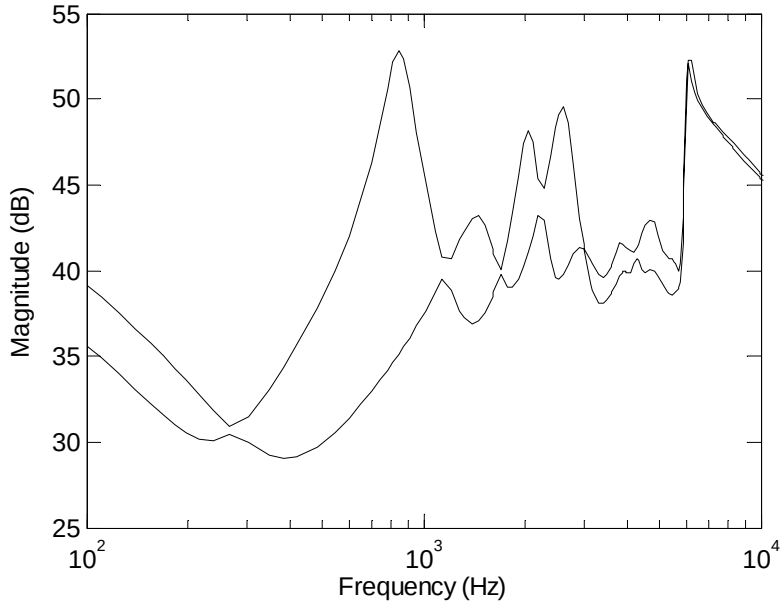

Figure D.4. Controller singular values

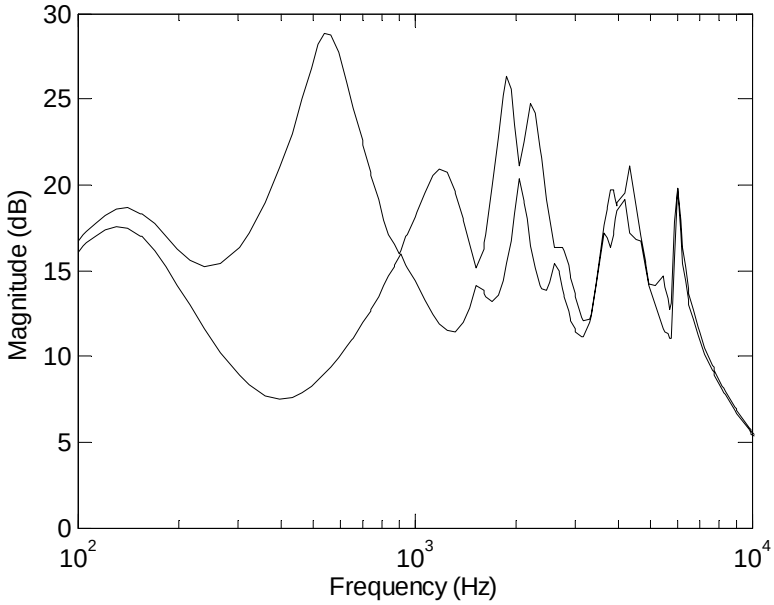

Figure D.5. Open loop singular values

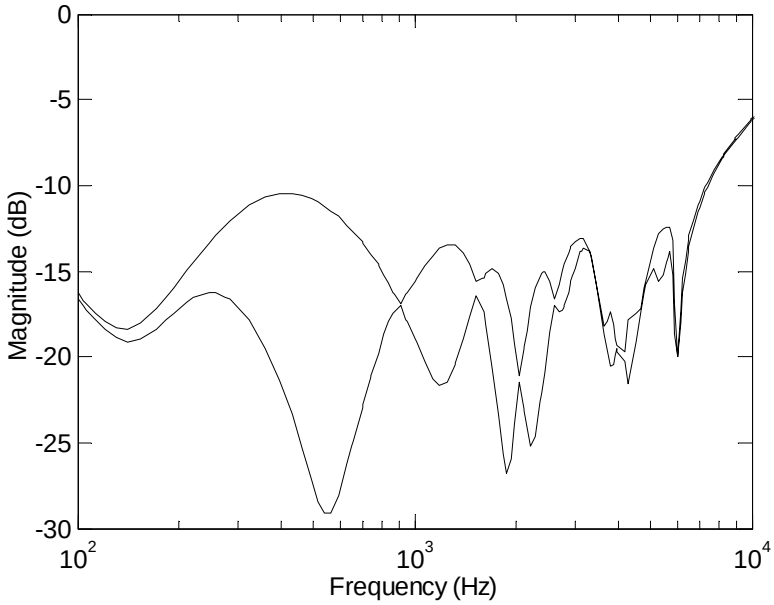

Figure D.6. Sensitivity singular values

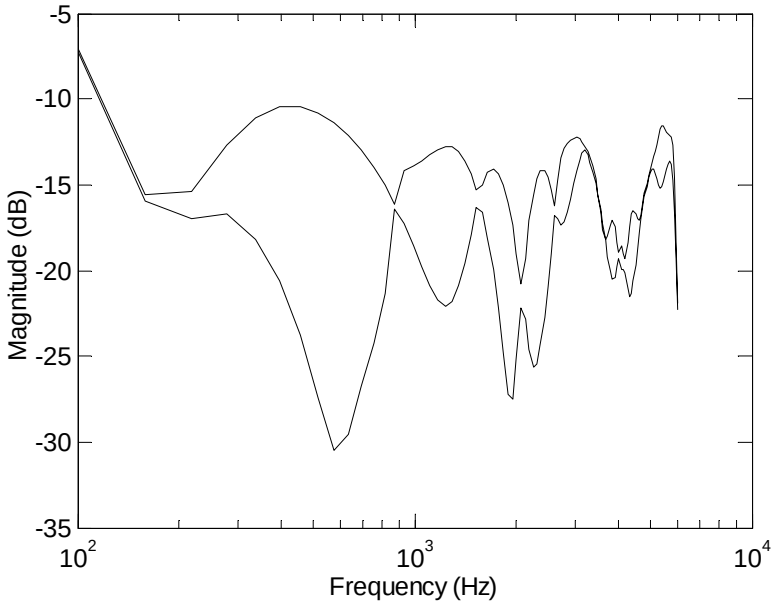

Figure D.7. Sensitivity singular values using original plant frequency responses

D.2. Segmented duct with 8x8 control (Chapter 3, Section 3.2)

The procedure is identical to the non-segmented duct case above except that the system is now 8x8 instead of 2x2. The following figures show the intermediate results obtained for the case of $\chi = 2$ (see Chapter 3 Section 3.2).

The sample frequency responses of the result of the ERA system identification of the plant are shown in Figure D.8 and D.9. The order of the identified plant model was set to 45. Figure D.10 shows the corresponding singular value plot of the identified plant model. Note that there are a total of eight singular values at each frequency corresponding to the 8x8 plant. Figure D.11 shows the singular value plot of the controller designed by the LQG design method and Figure D.12 shows the corresponding open loop singular value plot. Then the noise reduction performance are indicated by the singular value plot of the sensitivity transfer function matrix shown in Figure D.13. Figure 14 shows the sensitivity singular value plot obtained based on the original plant frequency responses.

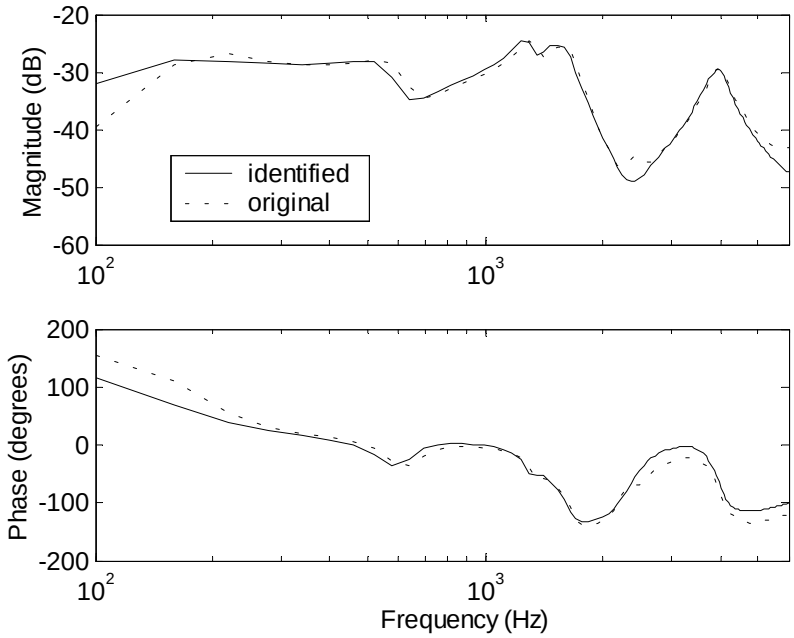

Figure D.8. Identified and original plant (direct path)

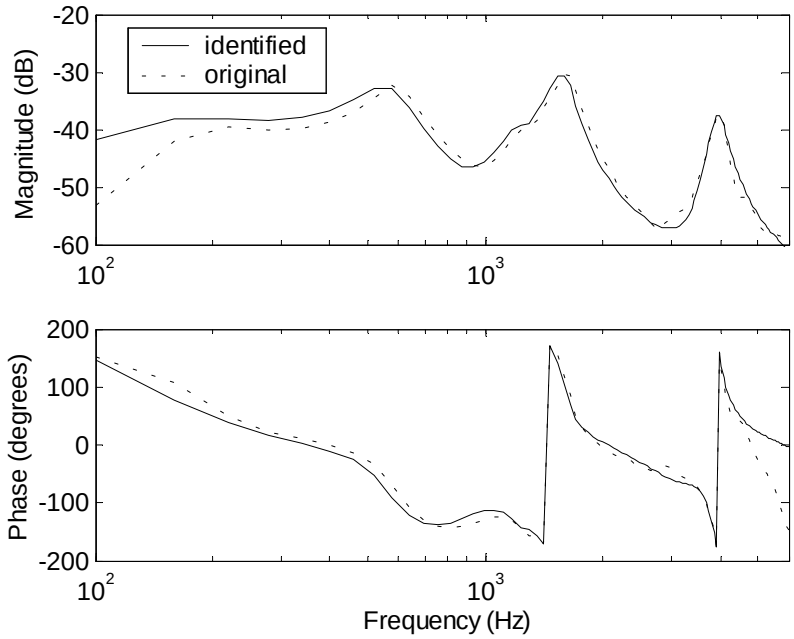

Figure D.9. Identified and original plant (cross path, input 1 to output 2)

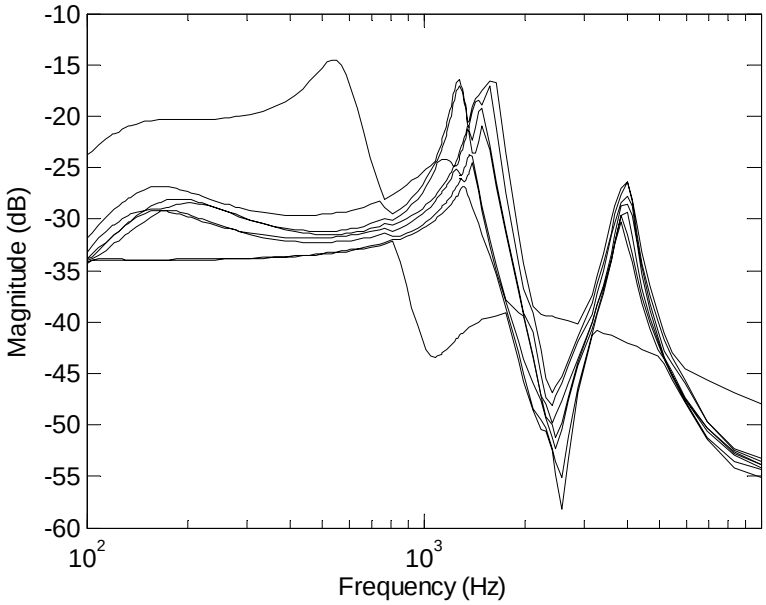

Figure D.10. Plant singular values

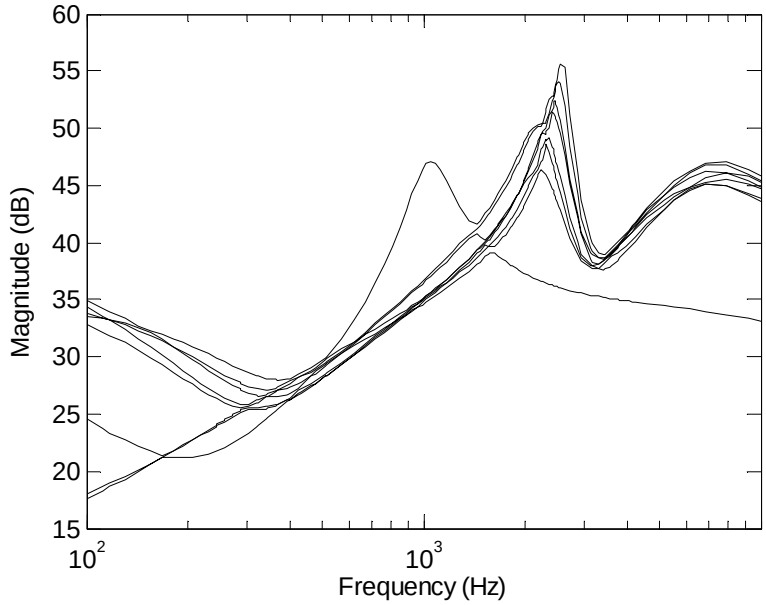

Figure D.11. Controller singular values

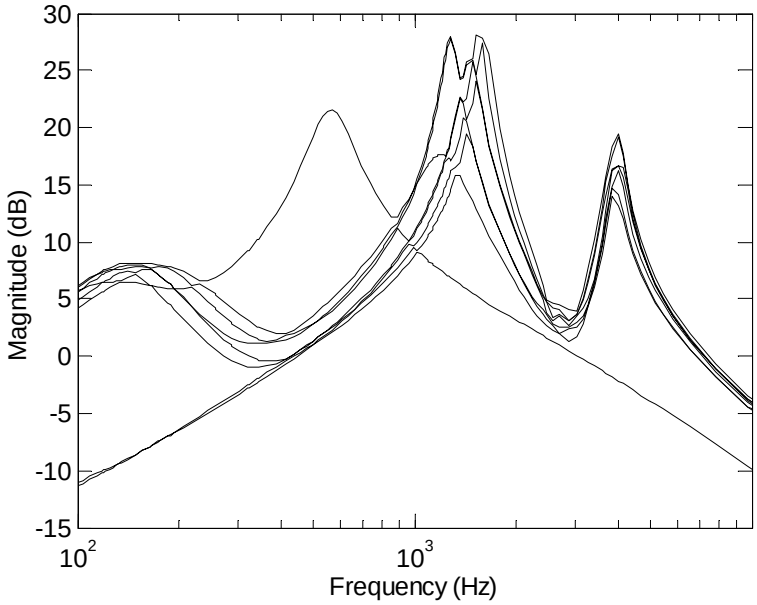

Figure D.12. Open loop singular values

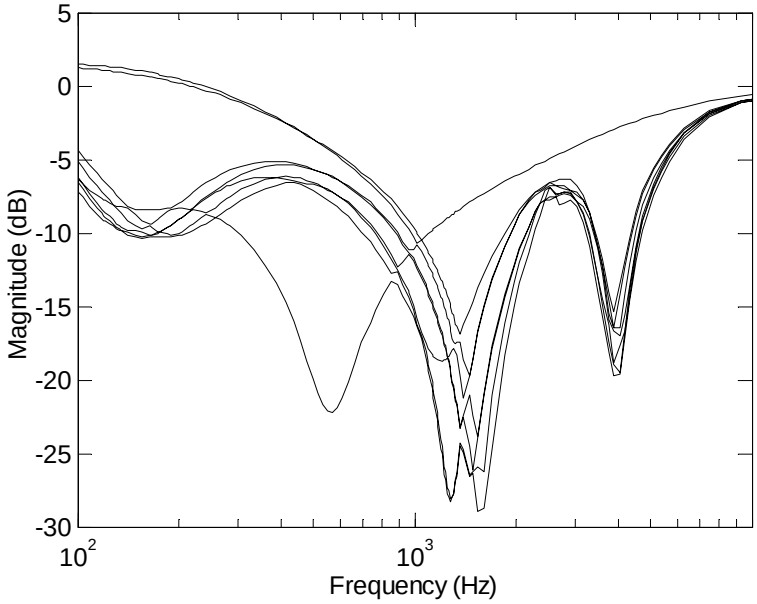

Figure D.13. Sensitivity singular values

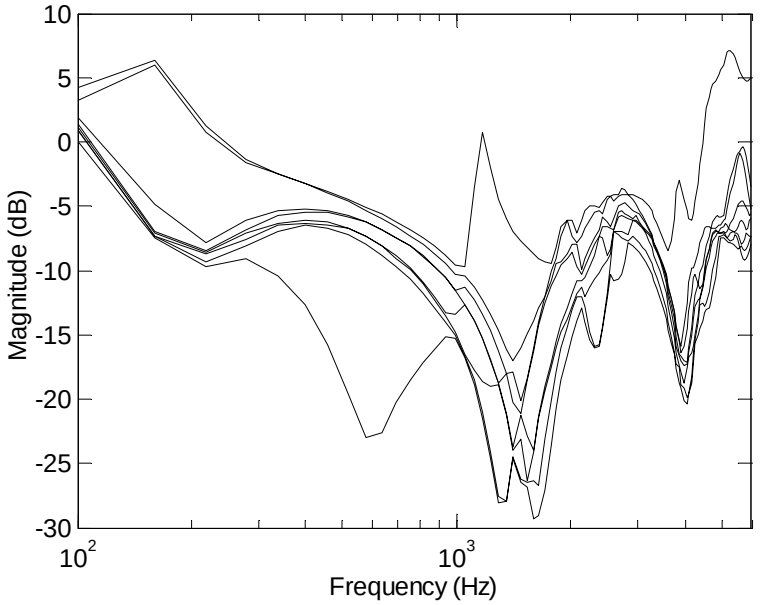

Figure D.14. Sensitivity singular values using original plant frequency responses

Appendix E

Controller Circuitry

The following figure shows the overall block diagram of the implemented hybrid feedforward-feedback controller. The controller combines eight independent channels of feedback control loops and a 2x2 digital feedforward controller.

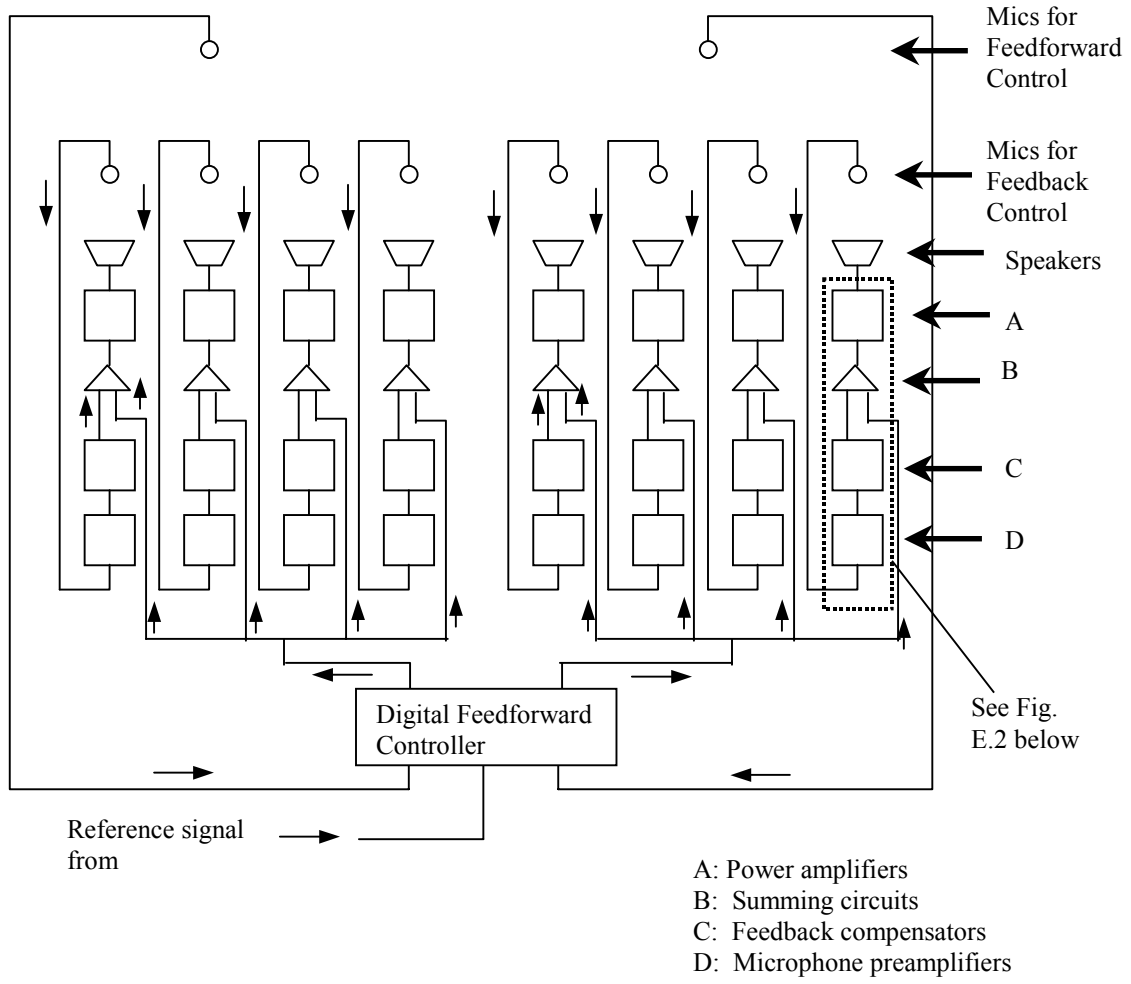

Figure E.1. Hybrid Feedforward-Feedback Controller

The following figures show the details of the feedback controller circuit (enclosed in dotted line) in the Figure E.1.

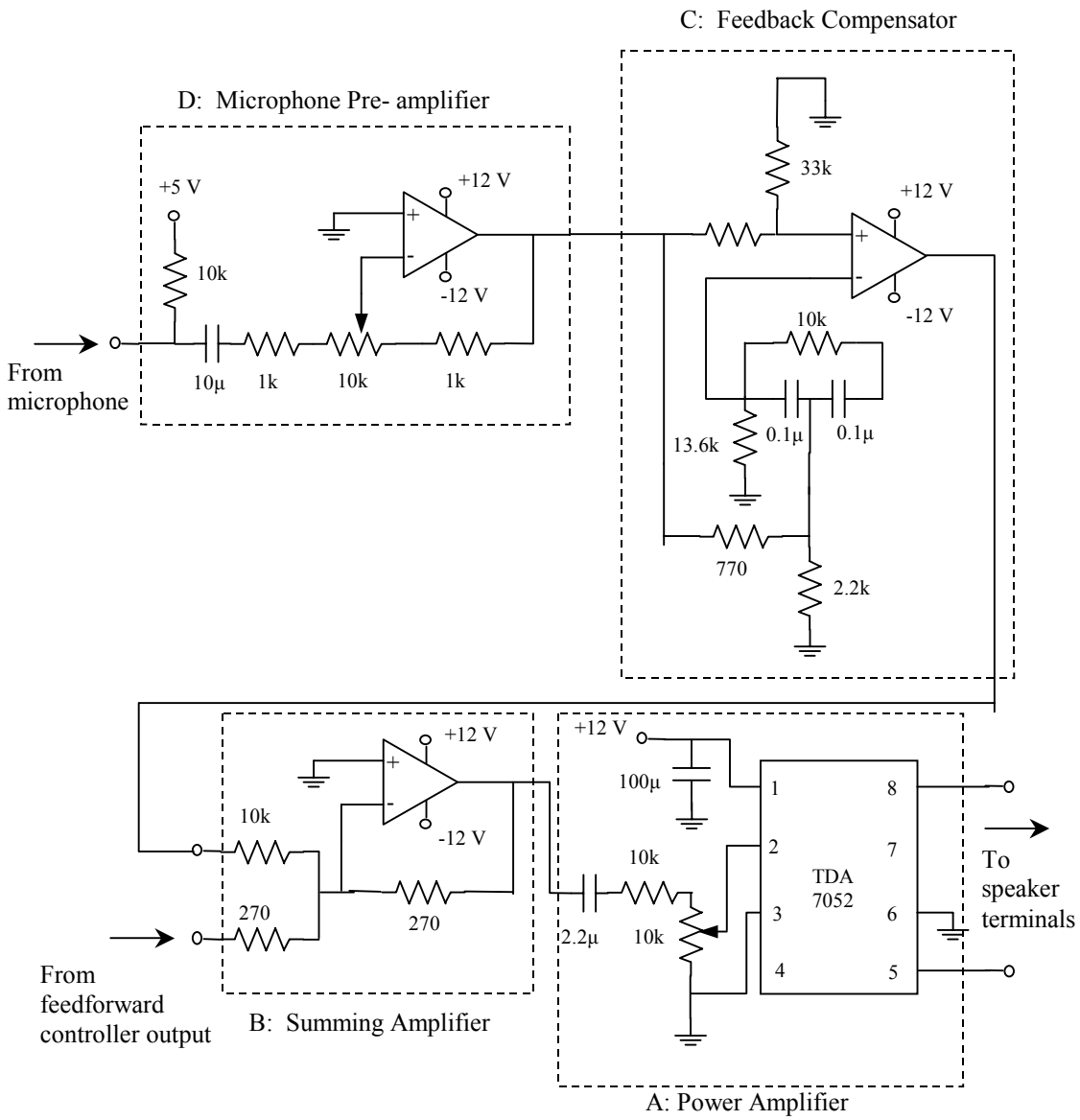

Figure E.2. Circuit detail

Figure E.3 below shows a photo image of the implemented analog circuit.

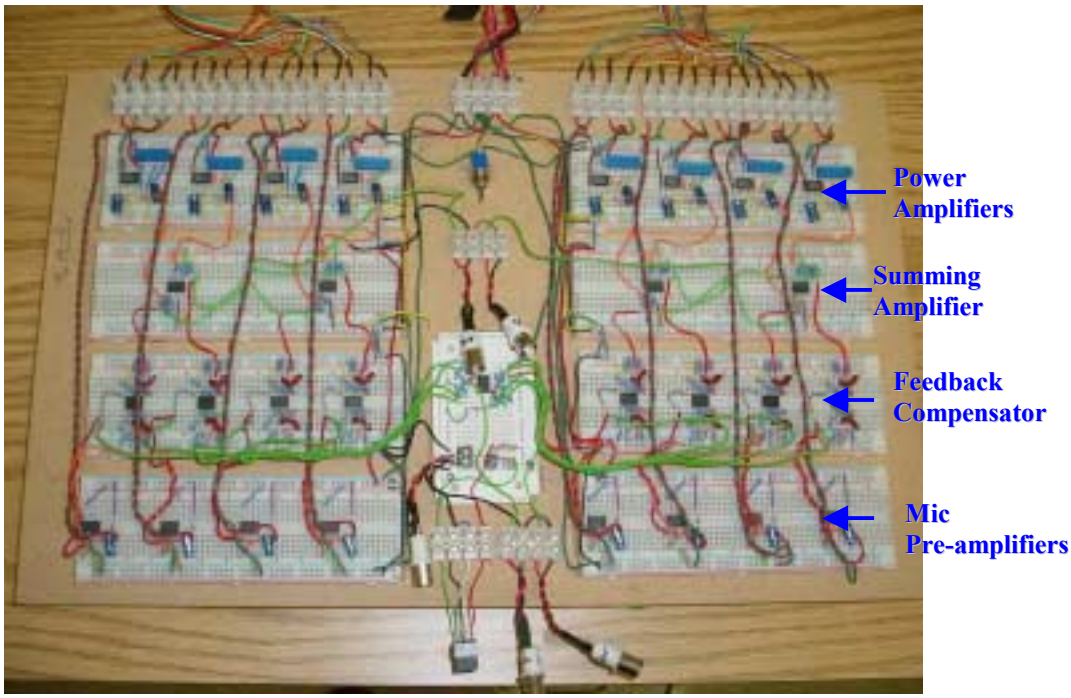

Figure E.3. Implemented analog circuitry

Vita

Kenji Homma was born on January 11, 1972 in Kawasaki, Japan. He came to the U.S. to attend college in March, 1992. He graduated from Texas Christian University in the U.S. with B.S. in mechanical engineering in May 1996. Then, he continued his education in mechanical engineering at Texas A&M University at College Station, TX, and received his M.S. in August 1998. After obtaining M.S. degree, he went back for a short period to Japan, then returned back to the U.S. in year 2000 to begin his Ph.D. study at Virginia Polytechnic Institute and State University. He graduated with Ph.D. in mechanical engineering under the supervision of Dr. Chris Fuller in September, 2004.